Fabrication of spin crossover nanocomposites and devices for electromechanical applications

Mario Piedrahita-Bello

Université Fédérale
Toulouse Midi-Pyrénées

THÈSE

En vue de l'obtention du

DOCTORAT DE L'UNIVERSITÉ DE TOULOUSE

Délivré par :

Université Toulouse 3 Paul Sabatier (UT3 Paul Sabatier)

Présentée et soutenue par :
Mario PIEDRAHITA BELLO
le vendredi 4 décembre 2020

Titre :

Fabrication de nanocomposites et dispositifs à transition de spin pour des applications électromécaniques

---

École doctorale et discipline ou spécialité :
ED SDM : Chimie organométallique de coordination - CO 043

Unité de recherche :
LCC - Laboratoire de Chimie de Coordination

Directeur/trice(s) de Thèse :

Lionel SALMON et Bertrand TONDU

Jury :
Prof. Anna Proust - Sorbonne Université - Rapporteuse
Prof. Daniel Talham - University of Florida - Rapporteur
Prof. Christophe Laurent - Université de Toulouse - Examinateur
Prof. Matteo Mannini - Università degli Studi di Firenze - Examinateur
Dr. Lionel Salmon - Université de Toulouse - Directeur de Thèse
Prof. Bertrand Tondu - Université de Toulouse - Codirecteur de Thèse
Dr. Azzedine Bousseksou - Université de Toulouse - Invité

To my brother.
Always move forward. Never look back.

Acknowledgements

My deepest thanks to:

All members of the jury: Prof. Anna Proust, Prof. Daniel Talham, Prof. Christophe Laurent and Prof. Matteo Mannini for their time and energy to read the manuscript and to participate in the defense of this thesis.

My supervisors Lionel Salmon and Bertrand Tondu for guiding me throughout this work and giving me to opportunity to take one step further in my scientific career. In particular, to Lionel for his support over these four years, his kind disposition and his keen insight; this work is a result of his constant guidance. His integrity, both as a person and a researcher, warm attitude and genuine, honest character have left a mark that will remain with me for years to come. I am deeply grateful to have been guided by him throughout these unforgettable years. I would also like to thank Gabor Molnar for his clever, creative insight that helped shape this work, and his direct, precise feedback, which helped steer my research work in the right direction. I would also like to thank William Nicolazzi for his amiable presence and invaluable smile. I also thank Azzedine Bousseksou both for giving me the opportunity to work in this group, in this project, and for his clear and concise vision, which guides the work of the team.

Everyone in the Switchable Molecular Materials Team (Equipe P) for their presence and support. They made this work much more enjoyable and their presence breathes life into this team: Sylvain, Lucie, Karl, Mirko, Alaa, Amalia, Yue, Barbora, Alin, Oleksandr, Shiteng, Yuteng, Lijun. Special thanks to Elias, Alejandro and Montserrat, a little corner of Mexico in Toulouse making this place a bit warmer.

Our collaborators, Remi Courson, Christophe Thibault and Laurent Malaquin, from the ELiA team at LAAS, Philippe Soueres from the Geppetto team at LAAS, Aurelian Rotaru of the University Stefan cel Mare of Suceava, and finally Philippe Demont and Baptiste Martin from the CIRIMAT team at the Paul Sabatier University,

Jean-Francois Meunier and Lionel Rechignat for their aid in magnetic and thermal measurements, Vincent Collière for electronic microscopy measurements and Laure Vendier for X-ray diffraction measurements.

The trainees who worked with me during this process: Florian Meunier, Adam Berrais, Gaspard Cereza and Zheng Zhou.

My friends both in Toulouse and elsewhere: Camila, Angelica, Rafael and many others who have supported me throughout these years and with whom I've shared both joy and sorrow. Without you this journey wouldn't have been possible.

My family, Doris, Mario and Santiago. You were the light that kept me from straying off, and I will keep you in my heart always. Thank you for being there for me at every step of the way. Even from a distance, your presence here was priceless.

Finally, to the memory of Cruz, in my heart always.

Table of contents

General introduction:

There is a great interest in material science for **switchable smart materials** [1]. Materials that can change their intrinsic properties in response to an external stimulus are highly sought-after, as well as multifunctional materials that change multiple properties in a reversible manner. The fabrication of smart devices employing these materials remains the most direct and attractive application of this principle.

Spin crossover (SCO) materials can be of particular interest in this domain due to their capability to reversibly modulate their properties [2]. Indeed, spin crossover materials can switch between a high spin (HS) and low spin (LS) state in a reversible manner when triggered by a series of different external stimuli: temperature, pressure, light, magnetic fields and the adsorption of a chemical compound. This reversible switching between the two molecular states of the material, which can be operated at controllable temperature, gives rise to a change in magnetic, optic and dielectric properties [3]. However, most interestingly for the present PhD research work, these materials can also **reversibly change the volume of their crystal lattice** by as much as 15% [4]. This volume change is very interesting as these materials have relatively high stiffness, affording them the possibility of exerting significant force. Nevertheless, spin crossover materials are crystalline, rigid and dielectric materials, which means that additional processing is necessary in order to integrate them into functional electrical devices.

A common approach that has been successfully employed before to effectively integrate spin crossover materials into functional devices is the **composite approach** [5]. Under this approach, spin crossover materials are incorporated into a matrix, granting the final material both the intrinsic switching of the spin crossover material and the properties of the matrix. Of special interest to us is the use of **polymer matrices** to confer spin crossover materials with properties more suited to **integration into soft devices**: flexibility and mechanical stability. **Spin crossover polymeric composites** have been used before and there is a wide variety of examples in the literature which have been proposed for a variety of different applications [6], however very little work has been done towards the exploitation of the volume change of the spin transition [7].

The first chapter of the present PhD work will concern a brief explanation of the spin crossover phenomenon, a review on the fabrication of spin crossover nanoparticles, well adapted for the fabrication of composite materials, and a state of the art on polymeric spin crossover composite and nanocomposite materials. This is mainly to lay down the groundwork towards their successful application in functional devices.

In the present work, we will focus our attention on the development of composite materials which synergistically employ the volume change of spin crossover materials for

different applications. The two main applications that will be worked upon are energy harvesting and electromechanical actuation. **In fact, the final goal of this work is the fabrication of energy harvester devices and artificial muscles which employ the volume change of the spin crossover phenomenon.**

Energy harvesting refers to recovering ambient energy lost in various processes to power electrical devices. A common example is a thermoelectric watch[8] which uses the body heat as a source of energy. In the present work however, we will employ **the piezoelectric effect coupled with the volume change of the spin transition** to fabricate materials which generate **electrical discharges from a thermal stimulus**. Indeed, by coupling the volume change of the spin transition with a piezoelectric material which produces an electrical discharge when mechanically activated, we can transform the volume change of the spin transition phenomenon into an electrical source of energy. In order to achieve this we will couple various spin crossover materials with P(VDF-TrFE) piezoelectric copolymer materials, via the composite approach.

Thus, the second chapter of this PhD work will first cover a brief introduction to energy harvesting, before going further in-depth into the strategies chosen to synergistically couple energy harvesting [9] to the spin crossover phenomenon. After this introduction, the chapter will then delve into the choice of spin crossover material for this application and the characterization of two generations of composite films fabricated with this principle and application as a goal.

The third chapter of this PhD work pertains the use of spin crossover materials as the basis for **artificial muscles** [10]. An artificial muscle is a device which can perform work and exert force in a reversible manner without the use of multiple pieces, just by stimulation of a material which intrinsically performs movement when activated. Spin crossover materials have been used before by the group in electromechanical applications as a proof of concept [11]. However in the present work we intend to take this work one step further, by going from thermally activated proofs of concept and micromechanical actuation to **actuation at the macroscale, employing spin crossover devices to perform work in an electrically driven, controllable, reliable and robust manner**.

To achieve this goal, we used a **bilayer approach** [12], using the mismatch of the thermal expansion between two layers of a material to cause reversible deformation and movement as a result . Two fabrication approaches were used to fabricate these bilayer devices: **3D printing and polymer casting**. On one hand, 3D printing allows for the incorporation of SCO materials into composites with highly controllable morphologies, and through this morphology control, fabricate thermal actuating bilayer devices. The solvent casting method on the other hand allows for the fabrication of conductive actuator devices, and in turn, electrical control of the fabricated devices, allowing for reliable and resilient actuation. The highly generic and adaptable technique lends itself well to an optimization process where, through smart material design, integration of **anisotropic particles multiply the effect of the actuation**. The use of an electrical control facilitates the integration of these muscles into a demonstrator device.

Thus, the third chapter of this research work will thus first give a brief introduction on materials used for artificial muscles applications and their different advantages and disadvantages. Then it will present spin crossover materials as a viable alternative that can be of value in the pool of materials commonly employed for this application. **In fact, the concomitant need for softness and force; adaptability and accuracy, is the key challenge of the field.** The chapter will then delve into the research process required to achieve 4D printed composite materials, conductive devices, optimization of the composition and reliable electrical control before finally showcasing the properties of the **fully realized artificial muscle and its application in a gripper device**.

Finally, the last section of this PhD work will be a general conclusion, summarizing the results of this work and outlining possible research perspectives that can be worked upon as a continuation of the present work.

Chapter I: Spin crossover composite materials: principle and state of the art

This chapter is an introduction to the present PhD research work. In it, the **concepts of spin crossover nanomaterials and composite materials** will be introduced and the latest state of the art in the topic will be explored. This chapter begins with a brief explanation of the spin crossover (SCO) phenomenon, from both a chemical and physical point of view. Particular attention will be given to the molecular basis of the phenomenon, namely the crystal field theory and thermodynamic considerations.

In order to better integrate the concept of the spin crossover phenomenon with that of composite materials, the solid-state dynamics of the phenomenon must be understood. As such, this chapter will then approach the topic of **SCO in the solid state**. A brief explanation will be detailed on a crucial concept for the understanding of the solid-state SCO: the cooperativity effect.

Having introduced the concept of SCO and their solid-state properties, this chapter will then delve into the subject of the Integration of SCO compounds into composites. Using SCO nanoparticles as fillers for the fabrication of these composites is a common approach, so a brief overview of **SCO nanoparticles and size effects** will be given. Composite materials are the main subject of this research work and as such, special attention will be given to previous work related to the development of **SCO composites**. The last section of this chapter concerns the main objectives of this research work, namely the fabrication of composite materials and devices for thermal harvesting and electromechanical applications. Indeed, the outstanding properties of SCO materials offer the possibility of their use as both **energy harvesters**, recovering thermal energy to be used to power electronic devices, or **artificial muscles**, exploiting their volume change to perform mechanical work.

I.1: The spin crossover phenomenon

The spin crossover (SCO) phenomenon consists of the reversible switching of a coordination complex between two electronic states: the high spin state (HS) and the low spin state (LS). This reversible switching is triggered by the influence of an external perturbation of the system [13–15]. This perturbation can be in the form of temperature, pressure [16], electromagnetic irradiation [17], the adsorption/desorption of a guest molecule [18] or the magnetic field [19].

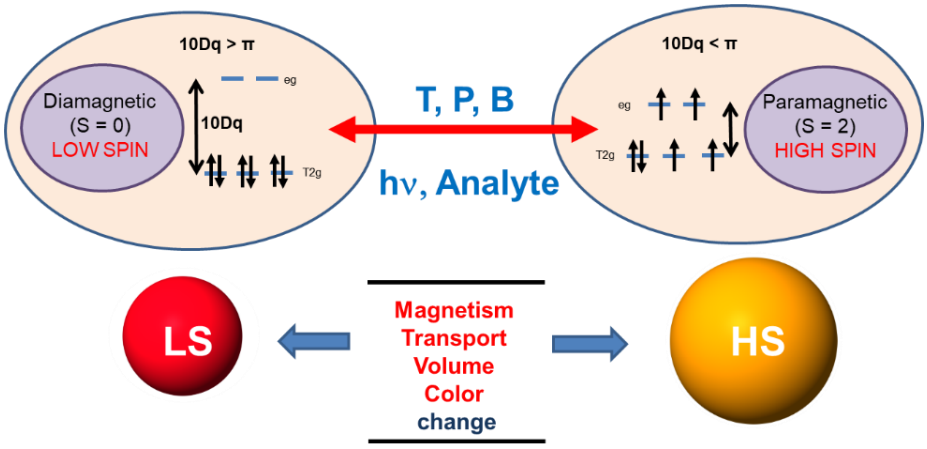

Fig 1.1) General outline of the SCO phenomenon for the case of Fe(II).

This phenomenon has been observed and characterized for a large variety of metallic complexes of transition metals with electronic configurations between $3d^4$ to $3d^7$ such as Fe(III), Co(II), Co(III), Cr(II), Mn(II), Mn(III), and finally the Fe(II) ion which is the one that has received the most scientific attention [20].

In the case of the Fe(II) ion, the change in electronic configuration leads to a change in magnetic properties, as the LS state is diamagnetic and the HS state is paramagnetic. However, this reversible switching does not entail only a change in electronic properties; it also causes the complex to change its optical properties and, most interestingly for this research work, its mechanical and structural properties. Specifically, we observe a change in the Young's modulus of the material [21] and a volume change of the crystalline structure [13–15]. This change in structural properties hints at the possibility of employing this phenomenon and exploiting the volume change for mechanical applications [11]; and indeed, such will be the focus of this research work.

I.1.1: Crystal Field Theory

Crystal field theory can be employed to understand the origin of the SCO phenomenon. Under crystal field theory, the interaction between the metallic center and the ligands is considered to be mainly electrostatic. The metallic ion is positively charged while the ligands play the role of negative charges. The electronic distribution of the ligands determines the external electrostatic field, which will in turn influence the transition metal core [22].

A commonly used exampled to illustrate this theory is the Fe(II) ion, which has the energy level of its five 3d orbitals in a degenerate state. This ion coincidentally is also the one used in the SCO systems that we study in this research work. A Fe(II) ion is placed in a field with a perfect octahedral geometry, formed by six negatively charged ligands. According to the crystal field theory, the population of the d orbitals will be determined by the minimization of the electrostatic interactions. As a result, there are two partially degenerate energy levels: the lower energy t_{2g} level, which has the degenerate orbitals d_{xy}, d_{xz} and d_{yz}, and the higher energy level e_g

which has the degenerate orbitals $d_{x^2-y^2}$ and d_{z^2} (Fig 1.2). The energy difference between those two levels is Δ_0, and is determined by the ligand field strength, which has a value of 10*Dq*. *Dq* is a semi empirical parameter associated to the strength of the ligand field, which depends on the metal-ligand distances *r* and the charge distribution around the metal ion [23].

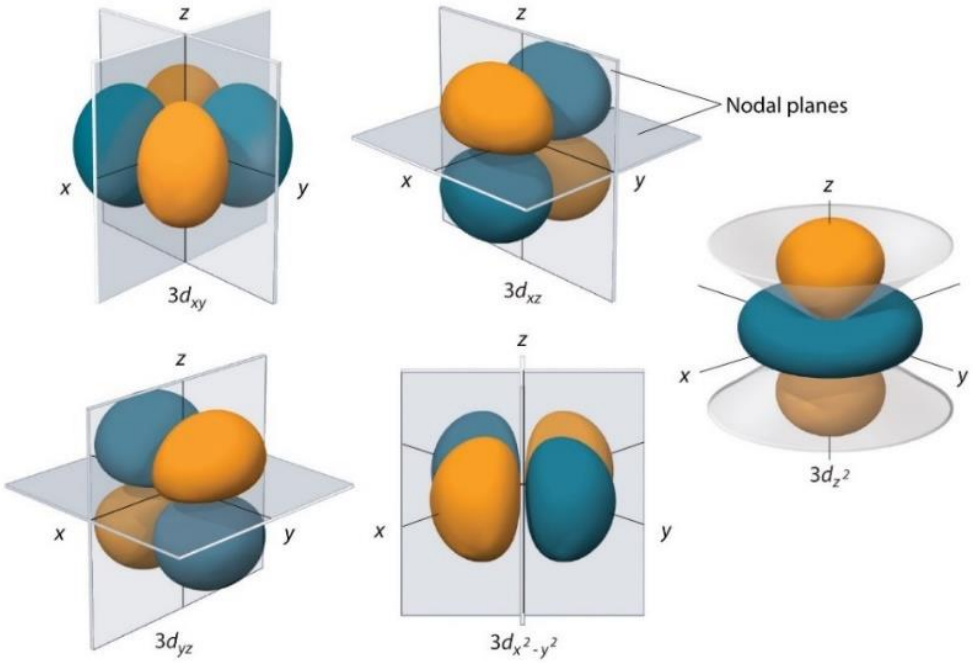

Fig 1.2) Schematic representation of the 3*d* orbitals.

From this theory, a simple mathematical model to explain the splitting of the energy levels arises in a natural fashion. However, the model does not properly account for non-charged ligands. It thus becomes necessary to incorporate another theory: the **ligand field theory** which uses the molecular orbital theory applied to a system composed of a metallic center in an octahedral complex. Taking into account covalent metal-ligand σ or π bonds, one arrives to a similar energy splitting to the one found by the crystal field theory.

According to this model, there are two competing effects in the electronic orbitals of the metallic ion. On the one hand, electrons will try to fill out the lower energy t_{2g} level first before filling out the e_g level, to minimize energy. On the other hand, electrons will try to follow Hund's rule and occupy unoccupied orbitals first, to minimize the electron pairing energy Π. As a result of these two effects, two possible configurations arise (Fig 1.3):

- If Π < 10*Dq*, that is to say, with a strong ligand field (such as in a $[Fe(CN)_6]^{4-}$ sphere), the lowest energy configuration is one where the t2g orbitals are completely occupied and the electrons do not follow Hund's rule. This is the Low Spin state (LS) and in the case of Fe(II) is a diamagnetic state with a spin S = 0.

- If Π > 10*Dq*, that is to say, with a weak ligand field (such as in a $Fe(H_2O)_6]^{2+}$ sphere), the lowest energy configuration is one where the electrons follow Hund's rule and are distributed

populating the highest possible number of orbitals. This is the High Spin state (HS) and in the case of Fe(II) is a paramagnetic state with a spin S = 2.

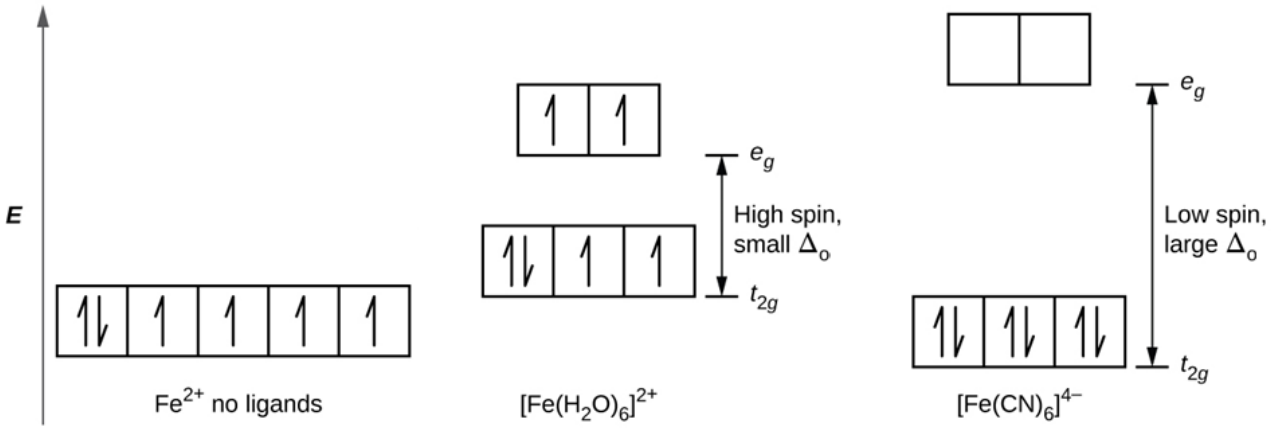

Fig 1.3) HS and LS states of Fe(II) complexes.

I.1.2: Thermodynamic component of the spin crossover phenomenon

In SCO complexes there is a very significant difference between the two electronic configurations in terms of the vibration modes of the molecule. This can be seen from the fact that the iron-ligand bond length *r* changes significantly when the molecule goes from low-spin to high spin and vice versa. Specifically, the HS configuration leads to an increased bond-length between the Fe(II) ion and the ligands. This is because in the HS configuration, the eg antibonding orbitals are occupied, which de-stabilizes the Iron-ligand bond. In the case of a FeN_6 molecule, the difference is approximately 10% as $r_{LS} \approx 2.0$ Å et $r_{HS} \approx 2.2$ Å.

In a configurational diagram (fig 1.4), the two molecular states can be represented as two adiabatic potential wells, where the minimums are shifted both in terms of energy and metal-ligand distance. The well minimum E_0 is defined by the energy at the ground state and is the sum of two different energetic contributions: the electronic energy E_{el} and vibrational energy E_{vib}. As such $E_0 = E_{el} + E_{vib}$. For spin transition to be possible it is necessary that the energetic difference between the two ground states is on the same order of magnitude as the thermal excitation energy: $E_0^{HS} - E_0^{LS} \approx K_bT$. At high temperature, the high spin state is the most stable, due to the fact that the entropic contribution is higher in the HS configuration (specially the vibrational component). This is due to two factors: the electron configuration in the HS state has a higher degeneracy and the vibration states in the HS states have a higher density. The thermally-induced SCO phenomenon is thus governed by entropic effects [23].

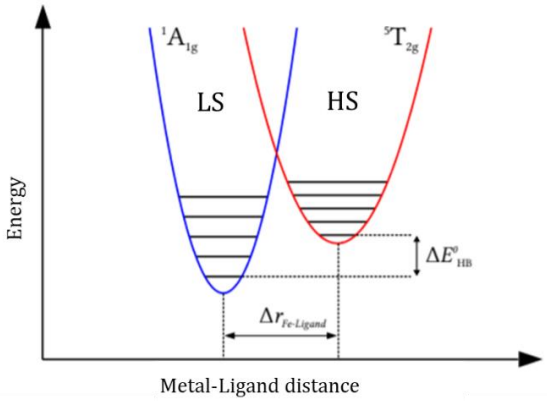

Fig 1.4) Schematic representation of the configurational diagram of the LS and HS states. The electronic configurations are represented as harmonic potential wells.

When considering the thermally-driven spin transition of a group of molecules, the system can be approximated to a system undergoing a phase transition. In normal temperature and pression conditions, the LS-HS transition corresponds to a phase equilibrium for which the pertinent thermodynamic function is the Gibbs free energy *G*. At constant pressure, the difference between the Gibbs free energy of both spin states is:

$$\Delta G = \Delta H - T\Delta S = (G_{HS} - G_{LS}) \quad (1)$$

Where ΔH is the difference in enthalpy between the two spin states (H_{HS}-L_{HS}) and ΔS is the difference in entropy between the two spin states (S_{HS}-S_{LS}). The equilibrium temperature for the two spin states is thus when ΔG = 0. Described by the equation:

$$T_{1/2} = \Delta H/\Delta S \quad (2)$$

Going by these two equations, it becomes clear that if $T > T_{1/2}$ the entropy term in equation 1.1 becomes dominant and $\Delta H < T\Delta S$ meaning that $G_{LS} > G_{HS}$ and thus the most stable state for the system is the HS state.

Likewise, if $T < T_{1/2}$ the enthalpy term in equation 1.1 becomes dominant and $\Delta H > T\Delta S$. Meaning that $G_{LS} < G_{HS}$ and thus the most stable state for the system is the LS state [24].

This shows that the free energy of the system is stabilized or de-stabilized by changes in the temperature thanks to the entropic term, and thus that temperature-driven SCO is fueled by entropy.

I.1.3 Spin transition in the solid state: the concept of cooperativity

So far in the present work the SCO phenomenon has been approached without taking into consideration intermolecular interactions and treating each molecule as an independent isolated entity. This approach would be close to the behavior of a highly diluted solution and in such a scenario, the spin conversion would follow a Boltzmann distribution. However, in a solid material, the intermolecular interactions can no longer be ignored.

The model most commonly accepted to approach intermolecular effects of the spin transition in a crystalline or solid material is the **cooperativity model** [25]. According to which, when a molecule undergoes spin transition, the change in properties that accompanies the transition has repercussions both in its immediate environment, and on a larger scale, on the entirety of the crystal lattice. The transition of a molecule from the LS state to the HS state in a lattice which is the LS state generates an important local deformation due to the volumetric expansion of the molecule. The HS molecule is then subjected to compressive tension from its neighbors, which can provoke a return to its original state. By this mechanism, a collective effect can be induced which, if strong enough, can provoke a first-order phase transition to the HS state.

From a microscopic point of view, the two factors which play a fundamental role in this mechanism are the strength of the intermolecular interactions and the number of interactions affecting each molecule. Cooperativity represents the sum of these elastic intermolecular interactions, from a macroscopic point of view the key factors are the volume change upon spin transition ($\Delta V/V_0$) and the compressibility of the crystal lattice (Fig 1.5).

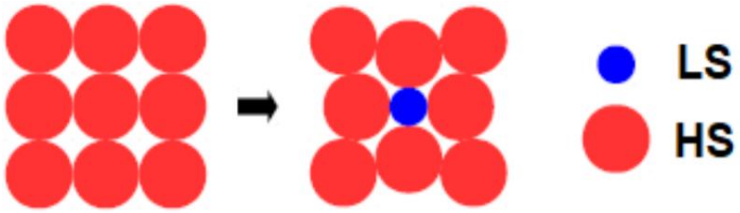

Fig 1.5) Schematic representation of the crystal lattice tension for a molecule in the LS state in a crystalline lattice in the HS state.

A spin transition curve is often represented by the fraction of molecules in the HS state at a given temperature and pressure $n_{HS} = N_{HS}/N$.

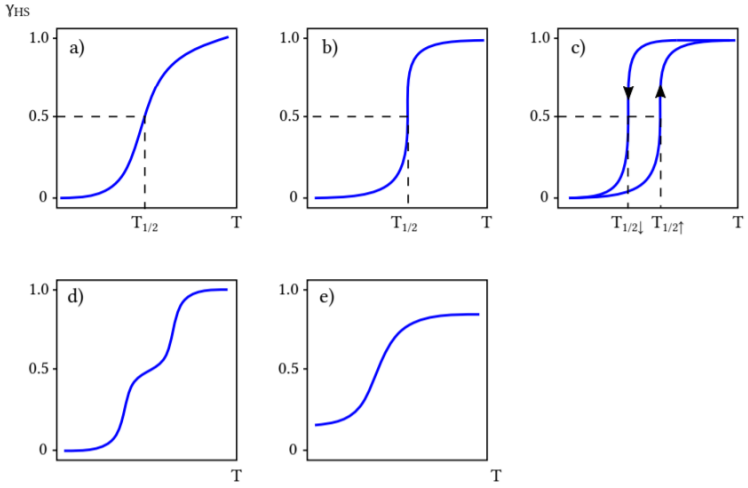

Fig 1.6) Principal types of thermally-driven spin transition curves. a) Gradual spin transition. b) Abrupt spin transition. c) Spin transition with hysteresis. d) Multi-step spin transition. e) Incomplete spin transition [13–15].

There are different types of spin transitions, depending on the nature of the SCO complex (see Fig 1.6). The first is gradual spin transitions, which as a general rule are characteristic of complexes with weak cooperativity due to weak interactions between the molecules. As a result, each molecule in the system undergoes spin transition independently. The second type is abrupt spin transitions. In these type of materials, the intermolecular interactions lead to a phase transition within a small temperature window due to the significant cooperativity of the system. The third type is abrupt spin transition with hysteresis. In these complexes, strong intermolecular interactions cause the system to become highly cooperative. This leads to the appearance of a first-order spin transition. However, the strong cooperativity also causes mixed transition states to be highly unstable, which leads to an energy barrier between the two pure phases, and the creation of a metastable state, thus giving rise to a hysteresis loop. In these hysteresis cycles, the transition temperatures are described as $T_{1/2}^{\uparrow}$ and $T_{1/2}^{\downarrow}$ for the LS-HS and the HS-LS transitions, respectively ($T_{1/2}$ being the temperatures at which n_{HS} = 0.5). As a fourth type, it has been observed for some complexes the existence of spin transitions in multiple stages, or multiple steps. There are several possible origins for such behavior. It can be as a result of distinct crystalline sites undergoing spin transition at different times [26]. It is also commonly seen for polynuclear complexes (SCO complexes which have multiple metallic ions in the molecule), even for polynuclear complexes with identical chemical environments on each metallic ion. This is because when in a polynuclear complex one metallic center undergoes spin transition, the resulting deformation of the molecule renders the transition of the associated metallic centers unfavorable [27]. This effect was notably illustrated by the work of Salmon et al [28]. They found that the two-step transition is the result of antagonistic interactions in the crystal lattice.

In general terms, the spin transition properties offer a glimpse of the intermolecular interactions in the solid material and reflect the degree of cooperativity in the lattice. They depend mostly but not exclusively on the structural properties of the SCO complex, as it has been shown that morphology changes and size variations can have drastic effects in the SCO properties of a given complex.

The effect that size variations might have on the SCO properties of a material are of special interest to the present work, as SCO nano-objects often play a crucial role in the fabrication of composites. In order to further explore this field of SCO research, a brief overview of SCO nanoparticles will be described below.

I.2 Spin crossover nano-objects:

The fabrication of SCO composites often requires the integration or in-situ formation of nano-objects into a matrix. In this section a brief overview of different fabrication techniques for these objects and their principles will be explored [29]. There are three main methodologies to obtain these SCO nano-objects: hard-template, soft-template and template-free (Fig 1.7). There is a wide variety of individual techniques for each of these methodologies, so rather than an exhaustive overview we will present a few of the most important works in the field.

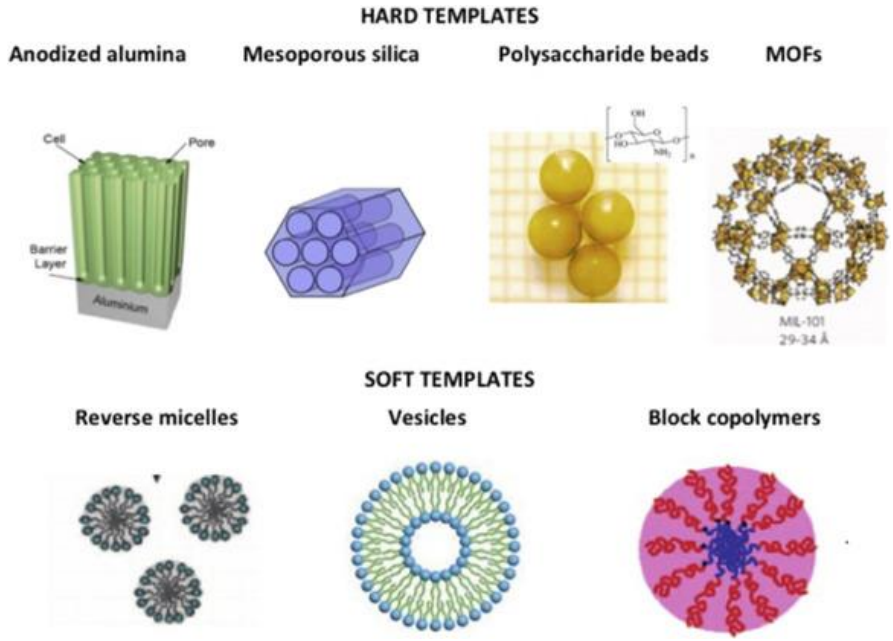

Fig 1.7) Template methods for the synthesis of SCO Nano-objects [29].

I.2.1 Hard template methods

The principle of this synthetic strategy is the use of mesoporous material nanoreactors to confine the growth of SCO NPs. The main advantage this method presents is that the shape and size of the resulting objects can be easily controlled by the porosity of the template material. However, keeping the growth of the nano-objects confined to the pores and ensuring no precipitation on the outside of the template is a synthetic challenge. A way to tackle this challenge is the use of functionalized internal pores, ensuring the reaction is confined to the pores. One of the main drawbacks of this technique is that the template itself often plays a non-innocent role in the spin crossover properties, often tampering with the cooperativity, completeness and temperature of the spin transition.

One of the first approaches used for these kind of syntheses was the use of a sol-gel method to confine the particle growth process in a silica xerogel derived from the hydrolysis of alkoxysilanes [30]. In this work however, the synthesis of the template and the particles are not decoupled.

In another example using silica xerogel, an aqueous solution of the preformed SCO complex $[Fe(Htrz)_2(trz)](BF_4)$ was added to a solution of alkoxysilane followed by aging and drying. Drying in different containers allows the shaping of the resulting composite. The NPs themselves had a size between 2.5 and 5 nm [31].

Polysaccharides have been used as templates for SCO-NP synthesis as well, by successive impregnation of the chitosan or alginate beads with the reaction precursors (fig 1.8) [32]. These templates offer the advantage of a feasible post-synthetic dispersion of the synthesized

nanoparticles in a solvent without having to use the aggressive conditions that would be necessary in the case of metallic oxides or silica as templates.

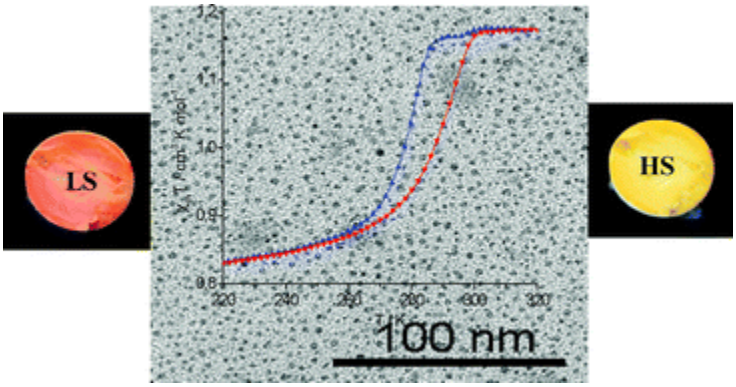

Fig 1.8) TEM Imagery, thermal magnetic measurements and thermochromism of SCO NPs prepared in a chitosan matrix.

Alumina membranes have been used as templates as well (Fig 1.9). Their pore morphology, which is around 50-300 nm of radius and several microns long, favors the formation of SCO nanowires [33]. In this study, a ligand with very long alkyl chains giving the molecule a total length of 3 nm is used to favor the growth of anisotropic nanowires. The silica template is dissolved after the fabrication of the complex, leading to isolated SCO nanowires.

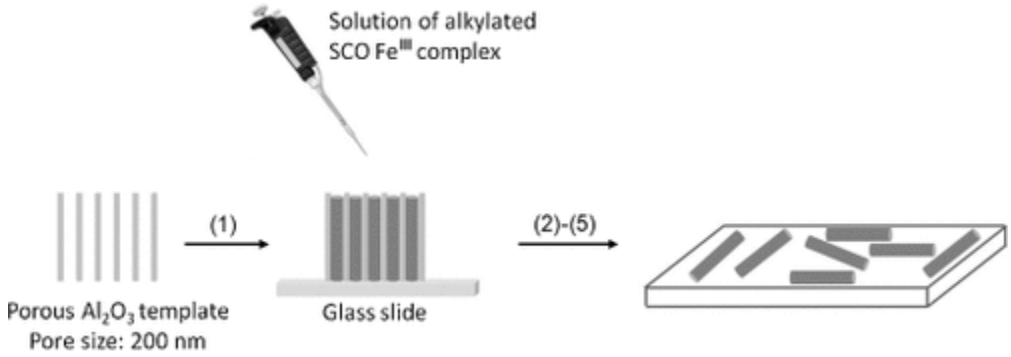

Fig 1.9) Fabrication of SCO nanowires using a long chain alkylated ligand.

I.2.2 Soft Template Methods:

In soft template techniques, self-assembled nanostructures based on surfactants or polymers are used to control the nucleation and growth of the nano-objects. In these systems, nanometric pools confine the growth process of the synthesis. A classic example of such a system is a water and oil microemulsion, a thermodynamically stable dispersion of water in an apolar solvent, stabilized by a surfactant (Fig 1.10). A reverse micelle is a micrometric water pool In an apolar media stabilized by surfactants with low packing parameters, and are widely used to confine the growth of inorganic nano-objects [34].

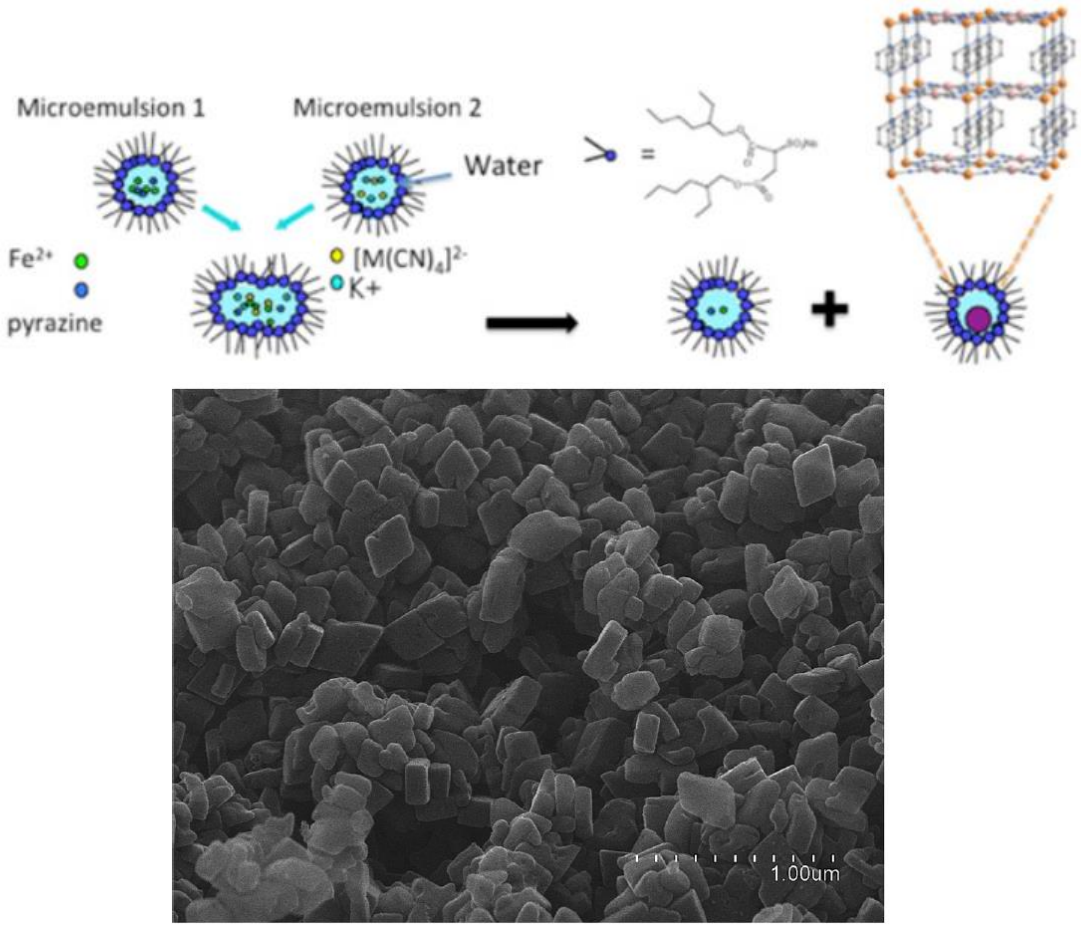

Fig 1.10) Reverse micelle synthesis of SCO NPs and scanning electron microscopy image of the SCO NPs [35].

This technique lends itself well to complexes synthesized from aqueous solutions, with water-soluble precursors, which form insoluble complexes. It has been successfully applied to the synthesis of Hofmann clathrates [35–38] and 1-D SCO polymer chains [39–41]. Both spherical nanoparticles and nanorods with a wide variety of size distributions have been obtained, showing the versatility and tunability of the method. One of the crucial factors in tuning these syntheses is the water/surfactant ratio ω, which controls the size of the micelle.

Block copolymers (BCP) can also be used to form micellar structures, due to the difference in solubility between the two blocks of the polymer for a specific solvent, given that the blocks have significantly different polarity. This method has four main advantages: It can be used for any solvent, it allows for the formation of larger particles, the BCP can be functionalized in key sites to control the reaction, and the obtained colloids are easily processable. An interesting example uses this technique to synthesize nanoparticles of an SCO complex using polystyrene-poly-4-vinylpridiidine blockcopolymer micelles as the template (fig 1.11) [42].

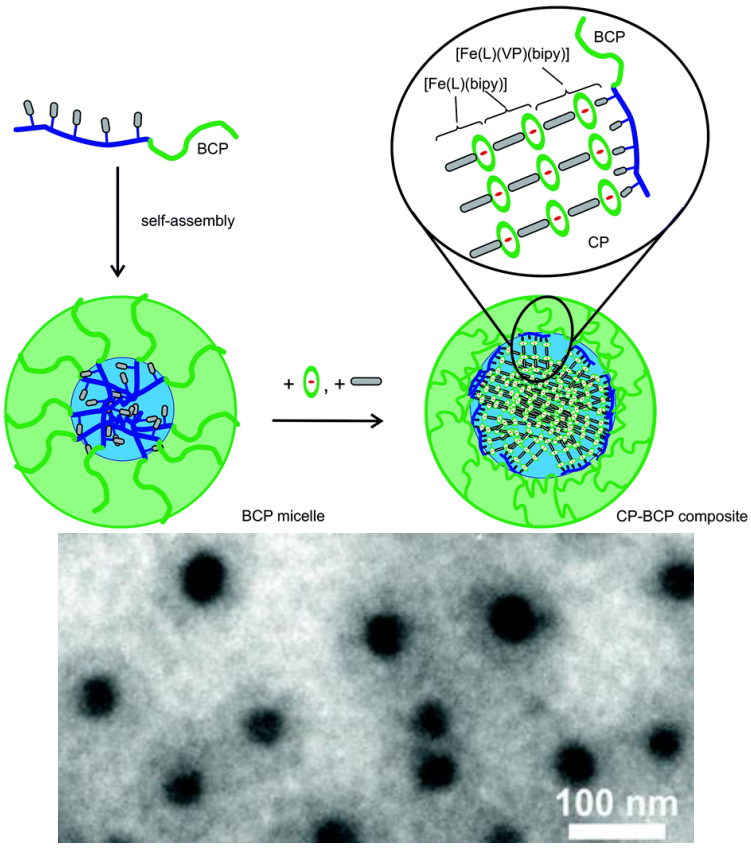

Fig 1.11) Schematic representing the formation of SCO nanoparticles in BCP micelles, forming a composite material and transmission electron microscopy image of the SCO NPs[42].

I.2.3 Template-Free Methods:

It is also possible to synthesize SCO NPs in absence of a surfactant or a template. The most important requirement in these methods is the generation of an efficient nucleation step which is clearly differentiated from the growth step. This has been achieved for SCO complexes by using stabilizing agents, or even in the absence of stabilizing agents by fine-tuning of the physicochemical conditions of the reaction [41].

In particular, a wide variety of reaction conditions was used in the fabrication of $[Fe(hptrz)_3](OTs)_2$ (hptrz = 4-heptyl-1,2,4-triazole, OTs= Tosylate) particles. Different solvents, stabilization agents and stabilization agent concentrations are used to produce a wide variety of morphologies and sizes of the resulting particles (Fig 1.12). Microcrystals, plates and rods are obtained by this method, showing the sensitivity of these complexes to the reaction conditions (fig 1.12).

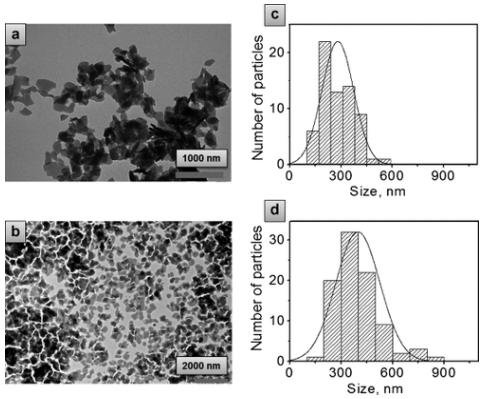

Fig 1.12) Microcrystalline particles of $[Fe(hptrz)_3](OTs)_2$ TEM images (left) and size distribution histograms (right)

Another interesting example uses epitaxial growth of cyano-bridged coordination networks to generate a wide variety and highly tunable set of nanoparticles [43]. This technique allows for highly-controlled synthesis of nanoparticles using well-defined seeds, but it has a limited scope of applicability for SCO complexes given the neutrality of the network and the highly diluted conditions necessary.

More recently, an attractive methodology to obtain SCO nanoparticles without the use of surfactant using state-of-the-art technology has been the use of microfluidic synthesis [44]. In this type of synthesis, the nanoparticles are fabricated using a continuous flow of the reagent solutions, and the product crystallizes as the reaction advances through different purification steps, leading to a continuous synthesis of a pure product (Fig 1.13). In this particular example, a flow methodology was used to fabricate the hallmark $[Fe(Htrz)_2(trz)](BF_4)$ SCO complex. By using this synthesis setup, nanoparticles of 120 nm were obtained with highly homogeneous size and shape (fig1.13).

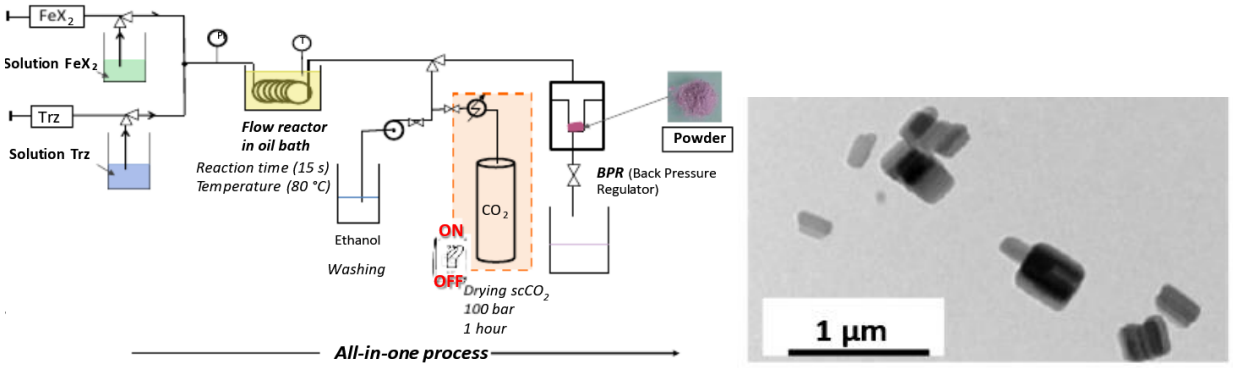

Fig 1.13) One-step flow synthesis of $[Fe(Htrz)_2(trz)](BF_4)$ nanoparticles and transmission electron microscopy of the SCO NPs [44].

This methodology allows for scalable, highly technical and very reproducible synthesis of SCO nanoparticles. It can also be easily adjusted to a wide variety of complexes without fundamentally changing the operating principle.

I.2.4 Anisotropic SCO micro and nanoparticles

The possibility of exploiting the volume change of the SCO by directing it along a preferential axis through alignment of anisotropic objects is of great interest to us, as it could allow us to further amplify the already significant volume change associated with the SCO phenomenon and translate it to a robust linear expansion. For this reason, fabrication methods to obtain anisotropic SCO objects are of particular interest to this work.

A very interesting example was the research work by Peng et al [45]. In this work, the authors have developed a surfactant-less method to crystallize 1D polymeric chains of $[Fe(Htrz)_3](CF_3SO_3)_2$ as rods ranging from 1 to 40 µm long, and from 0.1 to 0.3 µm diameter (fig 1.14).

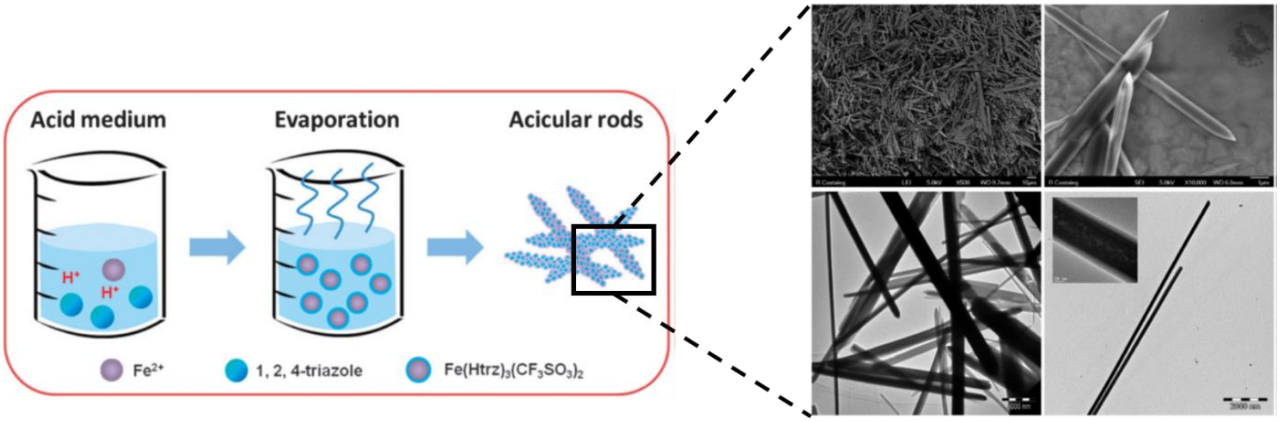

Fig 1.14) Fabrication of $[Fe(Htrz)_3](CF_3SO_3)_2$ micro-rods and TEM/SEM imagery of the corresponding micro objects [45].

The authors propose that slow crystallization in an acidic medium allows for the formation of the SCO needles with an extremely high anisotropic ratio. In order to explore this hypothesis, a follow-up study was performed where a series of SCO nano and microrods are synthesized using this crystallization method with a different acidity of the reaction solution [46]. In this case the complex of choice was the hallmark $[Fe(Htrz)_2(trz)](BF_4)$ complex. Interestingly the study revealed that with increasing acidity of the reaction media, the crystallization took a longer time and the resulting anisotropic objects were larger and with a higher anisotropic ratio (fig 1.15).

It should be noted, however, that increasing the acidity of the reaction media also significantly affected the chemical composition of the resulting SCO complex. In the more acidic reaction conditions, the resulting complex was the fully protonated $[Fe(Htrz)_3](BF_4)_2$ rather than the hallmark $[Fe(Htrz)_2(trz)](BF_4)$.

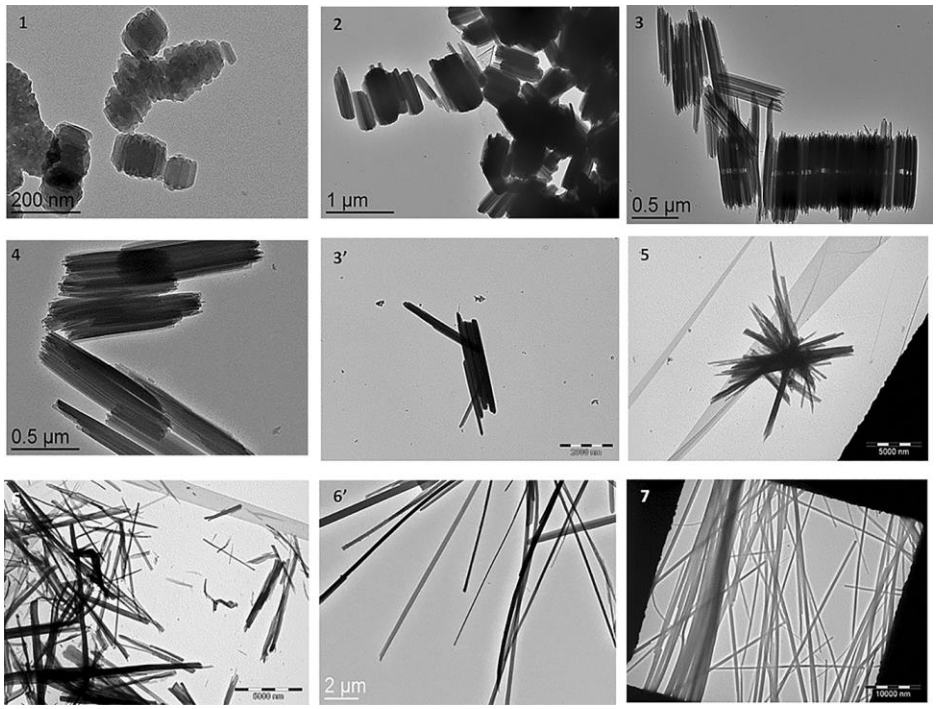

Fig 1.15) $[Fe(Htrz)_2(trz)](BF_4)$ Nano and micro rods fabricated with an increasing acidity and crystallization time [46].

The synthetic methods that we have explored so far open up the possibility of obtaining SCO nanoparticles of a wide variety of sizes and shapes. However, the effect that the particle size might have on the spin crossover properties of the complexes has not been properly explored so far. Thus, we will delve into this topic in the following sections.

I.2.5 Nanoparticle size effect on the spin transition

It is well known that cooperativity, which arises from the intermolecular interactions of an SCO complex, is the main driving force behind the first order phase transition and the thermal hysteresis of SCO systems. Likewise it has been shown that, by "diluting" an SCO complex, via the inclusion of isomorphic (Zn) complexes into the crystalline structure, the width of the hysteresis loop can be controlled [47]. This shows that for a given complex, the hysteresis loop can be modified by altering the chemical environment and cooperativity of the complex. This has however important theoretical implications in the field of SCO nanoparticles. Indeed, the iron atoms corresponding to molecules on the surface of a particle will have a radically different chemical environment, due to the fact that they have a diminished range of intermolecular interactions. Likewise, the cooperativity networks even on non-surface atoms should be significantly reduced. This means that, for very small nanoparticles, dramatic effects should be observed on the width of the hysteresis loop and possibly even in remnant HS or LS fractions which do not undergo SCO.

Theoretical studies predict that the cooperativity of the system will go down with the size of the nanoparticles, which should lead to a reduction in the width of the hysteresis loop [48,49].

According to these findings, there is a size limit, which will depend on the properties of each SCO system, at which the system shows bistability. This means that for very small SCO particles, it should be possible to observe that a complex which presents a wide hysteresis in the crystalline bulk, shows instead no hysteresis at all at very small nanoparticle sizes.

Experimental results on different kinds of complexes would seem to generally back these theoretical hypotheses [50,51]. Studies have found that as particle size decreases after a certain point, so does the width of the hysteresis loop. These findings confirm the theoretical predictions, and have important implications regarding the possible tuning of the SCO properties of a complex via the particle size. These studies have also found a nanoparticle size limit after which there is indeed a complete loss of the hysteresis loop (Fig 1.16 and 1.17).

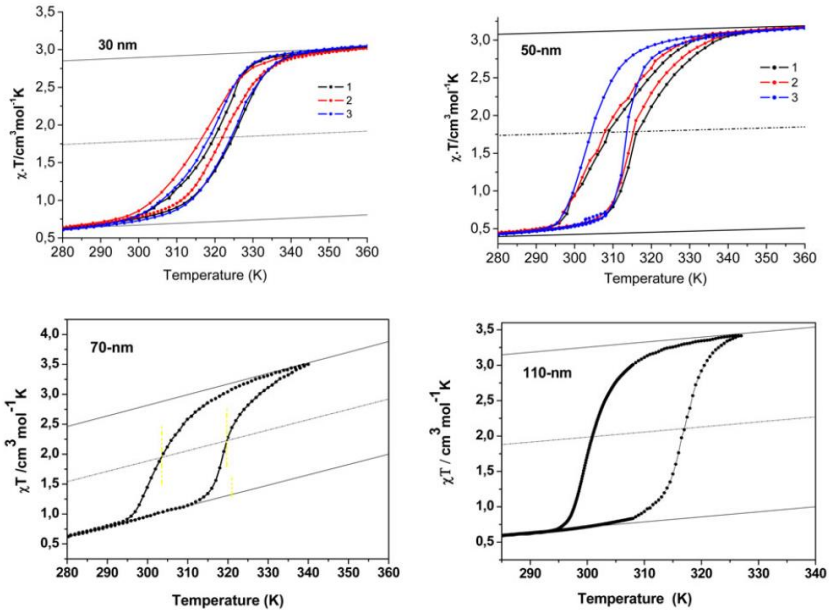

Fig 1.16) Size-dependence of the hysteresis loop of $[Fe(NH_2\text{-}trz)_3](Br)_2 \cdot 3H_2O$ determined by thermal magnetic measurements. (1, 2 and 3 represent the number of thermal cycles) [50].

A striking experimental result, which seems to deviate slightly from the theory has been however found in the case of ultra-small SCO nanoparticle systems [38]. In this study, a series of nanoparticles of the 3-D Hofmann Clathrate $[Fe(pz)\{Pt(CN)_4\}]$ was synthesized and its properties studied. As expected from the theory, as particle size decreases (from *ca.* 100 to 10 nm), so does the width of the hysteresis loop, and the residual fraction becomes more important, meaning that the spin transition becomes incomplete. This can be attributed to surface effects, as a decreasing particle size would entail a larger surface/volume ratio. There is a size threshold as described in previous studies after which the system would seem to present no bistability.

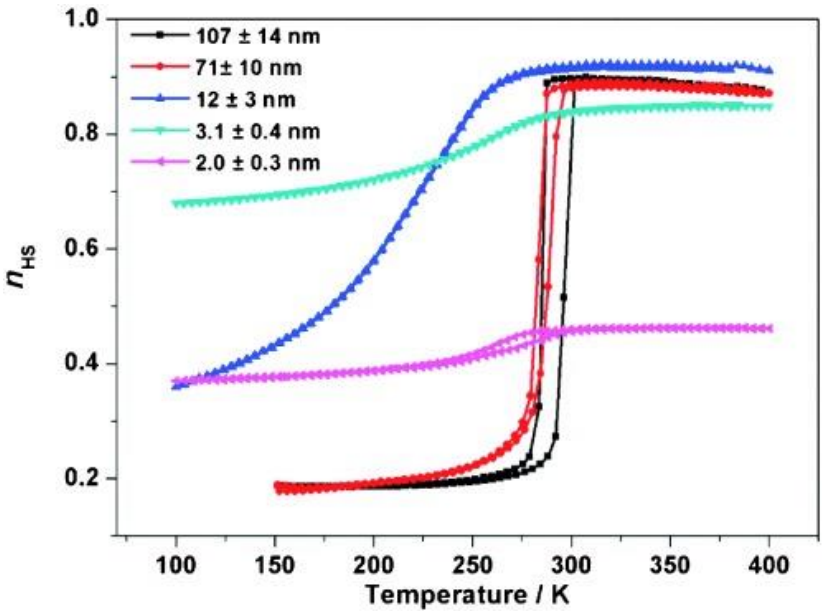

Fig 1.17) Size-dependence of the hysteresis loop of [Fe(pz){Pt(CN)$_4$}].

The main result, however, is the re-appearance of the hysteresis loop at extremely small particle sizes (2 nm, fig 1.17). This can be attributed to size-dependent elastic properties of the SCO nanoparticles, related to surface strain. This hypothesis is supported by the Mossbauer analysis, which shows an increased Debye temperature for the smaller particles, which would imply an increased stiffness of the crystal lattice.

I.2.6 Nanoparticle surface and matrix effect on the spin transition

Nanoparticles are characterized by having a very high surface/volume ratio. This means that for nanoparticles, more so than for macroscale solids, surface effects play a crucial role in their physical properties. In the case of SCO nanoparticles, the bistability and the corresponding hysteresis loops are deeply dependent on the cooperativity and the intermolecular interactions in the system, and in turn, these interactions are deeply tied to the solid-state characteristics of the particles. This would mean that we would expect SCO nanoparticles to be particularly sensitive to surface effects, especially in terms of their spin transition temperatures and residual HS and LS fractions.

Experimental results corroborate this conclusion [37]. In an interesting work, the matrix effect on a series of nanoparticles was successfully demonstrated by varying the composition of the matrix around the SCO nanoparticles. 10 nm nanoparticles of Fe(pz)Pt(CN)$_4$ were synthesized with three different coatings as a stabilizer agent. The first coating was a calixarene-based ligand (2 nm), the second was a thin (2 nm) silica shell, and the third was a thick (4 nm) silica shell. The first series of particles presents no hysteresis loop while the second one shows similar transition temperature but with a hysteresis loop (fig 1.18). This result suggests that just by changing the nature of the surface interactions around a nanoparticle, the effect in cooperativity is important

enough to modulate the presence or absence of a hysteresis loop. Very interestingly, with the addition of a thicker silica shell, the third sample of particles shows not only a significantly lowered spin transition temperature, but also once more the loss of the hysteresis loop. This is probably due to a change in the rigidity of the surface, associated with the phonons traveling through the solid, and has the implication that not only does the chemical environment on the surface affect the spin transition properties of nanoparticles, but also purely physical properties such as the stiffness play a crucial role.

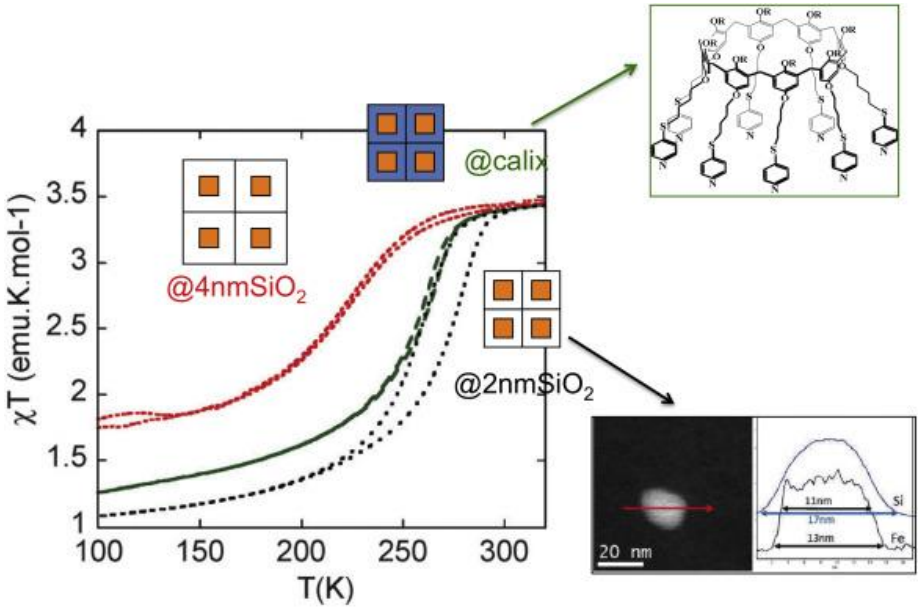

Fig 1.18) Thermal evolution of χT for [Fe(pz){Pt(CN)$_4$}] nanoparticles surrounded by a calixarene ligand (green curve) and silica shell of variable thickness (2 nm, black curve; 4 nm, red curve). STEM-EELS profile of the composition obtained across a particle surrounded by 2 nm of silica (inset) [29,37].

Another interesting experimental result which highlights the sensitivity of the SCO properties in regards to the surface of the nanoparticles comes from a study in which ultra-small Hofmann clathrate nanoparticles (3-5 nm) with the general formula [Fe(pz){M(CN)$_4$}] (M = Ni^{2+}, Pt^{2+}, Pd^{2+}) were prepared in polysaccharide matrices (fig 1.14) [32]. In this case the molecules on the surface of the nanoparticles are covalently-linked to the polysaccharide matrix by the amino group, and there could be interaction via hydrogen bond-networks through remnant solvent molecules as well.

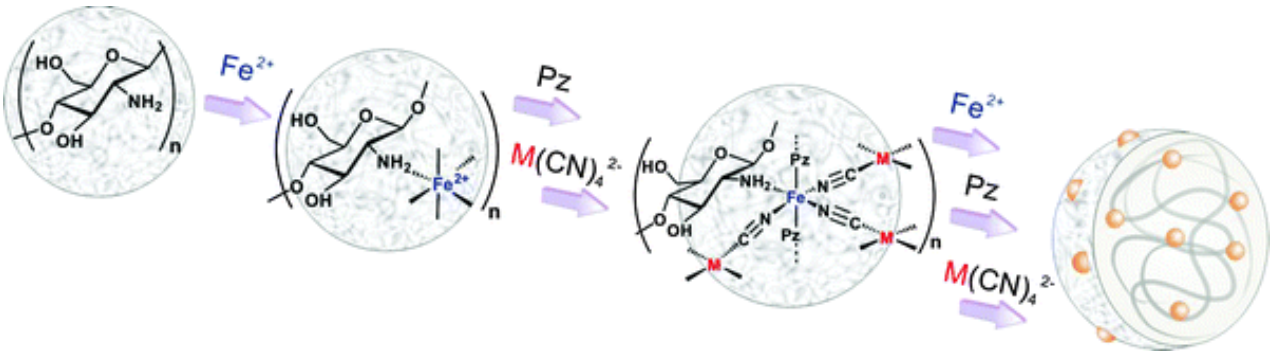

Fig 1.19) Schematic representation of the synthesis of [Fe(pz){$M(CN)_4$}]–chitosan nanocomposite beads [32].

For [Fe(pz){$M(CN)_4$}] particles of this scale (3-5 nm), there is normally a loss of hysteresis due to the size effect. However, the particles in the chitosan matrix retain their hysteresis loops and abrupt transition at the ultra-small scale. This suggests that the strong matrix-particle interactions counteract the change in properties associated to the size-effect of the nanoparticles by inducing a strong cooperativity. The physico-mechanical properties of the matrix then play a crucial role in the surface characteristics of the nanoparticles. To assess this role, chemical modification of the chitosan matrix and a substitution of chitosan were performed, and in all cases led to a loss of the hysteresis loops of the nanoparticles, thus signaling that the rigidity and texture of the matrix plays a crucial role in the spin transition.

I.3. Spin Crossover Composite materials

A composite is a material made from two or more constituent materials. In a composite, the component materials remain separate and distinct, thus differentiating them from solid solutions and alloys. These materials inherit some properties of their components and can even show new properties arising from a synergy between their components. This allows for the possibility to imbue one material with the properties of another. Given the wide array of possible combinations and conformations, a convenient way to categorize composite materials is by their connectivity, which is a way to represent the possible conformations of the component materials in the final solid [52]. In the case of bi-material composites, there are 10 connectivity families, and depending on the connectivity of the material, the physical properties of the composite can vary widely (fig 1.20).

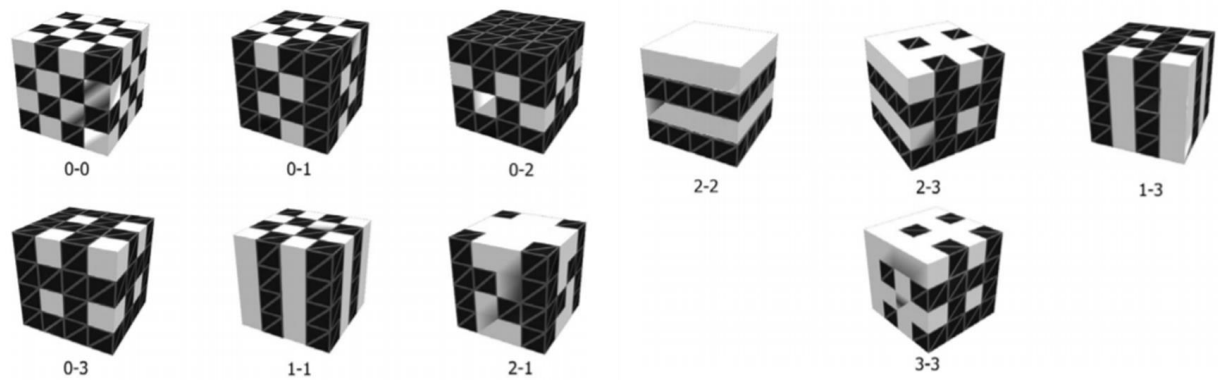

Fig 1.20) Schematic representation of the connectivity families for bi-material composites [52].

In the case of SCO composite materials, one of the constituent materials is an SCO complex, and the objective is either to imbue a particular material with spin transition properties, or to add novel functionalities to SCO complexes. The composite approach allows for smart development of new materials with specific applications in mind.

The present work will focus on polymeric SCO composite materials, and more specifically on **SCO complexes embedded in a polymeric matrix**, obtained via solvent casting, although an overview of different kinds of **SCO composites** and **SCO organic polymers** will also be outlined.

I.3.1 Spin crossover polymer systems

Polymer composites are multi-phase materials wherein at least one phase is a polymer. In the majority of cases, they are composed of organic polymers as matrix and different fillers that act as reinforcement. Nevertheless, the scope of advanced polymer composite materials extends beyond the thermomechanical aspects, providing opportunities to develop a large variety of original physical properties as well as material processing methods.

Alternative to multi-phase, composite materials, several groups have also undertaken syntheses of **'spin crossover organic polymers', i.e. organic polymers functionalized by SCO entities.** The primary interests of 'SCO organic polymers' with respect to SCO-polymer composites is that phase separation, inherent to composites, is avoided and a better dispersion of the SCO centers can be achieved. On the other hand, the price to pay is that the SCO properties in these systems are usually not cooperative and therefore the spin crossover behavior is usually gradual an incomplete.

It is important to differentiate between 'SCO polymer composites', 'SCO organic polymers' and 'SCO coordination polymers' (fig 1.21). 'SCO polymer composites' refers specifically to multi-phase materials, there is no direct chemical bond between the SCO complexes and the polymer. 'SCO organic polymers' are materials where the coordination sphere is bonded to, or part of an organic polymeric chain. And finally, 'SCO coordination polymers' refers to complexes which form a polymeric network via the coordination bonds of the metallic centers.

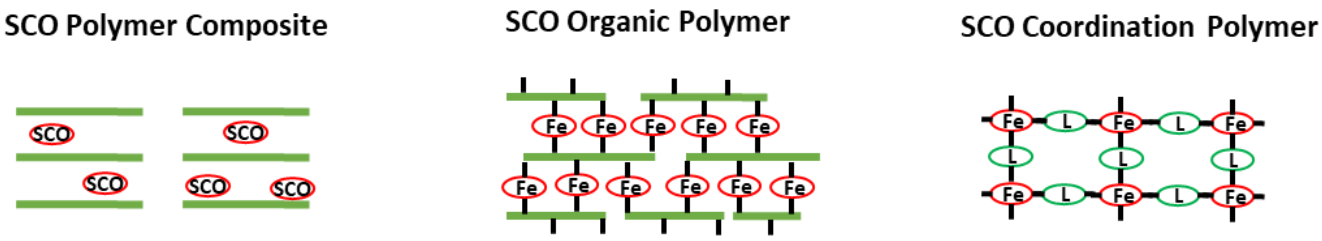

Fig 1.21) Schematic representing the differences between SCO polymer composites, SCO organic polymers and SCO coordination polymers. The green lines represent organic polymeric chains and the black lines represent chemical bonds.

In the field of SCO materials, polymer composites were at first simply fabricated to facilitate or make possible some physical characterizations that were unfeasible or meaningless for microcrystalline samples or liquid solutions. These early composites were prepared by simple methods such as spin coating or drop casting [53,54]. As novel application ideas were introduced into the field by O. Kahn [55,56], the paradigm shifted towards finding ways to exploit the extraordinary properties of SCO complexes, namely their change in magnetic, optical, mechanical and thermal properties.

In this context, the development of new smart functional materials has become an attractive line of research [57], and SCO polymer composites fulfill an interesting role in this regard, allowing for the integration and processing of SCO materials in different shapes and sizes. As new materials were developed in this manner, it became apparent that the properties of the SCO complexes often do not remain unchanged when encased on a polymer matrix. There is a possible matrix effect which affects the transition properties of the complexes. There has been a series of theoretical studies to attempt to elucidate the origin of this matrix effect [58–64].

An interesting approach to understanding the nature of the matrix effect is the one used by Enachescu et al [61] in which the mean-field model is applied to a system with an SCO particle surrounded by a polymer matrix (fig 1.22). Under this model, the interaction with the matrix exerts a force on the particle which can be modeled as a spring constant. This force is then interpreted as a 'negative pressure' that the matrix exerts on the particle. In this model, the negative pressure is variable and changes along with the spin state. This is because, as the particle goes from HS to LS, it becomes smaller and the elastic interactions and negative pressure become stronger as a result. There is however a cut-off point after which there is simply no longer any particle-matrix interaction and the negative pressure vanishes. This model fits the experimental data presented by Enachescu et al for the archetypal SCO complex $Fe(phen)_2(NCS)_2$ in a series of different matrices (glycerol, nujol and eicosane) and gives some insight on the nature of this commonly observed matrix effect.

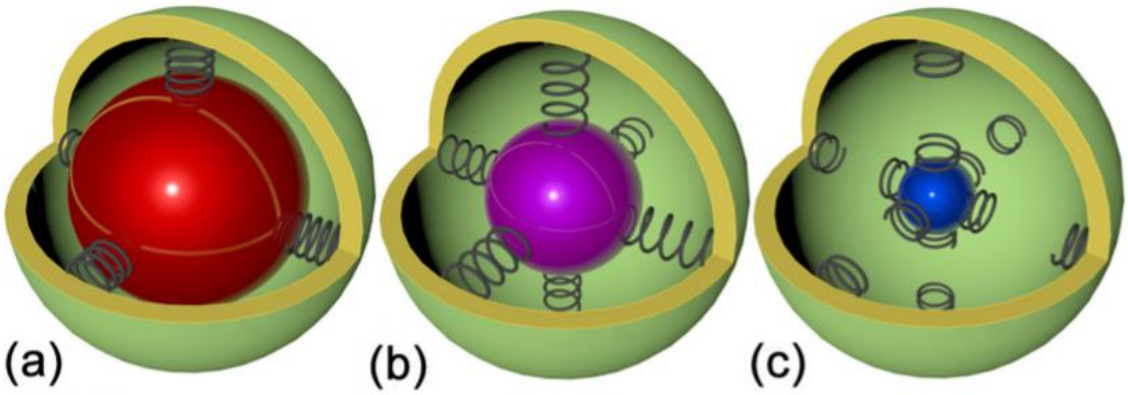

Fig 1.22) Schematic representation of the forces acting on an SCO particle in a matrix. a) preexisting elastic forces between the matrix and the particle. b) As the particle goes from HS to LS, the matrix induced pressure becomes a 'negative pressure'. c) The particle size is too small and no longer has elastic interactions with the matrix [61].

An alternative to phenomenological approaches is to develop an elastic model for a nanocomposite with coherent interface in the framework of continuum mechanics. The main advantage of this method is to derive analytical expressions of the interfacial elastic energy and the interfacial stress as a function of experimentally accessible mechanical quantities [65]. Under this model, the differences in the spin transition properties of a SCO nanoparticle embedded in a matrix can be associated with mismatches in the lattices of both materials. According to this model, interface effects play a crucial role in determining the mechanical behavior of SCO objects embedded in a matrix [66].

Research on polymer composites has recently shifted to more sophisticated SCO polymer composite materials exhibiting synergies between the properties of the SCO particles and the polymer matrix. Notably, strain-coupled electroactive polymer-SCO composites have been developed with promising properties for the development of actuators, sensors and energy harvesters [67–69].

From a conceptual point of view, it is interesting to separate SCO composite materials into two main categories: **composites prepared from solutions** (whether using a solubilized SCO complex or the corresponding precursors) and **composites prepared from preformed SCO particles**. In both cases, a variety of methods of different sophistication were employed, which range from simple casting techniques to advanced methods such as stereo-lithography. In the present work, an outline focusing on the state of the art of composites prepared from solutions will be presented first, followed by a section focusing on composites prepared from preformed SCO powder. Finally, a brief overview of SCO organic polymers is provided. Beyond the method used for the fabrication of the composites, special attention will be given to the proposed **applications of these materials**.

I.3.1.1. Spin Crossover Polymer Composites prepared from solutions

I.3.1.1.1. Solution casting method

Whenever an SCO compound and a polymer have a common solvent, this simple method provides a straightforward means for dispersing the complex within the matrix and process the composite as a film on various substrates. Yet, the resulting morphology and microstructure of the SCO complex is not always trivial to control (e.g. crystalline vs. amorphous, aggregated vs. dispersed, etc.).

The first example of this kind of composites is a mixture of $[Fe(6\text{-}Me\text{-}py)_2(py)(tren)](ClO_4)_2$ in a PSS (polystyrene sulfonate) matrix prepared by dissolving the two compounds in water and allowing the solvent evaporate on a glass substrate [53]. In this study, the possibility of an interaction between the sulfonate groups of the polymer and the SCO complex was proposed to explain the significant difference in the SCO behaviour of the composite in comparison to the nude complex, already raising the possibility of a matrix effect. A similar composite was fabricated using using the $[Fe(2\text{-}mephen)_3]^{2+}$ complex embedded in PVAc (poly-vinyl-acetate) and Nafion films. PVAc was doped by the SCO cation by co-dissolving the two compounds in methanol and then let the solution dry on a glass slide. The Nafion films were simply immersed in an aqueous solution of the cation [70]. This composite however showed no effect of the matrix upon the spin transition.

In a quest towards materials fabricated with technological applications in mind, a new series of composites was prepared, which consisted of a mixture of PMMA (poly(methyl methacrylate)) and different loadings of the complex $[Fe(hptrz)_3]X_2$ (hptrz= 4-heptyl-1,2,4-triazole; X = ClO_4^-, BF_4^- or Br^-) obtained from DMF solutions followed by vacuum distillation. Interestingly, the spin transition curves of the complexes in the composites remained relatively abrupt and the hysteresis widths even increased (vs. the bulk microcrystalline powders), despite the fact that x-ray diffraction analysis did not reveal any evidence of a better crystallinity in the composites [71].

Another interesting composite material fabricated with technological applications in mind was a mixture between an SCO complex and a liquid crystalline polymer. It was fabricated by mixing $[Fe(ODT)_3](OTs)_2$ or $[Fe(HET)_3](OTs)_2$ (ODT = 4-octadecyl-1,2,4-triazole, HET = 4-(2-hydroxyethyl)-1,2,4-triazole, OTs = p-toluenesulfonate) with the liquid crystalline polymer poly(oxetane) (POx) in an effort to combine both magnetic and liquid crystal transitions in a multifunctional material [72]. Following vacuum drying of the THF solutions of the materials, the authors obtained composites where the temperatures of the different transitions (glass transition, spin transition and isotropisation) were lowered in comparison to the bulk materials. However, no interplay between these phenomena was reported.

In an interesting study, a composite film was prepared by mixing precursors of $[Fe(NH_2trz)_3](ClO_4)_2$ with PVP (polyvinylpyrrolidone) in ethanol (fig 1.23) [73]. Due to the strong hydrogen bonds formed in between the amino groups of the complex and the carbonyl groups

of the PVP, a microstructure consisting of a regular stripped pattern with 0.3 nm inter-line distance is formed, which can be clearly seen in the transmission electron microscopy images of the composite film. This microstructure is not observed when the film is prepared with the similar complex with the Htrz ligand for which the hydrogen bonds are not feasible. This suggests that strong hydrogen bond interactions between the polymer and the SCO complex are essential for obtaining a regular structure.

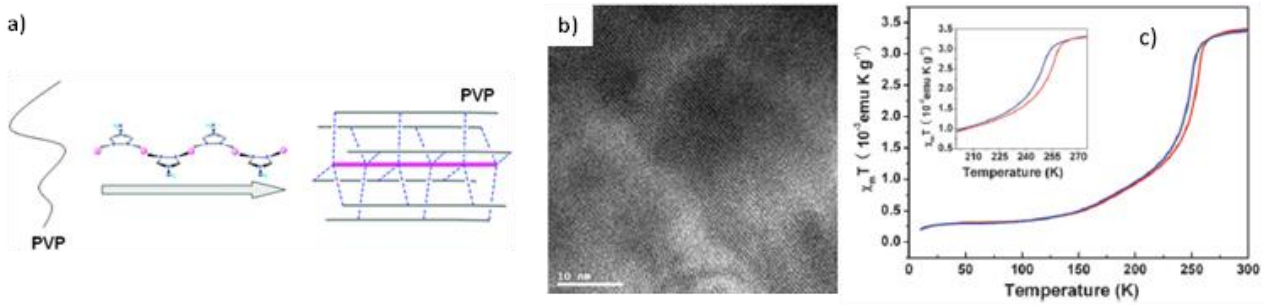

Fig 1.23) a) Schematic representation of the $[Fe(NH_2trz)_3](ClO_4)_2$@PVP composite where the blue dashed lines represent the hydrogen bonds. b) TEM image of the composite film with regular striped patterns. c) Temperature dependent magnetic behavior of the composite [73].

A study pertaining the development of smart synergistic materials studied the properties of isotactic polystyrene (i-PS) when $[Fe(ODT)_3](ClO_4)_2$ (0.5 - 5 w%) is dispersed in it [74]. Blend films of different composition were prepared by mixing homogeneous toluene solution of the two compounds at 100°C and evaporating the solvent. Interestingly, the degree of crystallinity of i-PS increases due to the presence of the complex, which indicates that the complex has some nucleating effect for the crystallization of the polymer. This result is important in that it shows that not only the polymer matrix can influence the SCO behavior, but also the SCO complex can significantly alter the physical properties of the polymer, going one step forward towards the formulation of synergistic SCO polymer composites (fig 1.24).

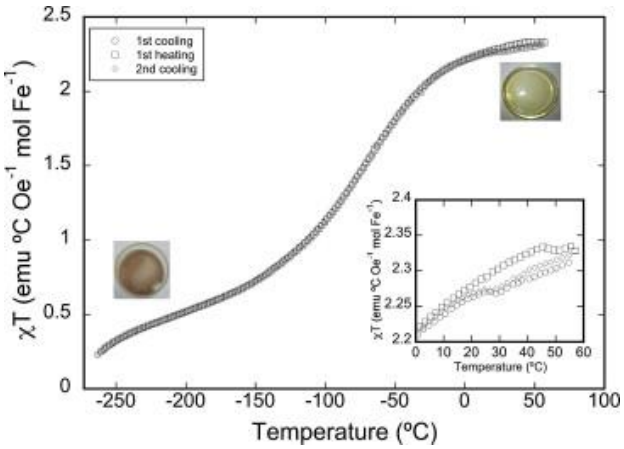

Fig 1.24) Variable temperature magnetic measurements of an Isotactic Polystyrene (i-PS) SCO composite with $[Fe(ODT)_3](ClO_4)_2$. Inset shows a small RT hysteresis loop.

Moving forward towards more fabricated techniques of composite synthesis, one study prepared electrospun fibers of atactic polystyrene (a-PS) with $[Fe(ODT)_3](ClO_4)_2$ for which the formation of *ca*. 3 μm diameter fibers was observed for loadings of the complex up to 13.5 w% [75]. However, as the concentration of the complex increases, the fibers become less uniform.

A new technique to fabricate SCO composites using technological methods was very recently proposed by Baumgartner et al [76]. In this methodology they use the highly soluble SCO complex $[Fe(NH_2trz)_3](2ns)_2$ and co-process it with ultrahigh molecular weight polyethylene (UHMWPE) to exploit its mechanical properties. They fabricate solutions of the SCO complex and UHMWPE in stearic acid, and this mixture is extruded using a micro-compounder to fabricate ribbons and fibers (fig 1.25). The post-processed material is treated with diethyl ether to eliminate the solvent, leading to homogeneous SCO@UHMWPE composite materials with a wide variety of morphologies and compositions.

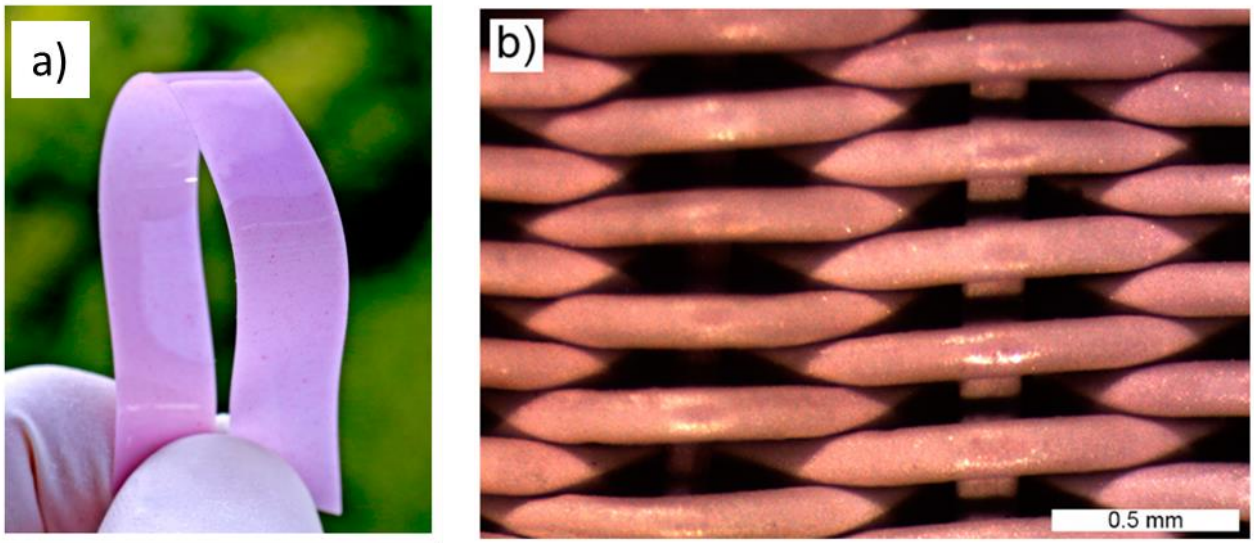

Fig 1.25) $[Fe(NH_2trz)_3](2ns)_2$ UHMWPE composite. a) Ribbon. b) Knitted fibers.

So far, all the composites shown in the present work have had a morphology of individual SCO particles dispersed in a polymer matrix, resembling 0-3 connectivity composites. In one particular study however, a micro-patterned film of the SCO complex $[Fe(Oct\text{-}BPP)_2](BF_4)_2$ (4,4''-dioctyl 2',6'-bispyrazolylpyrine) was embedded within a flexible polymer film [77]. The resulting composite film most closely resembling a 1-3 connectivity system (see Fig 1.26). First, they prepared a thin film of PS by drop casting and then on top of it a rectangular stripe of the SCO complex was fabricated by lithographic patterning using a PDMS (polydimethylsiloxane) stamp, followed by spin coating a PS solution in top of the SCO layer. This resulted in a flexible polymer film in which the embedded SCO grating shows optical diffraction phenomena.

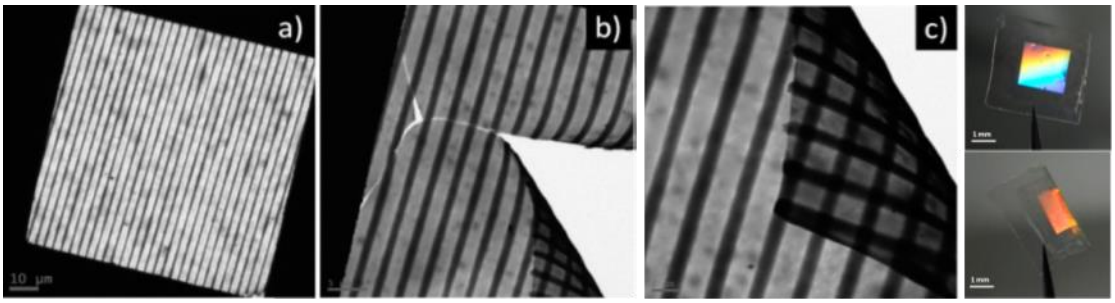

Fig 1.26) TEM images of regular stripes of the SCO complex $[Fe(Oct\text{-}BPP)_2](BF_4)_2$ embedded in a polystyrene film (a,b,c) and photographs showing the flexibility of the thin film [77].

I.3.1.1.2 Adsorption into matrix

This approach is developed mostly using ionomers, i.e. polymers with ionic properties (often with sulfonate, carboxylate or amino groups), which allow for the immobilization of SCO complexes or their precursors by electrostatic interactions using simple impregnation methods.

A series of investigations of various SCO-Nafion composites was carried out by the group of Kojima [78–83]. These composites were prepared by a simple two-step impregnation method. The first step is impregnation of the polymer film into the solution of the metal ion and then the second step is likewise an impregnation into the ligand solution. They fabricated $Fe^{II}(Htrz)_3$@Nafion films, providing the polymeric backbone to the final complex (fig 1.27). Nafion is well known to form reverse micelles, that consist of clusters of about 4 nm in diameter and are separated by a distance of about 5 nm [84,85]. It is inside these clusters that the $Fe^{II}(Htrz)_3$ species are likely located.

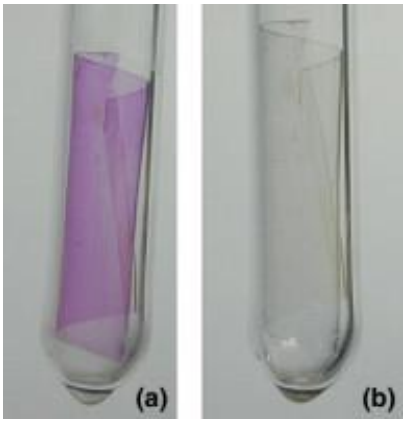

Fig 1.27) Demonstration of the thermochromism due to the spin crossover phenomenon for $[Fe(H\text{-}trz)_3]$@Nafion, (a) purple in the low-spin state (T = 77 K) and (b) colorless in the high-spin state (T = 300 K).

Following a similar research vein but with the goal of developing materials with added functionalities, Kamebuchi et al [86] replaced the iron-triazole complex by Fe^{II}(diAMsar) (diAMsar = 1,8-diaminosarcophagine) in the Nafion film, providing a pH dependent SCO complex. Under acidic conditions, the amino groups of diAMsar are protonated resulting in an electrostatic

repulsion between the ligand and the iron center leading to the absence of SCO properties. Under basic conditions at room temperature the LS state is stabilized, whereas at pH = 7, the HS state is stabilized. In a subsequent study [87], a composite was fabricated using Fe^{III}-formazan complex immobilized in the ion-exchange polymer AN-18-10P. It is suggested that immobilization occurs via ion exchange between the sulfo group of the ligand and the functional groups of the resin.

Intending to use the matrix itself as a means to control the growth of the SCO nanoparticles, composite xerogels were prepared by immersing a previously prepared monolith of silica in an $Fe(BF_4)_2$ solution and then in a solution of the triazole ligand [88]. Nanoparticles of the SCO complex were formed in the pores of the silica monolith with an average size of 3.2 nm. Remarkably, despite the very small size of the particles, the magnetic behavior of the composite showed a partially reversible spin transition with a wide hysteresis (375 K on heating and 310 K on cooling). Following the same approach using the matrix as a mold for the growth of SCO nano objects, Wang [89] prepared nanorods of $[Fe(Htrz)_2(trz)](BF_4)$ using a cation-exchange polymer resin, in which the sulfonate groups on the resin served as the nucleation sites for the growth of the anisotropic SCO particles. This was achieved by immersing the resin for different times in a solution of $Fe(BF_4)_2$ and then into a solution containing triazole and $NaBF_4$, resulting in SCO@resin nanorods. Interestingly, despite the fact that there is a clear difference in the size of the resulting nanorods depending on the duration of the immersion period, there seems to be no difference in the SCO properties of the resulting composites (fig 1.28).

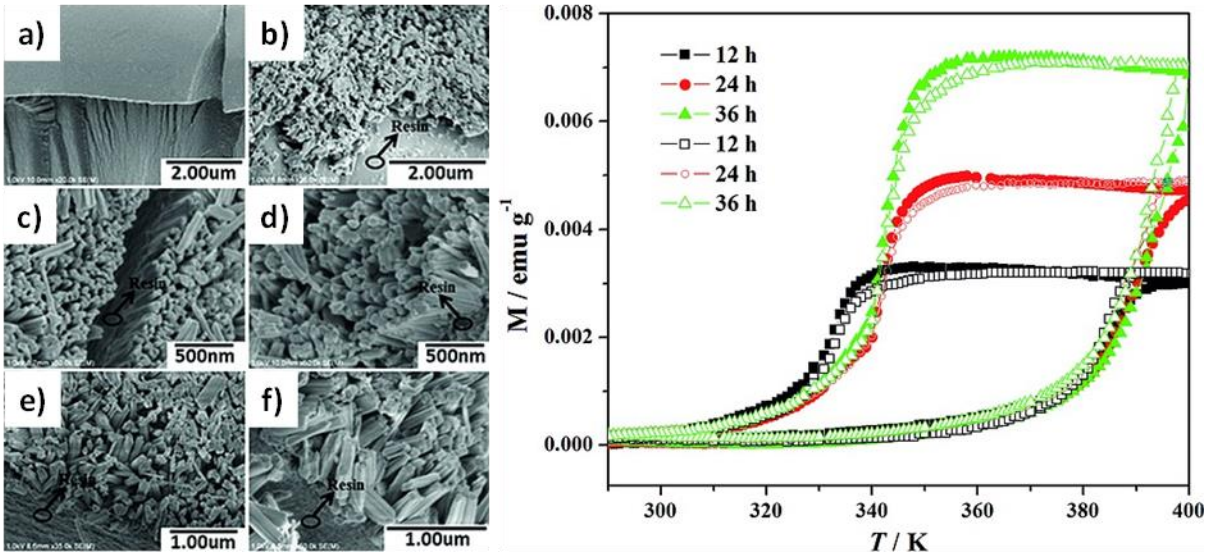

Fig 1.28) SEM images of a) the blank resin and $[Fe(Htrz)_2(trz)](BF_4)$ nanorod arrays with immersion times of b) 12, c) 18, d) 24, e) 36 and f) 42 h. (right) Magnetic measurements of the SCO nanorods for different immersion times [89].

In a similar research line, a study [51] reported the use of porous chitosan beads as a polymer matrix to obtain ultra-small nanoparticles (ca. 3.8 nm) of the 3D spin crossover coordination polymer $[Fe(pz)\{Ni(CN)_4\}]$. A multi-step sequential assembly was employed, which consisted of consecutive impregnations of the chitosan beads into methanol solutions of

$Fe(BF_4)_2{\cdot}6H_2O$, pyrazine and $(N(C_4H_9)_2[Ni(CN)_4]$. Using a similar principle, but going one step further in terms of fabrication, a series of nanocomposites were synthesized using not only chitosan, but also alginate beads for hosting particles of the complexes $[Fe(pz)\{M(CN)_4\}]$ (M = Ni, Pd, Pt) [32]. In this case, the chitosan composites were dried either in vacuum to obtain hydrogels or under CO_2 supercritical conditions obtaining aerogels, resulting in a variety of chitosan composite beads. The chitosan beads were dissolved in water at 70 °C and then placed in a petri dish for slow evaporation of the water resulting in a yellow film. Showing that by this method, using water soluble matrixes, great control over the morphology of the composites can be achieved.

I.3.1.1.3 Sol-Gel method

The sol–gel process is a widespread method for the fabrication of glassy and ceramic materials. In this process, a colloidal solution (sol) is formed, which evolves gradually towards a gel-like network from which the final form of the material is obtained using various drying and firing approaches. In the context of SCO research, this method is particularly useful to synthesize SCO-silica composite materials, which can then be used for the fabrication of SCO-active films, coatings and other objects.

In an interesting example of this method, a composite gel of sulfonate-functionalized SiO_2 nanoparticles with the SCO complex $[Fe(NH_2trz)_3](SO_4)$ was prepared by suspending the nanoparticles in a mixture of ethylene glycol: water solution to which the iron salt and the ligand was added [90]. After 20 h, gelation occurred resulting in a white gel. SEM images showed a good dispersion of the SiO_2 nanoparticles in the matrix of the SCO gel, which is mostly composed of needles (Fig 1.29). Using freeze-fractured TEM, particle imprints are seen, indicating that the silica surface is physically interacting with the SCO coordination chains.

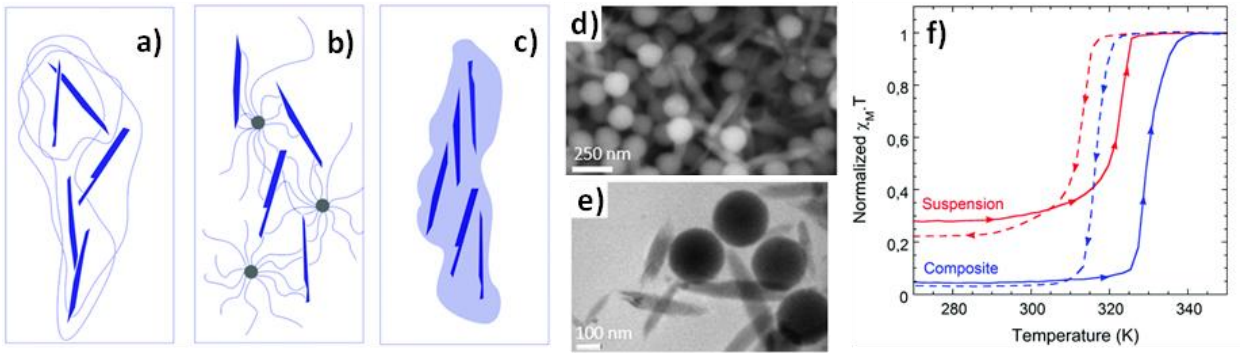

Fig 1.29) Schematic representation of a) the particle free suspension, b) composite gel $[Fe(NH_2trz)_3](SO_4)@SiO_2$, c) dry particle free system. Composite gel imaged by d) SEM-FEG and e) cryo-TEM; f) magnetic measurements of the composite gel and the particle free suspension [90].

In a follow-up study, the authors used the composite gel $[Fe(NH_2trz)_3](SO_4)@SiO_2$ and casted it onto a PTFE (polytetrafluoroethylene) mold, which was exposed to an alkoxysilane vapor in a closed desiccator to obtain a flexible macroporous hybrid silica network (Si@Si-SCO), which

was eventually coated with PDMS (Si-SCO@Si@PDMS) [91]. This way they obtained a flexible polymer nanocomposite material with PDMS protection, which provided long-term stability to the material (> 80 days), prevented its decomposition when immersed in hot water and allowed to preserve its SCO properties over >15 thermal cycles.

I.3.1.2. Spin Crossover Polymer Composites prepared from solid dispersions

As a method for obtaining SCO composites, mixing **polymers with preformed SCO particles** (including micro- and nanocrystals, nanorods, etc.) provides the advantage of better control over particle morphology and SCO properties. In addition, weakly soluble SCO compounds can be also processed. On the other hand, particle aggregation may be an issue for their integration and their homogeneous distribution in the composite materials.

I.3.1.2.1 Drop Casting

Drop casting is a simple and straightforward technique which has been employed at several instances as a simple means to obtain functional SCO particle – polymer composites, which can be used as mechanical actuators, optical sensors or smart papers. It is the simplest way to process soluble thermoplastics.

One of the earliest examples of a composite fabricated from a particle dispersion via drop casting was developed by our group. In this study, SCO-polymer composite based bilayer mechanical actuators of PVP and PMMA were fabricated, the latter with different SCO particle loadings [11]. This study showed for the first time that the strain associated with the spin transition can be used to produce useful mechanical work. It is interesting to note that while the SCO-Polymer layer can be understood as a 0-3 connectivity composite like those presented before, the bilayer as a whole closely resembles a composite with 2-2 connectivity, and it is this unevenness that gives rise to new properties such as the ability to perform work.

Later, a follow-up study investigated more in depth PMMA $[Fe(trz)(Htrz)_2](BF_4)$ (10-50% wt.) composite films in combination with a silver-based conducting polymer composite layer [92]. The resulting film was used for the electrothermal actuation of the device. Upon Joule-heating, a switching from the LS to the HS state was observed accompanied by the bending of the bilayer cantilever with frequencies up to a few Hz over a few hundreds of actuating cycles without noticeable fatigue (fig 1.30).

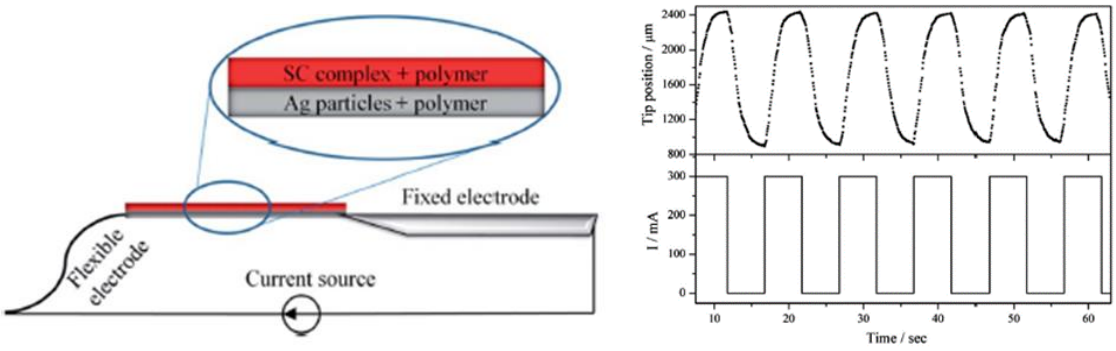

Fig 1.30) Schematic representation of a bilayer SCO-polymer composite cantilever with electrothermal actuation and the experimentally observed variation of the cantilever tip position (in ambient conditions) upon the application of an alternating current [92].

Using a similar approach, another study explored the possibility of using bilayer composites to exploit the volume change inherent to spin crossover composites [93]. A bilayer device consisting of a $[Fe(Htrz)_2(trz)](BF_4)$@Polycarbonate (PC) composite layer and a piezoresistive layer was fabricated (fig 1.31). The mechanical stress induced by the SCO particles in the device gave rise to a change in the electrical resistance, which was detected through a Wheatstone bridge, allowing for direct electrical detection of the SCO phenomenon, which opens the door for multiple applications.

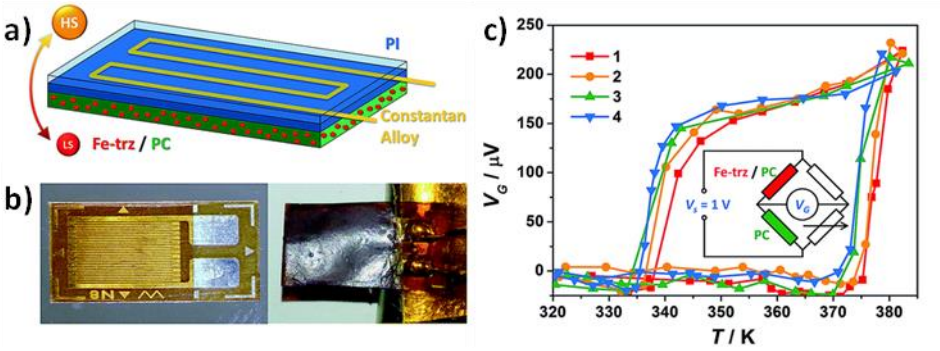

Fig 1.31) Schematic structure of the bilayer SCO-piezoresistive cantilever and (b) photos of the prefabricated polyimide/constantan alloy/polyimide stress-sensitive plate before (left) and after (right) drop-casting of the SCO-active composite. c) Bi-stable voltages of the Wheatstone bridge upon 4 thermal cycles [93].

Thermochromic thin films of $[Fe(NH_2trz)_3](BF_4)_2$ particles in different polymer matrices were studied in a series of studies [94,95]. They evaluated the effect of the interaction of the particles with the polymer matrix via the color change of the composite. Significant differences were observed in terms of aggregation and clustering when using solvents and polymers of different polarity. For example, in the case of PMMA composites, the size of the clusters is reduced when they are prepared in THF, whereas aggregation of the nanocrystals is observed when they are prepared in toluene. In contrast, in the case of hydrophilic polymers such as Nafion

or polyurethane-D6, fiber-shaped particles are observed. Notably, in the case of polyurethane-D_6 the particles are needle-shaped with a width of 250-500 nm and several micrometers in length and differ with the large clusters of *ca*. 500 nm observed for the bulk sample. Such evolution of the material morphology in the different matrixes can explain the change in the SCO properties and was used as a tool to develop a colorimetric sensor array based on a photographic digital camera [96].

An interesting study looking into how to add new and versatile functionalities to these composites used $[Fe(NH_2trz)_3](NO_3)_2$ particles embedded in polystyrene (PS) to prepare films with a thickness above 10 µm. The resulting composites retained the SCO properties of the bulk material showing different spin transition temperatures depending on the water content [97]. The vapochromic behavior of these films were tested, by exposing them to HCl, HBr + Br_2, HBr, HNO_3 and NH_3 vapors resulting in drastic color changes (implying the decomposition of the composite), suggesting their possible application as single-use detectors (Fig 1.32).

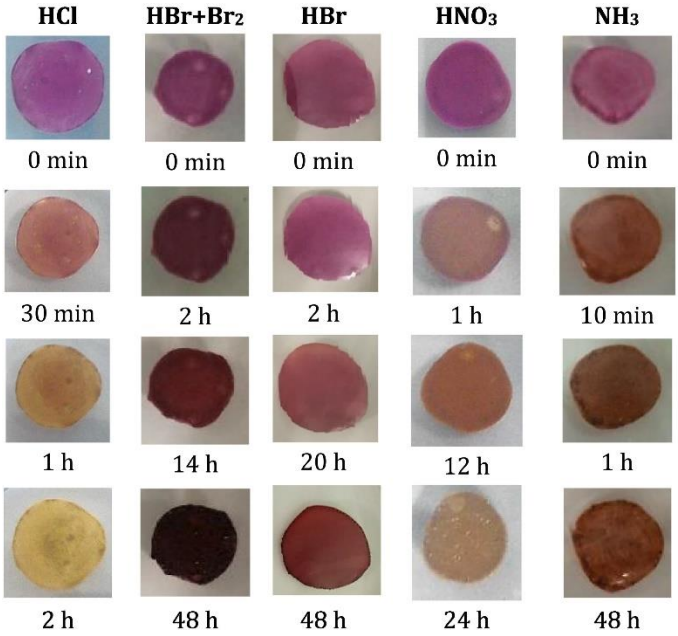

Fig 1.32) Color changes after exposing $[Fe(NH_2trz)_3](NO_3)_2$@PS films to HCl, HBr, HNO_3 and NH_3 vapors [97].

I.3.1.2.2 Spray Coating

Spray coating consists of depositing microdroplets (i.e., an aerosol) of the desired material on a surface by forcing the dissolved (or dispersed) material through a nozzle. This versatile method allows for fabricating smooth, homogeneous coatings with well-defined compositions, and geometries on various substrates.

The first SCO composite synthesized using this technique was a spray coated film fabricated with $[Fe(NH_2trz)_3]Br_2 \cdot 3H_2O$ and $[Fe(NH_2trz)_3](NO_3)_2 \cdot H_2O$ particles with ~1 µm diameter on a polyester film [98]. The spin transition was successfully induced from the LS to the HS state

of the SCO complex via IR laser-induced heating of the matrix by means of a CO_2 laser. With this technique, the authors were able to write the letters “CNRS” in the thin film in less than 1 s at room temperature. As long as the temperature of the film was kept within the hysteresis loop (10 °C < T < 45 °C) the stored information persisted.

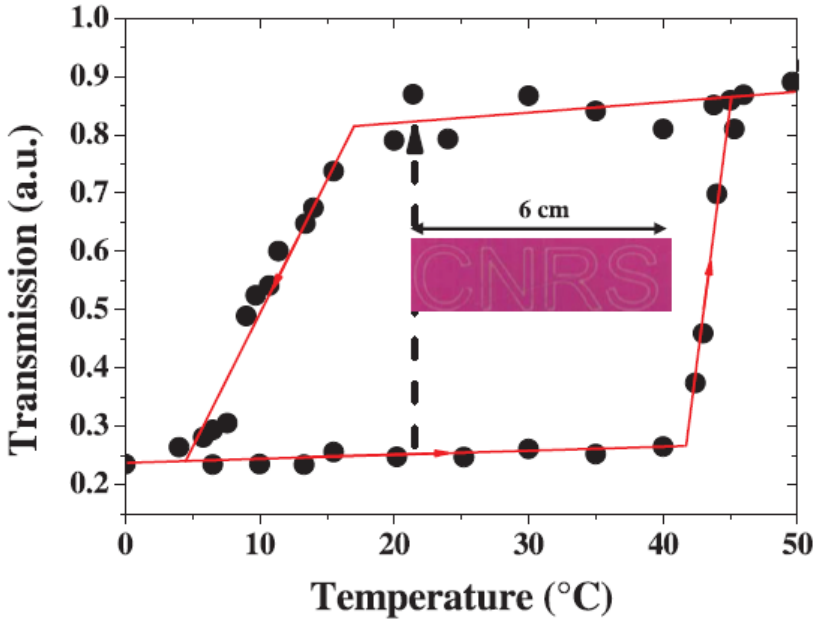

Fig 1.33) Demonstration of laser writing within the thermal hysteresis loop of a polymer thin film doped with the [*Fe*(NH_2-trz)$_3$](NO_3)$_2$·H_2O compound. The solid lines underlying the thermal hysteresis loop are shown as a visual guide. The characters “CNRS” shown in the inset, written by the CO_2 laser beam, remain as long as the temperature of the sample is kept inside the thermal hysteresis loop.

In another study to exploit the volume change of SCO to perform actuation, a composite consisting of [Fe(H-trz)$_2$(trz)](BF_4) nanoparticles in an epoxy-based photoresist (SU-8) was prepared via spray coating [99]. The composite was spray-coated over silicon micro-cantilevers (MEMS) and crosslinked by UV light exposure and consequent baking steps. Thermally-driven actuation of the cantilevers in the MEMS was observed, resulting in an abrupt bending at the temperature of the spin transition with a stable amplitude of actuation (fig 1.34). The actuating behavior of these SCO-MEMS devices was evaluated in static as well as in dynamic modes and a considerable change of the resonance frequency was detected at the SCO. This composite was also spray-coated over a free-standing polyester film, to develop a macroscopic bilayer actuator. Six flower-petals were cut from the bilayer, in which a reversible opening and closing of the flower together with a color change was observed by thermal cycling (fig 1.34).

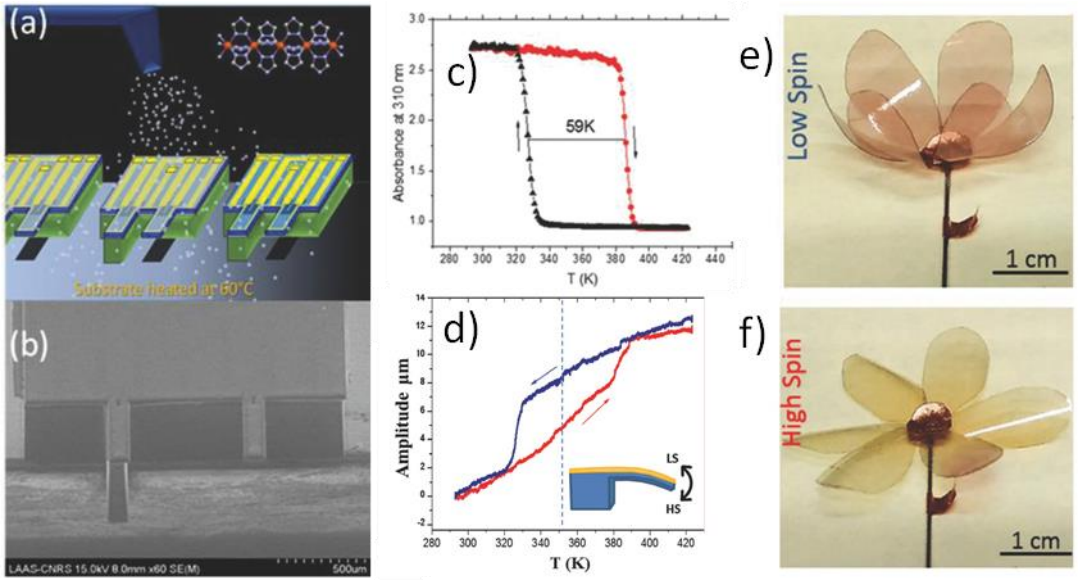

Fig 1.34) Scheme of spray-coating of an SCO-polymer composite on silicon microcantilevers, b) SEM image of the resulting MEMS, c) variable temperature UV absorption at 310 nm of the SCO/SU-8 composite, d) variable temperature actuation amplitude in the MEMS, e-f) macroscopic SCO/SU-8 actuator in the LS and HS states [99].

I.3.1.2.3 In-Situ Polymerization

Some composites have been reported using an insoluble SCO complex (which precludes any attempt at synthesizing the complex from an SCO solution) and an insoluble polymer (which precludes the use of any kind of casting technique). In these cases, to obtain a dispersed mixture of SCO particles in the polymer, the matrix is polymerized around the SCO material, meaning that the matrix itself is formed during the composite formation stage.

The first study of a composite developed using this technique studied the effect of PVA (poly(vinyl alcohol)) and SLS (sodium lauryl sulfate) as additives in the polymerization of TFEMA (trifluoroethylmethacrylate) mixed with 1% wt of a Fe(II)-triazole SCO complex [100]. Microscopy analysis showed that the nanodispersed SCO complex, displaying bistability, was incorporated into the cores of polymer particles covered with PVA shells.

In a step towards electroactive SCO polymer composites, SCO/ppy (polypyrrole) composite films with $[Fe(H\text{-}trz)_2(trz)](BF_4)$ and $[Fe(NH_2trz)_3](SO_4)_2$ were developed in a groundbreaking study [101]. The composite materials were prepared by a two-step synthetic method. First, a chemical oxidation of the py monomer takes place in the presence of the polycrystalline powder SCO complex resulting in ppy-covered SCO particles. Then, the particles are sintered into a thick film. The magnetic properties of the complexes in the composite film were identical to those in the bulk. Remarkably, a pronounced coupling between the conductivity of the polymer matrix and the SCO properties were observed in the composite films, with a thermal hysteresis loop of the electrical conductivity (fig 1.35). Different parameters, such as the ppy/SCO ratio, the pressure applied during the sintering process, and the thickness of the film,

were shown to have an impact on the σ_{HS}/σ_{LS} ratio. This work is the first example for strain-coupling of SCO to electroactive polymers (EPA) in a composite material, with interesting perspectives for the development of sensors, actuators and energy harvesting devices.

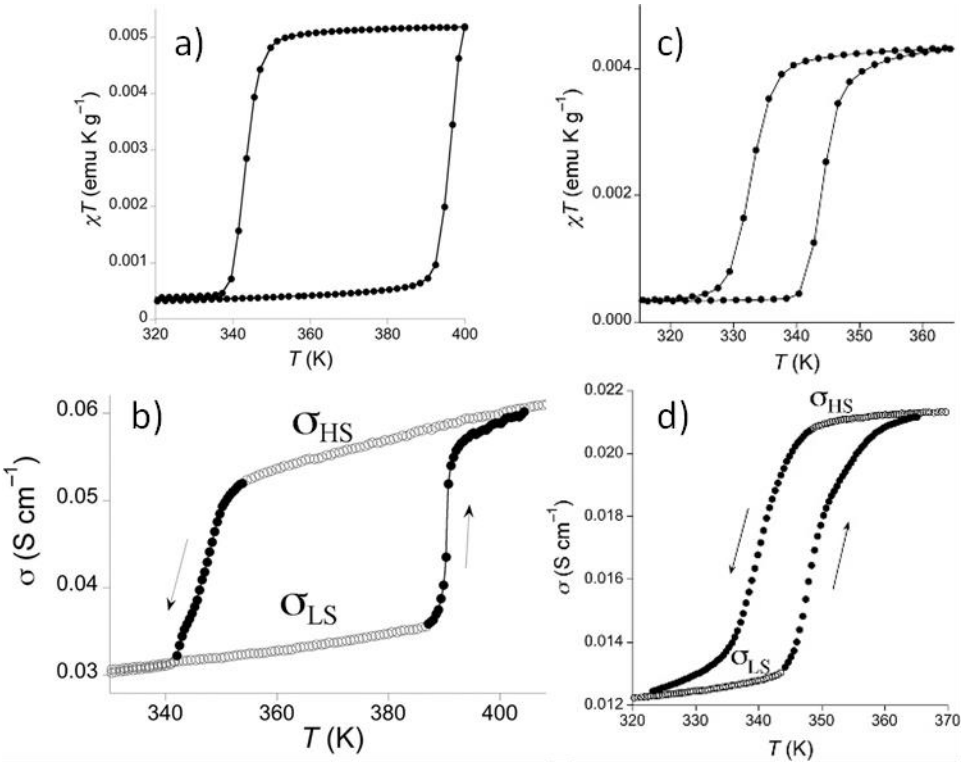

Fig 1.35) Variable temperature magnetic susceptibility and electrical conductivity data for ppy/SCO composites with a-b) $[Fe(H\text{-}trz)_2(trz)](BF_4)$ and c-d) $[Fe(NH_2trz)_3](SO_4)_2$ [101].

I.3.1.2.4 Other techniques for solid dispersion

An innovative study observed that if the SCO complex $Fe(Htrz)_3$ is used during the preparation of mesoporous silica thin films by electrochemically assisted self-assembly (EASA), it can act either as an additive when used at low concentrations (≤ 3 mM) or as a template in higher concentrations (5 mM) [102]. As a result, one may obtain either a vertically aligned mesostructure where the complex is incorporated with the surfactant species, resembling an ideal 0-3 connectivity composite (low concentration) and can be removed by solvent extraction or a worm-like mesoporous film filled with the complex immobilized in the silica matrix resembling an ideal 1-3 connectivity composite (high concentration).

MAPLE (matrix-assisted pulsed laser evaporation) is a variant of pulsed laser deposition, which was developed to deposit thin films of soft and fragile materials (fig 1.36). In the MAPLE approach, the target is a frozen solution or suspension of the desired material. In a study which explores very fabricate techniques for the synthesis of SCO complexes [103], the MAPLE technique was used to deposit nanocrystalline thin films of the SCO complex $[Fe(pz)Pt(CN)_4]$ impregnated with polyethylene glycol (PEG). A cryogenically cooled suspension of nanocrystals of the SCO complex in a mixture of 1,1-dichloroethane and the polymer was used.

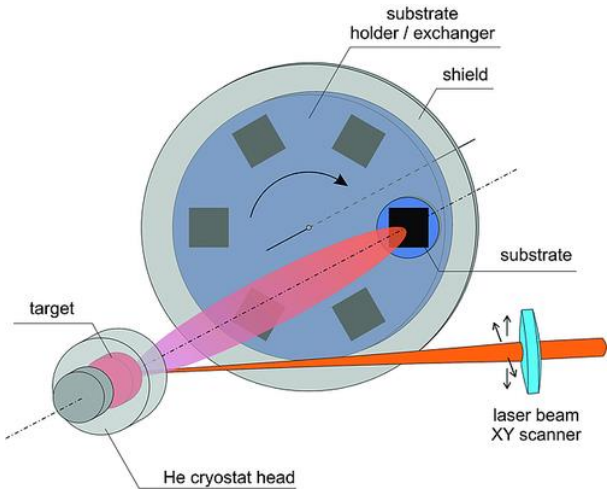

Fig 1.36) MAPLE experimental setup applied for thin film deposition of the nanocrystalline $[Fe(pz)Pt(CN)_4]$ [103].

I.3.2 SCO Organic Polymers

Fundamentally, we can divide 'organic polymer SCO complexes' into two basic categories based on the way the polymer is attached to the SCO complex: a) when the polymer is attached by supramolecular interactions to the SCO complex, for example representing the counter-anion of the complex (polymer backbone) such as in Nafion-SCO composites and b) when the polymer is covalently attached to the SCO ligands of the SCO complex. In this section, we focus exclusively on the second approach (the supramolecular approach was discussed in section 1.3.1.1.2.)

In a first report, by using ligands covalently attached to a polymer, a series of amorphous iron(III) complexes were obtained from copolymers of PVP (poly(4-vinylpyridine)) or poly(1-vinylimidazole) and various Schiff base ligands like H_2Salten [104]. As it can be expected in such materials with highly diluted iron centers, magnetic measurements revealed that the spin crossover is very smooth, spans over a broad range of temperatures and remains largely incomplete.

In a similar vein, Fe(II) SCO complexes were synthesized using PGMA (poly(glycidyl methacrylate)) [105] and MPEG-750 (methoxy polyethylene glycol) [106] based PGMA-trz and MPEG-trz ligands. Variable temperature magnetic susceptibility measurements showed that, in the case of PGMA, the complex is in the HS state at room temperature and the spin crossover is gradual along a vast range of temperatures (mainly 150 - 250 K), which eventually never reaches a full LS state. Interestingly however, the most abrupt transition was obtained for the complex $[Fe^{II}(MPEG\text{-}trz)_{1.5}(NH_2trz)_{1.5}](BF_4)_2$ in which the transition temperatures are $T_{1/2}\downarrow$ = 248 K and $T_{1/2}\uparrow$ = 251 K denoting a small hysteresis (ΔT = 3 K), which makes it the first SCO organic polymer with an abrupt transition (fig 1.37).

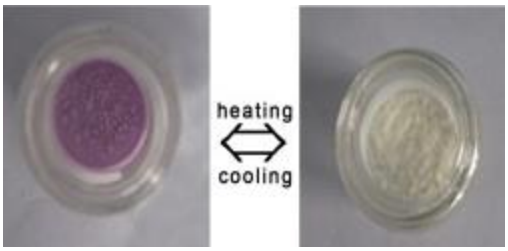

Fig 1.37) Demonstration of the thermochromism of $[Fe^{II}(MPEG\text{-}trz)_{1.5}(NH_2trz)_{1.5}](BF_4)_2$ [105].

In an interesting study exploring the effect of polymerization itself on the SCO properties [107], the ligand 11-(4*H*-1,2,4-triazol-4-yl)-undecylmethacrylate (L) was prepared to form the complex $(FeL_3)(BF_4)_2$, which was later polymerized *in situ*, obtaining an oligomer that contains *ca.* 6-7 monomeric units. The magnetic behavior of the polymerized SCO complex reveals a gradual, but complete spin crossover, which remains similar to the starting monomeric complex. This similarity provides an additional proof for the lack of influence of the polymerization reaction on the SCO active part of the system. The authors attributed this successful synthesis to the relatively large distance between the groups involved in the polymerization reaction and the SCO.

In another study following this idea of exploring the effect of polymerization, an iron(III) Schiff base with pendant thienyl groups was prepared [108]. A film of around 130 nm thickness was obtained by *in situ* electro-polymerization of a solution of the Schiff base complex on an ITO-coated glass. The magnetic behavior of both the monomer and the polymer are similar, showing a smooth decrease of the magnetic moment when the temperature is decreased. Remarkably, these systems not only display SCO, but they exhibit also a high electrical conductivity. However, no clear correlation between the temperature dependence of the magnetic moment and that of the conductivity could be established. In a follow-up study, aerobic oxidation in solution allowed the formation of SCO-polymer microspheres of a similar thienyl iron (III) Schiff base [109], which shows similar magnetic behavior to the parent monomer (fig 1.38).

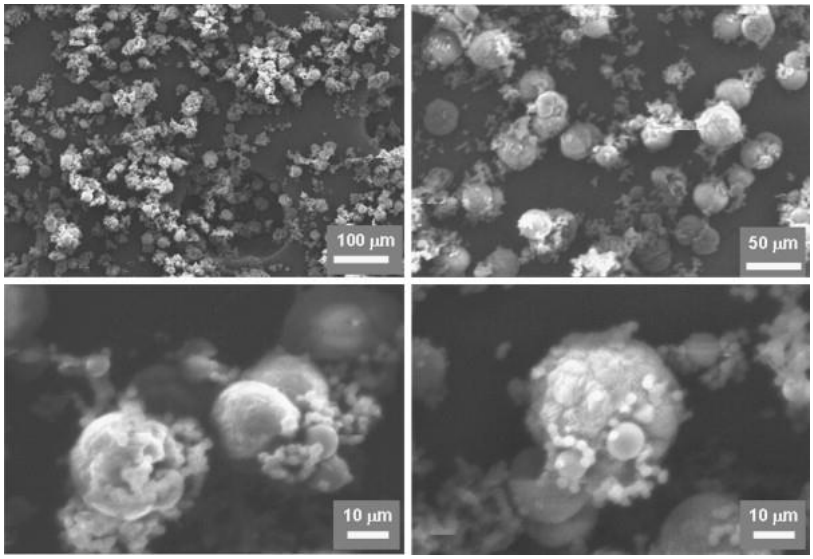

Fig 1.38) SCO-polymer microspheres of a thienyl iron (III) Schiff base [109].

Interesting follow-up studies have been developed using similar approaches, focusing on the electro-polymerization or thiophene derivatives [110] and more recently [111] in combination with a valence tautomeric cobalt bis(semiquinone) complex and $\{Fe_4Co_4\}$ cages, respectively. Both types of polymers were shown to display charge transfer-induced spin transition upon temperature variation or light irradiation. Overall, this approach of electro-polymerization not only affords for processing the compound as smooth, ultrathin films, but also provides potentially an interesting means to develop synergies between the magnetic switching behavior, inherited from the metal complex, and electroactive properties arising from the polythiophene part.

As seen in this work, SCO composites can be used for a variety of different applications. In this research work we will however focus on two main applications: thermal energy harvesting and mechanical actuation. A brief introduction to the principles of energy harvesting will be given in chapter 2. Likewise, an introduction to materials for mechanical actuation will be presented in chapter 3.

I.4 Objectives of this research work

As we have seen in this introductive section, there has been a wide array of studies approaching the fabrication of SCO composites. This research field is now less oriented towards the development of new synthetic methods, and more towards the integration of these concepts into smart functional materials and devices. In this regard, there has been a very **limited amount of studies focusing on exploiting the volume change of the spin transition** via new synergistic materials, and while advances have been done in terms of proof-of-concepts of these materials as actuators, **the field remains open regarding their implementation into functional devices**.

There are two main objectives in this research work: The first one is the **development of novel, synergistic SCO composite materials** with the aim of exploiting their volume change during the spin transition to obtain a mechanical or electromechanical effect. To this end, a variety of fabrication techniques will be explored, from straightforward drop-casting method to more sophisticated multimaterial 3D printing technology. The second objective of this research work is the **fabrication of functional SCO composite devices for energy harvesting and mechanical actuation**. The first application aims to fabricate harvesting materials and devices capable of recovering thermal energy as electrical energy. The second application aims to obtain a programmable and controllable artificial muscle, fit for automatization, and a demonstrator device integrating such artificial muscles in a functional device.

Thus, the second chapter of this research work will thus focus on the exploitation of the volume change due to the spin transition to obtain electroactive SCO P(VDF-TrFE) composites showing novel properties arising from the coupling of a piezoelectric matrix and the SCO phenomenon. The choice of the materials, the detailed fabrication and optimization to obtain interesting electroactive properties will be presented.

The third chapter of this work will concern the use of SCO fillers to fabricate spin transition composite actuators. First we will describe the process of optimization of the 3D printing methodology used to incorporate SCO complexes in a printed composite. Then we will characterize the thermal actuation properties of these devices printed using this novel methodology. Finally, the chapter will describe the fabrication process of highly controllable, resilient and electrically driven solvent-casted SCO actuators, and then the process of setting up a controller system for the device and the fabrication of a demonstrator.

Chapter 2: Electroactive spin crossover composite materials for thermal harvesting applications

This chapter details the research process involved in the fabrication of **P(VDF-TrFE) based SCO electroactive composite materials**. These composites are developed with the goal of their application in thermal energy harvesting. The chapter will be divided in two main sections.

The first section is a brief introduction to the **concept of thermal harvesting** and more specifically of the composite materials being developed for this purpose. This requires an understanding of the **concepts of piezoelectricity and pyroelectricity**, and a general overview of the body of research on **PVDF polymer, copolymer and composites**.

The second section of the chapter details the fabrication of these materials. First focusing on the chemical aspect, the choice of the SCO complex used and their physico-chemical characterization. Then it will go into detail on the process of fabricating the **composite films**, all the various attempts that were needed before obtaining materials with optimized properties, and finally, go over the physical characterization of the materials, with a strong emphasis on the **electroactive properties of the composites**.

2.1 Piezoelectricity, pyroelectricity and ferroelectricity

This chapter will focus on the development of electroactive SCO composite films, this will be achieved by synergistically coupling the properties of SCO complexes with the properties of an electroactive polymer matrix. However, in order to properly understand these materials, we must first delve into the concepts of piezo, pyro and ferroelectricity. This section will offer a brief theoretical overview of these concepts.

A crucial concept to describe the behavior of **ferroelectric and piezoelectric materials** is their response to an applied electrical field. When a polar material is placed in an externally applied electrical field, the material adapts to this stimulus by rearranging the polar domains in the structure. As a result, dipoles are created, and the material undergoes polarization [112]. Ferroelectric materials are materials which exhibit spontaneous polarization, namely they have oriented polar domains even when the external field is removed. These materials undergo a phase transition from a high-temperature para-electric phase to a low temperature ferroelectric phase. The temperature at which this phase transition occurs is called the Curie temperature.

All ferroelectric materials are a class of piezoelectric materials, and they all show to some degree this property. **Piezoelectrics** are materials which can be polarized not only by application

of an electrical field, but also by a mechanical stress. This phenomenon can be understood with a simple molecular model as shown below (fig 2.1): when a neutral polar unit with clearly differentiated positively and negatively charged domains undergoes a deformation, these domains align, giving rise to small dipoles. Opposite facing poles inside the material cancel each other and fixed charges appear on the surface. This means that for a material with well aligned polar units, the internal small dipoles of the material will be less likely to cancel out, and the charges appearing on the surface of the material will be larger [112].

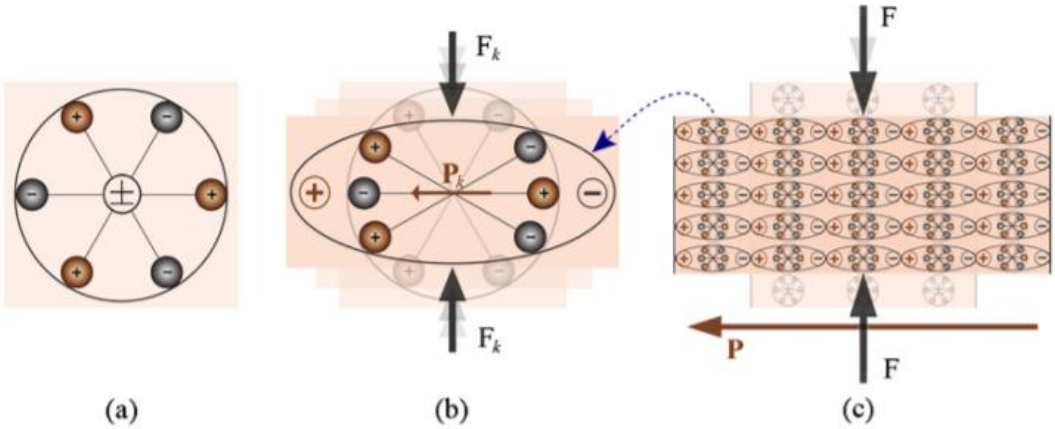

Fig 2.1) Simple molecular model of the piezoelectric effect. a) A neutrally charged polar unit at rest. b) The application of an external force F_k generated a polarization P_k in the material. c) Alignment of the internal dipoles of the material generates a charge at the surface [112].

Polarization of the material in this manner generates an electric field across the surface, and in the case of the material being placed between two connected electrodes, it causes the flow of the free charges existing in the conductor. This flow of free charge continues until the free charge neutralizes the polarization effect. This means that in a steady state, even under deformation, the flow of free charge eventually becomes zero.

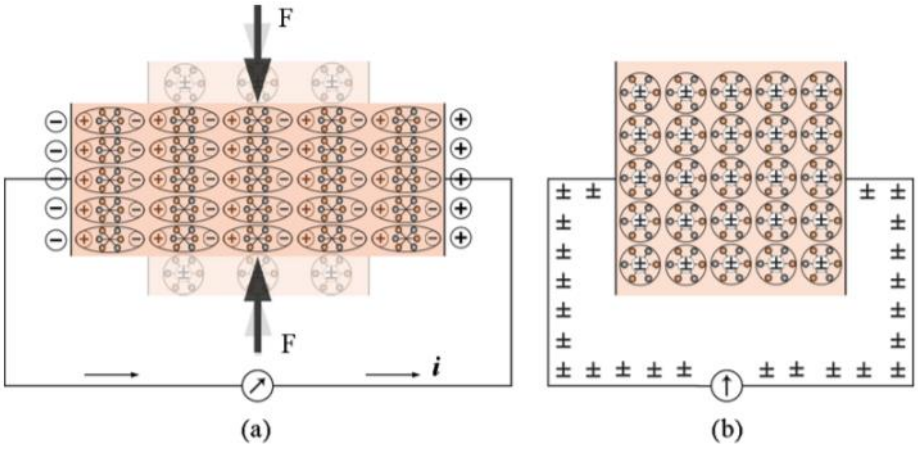

Fig 2.2) Flow of charge in a piezoelectric material. a) Under a constant force F, the material becomes polarized and charges appear on the surface. If placed between two connected electrodes, these charges induce the flow of electrical current in the circuit. b) The system at rest shows no free flow of charge [112].

When a piezoelectric material is mechanically strained it becomes electrically polarized, producing a charge on the surface of the material. The density of the generated fixed charge in a piezoelectric material is proportional to the external stress, and can be mathematically expressed by the following expression:

$$P_{pe} = d \times T \ (1)$$

Where P_{pe} is the piezoelectric polarization vector, d is the piezoelectric strain coefficient and T is the stress to which the piezoelectric material is subjected. When an electrical field E is applied to a material of dielectric constant ε, an electric displacement is created, generating a surface charge density. The magnitude of this electric displacement D is given by the following relationship

$$D = \varepsilon \times \mathrm{E} \ (2)$$

If the material is piezoelectric, the electric field E also produces a strain S_{pe}, expressed as:

$$S_{pe} = d \times E \ (3)$$

Given the vectorial nature of this model, the tensor relation to identify the dependence between mechanical stress, mechanical strain, electric field and electric displacement is given as:

$$D_i = \varepsilon_{ik}^{T} E_k + d_{iq} T_q \quad (4)$$

Where, ε_{ik}^{T} is dielectric constant tensor at constant electric field, d_{iq} is piezoelectric constant tensor, D_i is the electric displacement in i direction, T_q is mechanical stress in q direction, and E_k is the electric field in k direction. In case of polymeric materials, the stretch direction is "1", the axis orthogonal to the stretch direction in the plane of the film is "2", the polarization axis (perpendicular to the surface of the film) is "3", the shear planes are "4", "5", "6" and are perpendicular to the directions "1", "2", and "3" respectively (fig 2.3).

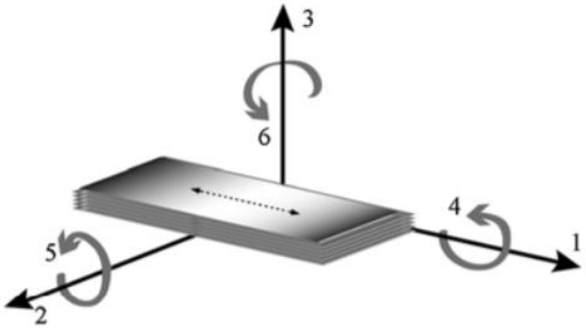

Fig 2.3) Direction notation for a piezoelectric film polarized on the axis 3 [112].

From this relationship we can obtain the electromechanical response of a piezoelectric material along the same or other direction as that of the stimulus. In the most commonly studied scenario, the electromechanical response of a film, when it is stressed in the same direction of the polarization axis, and the electrodes are placed along this axis as well, can be expressed as:

$$D_3 = d_{33}T_3 + \varepsilon_{33}^{T}E_3 \quad (5)$$

From this relationship we obtain the d_{33} coefficient, the most commonly used piezoelectric coefficient, describing the relationship between the stress exerted on a piezoelectric film along the polarization axis and the current displacement produced by the charges on the surfaces along the polarization axis.

Pyroelectric materials are a subtype of piezoelectric materials; these are characterized by the generation of a current discharge along the surface of the material when the material is subjected to a temperature change. Much like in the case of a piezoelectric discharge, this phenomenon occurs due to a change in the polarization of the material upon an external stimulus, in this case a thermal variation. The pyroelectric coefficient p_i can be expressed as the change in the spontaneous polarization vector with temperature:

$$p_i = \frac{\partial P_{S,i}}{\partial T} \quad (6)$$

It should be noted that similarly to the case of a piezoelectric material, after the pyroelectric material is thermally excited, as it remains in the steady state, the current will begin a leakage process as relaxation phenomena return the system to its original state even if the system remains at a high temperature [112].

These phenomena have been of great research interest for applications as sensors, actuators and thermal energy harvesters. In the following section we will explore a brief overview of these materials in the context of energy harvest.

2.2 Energy Harvesting.

Energy harvesting is the process by which ambient sources of energy such as kinetic energy, ionic gradients, temperature gradients or electromagnetic radiation can be captured, stored and used as electrical energy for the operation of devices [9]. It is important to note that the objective of these technologies is not to replace large-scale energy generation, but to assist in the powering of small wireless devices, which are meant to be autonomous.

A classic example of energy harvesters are piezo-electric harvesters [113]. These devices transform mechanical perturbations or change in pressure into electrical energy. Piezoelectric materials generate an electrical charge when exposed to mechanical stress, often due to perturbation of an anisotropic charged crystalline lattice. These materials, while often used in applications such as micromechanical sensors and actuators for devices such as AFM, STM and microbalances, also have potential for energy harvesting.

One of the most attractive opportunities for energy harvesting is thermal harvesting, which exploits small temperature gradients or shifts to generate electrical energy to power up lightweight devices. Thermal generators are limited in their output, with heat flow as the main limiting factor. However, the human body provides an almost constant thermal gradient and

source of heat, which can be exploited to fuel devices with very low energetic requirements, such as sensors, in a completely autonomous manner. For this reason, integration of thermal energy harvesters as flexible, wearable electronics is a subject of high interest in research.

There are two main types of thermal energy harvesters: thermoelectric devices and pyroelectric devices (fig 2.4). Thermoelectric devices transform thermal gradients into electricity via the Seebeck effect [114]. Thermoelectric devices have gotten ample attention as energy harvesters. However they cannot always operate effectively, as a thermoelectric device requires a spatial thermal gradient, and cannot operate on temporal thermal gradients.

An interesting example of thermoelectric energy harvesting is thermoelectric wristwatches, which convert body heat into electrical power to fuel the device. Such models have already been fabricated by various companies, showing the interest of this field of research even outside of purely scientific endeavor.

The second type of thermal harvesters is based on pyroelectric materials, which rely on a temperature change over time to generate electrical currents. They stand in contrast to thermoelectric harvesters by employing a temporal thermal gradient rather than a spatial one. This allows these devices to cover applications that thermoelectric devices cannot. The working principle behind pyroelectricity comes from the change in spontaneous polarization in a solid, arising from a temperature fluctuation.

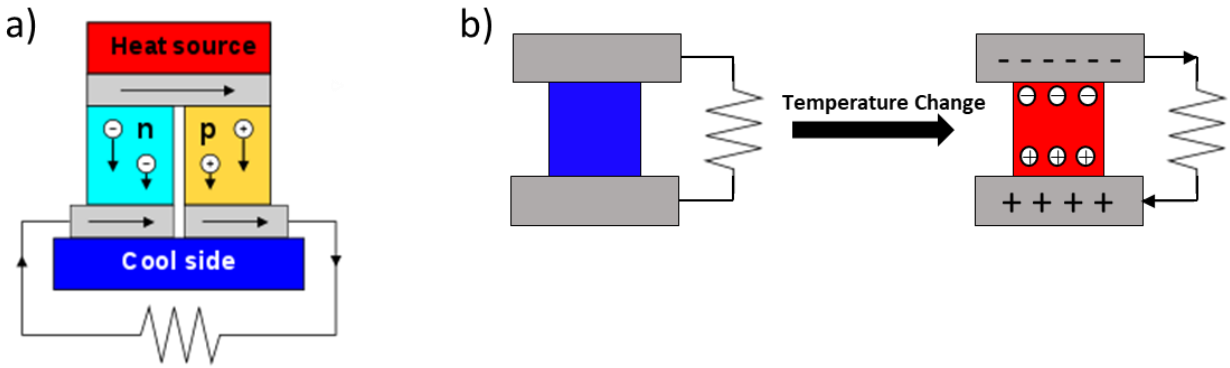

Fig 2.4) Schematic representation of the two types of thermal energy harvesters: a) Thermoelectric harvester. b) Pyroelectric harvester

There are two main mechanisms by which these polarized solids can generate electrical currents; these are the primary pyroelectric effect and secondary pyroelectric effect. The primary pyroelectric effect comes purely from the change in polarization with temperature. The secondary pyroelectric effect pertains the piezoelectric discharge contribution which comes from the thermal expansion of the pyroelectric material upon the temperature change. The total pyroelectric effect is thus the sum of these two effects. In this work we are concerned with the use of pyroelectric materials for thermal harvesting applications [8].

Ferroelectric inorganic materials are commonly used for their pyroelectric properties. Such is the case of lead zirconate titanate (PZT), $BaTiO_3$, $KNbO_3$, and some piezoelectric materials which have spontaneous polarization, such as ZnO and CdS. However, polyvinylidene fluoride (PVDF), an organic polymer with interesting mechanical and ferroelectric properties, has also been of interest in this field of research [114]. The mechanical flexibility and ease of manipulation of the soluble thermoplastic make it extremely interesting for multiple applications, when compared to the usually rigid inorganic materials commonly employed. If mechanical resilience, flexibility and toughness are desirable properties, PVDF becomes a highly attractive option for the fabrication of thermal harvesters [115]. This research work will thus focus on the use of PVDF as a base material for pyroelectric harvester devices.

2.2.1 Piezo and pyroelectric P(VDF-TrFE) copolymers.

PVDF is a thermoplastic linear polymer (fig 2.5). It is readily soluble in a variety of solvents and easily processable into films and devices. It is a chemically stable polymer, flexible and mechanically tough. More importantly, PVDF has a crystalline phase wherein it presents ferroelectric properties, which give rise to piezo and pyroelectricity in turn.

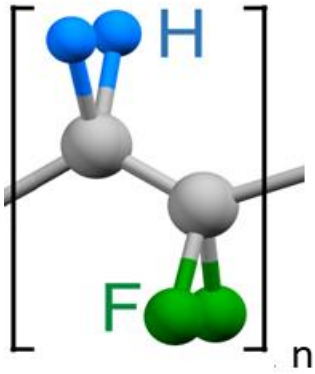

Fig 2.5) PVDF Structure.

In fact, PVDF can be obtained in three different crystalline phases, with significantly different properties. PVDF is rarely seen as a 100% crystalline polymer, and is usually obtained with coexisting crystalline and amorphous phases. The α-phase is a non-polar phase with a TGTG (trans-gauche-trans-gauche) conformation. The β-phase is the highly polar fully trans TTTT (trans-trans-trans-trans) phase. Finally the γ-phase has a TTTG (trans-trans-trans-gauche) conformation, which renders it polar as well. However, to obtain the γ-phase, the polymer must be super-cooled from a melt solution, which makes it inaccessible for many fabrication methods and applications [116].

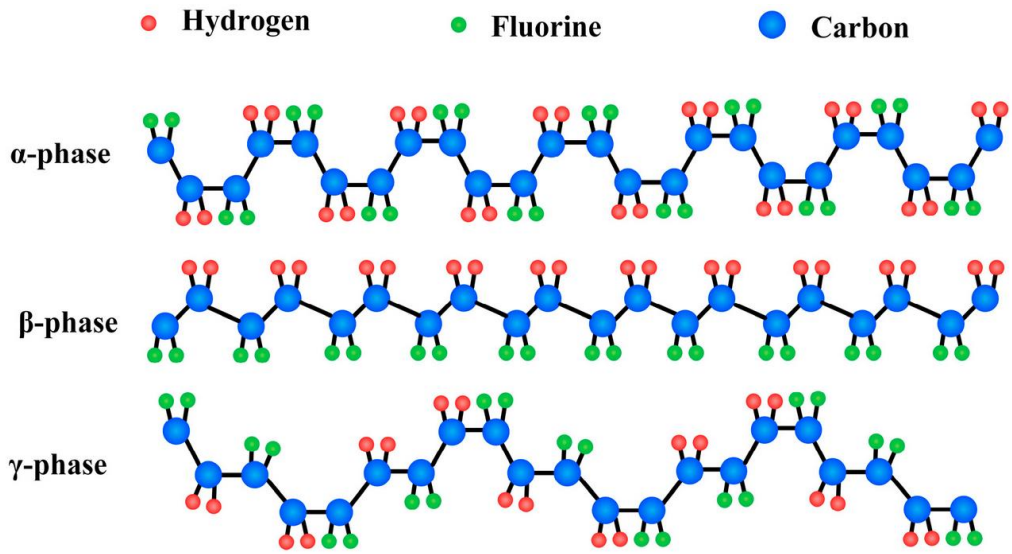

Fig 2.6) Crystalline conformations of PVDF [116].

PVDF crystallizes naturally in the α phase (Fig 2.6). However, this crystalline phase shows no ferroelectricity. In the β phase, the chains are aligned in such a way that the fluorine atoms are on the same side of the chain, giving rise to a dipole moment. By aligning these polar chains through an electrical field, the solid can be polarized, leading to piezo and pyroelectric discharges. To crystallize PVDF in the desired β phase, the solid must be heated to 100°C and mechanically stretched, which limits the range of applications in which in can be used [117].

The ferroelectric properties of a given PVDF sample depend on both the crystallinity of the material and the crystalline phases of the crystalline domains. The crystallinity of the material determines what proportion of the polymer chains are organized in a crystalline region, whereas the crystalline phases determine whether these crystalline regions of the film are in the electroactive β phase or not (fig 2.7). The proportion of the β crystalline phase can be analyzed via vibrational spectroscopy (FTIR, Raman) or from the x-ray diffraction (XRD). The crystallinity of the material, however, can be best assessed from thermal studies of the material, by calculating the enthalpy required for it to undergo a phase transition, usually the solid-liquid phase transition. A higher melting enthalpy would suggest more crystalline domains in the material, leading to a higher energy requirement to undergo phase transition. The relationship can be expressed as:

$$\Delta X_c = \frac{\Delta H_m}{\omega(VDF)\Delta H_0} \quad (7)$$

Where ΔX_c is the crystallinity of the polymer, ΔH_m is the melting enthalpy of the polymer, ω(VDF) is the mass ratio of VDF and ΔH_0 is the melting enthalpy of a 100% crystalline PVDF [118].

However, to better take into account the proportion of the β phase in the crystallinity of the polymer, we use the following relationship [119]:

$$\Delta X_c = \frac{\Delta H_m + \Delta H_C}{\omega(VDF)\Delta H_0} \quad (8)$$

Where ΔH_C is the enthalpy of the Curie transition. In this regard, both thermal (DSC) and structural (XRD, Raman, FTIR) studies complement each other and allow us to properly characterize the properties of PVDF films.

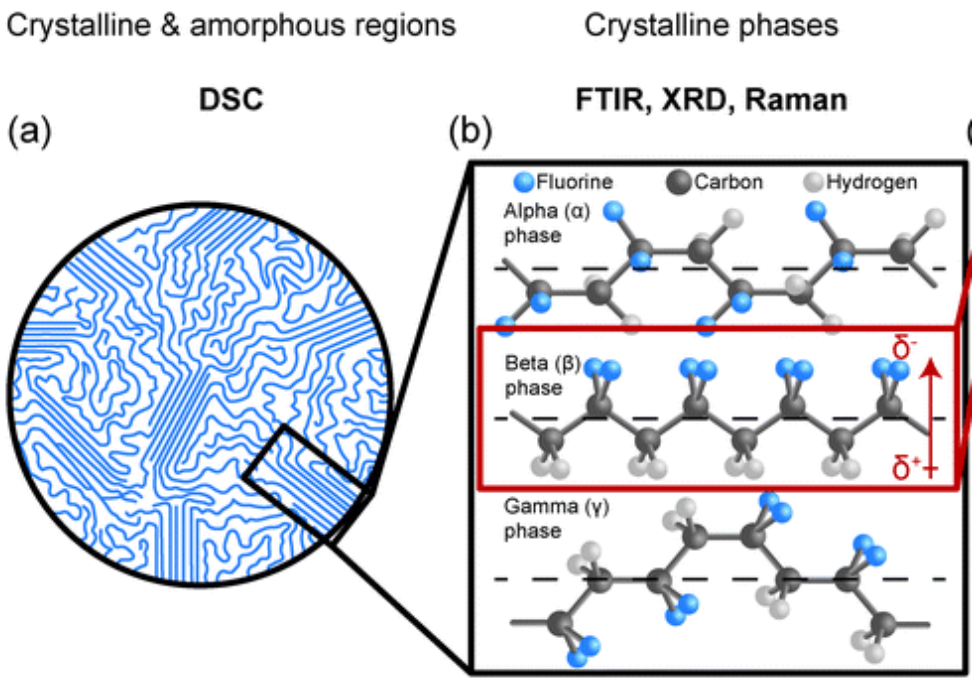

Fig 2.7) a) Schematic representing the crystalline and amorphous regions of PVDF. b) Schematic representing the crystalline phases of the polymer [120].

Poly(vinylidene fluoride-co-trifluoroethylene) (P(VDF-TrFE)), is a copolymer of PVDF with PTrFE (fig 2.8) which crystallizes spontaneously and mainly in the desired β crystalline phase. This is hypothesized to be due to the steric hindrance effect of the TrFE chains on the copolymer. This copolymer retains the solubility and mechanical resilience of PVDF. The crystallinity and β-phase proportion are both heavily dependent on both the fabrication of the polymer, annealing conditions and the proportion of TrFE. The temperature at which the copolymer loses its polarization and reversibly switches to the α phase is called Curie temperature. The Curie temperature is greatly dependent on the copolymer proportion, though the crystallinity plays a factor as well. This gives us a series of characteristics that can be adjusted in both composition and preparation to obtain the desired characteristics for a given application [121].

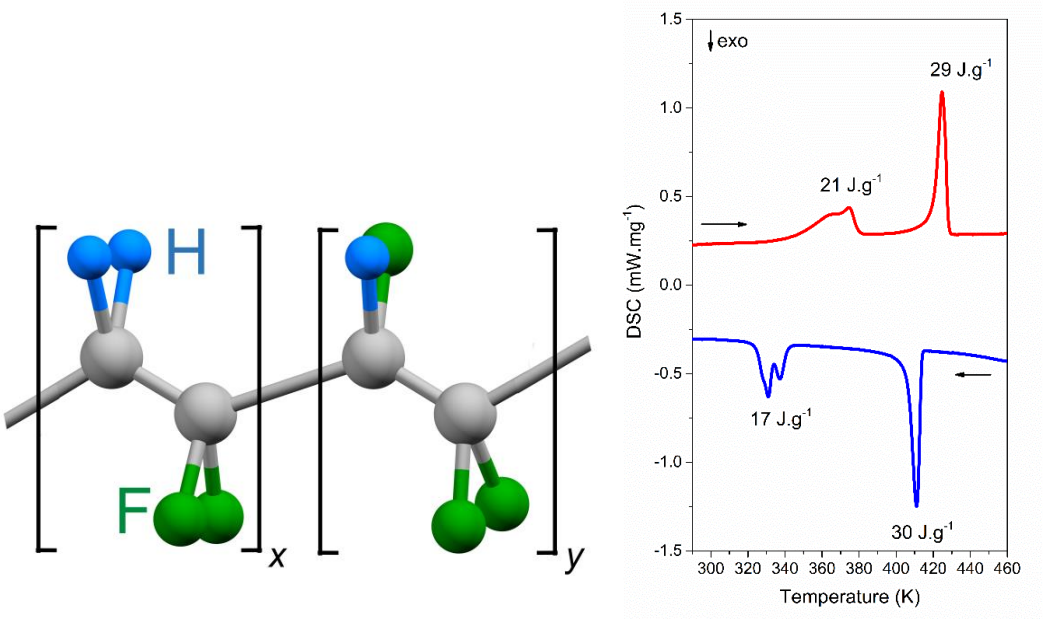

Fig 2.8) P(VDF-TrFE) structure (left) and Differential Scanning Calorimetry (DSC) of P(VDF-TrFE) 70-30.

Differential Scanning Calorimetry allows us to see the phase transitions in the material. For example, in the case of P(VDF-TrFE) 70-30 we can easily see the transition at 420 K which corresponds to the melting point, but also a transition centered around 370 K (on heating) which corresponds to the Curie transition (in which the β phase of the polymer rearranges to an α phase).

2.2.2 P(VDF-TrFE) Composites

An approach commonly used to enhance the electroactive properties of PVDF and P(VDF-TrFE) is the use of composite materials [122]. An important body of research exists on the incorporation of fillers into the polymer matrix of PVDF or its copolymer. For example, researchers have attempted to integrate piezoelectric nanoparticles, nanorods and nanowires, showing increased electrical output due to synergetic effects between the piezoelectric NPs and the piezoelectric polymer matrix [121].

In addition to this kind of filler, dielectric nanomaterials, such as graphene oxide and DNA, have also been integrated into PVDF polymer matrices. An interesting result of these inclusions is the increase of the β phase fractions of PVDF (see Fig 2.9 the fabrication of a harvesting piezoelectric device made with DNA). This suggests that some PVDF nanocomposites could enhance the electroactive properties of the matrix itself, in addition to the inclusion of novel functionalities in the composite, depending on the filler [123].

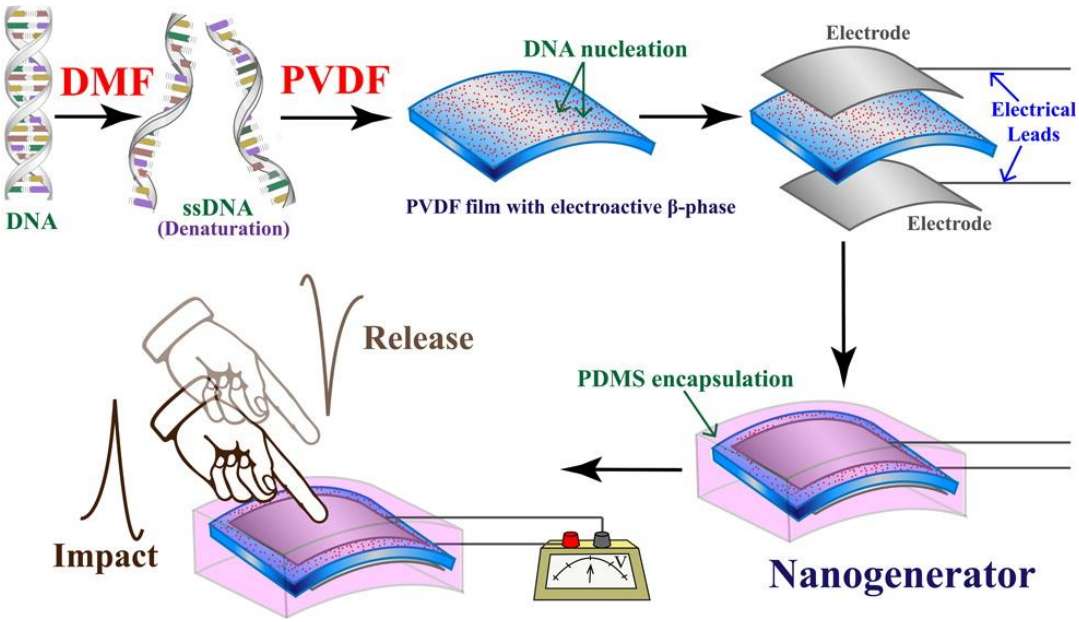

Fig 2.9) Integration of DNA fibers into a PVDF copolymer to fabricate a composite nanogenerator [123].

Metallic nanoparticles have also been used as composite fillers. Pd and Au nanoparticles are integrated into PVDF matrices, and the resulting composites show increased β phase fractions. These effects have been attributed to surface charge interactions [124,125]. Likewise, Ionic liquids have been investigated as fillers for PVDF composites with the objective of increasing the proportion of the β phase. The utilization of ionic liquids, due to their structure, has been suggested to aid preferential nucleation in PVDF composites via ion-dipole interactions [126].

Ionic liquid PVDF composites, however, open the possibility for another kind of PVDF composite. An approach where the intent is not to optimize the electroactive properties of the polymer matrix, but to add a synergistic filler, which directly interacts with the piezo and pyroelectric properties of the polymer. Indeed, ionic liquid composites have also been used to fabricate PVDF actuators, which respond to voltage stimulus with a bending motion [127]. In a similar vein, shape memory alloys have been integrated into PVDF matrices to fabricate thermal energy harvesting materials [128]. SMAs respond to thermal stimulus with a significant volume change, which in turn synergizes with the piezoelectric properties of the matrix, creating a pseudo pyroelectric effect and an increased electrical discharge upon thermal excitation.

This suggests the possibility of using SCO materials much in the same manner: the thermal stimulus would induce the SCO phase transition, which entails a volume change. This volume change would in turn interact with the piezoelectric P(VDF-TrFE) matrix to generate discharge currents around the spin transition temperatures, creating a synergistic composite. The SCO phenomenon is of special interest for this application as it allows for a significant volume change to take place within a narrow temperature window in a reversible manner. The development of such a material will be the main focus of this chapter.

2.3 Spin Crossover@P(VDF-TrFE) Composites

The development of the SCO composites will be divided in two generations. The first generation composites were a first approach to an fabrication method that could effectively couple SCO particles in an electroactive polymer matrix, and the results serve as a proof of concept for the coupling of SCO properties and piezoelectric and pyroelectric responses from a ferroelectric matrix.

Using the results of these first generation of complexes, the second generation optimizes the fabrication procedure and expands it to a wider set of complexes and matrices, delving deeper into **the interplay between the SCO and electroactive properties of the matrix**, while also proving the flexibility and reliability of this fabrication procedure.

2.3.1 First generation SCO@P(VDF-TrFE) composites

The fabrication of an SCO composite material has two principal considerations: determining the optimal matrix material and determining the appropriate SCO filler material. Among the available ferroelectric polymers, we use P(VDF-TrFE) copolymers. The use of copolymers instead of the pure PVDF is an effective method to tune the polymer structure and to increase the proportion of the ferroelectric β phase. Nevertheless, an additional thermal annealing process is generally used to increase the degree of crystallinity and a further high voltage poling is also necessary to align the ferroelectric domains.

Poling consists in aligning the polar ferroelectric domains of a material (Fig 2.10). This is achieved via a strong electrical field which induces the rearranging of the crystalline domains. In the case of P(VDF-TrFE), given the piezoelectric properties of the poled material, a common measure of the effective polarization of a given sample is determined experimentally by its piezoelectric coefficient, d_{33}. The piezoelectric coefficient quantifies the mechanical strain experienced by a piezoelectric material under a given electric field.

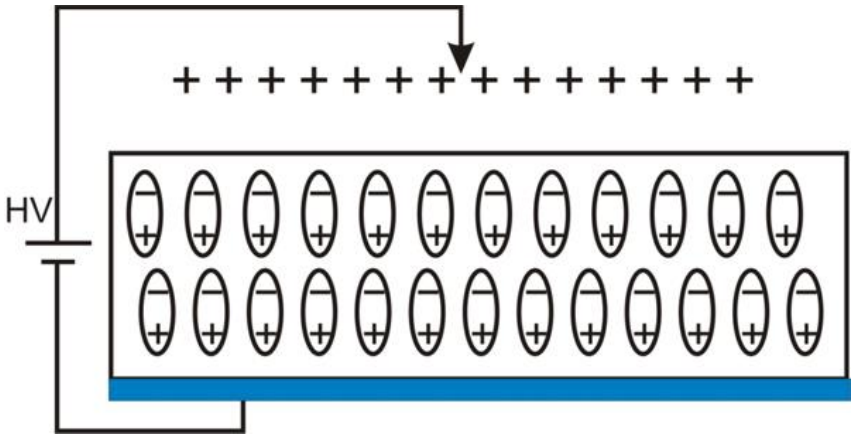

Fig 2.10) P(VDF-TrFE) poling process

The chosen matrix for this study, P(VDF-TrFE) 70-30 (70% PVDF, 30% TrFE), has a working temperature delimited by the glass transition temperature and the Curie temperature. Below the

glass transition temperature (238 K), P(VDF-TrFE) loses its ferroelectric properties [119], and above the Curie temperature of the polymer (370 K) it is unable to retain the β crystalline phase necessary for the polymer to show its electroactive properties.

2.3.1.1 Choice of the Spin Crossover Complexes

Given the properties of the polymer matrix previously established to be P(VDF-TrFE), it is necessary to use an SCO complex with a transition temperature well within the bounds determined by the polymer matrix. In addition to this condition, it is necessary to use a compound with significant volume change upon the transition to trigger the synergy between the SCO and the piezoelectric matrix. Finally, it is also important to use a complex which can form nanoparticles, to allow proper dispersion of the complex into the matrix.

With all these considerations, a complex was chosen for the study: the benchmark 1-D SCO polymeric coordination complex $[Fe(Htrz)_2(trz)](BF_4)$ (trz = 1,2,4-Triazole), see Fig 2.11. This complex has shown both a high degree of volume change upon spin transition (≈11%) [129] and the ability to be processed into nanoparticles. However, the transition temperature for the heating (380 K) is too close to the Curie temperature of the polymer. In order to lower the SCO temperature, a mixed-ligand approach was chosen. Using this technique, the complex is prepared with a mixture of ligands, specifically replacing a fraction of the original ligand (in this case the trz ligand) with a ligand that corresponds to a complex with a significantly reduced spin transition temperature. In this case the complex is $[Fe(NH_2trz)_3](BF4)_2$ (NH_2trz=1,2,4-4-NH_2-triazole) which has a transition temperature around 280 K.

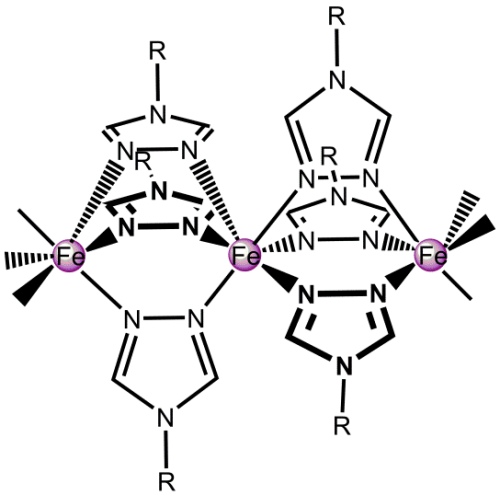

Fig 2.11) Chemical structure of the SCO 1D polymer chain triazole family of complexes.

The proportion of the NH_2trz ligand in the complex significantly changes its properties, which makes it necessary to perform a study investigating the effect of said proportion on the final physical properties of the material. In order to ascertain this effect, a series of SCO complexes was prepared, all identical in preparation with the sole difference being the addition of varying amounts of NH_2trz. The SCO properties of the series of mixed ligand complexes were

investigated, and so were the structural and mechanical properties of the material, which might play a role on its interactions with the PVDF matrix in the composites to be fabricated.

2.3.1.2 Synthesis of Spin Crossover nanoparticles

In order to incorporate the SCO material in the matrix in a homogenous manner, a smaller particle size is preferred, and so the main goal of this synthesis method remains the synthesis of homogeneous nanoparticles. For $[Fe(Htrz)_2(trz)](BF_4)$ and its derivatives, the most straightforward way to obtain nanoparticles would be from reverse-micelle methods [29]. However, there was the concern that any leftover surfactant around the nanoparticle could interfere in the interaction between the SCO and the polymer matrix. For this reason, we set out to devise a synthesis method for SCO NPs using no surfactant at all.

We opted for a methodology in which the particle nucleation process is accelerated as much as possible by starting the reaction at a high concentration of the reagents. In this case, we perform the reaction close to the solubility limit of the reagents. The methodology chosen is a simple homogeneous-media precipitation (fig 2.12), and while the lack of surfactant leads to aggregation and uneven geometry of the particles, the resulting solid is indeed composed of consistently sub 100 nm particles which are easily dispersed, favoring the fabrication of homogenous composites.

By decreasing the quantity of the trz ligand for the benefit of the NH_2trz ligand, a series of compounds with 0 (**1**) , 3.3 (**2**) , 6.6 (**3**) and 10% (**4**) of the NH_2trz ligand was obtained. These complexes follow the general formula $[Fe(Htrz)_{1+y-x}(trz)_{2-y}(NH_2trz)_x](BF_4)_y \cdot nH_2O$.

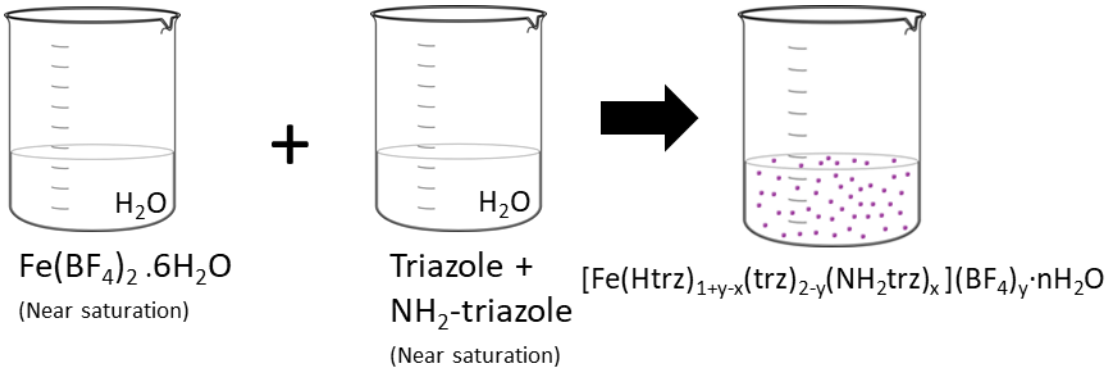

Fig 2.12) Fabrication of the mixed ligand complex nanoparticles.

The nanoparticles were prepared using the following procedure: a solution of 1 g of $Fe(BF_4)_2 \cdot 6H_2O$ in 2.5 ml of H_2O was added to a mixture of 613, 593, 572 and 550 mg of 1,2,4-4-H-triazole and 0 (0%), 25 (3.3%), 50 (6.6%) and 75 (10%) mg of 4-amino-4H-1,2,4-triazole in 2.5 mL of H_2O for sample **1-4**, respectively. The resulting solution was stirred for 1 hour and the formed precipitate was washed several times with ethanol (≈75% yield).

2.3.1.3 Characterization of the chemical composition and morphology of the particles

The general formula chosen for the complexes is $[Fe(Htrz)_{1+y-x}(trz)_{2-y}(NH_2trz)_x](BF_4)_y \cdot nH_2O$. This formula allows us to take into account in an independent manner both the fact that each mole of NH_2trz replaces a mole of trz, while also accounting for the fact that the $Htrz/trz^-$ ratio might vary with different proportions of NH_2trz ligand. The amount of BF_4^- anion in the structure is thus simply calculated from this ratio to balance out the charges in the structure.

TGA (Thermogravimetric analysis) of the SCO samples allowed us to quantify the amount of water in the structure, confirming the trend of an increase of water in the crystalline structure. The complexes seem to be stable well above 200°C, with a degradation temperature that starts at 300°C even for the complex with the highest proportion of NH_2trz ligand. This suggests that these particles could be used in applications where they go to very high temperatures without the chemical stability of the SCO complex being a major concern.

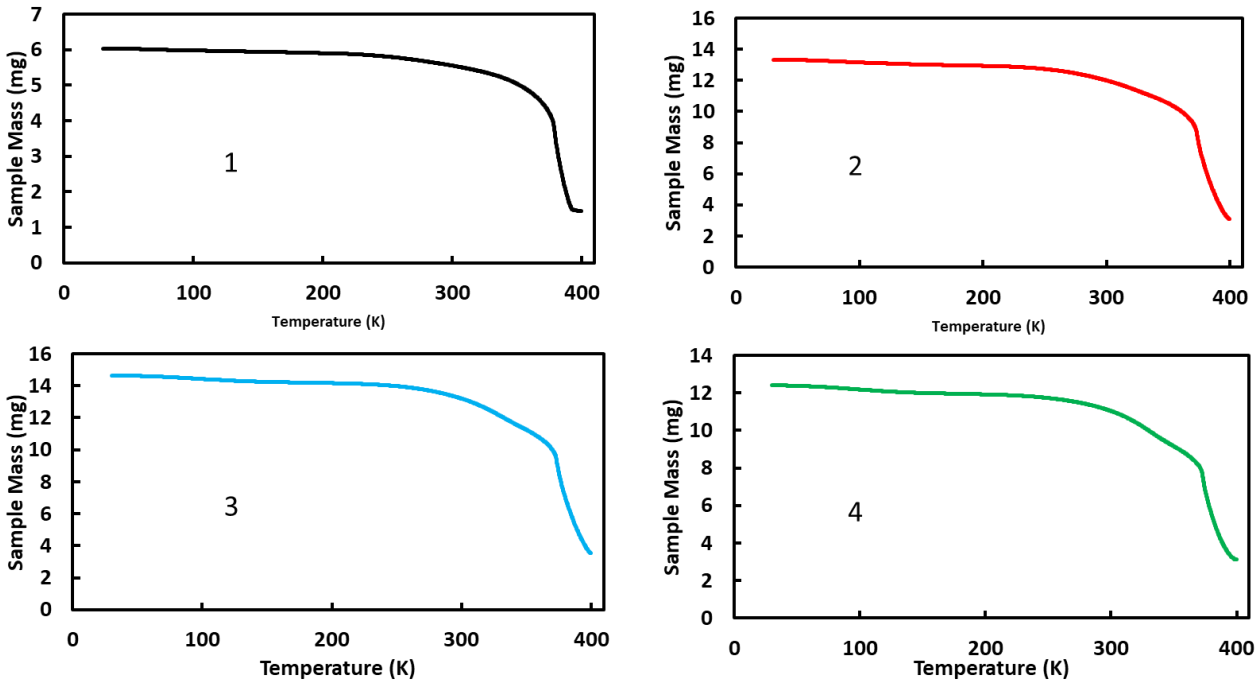

Fig 2.13) Thermogravimetric analysis of SCO complexes **1-4**.

Elemental analysis was performed, and the formulae of the synthesized complexes were elucidated as seen in Table 2.1. Interestingly, the $Htrz/trz^-$ ratio increases along with the addition of NH_2trz, which leads to a significant increase in the proportion of BF_4^-. Likewise, the amount of water in the complex varies with the percentage of NH_2trz, as seen by the thermogravimetric analysis (Fig 2.13).

Table 2.1) Elemental analyses and tentative composition of the SCO particles

		C / %	H / %	N / %	B / %	Fe / %	Calculated Formula
1	exptl	19.4	1.6	33.3	3.1	15.5	$[Fe(H\text{-}trz)_2(trz)](BF_4)\cdot 0.7H_2O$
	calcd	19.8	2.9	34.6	3.0	15.4	
2	exptl	18.5	1.6	32.1	3.4	14.7	$[Fe(H\text{-}trz)_{2.1}(trz)_{0.8}(NH_2\text{-}trz)_{0.1}](BF_4)_{1.2}\cdot 0.8H_2O$
	calcd	18.7	2.8	33.1	3.4	14.5	
3	exptl	18.2	1.6	31.8	3.45	14.1	$[Fe(H\text{-}trz)_{2.05}(trz)_{0.75}(NH_2\text{-}trz)_{0.2}](BF_4)_{1.25}\cdot 0.85H_2O$
	calcd	18.4	2.8	32.9	3.45	14.3	
4	exptl	17.7	1.6	31.4	3.5	14.0	$[Fe(H\text{-}trz)_2(trz)_{0.7}(NH_2\text{-}trz)_{0.3}](BF_4)_{1.3}\cdot 0.95H_2O$
	calcd	18.0	2.8	32.6	3.5	14.0	

Raman spectroscopy is a technique that allows us to characterize the vibrational properties of the molecular bonds in the complexes. It is particularly useful to this study as the low frequency region of the spectra can be attributed to metal-ligand bonds, and thus allows us to determine if there is a difference in the coordination sphere between the four complexes. The analysis was performed for the four complexes using an Xplora (Horiba) Raman microspectrometer (resolution ca. 3 cm^{-1}). The 532 nm line of a Nd-YAG laser (0.1 mW) was focused on the sample by a ×50 objective (numerical aperture, NA = 0.5), which was also used to collect the scattered photons. These latter were filtered by an edge filter. An acquisition time in the order of 10-15 minutes was necessary to obtain clean spectra.

High temperature Raman spectroscopy shows that there is a significant structural difference between the alloyed and unalloyed complexes in the HS state, as shown in the 50-300 cm^{-1} modes (Fig 2.14), which becomes more pronounced as the proportion of the NH_2trz ligand increases. It is interesting to note however that the three characteristic peaks of the $[Fe(Htrz)_2(trz)](BF_4)$ complex in this region (at 110, 144 and 200 cm^{-1}) remain unshifted, and the difference seems to come from the peak at 110 cm^{-1} becoming more intense. This region is often associated with metal-ligand interactions [130], and the fact that the characteristic peaks of the complex are not shifted, suggests that the difference in physical properties of the complexes might stem from intermolecular interactions.

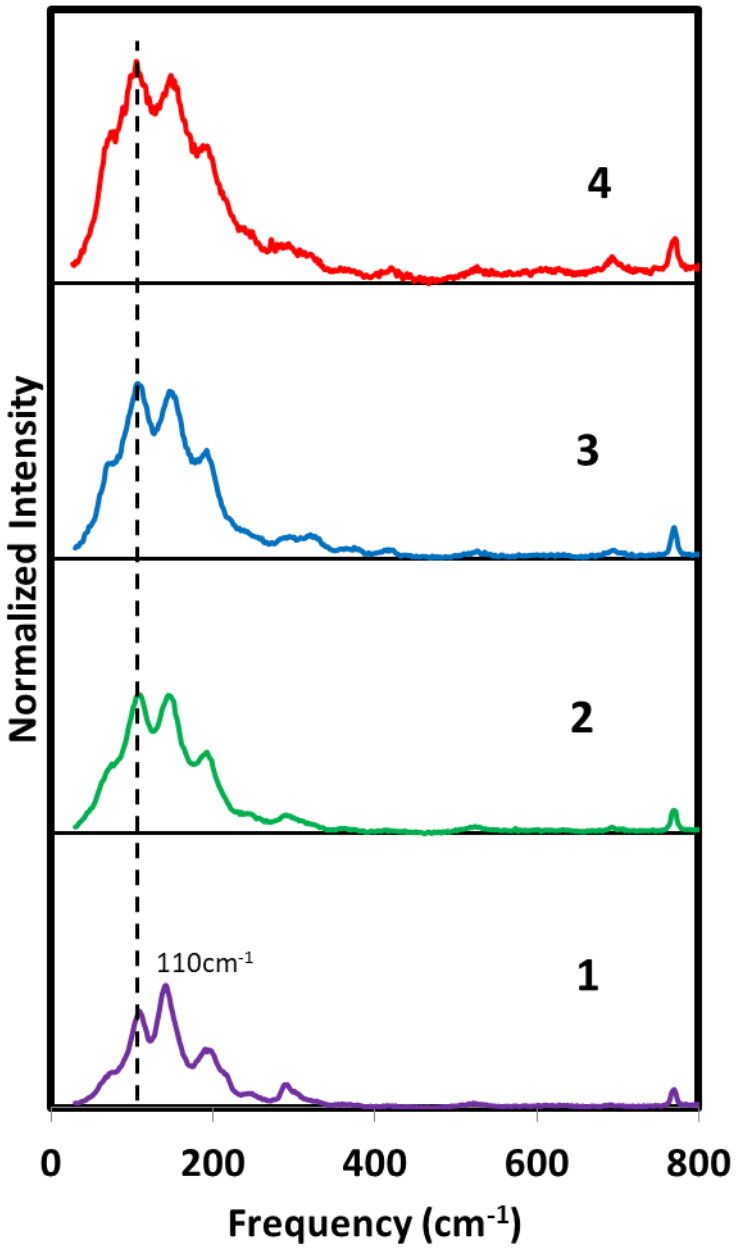

Fig 2.14) HS Raman spectra of SCO particles **1-4**.

Transmission electronic microscopy (TEM) was performed on the series of complexes to characterize the morphology and particle size of the sample. The TEM imagery of the particles reveals a series of particles with high aggregation and inhomogeneous size and shape. However, the particles are well within the sub 100 nm scale (Fig 2.15), which makes them viable candidates to be dispersed in a matrix. The irregular shape is to be expected from a synthetic method where there is no control of the growth stage of the nanoparticle synthesis. Yet, the relatively small particle size means that the nucleation stage happened very quickly, giving little time for the

growth stage to occur, probably due to the high-concentration conditions under which the synthesis took place.

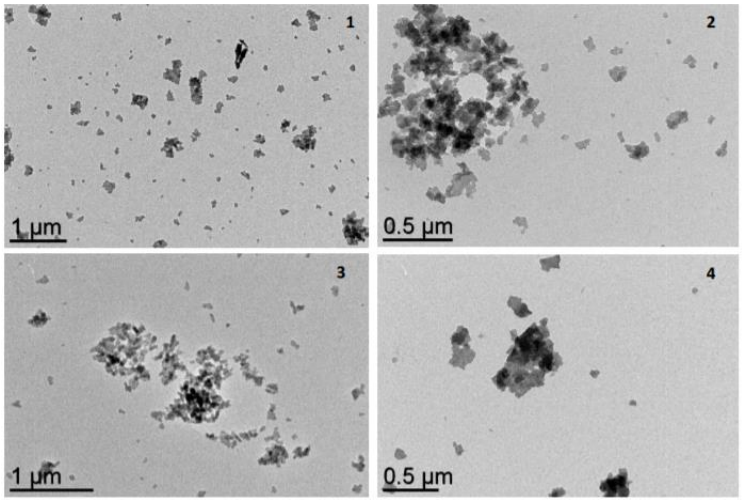

Fig 2.15) Representative transmission electron microscopy images of the SCO particles **1-4.**

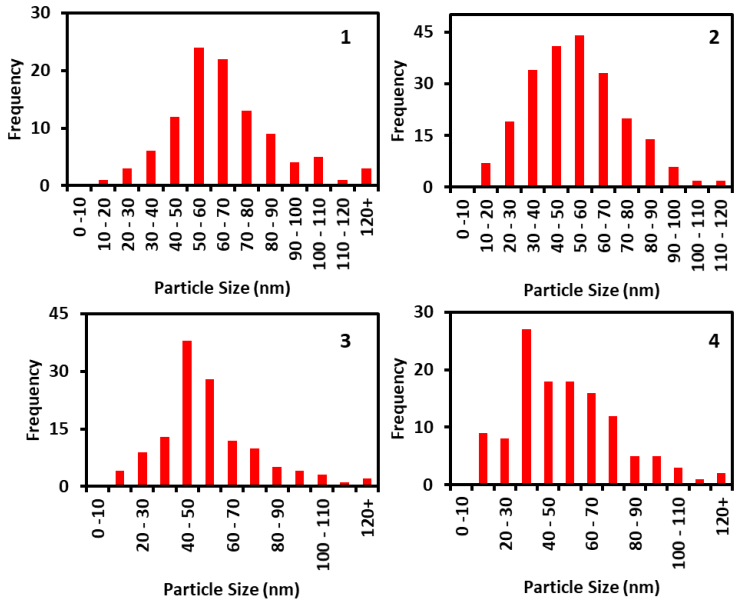

Fig 2.16) Particle size distribution of the SCO samples **1-4**, data obtained by manually counting particles.

Counting of a representative sample of particles showed an average size between 40 and 70 nm for all complexes. The wide size distribution of the particles is to be expected from a synthesis method with very little control over the growth phase of the crystallization. Moreover, it makes it difficult to draw any conclusions regarding a possible effect of the proportion of NH_2trz ligand on the size of the nano objects. What this analysis shows is that the vast majority of the particles in the sample are in the sub-100 nm scale, which should allow these particles to be easily dispersed in a solvent and homogeneously distributed in a polymer matrix.

2.3.1.4 Characterization of the physical and solid-state properties of the particles

This section shows the effect that the addition of the NH_2trz has on the SCO and crystalline properties of the particles. Magnetic measurements are used as a means to determine the SCO properties. DSC measurements allow us to determine the thermodynamics of the spin transition for each complex. Mossbauer spectroscopy is a means by which to probe the solid state properties of the complexes, in particular the stiffness of the lattice. Finally powder X-ray diffraction allows us to determine if there is a significant difference in crystalline structure between the complexes.

Magnetic measurements of the SCO particles allow us to determine precisely the spin transition temperatures of the complexes depending on their alloying. The spin transition curves shown here correspond to the second cycle of the spin transition, since the first cycle corresponds to a run-in effect. The effect of ligand substitution on the spin crossover properties of $[Fe(Htrz)_2(trz)](BF_4)$ nanoparticles is in agreement with that reported previously for the corresponding bulk material [131].

Indeed, the transition temperature is shifted toward room temperature with increasing NH_2trz inclusion (Fig 2.17). At the same time, the hysteresis width and the abruptness of the transition decrease. The loss of hysteresis and abruptness would suggest that the inclusion of the NH_2trz ligand compromises the cooperativity of the system. It is interesting to note that not only is there a significant loss of hysteresis, but also the transition seems to become incomplete for higher proportions of NH_2trz. However, the complexes prepared with 10% (**4**) and 6.6% (**3**) dilution are in a temperature range which allows for their intended use in conjunction with P(VDF-TrFE) 70-30, making them good candidates for the preparation of composites despite the loss of cooperativity and completeness of the spin transition (see table 2.2).

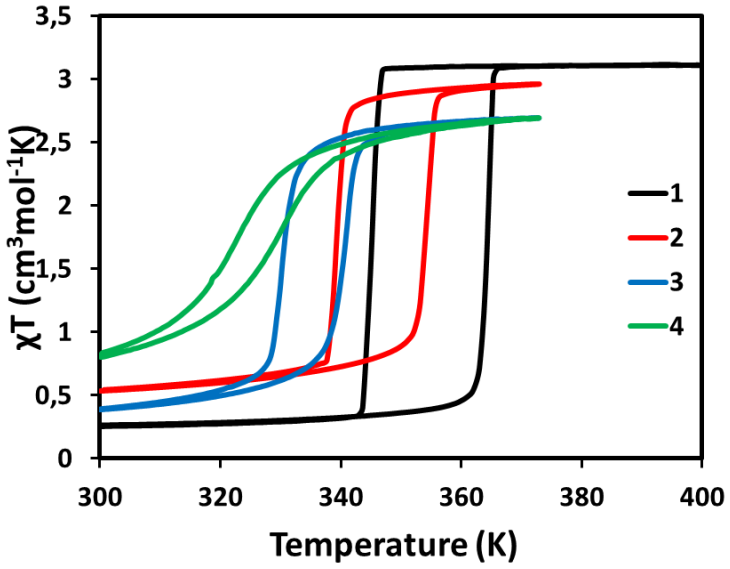

Fig 2.17) Variable temperature magnetic measurements of the nanoparticle samples **1**-**4** for the second thermal cycle.

Table 2.2) Spin transition properties of the SCO samples **1-4** obtained via variable temperature magnetic measurement.

Sample	T_{up} (K)	T_{down} (K)	ΔT (K)	$T_{1/2}$ (K)
1	364	345	19	355
2	354	340	14	347
3	340	331	9	335
4	330	325	5	327

Differential scanning calorimetry (DSC) measurements were also conducted on the different samples (see Fig 2.18 and Annex A.2.1 and A.2.2). In agreement with the magnetic data, the DSC peaks associated with the SCO shift to lower temperature when the quantity of the aminotriazole ligand increases.

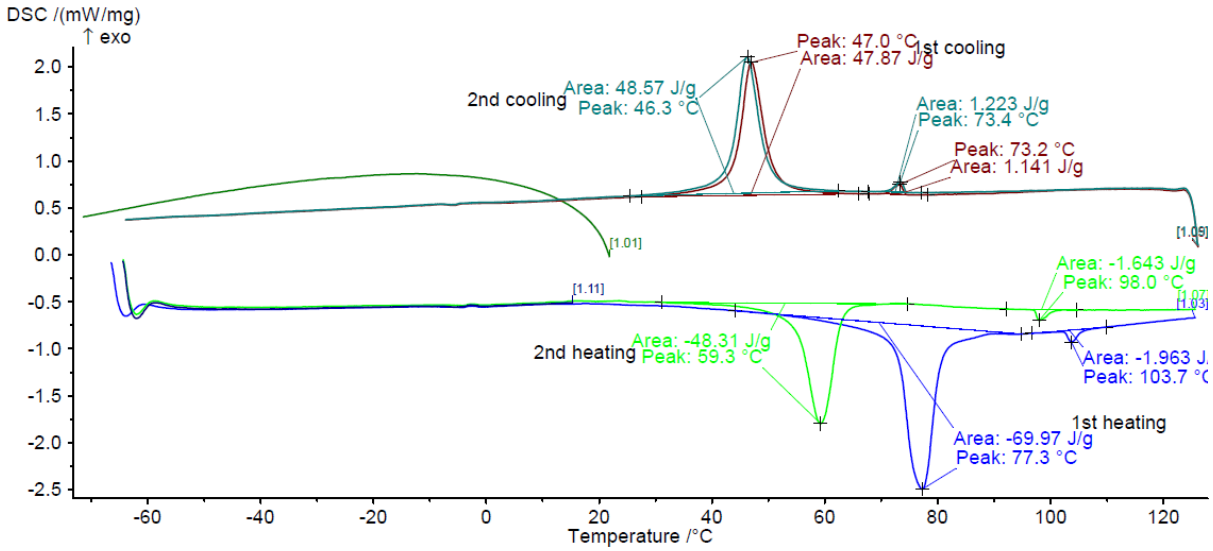

Fig 2.18) DSC analysis of complex **4.**

The DSC analysis of **4** (Fig 2.18) shows an endothermic peak during the first heating at 77°C. It is interesting to note that this transition has a significantly higher enthalpy than the corresponding cooling process and the subsequent heating, which attests to the irreversible nature of this effect (run-in effect). Another heating peak can be seen at 103°C during the first heating and 98° C during the second thermal cycle denoting that 10 % ligand substitution is the threshold from which phase segregation of complex $[Fe(Htrz)_2(trz)](BF_4)$ and the mixed complex

occurs**.** The heating and cooling peaks at 59°C and 46°C correspond to the spin transition temperatures obtained from magnetic measurements.

The primary aim of this DSC study was the assessment of the enthalpy (ΔH) and vibrational entropy associated with the spin transition in the different samples (table 2.3). (ΔSvib = ΔStotal – ΔSspin with ΔSspin = 13,4 JK^{-1} mol^{-1} for iron(II) spin crossover complexes). The SCO enthalpy is closely linked to the energy required to re-arrange the crystalline structure of the complex following a change in the coordination sphere, and for this reason offers an insight of the solid-state properties of the complexes. Remarkably, both ΔH and ΔSvib decrease by almost 35 % for only 3.3 % aminotriazole ligand substitution (sample **2**), while further substitution does not bring any noticeable changes (within the experimental accuracy) (Fig 2.19). This suggests that the substitution of even a small proportion of ligand in the complex leads to a very significant structural change, and further addition of the NH_2trz ligand does not significantly change this structure.

Table 2.3) Spin transition enthalpy, entropy and vibrational entropy of samples **1-4**.

Sample	ΔH (kJ mol^{-1})	ΔS (J K^{-1} mol^{-1})	ΔS_{vib} (J K^{-1} mol^{-1})
1	29	81	68
2	19	57	44
3	20	59	46
4	18	56	43

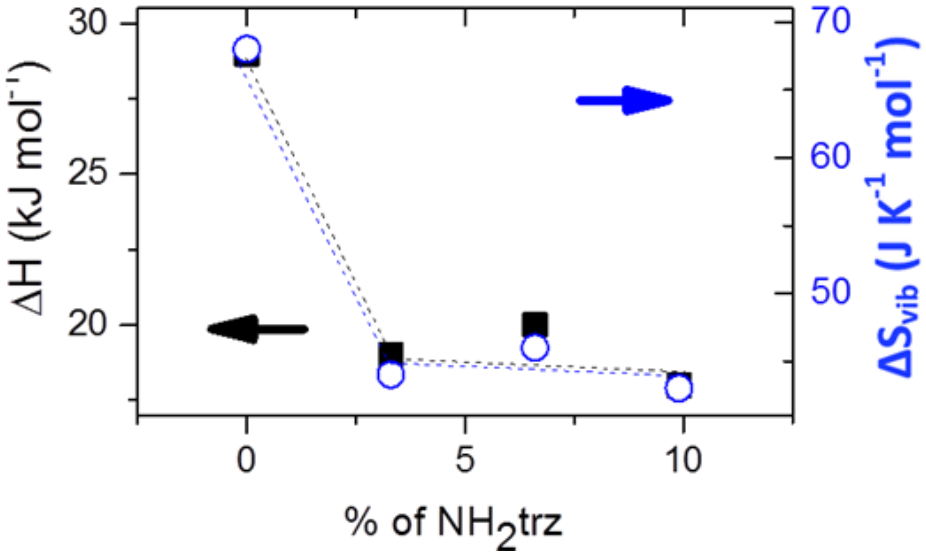

Fig 2.19) Excess enthalpy and vibrational entropy associated with the spin transition of samples **1-4.**

In order to further explore this significant discrepancy, Mössbauer spectroscopy was performed for each sample. The main goal of the Mössbauer study was to probe the influence of the ligand substitution on the lattice dynamics and the associated SCO hysteresis phenomena. Indeed, ^{57}Fe Mössbauer spectroscopy can sensitively probe the lattice vibrational properties through the investigation of the temperature dependences of the Lamb-Mössbauer factor (*f*) and the isomer shift (*δ*) [132,133]. The former is related to the mean-square amplitude of vibrations of iron atoms, while the latter to their mean-square velocity. In most cases, the temperature dependences of *f* and δ are described using a simplified vibrational spectrum, such as the Debye model. In this frame, the lattice dynamics is characterized by a single parameter, the Debye temperature (θ_D), which can be regarded as a measure of the 'local' lattice stiffness around the iron atoms and reflects the elastic properties of the material.

Interestingly, the Mössbauer spectra for complex **4** shows that at 80 K the complex has a small residual fraction, confirming the results found by the magnetic measurements (Fig 2.20) . The corresponding least-squares fitted Mossbauer data can be found in Annex A.2.3. The data shows that the HS residual fraction would seem to be relatively constant across all four complex samples, at approximately 4 % HS at 80 K. At 320 K, the temperature limit of our setup, we find in agreement with the magnetic data that only 15% of metal centres are in the HS state in sample **4**. Recent experimental results suggest that these HS residual fractions at low temperature in SCO nanoparticles might be associated with lattice defects or the inclusion of guest molecules, rather than a surface effect, as the HS fractions are distributed homogeneously across the whole volume of the particles [134].

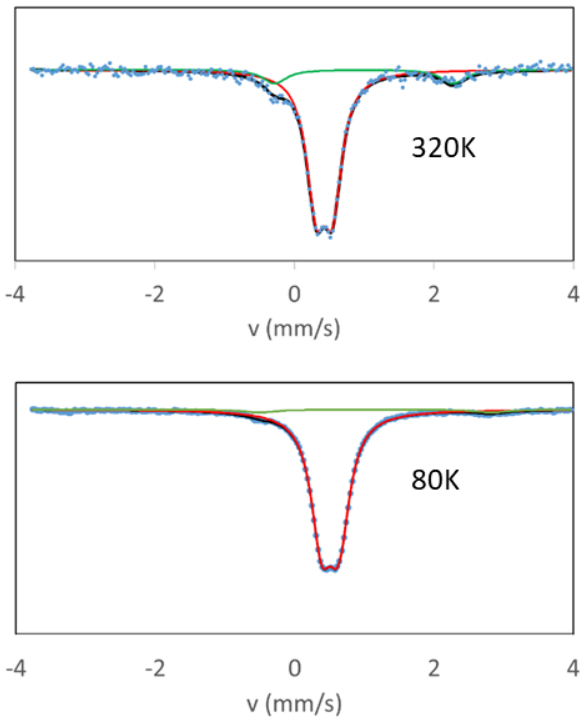

Fig 2.20) Fitted Mössbauer spectra for complex **4.**

Since the Lamb-Mössbauer factor is proportional to the full area (A) of the Mössbauer spectrum (divided by the baseline), one can extract the Debye temperature (θ_D^f) from a least squares fit of the temperature dependence of A using the relationship [135]:

$$\log(A) \approx \log(Cf) = \log(C) - \frac{3E_R}{2k_B\Theta_D}\left[1 + 4\left(\frac{T}{\Theta_{Df}}\right)^2 \int_0^{\frac{\Theta_D f}{T}} \frac{\alpha}{\exp(\alpha) - 1} \mathrm{d}\alpha\right] \quad (9)$$

With C a constant, E_R the recoil energy of iron, k_B the Boltzmann constant, T the temperature and α, a variable for the integral. For the non-substituted nanoparticle sample **1**, the obtained θ_D^f value of 285 ± 10 K in the LS state is one of the highest reported for a spin crossover compound (Table 2.4) and is in reasonable agreement with the value reported previously [136] for the bulk compound (315 ± 12 K). Indeed, typical low spin θ_D^f values of SCO compounds fall in the range of 140 - 300 K [17, 22-27]. Moreover, a decrease of 10 - 15 % of the θ_D^f value was systematically determined when going from the LS to the HS state in agreement with the overall lattice expansion [137].

Table 2.4) Debye temperatures of complexes **1**-**4** in the LS state, obtained from the least squares fit (θ_D^f) or the isomer shift (θ_D^d).

Sample	θ_D^f (K)	θ_D^d (K)	LS/HS Area (80 K)
1	285	793	92/8
2	226	801	96/4
3	215	804	97/3
4	205	791	96/4

Fig 2.21 represents the variation of θ_D^f as a function of the percentage of the triazole ligand substitution. It is important to note the significant decrease of the Debye temperature from 285 ± 10 K for the pure undiluted $[Fe(Htrz)_2(trz)](BF_4)$ complex, to 226 ± 13 K for only 3.3 % aminotriazole ligand substitution. On the other hand, a less pronounced variation occurs for further ligand substitution, decreasing θ_D^f to 205 ± 15 K for ca. 10 % substitution. It is interesting to note also that this latter value is substantially smaller than that reported previously for the pure bulk $[Fe(NH_2trz)_3](BF_4)_2$ complex (247 ± 12 K) [136]. Figure 2.16 shows also the variation of the Debye temperature extracted from the temperature dependence of the isomer shift (θ_D^δ).

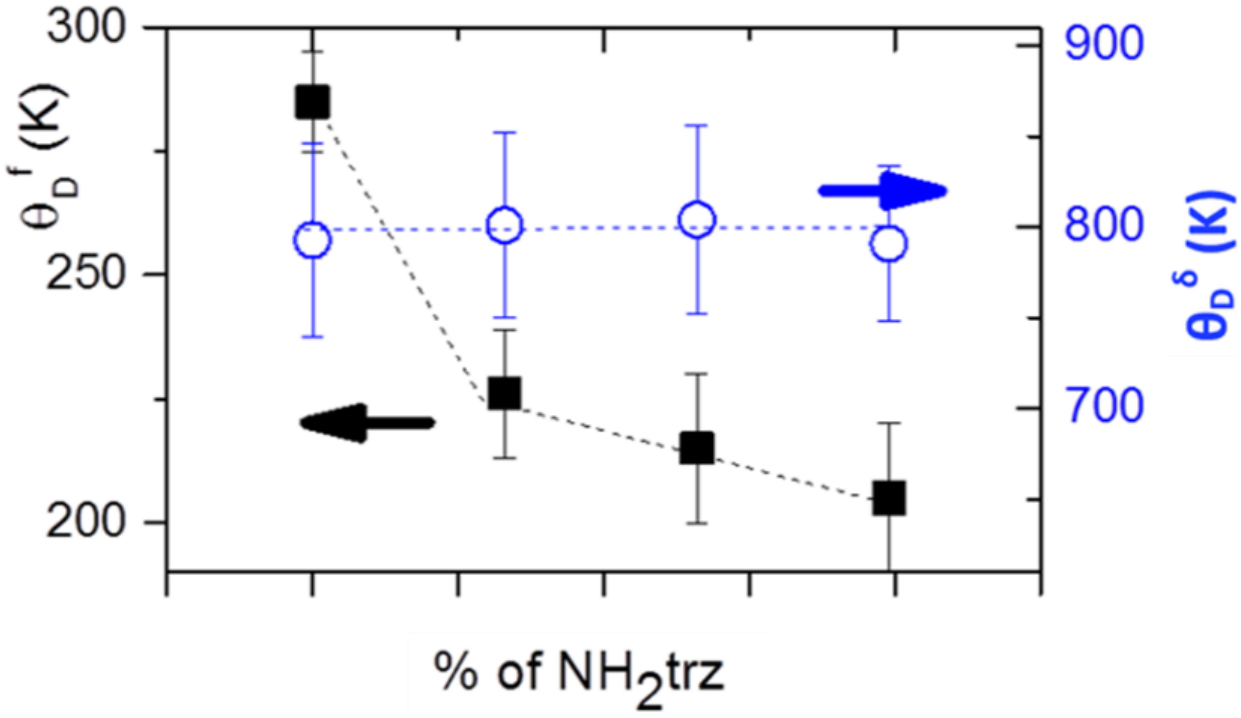

Fig 2.21) Debye temperatures obtained from the temperature dependence of the Mössbauer spectrum area (squares) and that of the isomer shift (circles) for samples **1-4** in the LS state**.**

The Lamb-Mössbauer factor (*f*) is associated with vibrational amplitude of the iron atoms while the isomer shift (δ) is associated with their velocity. From the markedly different behaviours of θ_D^δ and θ_D^f we can deduce that the origin of the stiffness decrease is associated to the modification of lattice properties and not to intramolecular effects. This conclusion is also in agreement with the observation that the signature peaks in the spectral region of metal-ligand vibrations (50 – 300 cm^{-1}) appear very similar in the Raman spectra of our samples (Fig 2.14). We can thus propose the following physical picture to account for the different experimental observations. The introduction of the bulkier aminotriazole ligand strongly destabilizes the crystal lattice resulting in a reorganization of the interactions between the Fe-triazole chains. This leads to a decrease of the lattice cohesion energy - reflected unambiguously by the drop of θ_D^f and ΔH.

In order to further explore this result and probe any structural changes in the crystal lattice, powder X-ray diffraction was performed for the series of complexes. In line with this result, inspection of the room temperature (LS state) powder X-ray diffraction patterns of **1**-**4** reveals a noticeable change between the structures of sample **1** and **2**, the latter being characterized by a higher symmetry. Specifically the peaks at 11°, 18.5° and 25° show a splitting in complex **1** that is completely absent in complexes **2-4.**

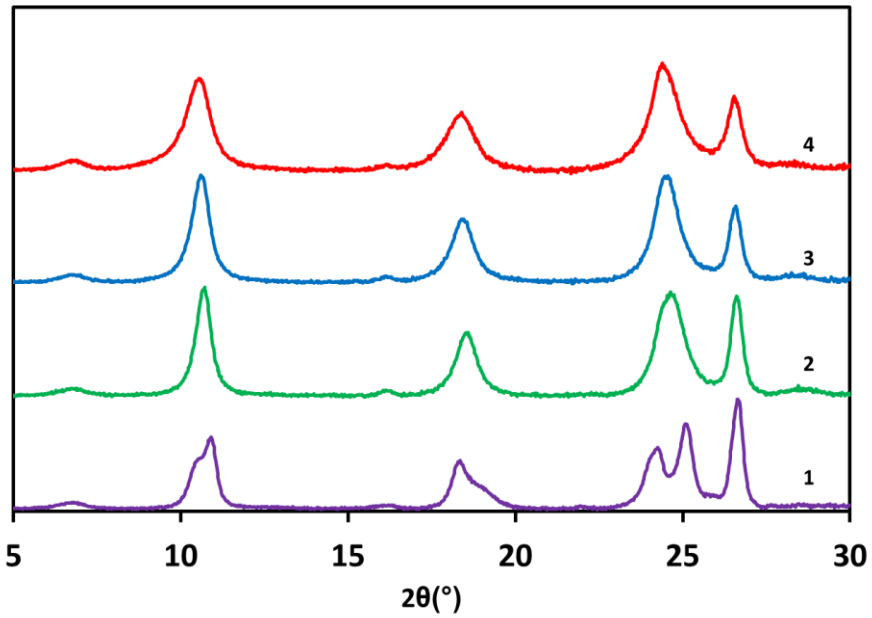

Fig 2.22) Room temperature powder X-ray diffraction patterns of SCO particles **1-4**.

As a first consequence, the cooperativity, which strongly depends both on the absolute value of the lattice stiffness as well as on the difference of the stiffness between the HS and LS phases, will also decrease, which is reflected in our experiments by a decrease of the hysteresis width. Another consequence is that the values of both ΔH and ΔS_{vib} strongly decrease. Since the decrease of ΔH is slightly more pronounced than that of ΔS, we can observe a slight downshift of the transition temperature.

2.3.1.5 Fabrication of the first generation SCO@P(VDF-TrFE) composite films

The study on the properties of $[Fe(Htrz)_{1+y-x}(trz)_{2-y}(NH_2trz)_x](BF_4)_y \cdot nH_2O$ mixed complexes allowed us to solidify our choice of complex. Indeed, both the 10% mixed and the 6.6% mixed complexes show spin transition temperatures which are compatible with the copolymer that will be used for the fabrication of the electroactive composites. Indeed, P(VDF-TrFE) 70-30, the copolymer of choice for this study, shows a Curie temperature between 363 and 373 K upon heating, so this becomes our temperature limit for the SCO complexes.

In particular, we chose to use the dilution approach at a larger scale to synthesize a complex with a 10% content of NH_2trz ligand. This technique however is very sensitive to the reaction conditions and the resulting complex **5** had slightly shifted SCO properties, despite having the same particle morphology.

Indeed, magnetic measurements (Fig 2.23) of SCO complex **5** show a spin transition slightly shifted towards high temperature when compared to complex **4**, with $T_{1/2}^{\uparrow}$ = 337 K and $T_{1/2}^{\downarrow}$ = 328 K and with a more abrupt and complete spin transition. However, TEM imagery shows nanoparticles very similar to those of complexes **1-4** suggesting the slight differences in properties are not associated to a difference in morphology. Regardless of these slight

differences, the transition temperature remains perfectly compatible with the temperature limits set by the copolymer, so complex **5** will be the complex of choice for the fabrication of the first generation of SCO@P(VDF-TrFE) composites. The formula was determined by elemental analysis to be $[Fe(H\text{-}trz)_{1,85}(trz)_{0,85}(NH_2trz)_{0,3}](BF_4)_{1,15}\bullet 1H_2O$.

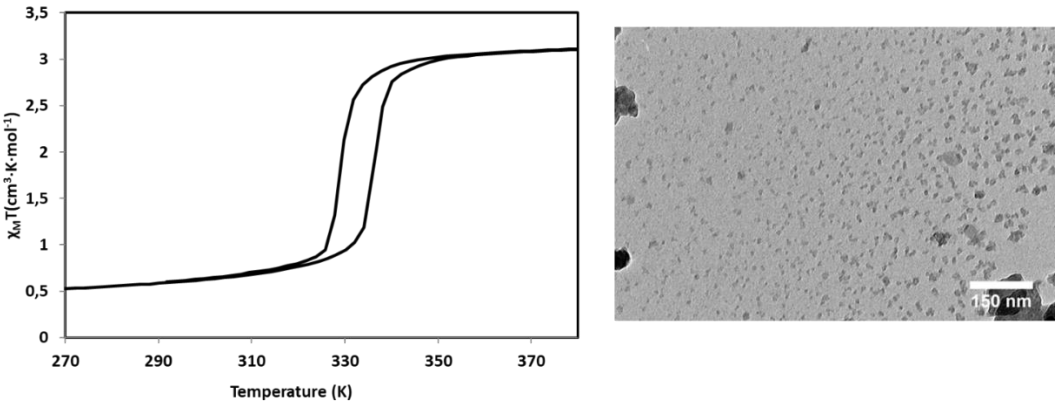

Fig 2.23) Variable temperature magnetic measurements of the nanoparticle sample **5** for the second thermal cycle(left) and a representative TEM image (right)**.**

To confirm the compatibility of the complex with the polymer matrix, DSC was performed on complex **5** (Fig 2.24). Differential scanning calorimetry confirms the spin transition temperatures found by magnetic measurements, with an approximately 10 K hysteresis and a phase transition centered around 335 K. As Fig 2.8 shows, the Curie transition of the P(VDF-TrFE) 70-30 copolymer is centered around 370 K so this result suggests that complex **5** undergo spin transition in the composite without having to go above the Curie phase transition, after which P(VDF-TrFE) loses its electroactive properties.

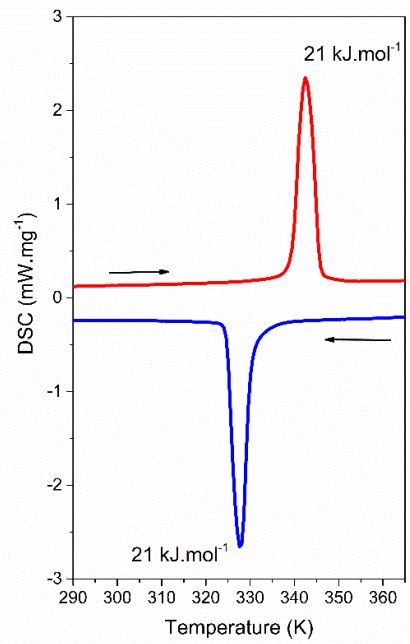

Fig 2.24) DSC measurement of complex **5** heating (red) and cooling (blue) (second thermal cycle).

The general procedure to fabricate these films is a straightforward drop-casting technique which consists of: (1) dissolution of the P(VDF-TrFE) polymer in DMF, (2) dispersion of the SCO particles in the solvent, (3) casting the films onto a glass slide, (4) simultaneous drying and annealing of the films, and (5) finally peeling the free-standing film from the glass substrate (Fig 2.25). There are several different parameters that must be evaluated when optimizing this procedure however: the amount of solvent, the concentration of SCO particles and the drying and annealing temperature.

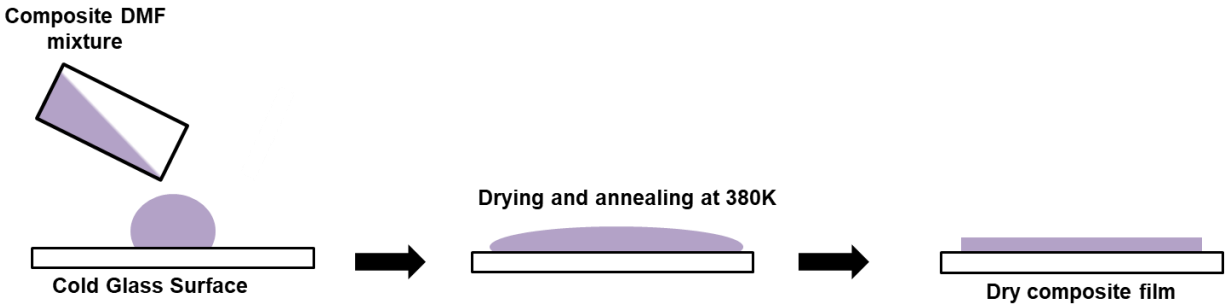

Fig 2.25) SCO@P(VDF-TrFE) composite film fabrication via drop-casting.

As seen before, the films must be polarized before they can show interesting electroactive properties. To achieve this, these films were poled at 293 K by applying several cycles of a sinusoidal electric field (100 mHz) with amplitudes up to 18 MV m^{-1}. Stability during the polarization process was an essential parameter to gauge the viability of the films. Indeed, inhomogeneities in the film and weak mechanical properties are the two main factors that lead to fractures in the film during the poling process.

Optimization of these parameters came after multiple composite synthesis attempts. The goal was to maximize the loading of the composite, while retaining sample homogeneity and good mechanical properties. Homogeneity and mechanical stability are the main figures of merit of sample quality as they are absolutely essential both for polarization of the sample and for the use of this material for electromechanical applications. On the other hand, maximizing the proportion of the SCO complex allows us to enhance the mechanical effects of the spin transition on the composite.

Composites with different proportions up to 50 wt% (sco/composite wt%) were synthesized (Fig 2.26). We observed that at high concentrations the composite became brittle, with very poor mechanical properties (Fig 2.26a). In the same manner, for concentrations above ca. 30 wt% a lack of homogeneity in the dispersion was observed, with aggregates of the complex visible to the naked eye on the composite (Fig 2.26b). Films with 12.5 wt% of complex were also synthesized to see if diminishing the concentration of the complex would improve the mechanical properties of the composite to make it less brittle. Unfortunately, a small SCO load (< ca. 15 wt%) made it impossible to recover the sample. This is because the volume change associated to the spin transition (contraction while cooling) in the composite favors its separation from the glass

substrate, but at lower charges this beneficial effect vanishes. A weight percentage of 25 wt% of complex was then chosen as a compromise between having a good sample quality and seeing the effect of the SCO complex as clearly as possible.

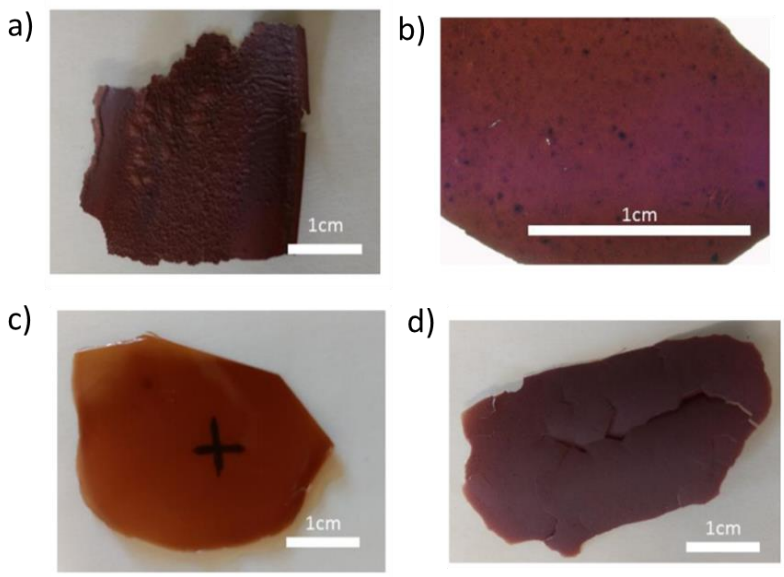

Fig 2.26) Initial SCO(**5**)@P(VDF-TrFE) 70-30 composite film samples. a) Film prepared at 50 wt% SCO loading. b) Film prepared at 30 wt% SCO loading. c) Semi-transparent 65 µm thick film. A '+' sign was drawn on the paper underneath the film to show its transparency. d) Film annealed at 410 K.

Different techniques for dispersion of the nanoparticles were also implemented: mixing the particles with the dissolved polymer under stirring, grinding the particles together with the polymer in a mortar and eliminating bubbles by drying the composite on a vacuum. Finally, the best results were obtained by sonication of the particles in the solvent before addition of the polymer.

Likewise, we controlled the thickness of the films via their viscosity during deposition by controlling the amount of solvent used to dissolve the particles. Using 3 mL of DMF (120 mg mL-1) we obtained semi-transparent films of around 65 µm, which despite being highly homogeneous were too brittle to be properly poled (Fig 2.26c). Using 2.25 mL of DMF (160 mg/mL of polymer in DMF) we obtained films of around 150 µm, which broke during the poling process. Using 1.5 mL of DMF (240 mg/ml of polymer in the solvent), we obtained films of ca. 250 µm thickness (Fig 2.27). We settled on 240 mg mL-1 of polymer as a compromise between film thickness and mechanical stability. Thickness of the films was measured using a Mitutoyo Digital Micrometer.

Another factor to consider was the annealing temperature. Composites were prepared in an identical manner, but annealed at a temperature of 410 K to improve crystallinity; these composites proved to be too fragile (brittle) and shattered during the poling process (Fig. 2.26d). It was under these considerations that we settled for the synthesis conditions that will be

described below, as a means to compromise the physical properties of the material and the desired effects, and to produce composites that remained stable during the poling process.

Table 2.5) Synthesis parameters for SCO@P(VDF-TrFE) composite films.

Parameter	Explanation
SCO proportion	50 wt% produces brittle samples. 25 % compromise.
Dispersion of particles	Via sonication in solvent before addition of polymer.
Film thickness	Under 250 µm produces brittle samples.
Annealing Temperature	410 K produces brittle samples. 373 K ideal.

The final protocol was: SCO particles of $[Fe(H\text{-}trz)_{1,85}(trz)_{0,85}(NH_2trz)_{0,3}](BF_4)_{1,15}\bullet 1H_2O$ (**5**) (120 mg to obtain a 25 wt%) were sonicated in DMF (1.5 mL) until a well-dispersed suspension was obtained. Grounded pellets of P(VDF-TrFE) copolymer 70-30% mol from Piezotech™ (360 mg) were then added and the mixtures heated at 60 °C under mild stirring. After 2 h, the viscous violet suspension was drop-casted on a glass slide and heated in an oven at 100 °C for 2 hours. The resulting film was detached from the glass substrate using a box cutter blade. The freestanding, flexible film shows thermochromism as expected from the inclusion of the SCO particles. ICP-AES of Fe gives 4.08 wt% which corresponds to 24.7 wt% of the complex in the composite.

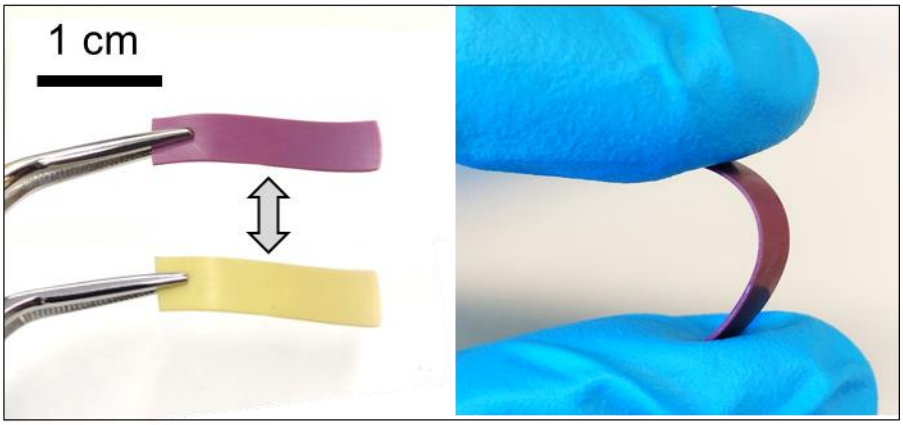

Fig 2.27) Freestanding, homogeneous SCO@P(VDF-TrFE) 70-30 composite.

2.3.1.6 Morphological and physical characterization of the first generation composite films

The most straightforward techniques for the characterization of the morphology of a composite film are Scanning Electronic Microscopy (SEM) (Fig 2.28-2.29) and Atomic Force Microscopy (AFM) (Fig 2.30). SEM is well suited for the characterization of the interior of the composite film. By taking an image of the cross-section of the film, it is possible to see the morphology and the organization of the polymer fibers. To achieve this, it becomes necessary to cleanly break the film rather than cut it, as cutting causes a deformation of the cross-section surface in the direction of the cut, while breaking exposes the interior fibers of the film. For this reason, the composite samples were cooled with liquid nitrogen before breaking, and the cross-sections that appeared as a result of this fracture were then analyzed.

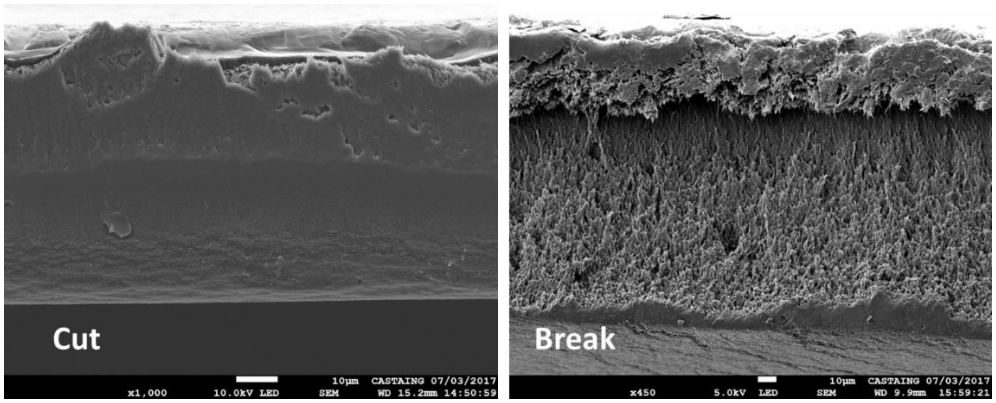

Fig 2.28) SEM cross sections of a SCO(**5**)@P(VDF-TrFE) composite film. The sample on the left had its cross section exposed via cutting with scissors and the sample on the right had its cross section exposed by breaking at low temperature.

Scanning electron microscopy (SEM) images reveal a homogeneous dispersion of nanoparticles inside the fibrous-like polymer structure, approaching the morphology of an ideal 0–3 connectivity composite material. By increasing the image magnification it is possible to observe the particle aggregates around the polymeric fibers. SEM microscopy suggests that there are no significant inhomogeneities in the composite film larger than 5 µm, which could possibly induce fractures of the film during the poling process.

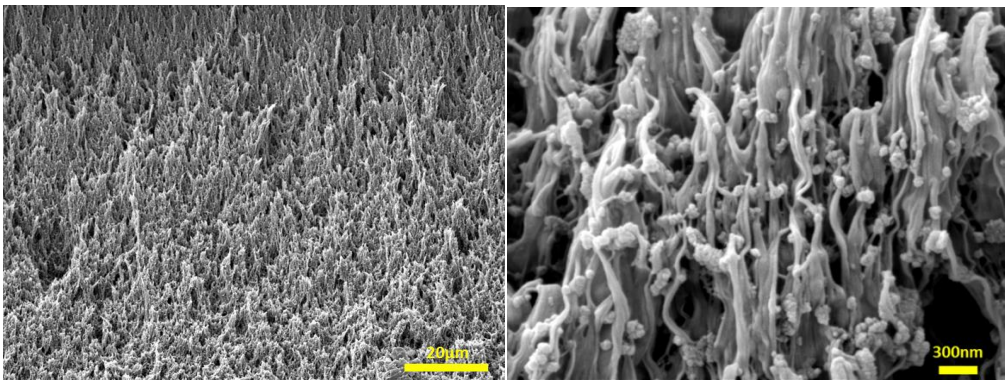

Fig 2.29) Scanning Electron Microscopy (SEM) zoomed images of the SCO(**5**)@P(VDF-TrFE) composite cross-section.

AFM is a technique better suited for the characterization of the surface of the film. In this case the analysis was performed in intermittent contact mode (IC-AFM) and two different kinds of images were acquired: Height and Phase image. Height images allow to determine the topography of the surface. Phase images however are sensitive to variations in composition, adhesion, friction and viscoelasticity. This allows us to use phase images for composition analysis of the surface, and in the case of a composite material, hopefully distinguish between the soft polymer matrix and the stiffer SCO filler [138].

Height images of the composite sample reveal a relatively homogeneous and smooth film. Phase images of the film show a random dispersion of particles and particle aggregates in the polymer film, with the SCO particles plainly distinguishable from the surrounding polymer matrix. Interestingly however, not all the topography features found in the height images correspond to high concentrations of particles in the phase imagery. This suggests that some of the morphological features are simply a natural result of the film fabrication method, rather than being caused by the presence of the SCO particles.

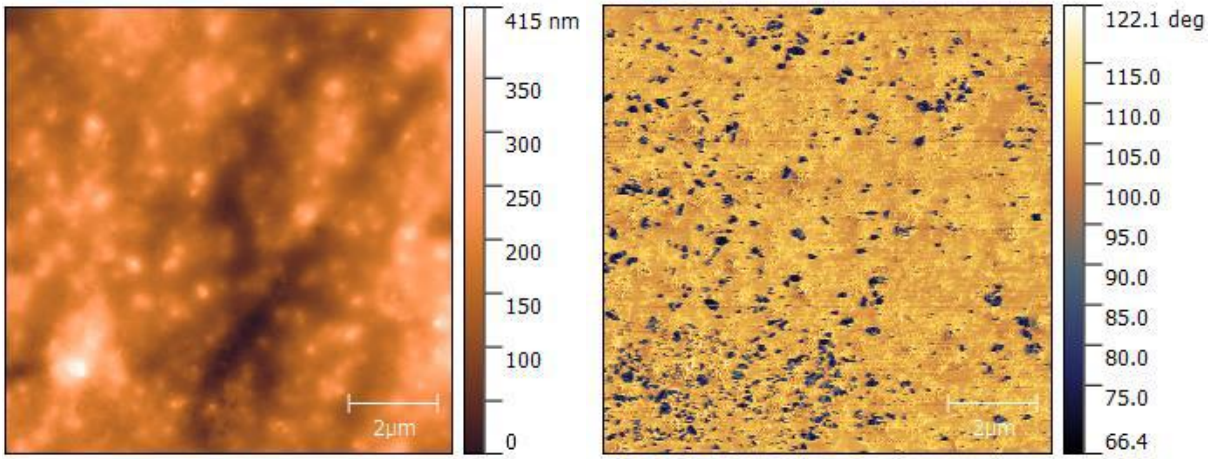

Fig 2.30) IC-AFM topography image of the surface of the SCO(**5**)@P(VDF-TrFE) composite with a 10 x 10 μm^2 scan size: height image (left), phase signal (right).

Variable-temperature magnetic susceptibility measurements reveal a virtually complete SCO in the composite with transition temperatures around $T_{1/2}$ = 340 K and $T_{1/2}$ = 327 K on heating and cooling, respectively. The hysteresis width in the composite (13 K) is notably larger in comparison with that of the particles alone (8 K) due, possibly, to elastic confinement effects of the matrix [61], though other reasons such as a solvent effect cannot be excluded. The spin transition in the composite is reproducible over several thermal cycles, except the first heating curve. This irreversibility of the first heating transition, or run-in effect, can be attributed to various phenomena such as the loss of solvents, particle morphology changes or polymorphism [139]. For this reason, we show material properties observed during the second thermal cycle.

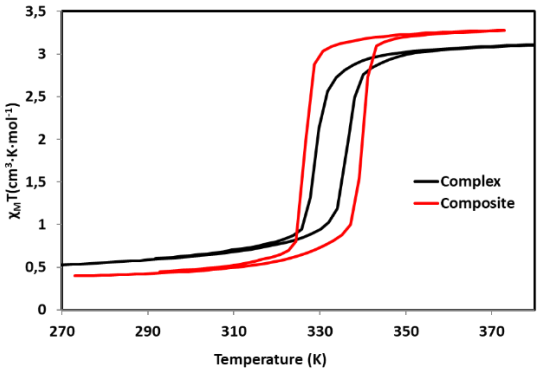

Fig 2.31) Variable temperature magnetic measurements of complex **5** and the SCO(**5**)@P(VDF-TrFE) composite film (second thermal cycle).

DSC analysis allows to simultaneously observe the copolymer phase transitions, (specifically the α-β phase transition and the melting) and the spin transition, as all of the aforementioned transitions have a latent heat, which is clearly visible in the DSC thermogram. Most importantly, DSC allows us to check if there is any overlap between the phase transitions, which could lead to a loss of polarization of the sample during the thermal cycling required to achieve the spin transition.

The DSC analysis shows, in good agreement with the magnetic data, endo- and exothermic peaks, which accompany the spin transition around 334 and 318 K, respectively. The associated transition enthalpy (ΔH = 20 kJ mol^{-1}) and entropy (ΔS = 60 J K^{-1} mol^{-1}) changes are comparable with those observed for the pure complex (Fig 2.24). The ferro/paraelectric transition is characterized by two peaks in the DSC thermograms (T_{C1} = 362/327 K, T_{C2} = 373/338 K upon heating/cooling). Most importantly, this transition does not seem to have a significant overlap with the spin transition of the complex, which means that it should be possible to heat the composite to the spin transition temperature without depolarizing the sample.

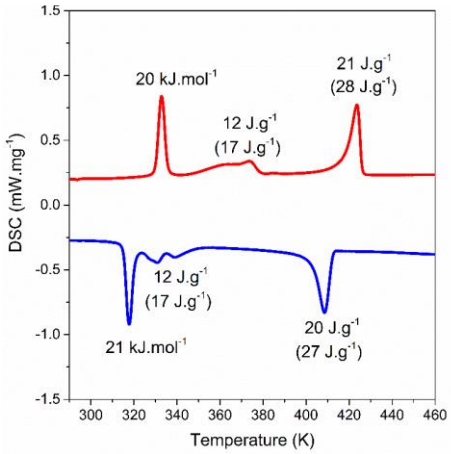

Fig 2.32) DSC Thermogram of the SCO(**5**)@P(VDF-TrFE) composite film. Peaks at 318 K (cooling) and 334 K (heating) correspond to the spin transition. Peaks at 338 K (cooling) and 373 K (heating) correspond to the α-β transition. Peaks at 408 K (cooling) and 425 K (heating) correspond to the melting of the copolymer.

It is important to note also that the Curie and melting temperatures and associated enthalpy changes of the polymer matrix (corrected for the wt%) are not considerably altered by the addition of the SCO complex (Fig 2.8), which indicates that the crystallinity of the polymer is preserved in the composite.

In order to ensure that it is possible for the full HS state of the SCO complex and the β phase of the polymer to coexist at a given temperature, an analysis that can detect both phase transitions would be necessary. Raman spectroscopy has often been used as a means to detect both the spin transition in SCO complexes[130] and the α-β phase transition in P(VDF-TrFE) [140]. The Raman spectra of the pure complex **5** shows that there are clear marker peaks in the 50-400 cm^{-1} region that can be used to distinguish between the HS and LS states (specifically the peaks at 105 cm^{-1} for the HS state and 290 cm^{-1} for the LS state). This is in agreement with experimental data for this family of complexes and given that the 50-400 cm^{-1} range is usually characteristic for M-L interactions, would imply that the spin transition markers come from a change in bond length between the Fe^{2+} ion and the ligands [130].

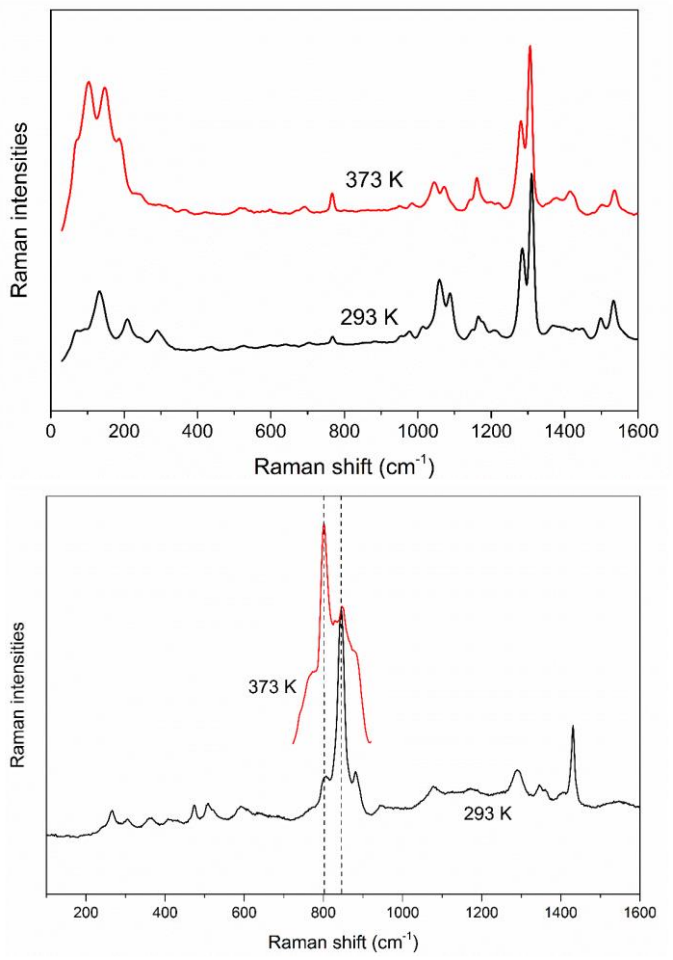

Fig 2.33) Raman spectra of complex **5** on the LS (black) and HS (red) states (up). Raman spectra of the pure P(VDF-TrFE) 70-30 copolymer at RT (black) and at the Curie temperature (red) (down).

The Raman spectra of the pure P(VDF-TrFE) 70-30 copolymer in agreement with the literature [140] shows marker peaks of 800 cm^{-1} for the non-polar α-phase and 847 cm^{-1} for the polar and electroactive β-phase. Conveniently, these peaks are very far from any characteristic peaks of the complex, allowing us to clearly differentiate between the two spin states and both crystalline phases simultaneously in the composite.

The Raman spectra of the composite consists of the superposition of the spectra of the SCO complex and P(VDF-TrFE) copolymer. At room temperature the fingerprints of the LS phase of the pure $[Fe(H\text{-}trz)_{1,85}(trz)_{0,85}(NH_2trz)_{0,3}](BF_4)_{1,15}\bullet 1H_2O$ complex (**5**) (131, 207 and 290 cm^{-1}) and the β phase of the P(VDF-TrFE) matrix (847 cm^{-1}) can be clearly discerned. When the temperature is increased above ≈340 K, a decrease of the intensity of the LS markers is observed while other peaks, characteristic of the HS phase, emerge around 105, 144 and 190 cm^{-1}.

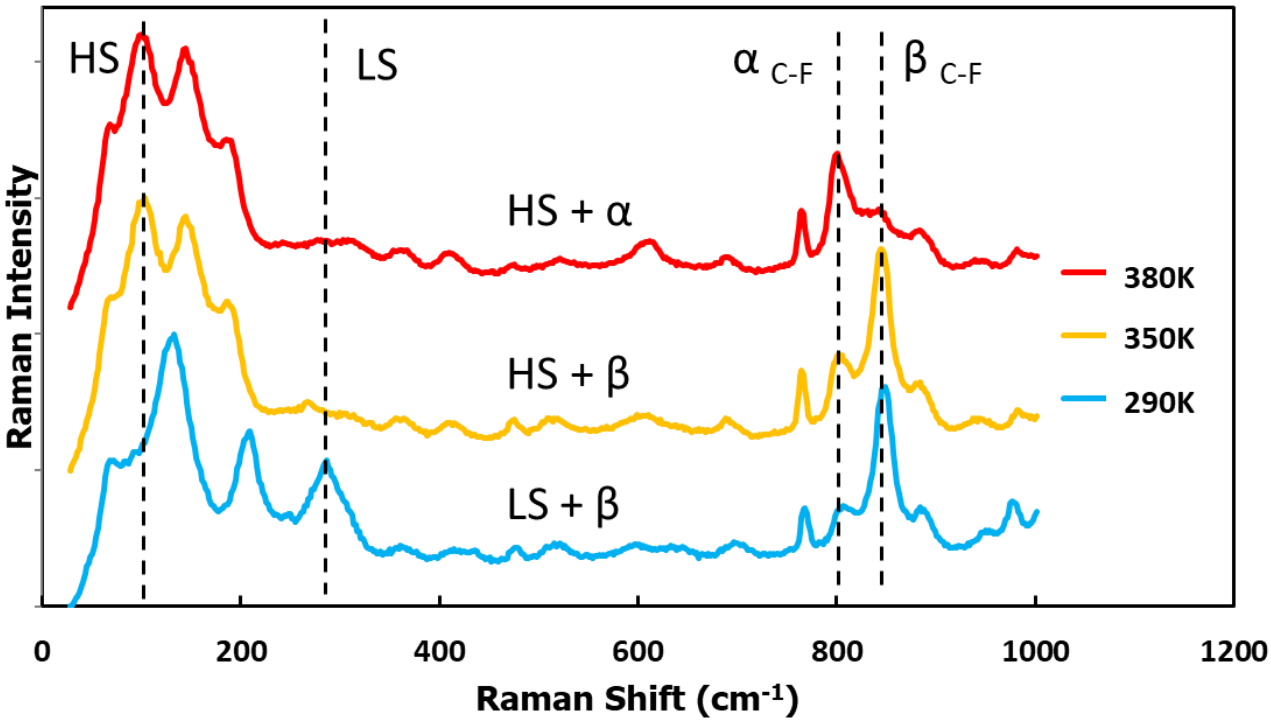

Fig 2.34) Raman spectra of the SCO(**5**)@P(VDF-TrFE) composite at three different temperatures.

In agreement with the magnetic data, the spin transition appears virtually complete in both directions. On further heating above the Curie temperature of P(VDF-TrFE) (≈360 K) the intensity of the Raman marker of the β polar phase decreases, while that of the α paraelectric phase (800 cm^{-1}) increases. The main result from this analysis is the confirmation of the fact that in the temperature range in which the spin transition occurs, the β phase signature remains intact, which suggests that once polarized, the composite can be reversibly cycled between the LS and HS states without losing the electroactive crystalline phase or the polymer chain organization corresponding to the poled polymer.

2.3.1.7 Mechanical properties of the first generation composite films

To assess the mechanical properties of the composite, we will use Dynamic Mechanical Analysis (DMA) which consists of subjecting a sample to a sinusoidal tensile stress while measuring its deformation to obtain mechanical and elastic properties of the sample. This analysis can be performed under variable temperature to determine the temperature dependency of the different mechanical properties of the complex.

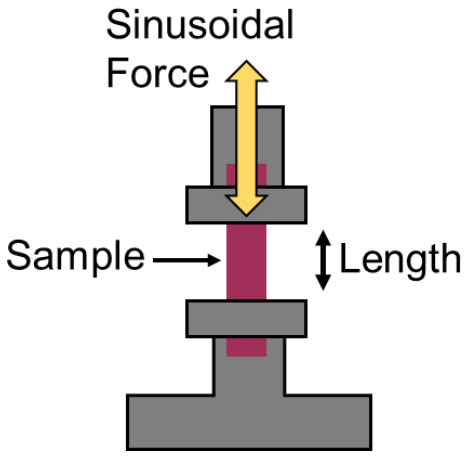

Fig 2.35) Schematic representation of a DMA (Dynamic Mechanical Analysis) experimental setup.

There are four main mechanical properties which will be deduced by the DMA: Engineering Strain $\Delta L/L_0$, Storage Modulus E', Loss Modulus E'' and Loss Tangent tan δ.

Engineering Strain $\Delta L/L_0$ is a measure of the change in length of the material. By measuring its dependency on the temperature, we can observe both the thermal expansion and the volume change of the composite associated with the spin transition. This is a key measure of the propagation of the intrinsic volume change of the complex inside the polymer matrix.

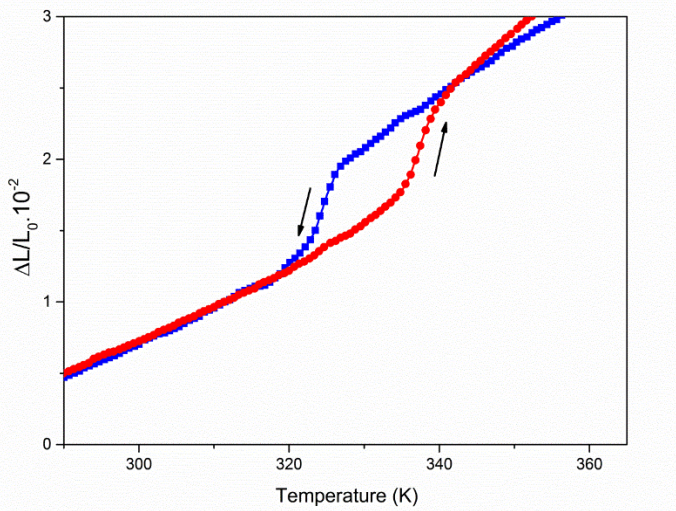

Fig 2.36) Temperature dependence of the engineering strain $\Delta L/L_0$ of the SCO(**5**)@P(VDF-TrFE) composite film under tensile testing. Arrows indicate heating and cooling.

When going from the LS to the HS state, an abrupt elongation of the sample can be observed (Fig 2.36). The elongation of the sample is reversible as it is mirrored by an identical contraction of the sample during the cooling phase when going from HS to LS. This actuation peak associated with the SCO shows the effective mechanical coupling of the SCO phenomenon into the P(VDF-TrFE) matrix. Taking into account the ≈25 wt% particle load, the 0.5% linear strain of the composite is mostly in line with the estimated ≈10% volume expansion of the crystalline lattice of the pure $[Fe(Htrz)_{1,85}(trz)_{0,85}(NH_2trz)_{0,3}](BF_4)_{1,15}\bullet 1H_2O$ complex (**5**) upon the SCO.

Another important mechanical parameter for viscoelastic materials is the **Storage Modulus** E' of the material which quantifies the resistance of the material to mechanical deformation. It also represents the stored energy of the material upon mechanical deformation, namely the elastic component of the viscoelastic behaviour. The elastic behaviour of the material is analogous to the movement of a mechanical spring which poses resistance against a given mechanical elongation and then stores this energy, releasing it as a contraction when the material is released.

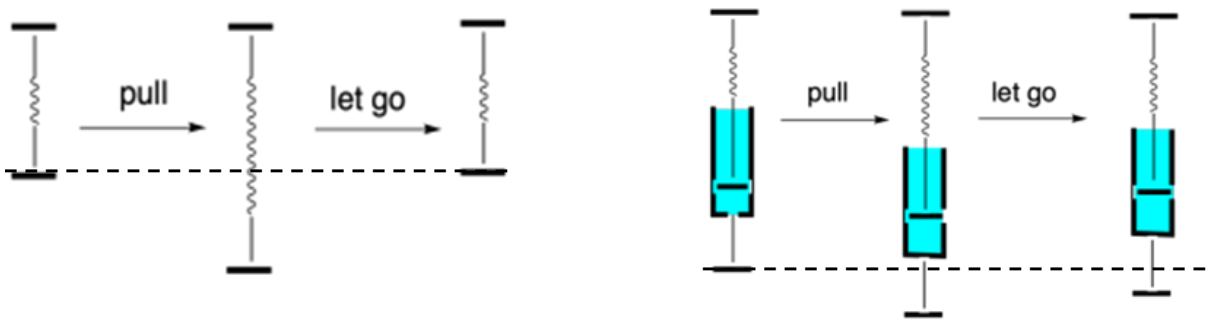

Fig 2.37) Elastic behavior of a mechanical spring (left). Viscoelastic behavior of a polymer material (right).

Viscoelastic materials such as polymers, however, do not show purely elastic properties. There is a fraction of the energy lost as heat due to the rearrangement of the chains (Fig 2.37). This lost energy is quantified as the **Loss Modulus** E'' and represents the viscous component of the mechanical behaviour of the sample.

The ratio between the Storage and Loss Moduli is called the **Loss Tangent**, tan δ. It is calculated simply as $\tan\delta = \frac{E''}{E'}$ and represents a measure of damping in the material.

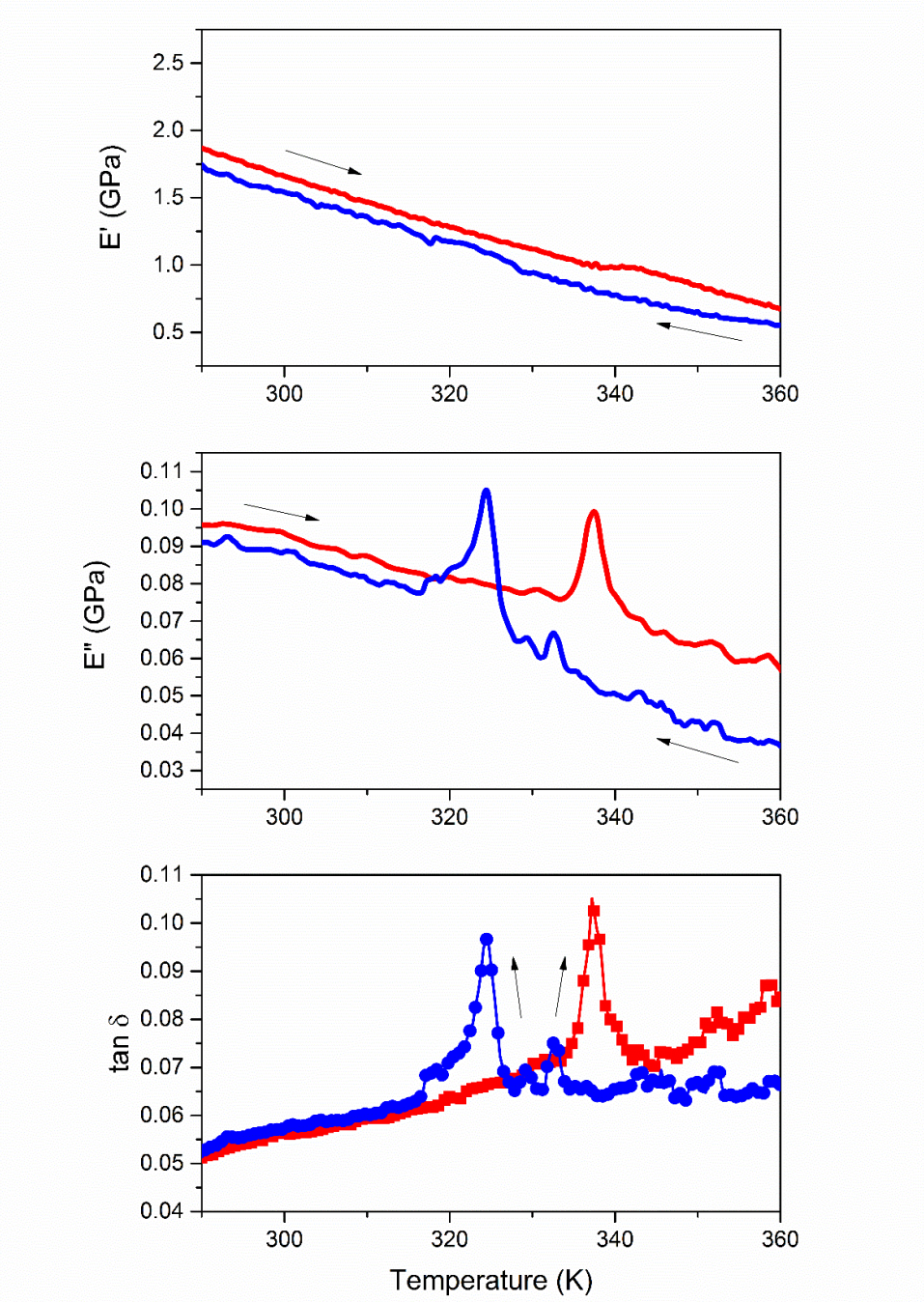

Fig 2.38) Dynamical Mechanical Analysis of the SCO(**5**)@P(VDF-TrFE) composite film. (a) Storage modulus *E',* (b) Loss Modulus *E"* and (c) tan δ.

The storage modulus E' of the composite seems to be virtually unaffected by the spin transition. The downward slope of E' with respect to temperature simply comes from the natural softening of a thermoplastic upon heating (Fig 2.38 top). This would suggest that the SCO has no effect on the elastic properties of the composite. The strong mechanical coupling between the particles and the matrix can, however, be clearly seen in the loss tangent (tan δ) and loss modulus

E'' behavior, which exhibit pronounced dissipation peaks around the spin transition temperatures (Fig 2.38 middle and bottom). Such anelastic phenomena are typical in materials with first-order phase transitions and can be associated with the internal frictions during the nucleation and domain growth process.

2.3.1.8 Electroactive properties of the first generation composite films

In order to measure the pyroelectric response of the composite material, which should arise naturally from the strong mechanical coupling between the particles and the matrix, a short-circuit setup was used (fig 2.39). In this setup, the poled composite film is placed between two electrodes and subjected to thermal cycling, while the electrodes simply measure the electrical response of the material as an electrical current produced by the film.

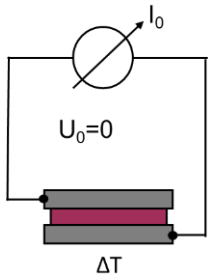

Fig 2.39) Schematic representation of a short-circuit pyroelectric experimental setup.

Poling of samples was undertaken at 293 K by applying several cycles of a sinusoidal electric field (100 mHz) with amplitudes up to 18 MV m^{-1} . The resulting piezoelectric coefficient d_{33}, which provides direct information on the mechanical to electrical (and vice-versa) conversion efficiency, was −2.3 and −3.3 pC N^{-1} , for different polarization intensities. These values are reduced with respect to the −20 pC N^{-1} measured for the pure P(VDF-TrFE) copolymer. A possible explanation is a disruption of the connectivity of the polymer matrix related to the existence of particle agglomerates. Using different sample preparation, increasing the proportion of solvent in the casting mixture to obtain a ratio 160 mg/mL of polymer in DMF and annealing at 410 K, we were able to increase d_{33} up to −9.0 pC N^{-1} (with a 24 MV m^{-1} applied field for a 150 µm film thickness), which was also stable in time for a month, indicating ferroelectric properties. However, this was achieved at the expense of mechanical properties (fragility) thus we were not able to pursue a full mechanical characterization with this sample.

As measured before, the spin transition in the composite is associated with a spontaneous volumetric strain of ≈ 0.5% (Fig 2.36). This mechanical strain should have an effect on the electroactive polymer matrix. A change of the polarization level of the P(VDF-TrFE) should take place due to the electro–mechanical coupling. Under short-circuit conditions one would therefore expect a transient current flow during the spin transition. As explained earlier, each sample was polarized at 293 K by applying several cycles of a sinusoidal electric field (100 mHz) with amplitudes up to 13.6 and 18 MV m^{-1}. It is important to note that all samples mentioned in the subsequent analysis correspond simply to fragments of the same sheet of SCO(**5**)@P(VDF-TrFE) composite, which have been individually polarized under a series of conditions.

In a first analysis, a composite sample polarized at 13 MV m^{-1} was heated beyond the Curie temperature, cooled back to room temperature and then heated beyond the Curie temperature once more (Fig 2.40a). Step 1 shows a pyroelectric discharge of the composite upon heating, as a result of the SCO causing a volume change in the piezoelectric matrix. Step 2 shows a cooling in which the composite produces a pyroelectric discharge in an opposite sign as the heating discharge of step 1, with similar intensity. Step 3 then shows a final heating step, with a much smaller discharge peak. This analysis shows the behavior of the polarized composite when subsequently depolarized. Once the polarization has been lost, we observe a significantly reduced pyroelectric response, with a small peak corresponding to the SCO temperature. There are two interesting results from this analysis: first, the depolarized sample still shows discharge peaks associated with the spin transition, and second the sign inversion of the pyrocurrent after the depolarization process.

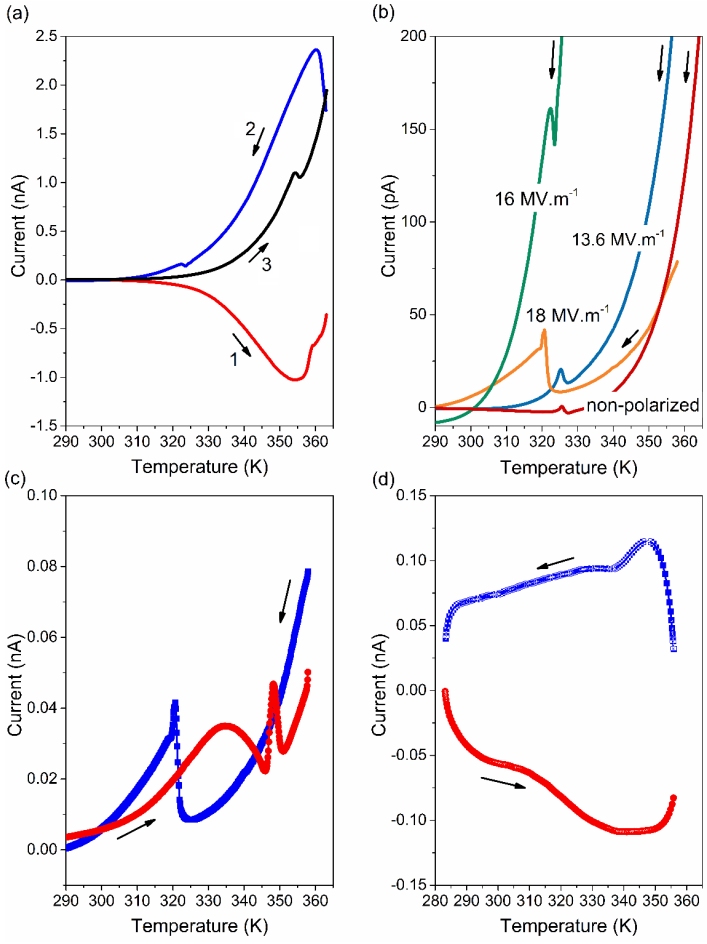

Fig 2.40) Short circuit measurements of a SCO(**5**)@P(VDF-TrFE) film. (a) Short-circuit current recorded at 7 K min^{-1} revealing the current sign inversion following a 13 MV m^{-1} poling. Step 1) heating, 2) cooling, 3) heating after losing the initial polarization (b) Current measurements on the cooling mode, non-polarized sample, samples poled at 16 and 18 MV m^{-1} (c) Current cycle with a 18 MV m^{-1} poled sample. (d) Reference data with the pure P(VDF-TrFE) 70-30 poled at 57 MV m^{-1} with no discharge peaks.

In a second analysis, a series of composite samples were polarized under different electrical field intensities (13.6, 16 and 18 MV m^{-1}) and each of the composite samples was cycled between 260 and 360 K without any applied voltage. The resulting thermally stimulated current curves reveal pronounced discharge current peaks around the spin transition temperatures, which are significantly enhanced with respect to the nonpoled sample (Fig 2.40b). The intensity of the discharge peak increases with the electrical field used to polarize the sample, further confirming the key role of the poling process.

It is interesting to note that there would seem to be small changes in the spin transition temperature between the samples. This is simply attributed to experimental error, stemming from the fact that to obtain intense pyroelectric responses that can be accurately measured, the temperature changes must be relatively fast (10 K min^{-1}) which leaves room for thermalization incertitude. In other words, the polarization of the sample does not seem to impact meaningfully the SCO temperatures.

The experimental result that proves the electroactive properties of the composite is the repeated experimental observation of this **"pseudo-pyroelectric" effect in the composite materials** in the form of discharge current peaks when submitted to temperature changes around the spin transition temperatures (Fig 2.40c).

To further explore the electroactive properties of the polymer, we analyzed the conductivity and permittivity of the composite sample. This is important because significant changes in permittivity could feasibly contribute to the observed pseudo-pyroelectric effect of the composite. Whereas an increase in conductivity could compromise this effect.

The temperature dependence of the dielectric permittivity of the composite is shown in fig 2.41. The room temperature value of $\varepsilon' = 17$ is similar to that of the pure P(VDF-TrFE) copolymer, but on heating across the spin transition temperature it drops (reversibly) by ≈40% indicating a significantly reduced storage capacity of the material in the HS state. On the other hand, owing to the highly insulating nature of the pure complex, the conductivity of the composite remains very low in both spin states ($< 10^{-6}$ S cm^{-1}), which is a useful property as it allows to keep small the leakage currents in the composite material. In fact, the observation of such important discharge peaks would be impossible with a conducting filler. Hence, the poor conductivity, considered in general as a drawback for SCO compounds, becomes here a key advantage.

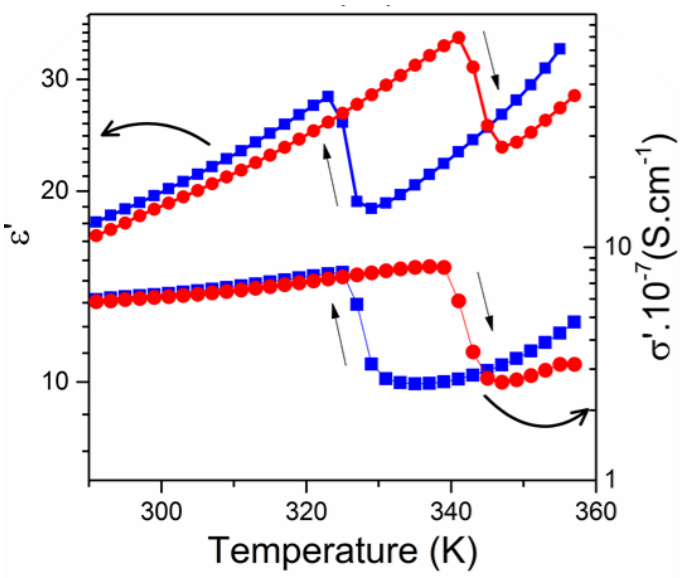

Fig 2.41) Dielectric permittivity (up) and electrical conductivity (down) at 100 kHz as a function of temperature for a SCO(**5**)@P(VDF-TrFE) film.

In summary, we succeeded in synthesizing high quality, homogenous P(VDF-TrFE) composites of $[Fe(H\text{-}trz)_{1,85}(trz)_{0,85}(NH_2trz)_{0,3}](BF_4)_{1,15}\bullet 1H_2O$ SCO nanoparticles in a reproducible manner allowing us to obtain flexible, freestanding, macroscopic objects displaying novel **electro–mechanical synergies** between the two components. This coupling leads to concomitant macroscopic thermal expansion and electrical discharge peaks at the spin transition.

However, there are multiple parameters that yet remain to be explored, such as the effect of the particle morphology, concentration and composition in the electromechanical properties of the composite. It would be interesting as well to address the dramatic loss of d_{33} observed in these composites to optimize the mechanical energy efficiency. For these reasons, a second, follow-up study was developed, to fabricate and characterize the second generation of electroactive SCO@P(VDF-TrFE) composites.

2.3.2 Second Generation SCO@P(VDF-TrFE) composites

The purpose of this follow-up study is the fabrication of a series of SCO@P(VDF-TrFE) nanocomposites, while varying the composition of the polymer as well as the composition, the concentration and the morphology of the spin crossover particles. The aim was to show that by tuning the matrix and particle properties it is possible to observe concomitantly the piezoelectric effect from the spin transition and the pyroelectric response of the polymer. An additional goal was to determine how each of these characteristics plays a role in the electromechanical properties of the composite.

In this work, the SCO compounds used belong to the family of $[Fe(Htrz)_{1+y-x}(trz)_{2-y}(NH_2trz)_x](BF_4)_y\cdot nH_2O$ showing thermal spin transitions between 50°C and 100°C (depending on the stoichiometry) as well as the mononuclear complex $[Fe(HB(tz)_3)_2]$ (tz =

1,2,4-triazol-1-yl) presenting a very stable abrupt spin transition around 60°C. The effect of the composition of the copolymer is studied as well. In the first generation films, the copolymer of choice was P(VDF-TrFE) 70-30. This copolymer displays a Curie point at 105°C, whereas for 75–25 mol% the Curie point shifts to 115°C. The latter co-polymer, despite being slightly less piezoelectric, appears thus more interesting for our work as it provides a broader 'temperature window' for the choice of the SCO complex.

2.3.2.1 SCO complexes for the second generation of P(VDF-TrFE) composites

A series of five complexes were chosen for this study. First is complex **3** from the first study detailing the dilution technique for the fabrication of nanoparticles. This complex is a NH_2trz substituted complex with 6.6% proportion of NH_2trz ligand, chosen for its transition temperature which is far from the Curie temperature. Next is complex **5** (10% proportion of NH_2trz ligand) from the first generation particles study. Both this complex and the composite synthesized with it correspond exactly to the first-generation films, and have been included in this study solely for the sake of comparison. Complex **6** is a NH_2trz substituted complex with 6.6% proportion of NH_2trz ligand. It was however synthesized lowering the reagent concentration to obtain a higher particle size to ascertain if the size of the SCO particles plays a significant role in the properties of the composite. Complex **7** is a NH_2trz substituted complex with 6.6% proportion of NH_2trz. It was however synthesized via reverse micelle under specific conditions to obtain 2 µm long rods, to determine if the particle morphology plays a role in the properties of the composite (See section 2.3.2.2). Finally complex **8** is the highly stable and reproducible molecular $[Fe(HB(tz)_3)_2]$ complex, chosen for its robust, abrupt spin transition well below the temperature of the polymer matrix. This particular complex will be also used for a series of composites detailing the effects of the concentration of SCO filler in the composite matrix.

The microcrystalline powder sample **6** was obtained by: mixing 7.5 ml of a 0.395 M water solution of $Fe(BF_4)_2 \cdot 6H_2O$ with a water solution containing a mixture of 50 mg of 1,2,4-4-NH_2-triazole (6.6%) and 572 mg of 1,2,4-4-*H*-triazole. The mixture became pink after a minute and was allowed to react for 12 h. The resulting pink solid was cleaned multiple times by centrifugation with ethanol and dried under vacuum (90% yield).

Rod-like microparticles (compound **7**) were prepared using a reverse micelle[131] technique. The technique consists in the use of a stable microemulsion of polar droplets in an oil phase, stabilized by a surfactant agent. The polar droplets act as nanoreactors, confining the growth of the SCO complexes to separate the nucleation and growth processes to obtain nanometric objects. In our case the polar phase is water, the oil phase is cyclohexane, the surfactant is Triton X-100 and pentanol is used as cosurfactant. The role of the cosurfactant is to increase the mobility of the surfactant in the medium and reduce the surface of the micelles, allowing their stabilization. The synthesis had to be optimized in order to obtain regular, long rods, the optimization process to obtain this sample will be described in the section below.

The microcrystalline powder sample **8** was obtained by the following procedure [141]: $KHB(tz)_3$ (3.72 g, 14.6 mmol) was mixed in a 2 : 1 ratio with $Fe(SO_4)_2 \cdot 7H_2O$ (2.01 g, 7.3 mmol) in water, which led to the formation of a purple powder purified by centrifugation (95% yield).

2.3.2.2 Synthesis of anisotropic SCO particles

With the goal of fabricating anisotropic nanoparticles to test the effect of particle morphology on the electroactive properties of SCO@P(VDF-TrFE) composites, we set out to adapt the reverse micelle technique used by Suleimanov et al [131] (Fig 2.42). Indeed, the author of this study found that for the mixed complexes of formula $[Fe(Htrz)_{1+y-x}(trz)_{2-y}(NH_2trz)_x](BF_4)_y \cdot nH_2O$, when synthesized via the reverse micelle technique, the addition of NH_2trz ligand leads to the formation of anisotropic rod-like particles, suggesting that these mixed complexes favor such a crystallization morphology.

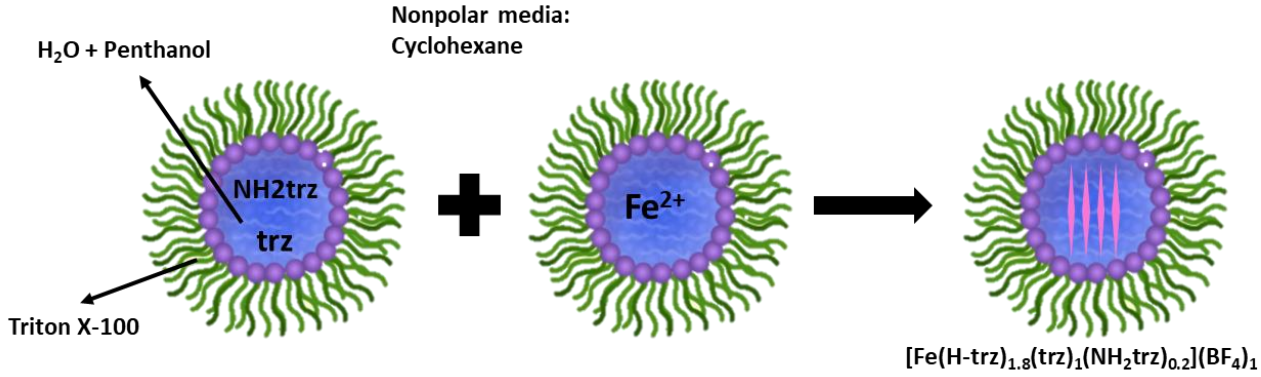

Fig 2.42) Schematic representation of the reverse-micelle method for the fabrication of anisotropic rods.

In order to obtain anisotropic nanoparticles we used a mixed complex of similar composition, with a 6.6% proportion of NH_2trz ligand. We hypothesized that the crystallization speed played a crucial role in the formation of these anisotropic particles. The work of Peng et al [45] had shown us that under extremely slow crystallization conditions, anisotropic objects with a large aspect ratio can be synthesized. To obtain a similar result, we used the concentration of reagent in the aqueous solution as our main variable parameter to control the kinetics of the reaction. To achieve this we performed a series of identical syntheses as described below, varying only the amount of water used in the polar phase of the micellar system.

In our synthesis procedure, two equivalent microemulsions were prepared mixing together 3.85 ml of Triton X-100, 3.6 ml of pentanol and 8 ml cyclohexane. To this mixture, a solution of 424 mg of $Fe(BF_4)_2 \cdot 6H_2O$ in X ml H_2O was added dropwise to obtain the first microemulsion, whereas a solution of 234 mg of 1,2,4-4-*H*-triazole and 32 mg of 1,2,4-4-NH_2-triazole (6.6%) in X ml H_2O was added to obtain the second microemulsion, with $0.75 < X < 3$ mL of water. These microemulsions were stirred at room temperature until clear solutions were obtained and then quickly mixed together. Several minutes after, the mixture became pink due to the particle formation. The resulting microemulsion was agitated for 24 hours to ensure that the microemulsion exchange was completed. Then, 30 ml ethanol was added to destroy the

microemulsion structure. The obtained nanoparticles were washed several times with ethanol to remove the traces of the surfactants and separated by centrifugation (4000 rpm, 10 minutes).

The particles were then characterized by TEM to assess the effect of the proportion of water in the micellar system. The first two samples were fabricated using 0.75 mL and 1 mL H_2O, respectively. The obtained particles are rather small (100 nm, ≈ 90% yield); they show structural anisotropy but at this size, the effect is almost negligible. The small sizes suggest a rapid nucleation step leading to a large amount of seeds during the growth process.

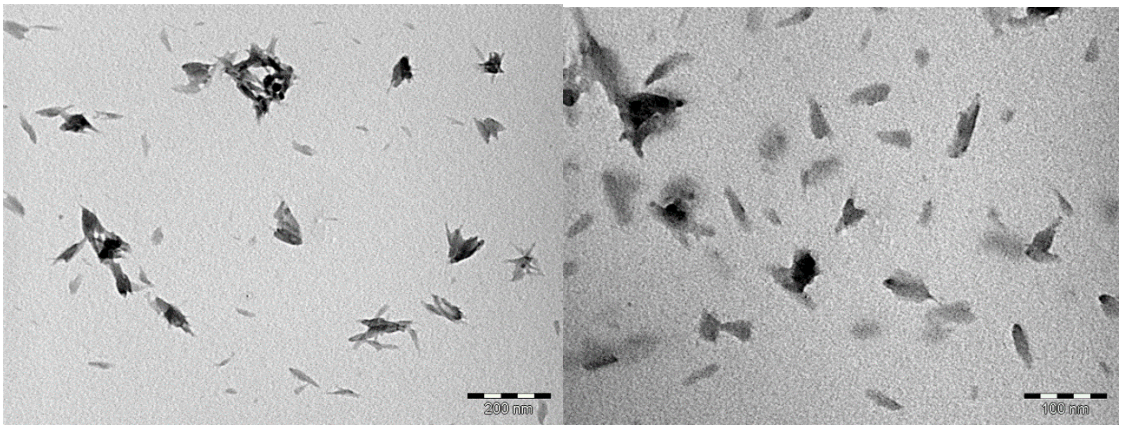

Fig 2.43) TEM images of $[Fe(H\text{-}trz)_{1.8}(trz)_1(NH_2trz)_{0.2}](BF_4)_1$ nano particles fabricated using 0.75 mL (left) and 1mL H_2O in the micellar system (right).

The next set of samples was fabricated using 1.5 mL and 2 mL H_2O in the micellar system. At 1.5 mL of water we obtain objects of 200-300 nm, with very clear anisotropy, confirming the hypothesis that a reduced concentration of reagents in the micelle and an increase in the proportion of polar phase leads to increased size and anisotropy of the particles. At 2 mL we obtain rod-like particles of 500 nm (≈ 80% yield) with an aspect ratio significantly higher than the samples synthesized before, showing the effect of the increase in water proportion.

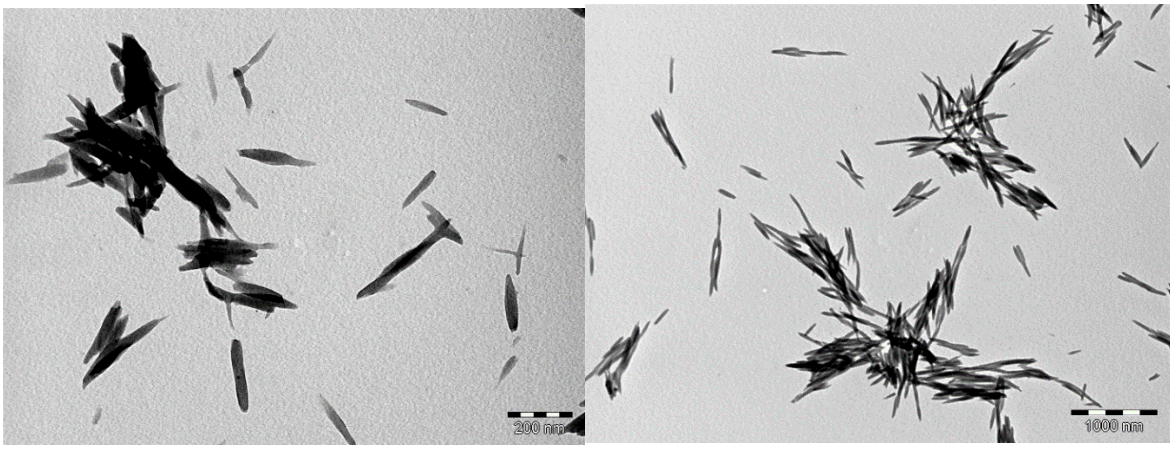

Fig 2.44) TEM images of $[Fe(H\text{-}trz)_{1.8}(trz)_1(NH_2trz)_{0.2}](BF_4)_1$ nano particles fabricated using 1.5 mL (left) and 2 mL H_2O in the micellar system (right).

Finally, the last set of samples was fabricated using 2.75 mL and 3 mL of water in the polar phase. At 2.75 mL we obtained highly anisotropic 2 µm needle-like particles. However, at this concentration and reaction speed, the yield is severely impacted, as we could not obtain more than 32% yield. Even repeating the reaction with a 72 hr reaction time had identical results. Interestingly, at 3 mL of water the reaction yield is minimal (< 5%) and the recovered product, while still anisotropic, has a relatively small size at 500 nm and a much lower aspect ratio. This suggests that at high amounts of water the micellar system is de-stabilized and the reaction probably takes place outside of the micelle, leading to an uncontrolled morphology.

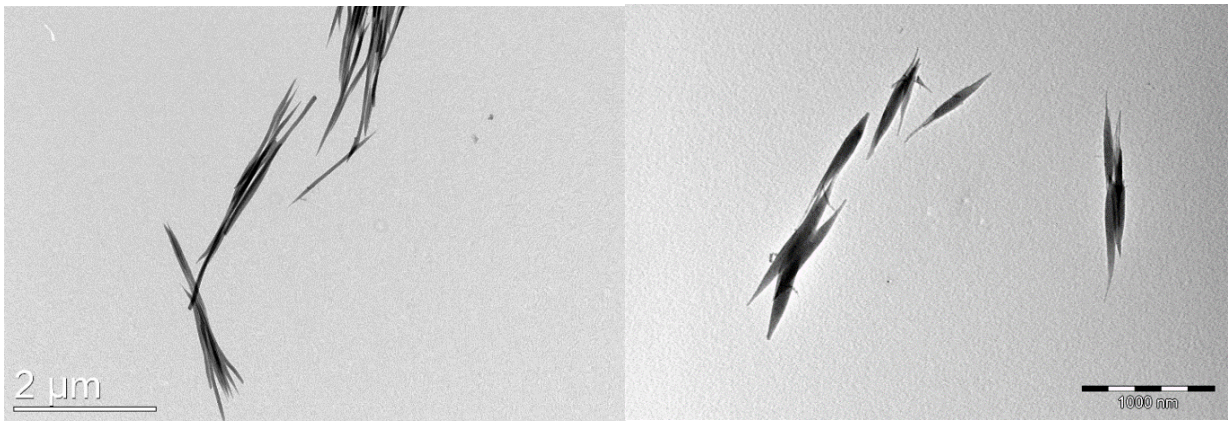

Fig 2.45) TEM images of $[Fe(H\text{-}trz)_{1.8}(trz)_1(NH_2trz)_{0.2}](BF_4)_1$ nanoparticles fabricated using 2.75 mL (left) and 3 mL H_2O in the micellar system (right).

From these results, we adopted the complex fabricated at 2.75mL H_2O in the micellar system as complex **7** for the following study**.**

2.3.2.3 Characterization of the SCO complexes for the second generation of P(VDF-TrFE) composites

The chemical formulae gathered in table 2.3 were determined via elemental analysis. Interestingly, complexes **3**, **6** and **7** all correspond to $[Fe(Htrz)_{1+y-x}(trz)_{2-y}(NH_2trz)_x](BF_4)_y \cdot nH_2O$ complexes prepared with a 6.6% proportion of NH_2trz and yet each of them has a different chemical formula and spin transition properties. This is probably due the different synthesis methods used and to small differences in the crystallization conditions, which lead to different $Htrz/trz^-$ ratios, which in turn significantly change the properties of the system. Mixed ligand complexes seem particularly sensitive to synthesis conditions in this regard.

Table 2.6) Elemental analysis of complexes used for 2nd generation composite films.

SCO sample	%C (found)	%C (calc)	%H (found)	%H (calc)	%N (found)	%N (calc)	%B (found)	%B (calc)	%Fe (found)	%Fe (calc)
3	18.2	18.3	1.6	2.84	31.8	32.6	3.4	3.4	14.1	14.2
5	18.8	18.6	2.2	2.9	33.4	33.6	3.2	3.2	14.8	14.4
6	19.3	19.5	2.0	2.8	35.6	34.9	3.1	3.1	15.7	15.2
7	20.3	20.6	2.1	3.1	32.9	34.1	2.7	2.8	15.2	14.8
8	24.3	24.2	3.9	4.4	41.7	42.3				

Table 2.7) SCO complexes chosen for the study.

SCO sample	Composition	Morphology
3	$[Fe(Htrz)_{2.05}(trz)_{0.75}(NH_2trz)_{0.2}](BF_4)_{1.25}\bullet 1H_2O$	20 nm particles
5	$[Fe(H\text{-}trz)_{1,85}(trz)_{0,85}(NH_2trz)_{0,3}](BF_4)_{1,15}\bullet 1H_2O$	20 nm particles
6	$[Fe(H\text{-}trz)_{1,85}(trz)_{0,95}(NH_2trz)_{0,2}](BF_4)_{1,05}\bullet 0.6H_2O$	Microcrystalline
7	$[Fe(H\text{-}trz)_{1.8}(trz)_1(NH_2trz)_{0.2}](BF_4)_1\bullet 0.7H_2O$	2 µm rods
8	$[Fe(HB(trz)_3)_2]$	Microcrystalline

Given the importance of the morphology of each sample, TEM imagery plays a crucial role in the adequate characterization of these complexes. Samples **3** (Fig 2.15) and **5** (Fig 2.23) have already been characterized.

TEM images of complex **6** reveal a microcrystalline morphology of the sample with particle size around 1 µm. Surprisingly enough, despite there being no control of the crystallization process, the sample presents a relatively regular structure consisting of anisotropic particles. No objects above 3 µm were found in the sample, attesting to the naturally limited size of the micro-objects.

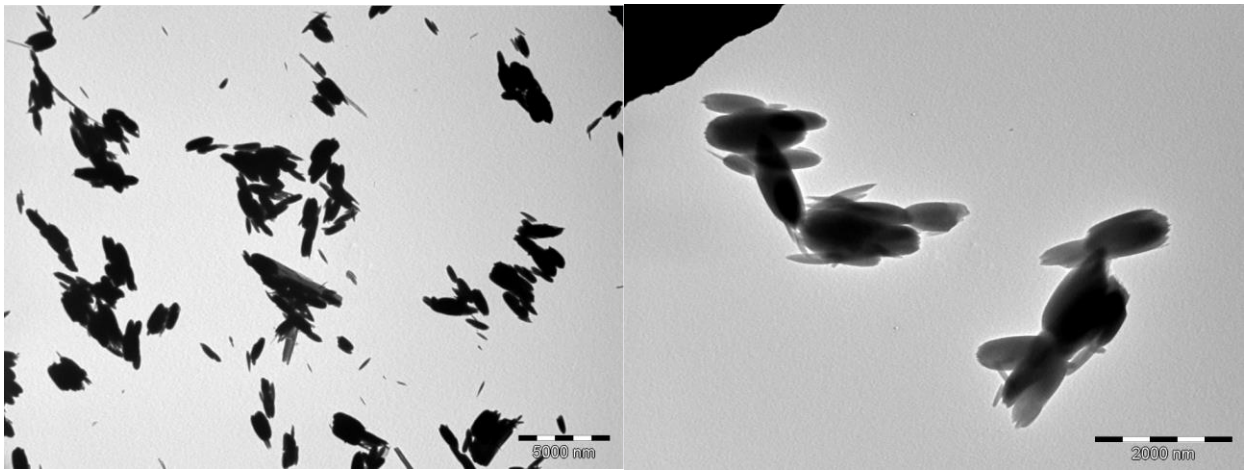

Fig 2.46) TEM images of complex **6.**

TEM Images of complex **7** show anisotropic objects with a length of 2 µm and an aspect ratio of 24. Owing to the well-studied reproducibility and robustness of reverse-micelle synthesis methods in the fabrication of SCO nano-objects, the particles of **7** show extremely regular shapes and sizes, with no significant outliers found in the TEM analysis.

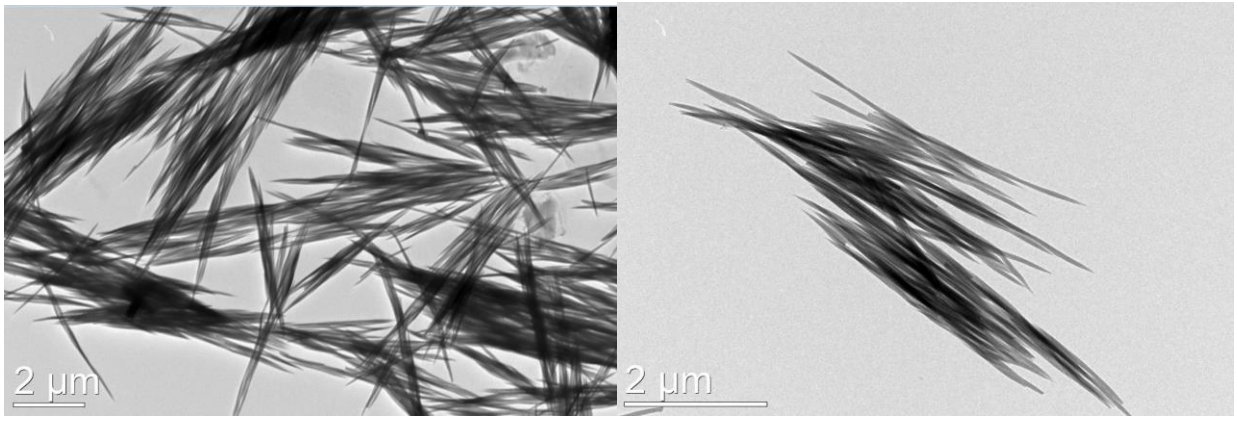

Fig 2.47) TEM Images of complex **7.**

TEM images of complex **8** shows a microcrystalline sample with a high variance in terms of particle size and shape. This is probably due to the fact that $[Fe(HB(tz)_3)_2]$ crystallizes readily and rapidly, making it extremely hard to control the growth stage of the crystallization process. It should be noted that $[Fe(HB(tz)_3)_2]$ is a partially soluble complex, so recrystallization might happen during any point of the fabrication process, leading to a highly heterogeneous distribution of microcrystals.

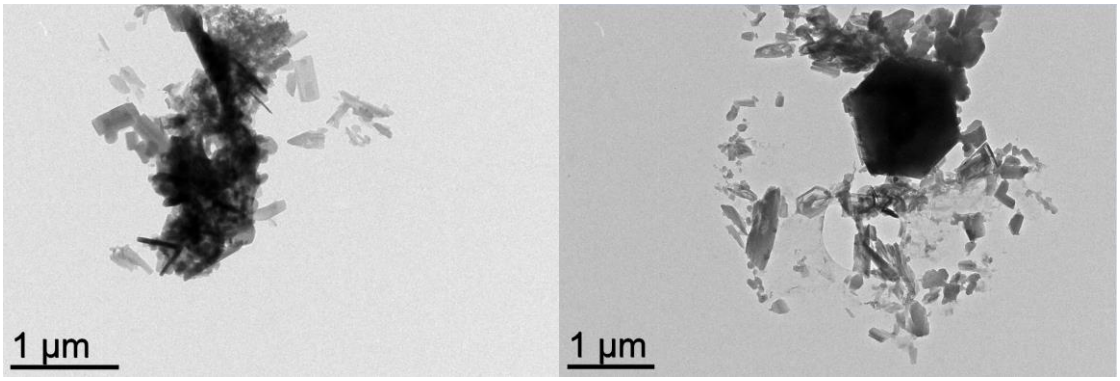

Fig 2.48) TEM Imagery of complex **8**.

In order to investigate the SCO properties of the newly synthesized complexes **6**, **7** and **8**, optical reflectivity was used as a means to follow the spin transition of the powder samples. This technique follows the thermochromism associated with the spin transition. Again, the thermal cycles shown here correspond to the second thermal cycle, due to the possible run-in effect. Complexes **3** and **5** have already been characterized (Fig 2.17 and 2.26).

Variable temperature optical reflectivity analysis of complex **6** shows an abrupt spin transition with temperatures $T_{1/2}^{\uparrow}$= 357 K and $T_{1/2}^{\downarrow}$= 335 K. Interestingly, the spin transition temperature is higher than for complex **3** which was prepared in the same manner and with the same proportion of NH_2trz ligand. This might be explained by the difference in chemical composition between the two complexes. Complex **7** shows an abrupt spin transition with temperatures $T_{1/2}^{\uparrow}$= 364 K and $T_{1/2}^{\downarrow}$= 344 K. This complex presents a much higher spin transition temperature, probably owing to its unique crystallization conditions. The SCO, however, risks overlapping with the Curie temperature of the copolymers in the composite.

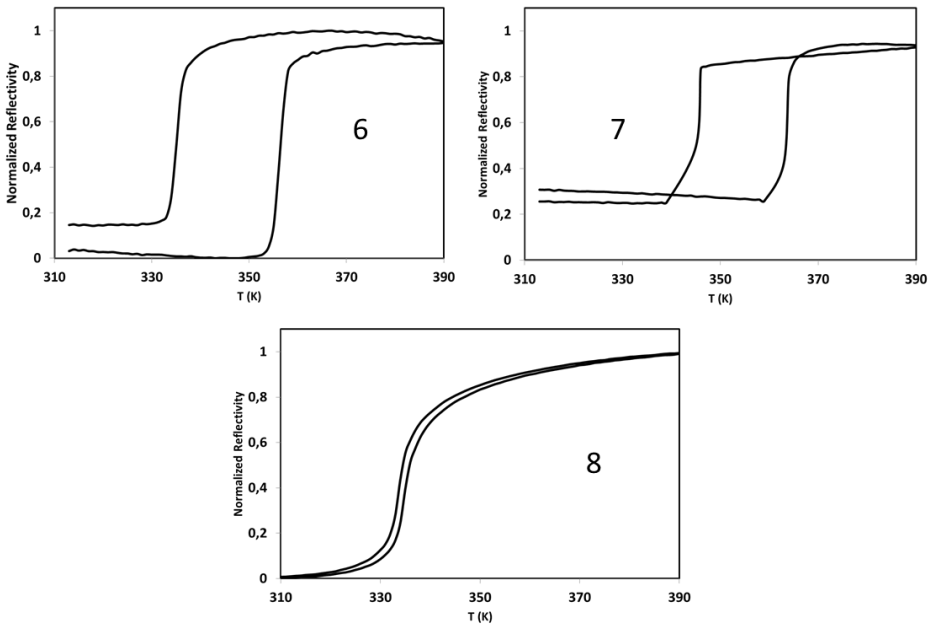

Fig 2.49) Variable temperature optical reflectivity of complexes **6, 7, 8**.

Complex **8** shows an abrupt spin transition with temperatures $T_{1/2}\uparrow$= 336 K and $T_{1/2}\downarrow$= 335 K. This complex presents no run-in effect and has a very reproducible hysteresis loop, making it perfect for an in-depth analysis where different fabrication conditions are explored. The spin transition of this complex is well in accordance with the one reported in the literature for the desolvated form of the complex [141].

Table 2.8) Spin transition temperatures of samples **3-8.**

	Spin transition temperature (K)		
Sample	T↑(K)	T↓(K)	ΔT(K)
3	346	331	15
5	338	330	8
6	357	335	22
7	364	344	20
8	336	335	1

2.3.2.4 Fabrication of second-generation composite films

The methodology used to develop the first series of films had serious limitations, which reduced its flexibility to be adaptable for different compounds, and as such, a new methodology to create the SCO@P(VDF-TrFE) films had to be established.

First, DMF is a deeply aggressive solvent, which favored the decomposition of several SCO complexes during the dispersion phase. In order to synthesize P(VDF-TrFE) composites with a $[Fe(HB(tz)_3)_2]$ filling, it was necessary to find another solvent capable of diluting P(VDF-TrFE), but which did not favor the decomposition of the complex. After several solvent tests, 2-Butanone (MEK) was found to be a suitable solvent, in which most SCO complexes can be dispersed and remain stable. Fig 2.50a shows the differences between composite films fabricated in DMF and in 2-Butanone, using complex **8**. The brown-colored film on the left showed no thermochromism, evidencing the loss of the SCO properties.

Fig 2.50) $[Fe(HB(tz)_3)_2]$(**8**)@P(VDF-TrFE) composites obtained by various synthesis conditions. a) Film prepared in DMF (left) and in 2-Butanone (right). b) Film prepared at high viscosity and high thickness. c) Film prepared at high temperature (105°C).

Another limiting factor for the development of a variety of films was the final detaching process from the substrate. Detaching from the glass substrate put significant mechanical strain on the composite, which limited the possible scope of film thicknesses and complex concentrations. By using a non-adhesive Teflon substrate, films are much more easily detached with little mechanical effort, a wider variety of films can be prepared, and there is a smaller chance of having internal fractures, which might cause breakage during poling.

With 2-Butanone as the new choice of solvent, the drying step becomes much faster. For high viscosity and high thickness films, this leads to the formation of internal bubbles, which leads to uneven and inhomogeneous films (Fig 2.50b). In order to limit this effect, it was necessary to reduce the thickness of the films. This was achieved via blade casting which also allows us to control the thickness. With this technique, after the composite has been deposited onto the substrate, the top part of the deposit is smeared across the substrate by using a doctor blade at a fixed height. In our case, the height that provided the best results in terms of homogeneity was 150 µm.

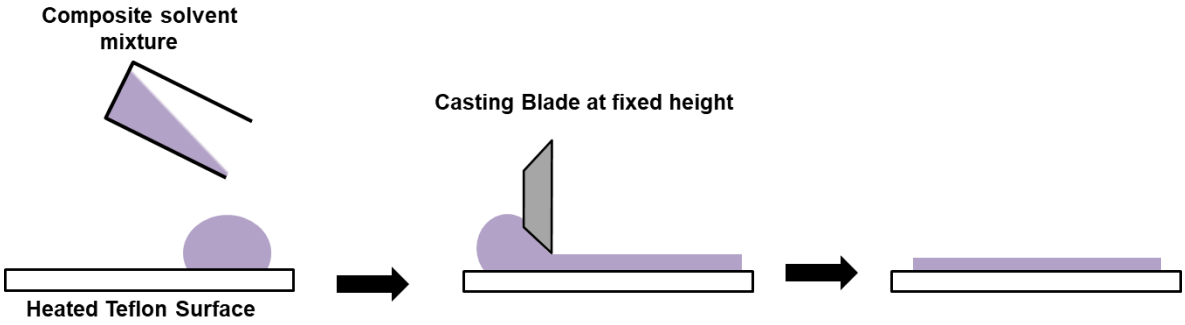

Fig 2.51) Blade Casting technique for SCO@P(VDF-TrFE) composites.

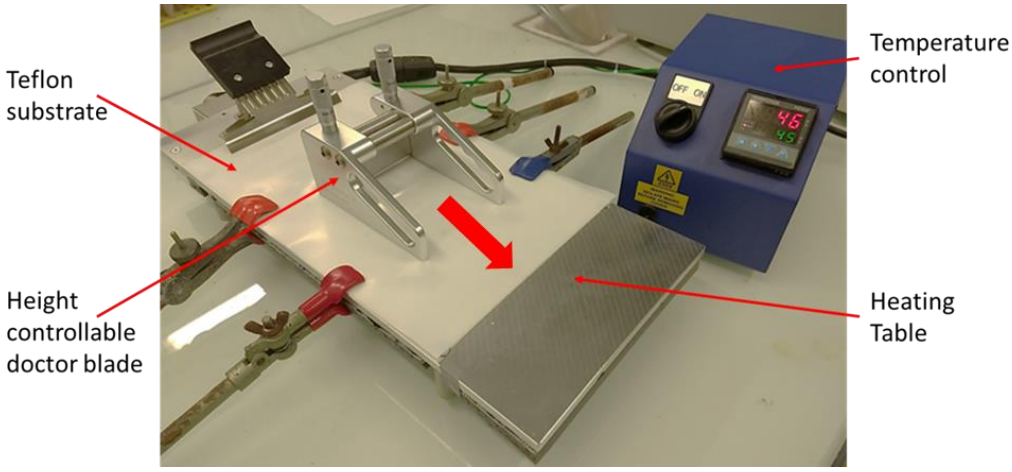

Fig 2.52)Temperature controlled blade Casting experimental setup.

Drying the composite at the annealing temperature (105 °C) as we did for the first-generation films, leads to the formation of bubbles inside the composite, a rapid and uneven drying process and ultimately a coffee-ring effect. While blade-casting diminishes this effect, it does not eliminate it entirely (Fig 2.50c). This means that it becomes necessary to separate the

drying and annealing processes to obtain homogeneous films. To obtain the slow evaporation needed for the film deposit to be free of internal air pockets and with no coffee ring effect, the optimal deposition and drying temperature was found to be 50 °C. Once the film is dry and mechanically stable, it is detached from the substrate and annealed at 105 °C to optimize the crystalline properties.

Regarding the concentration of the SCO complex in the matrix, we observed that for a high SCO load, the composite becomes inhomogeneous and brittle, with very poor mechanical properties. A maximum load of *ca.* 15–33 wt% could be reached, depending on the SCO sample used, while keeping a good sample quality. Different film thicknesses were also examined. Films under 50 µm, despite being highly homogeneous, were too fragile to be properly poled. We found a thickness of *ca.* 100 µm as a good compromise to obtain homogenous samples, which could be easily handled.

With all these adjustments to the film fabrication procedure, the final procedure for a concentration of 25 wt% for example, consisted of: first, dispersing each SCO complex (90 mg) in 2-butanone (1.8 ml) in an ultrasonic bath for 40 min. Then, the corresponding P(VDF-TrFE) copolymer (270 mg) was added to the mixture and dissolved at 45 °C. The resulting suspensions were then blade-cast at a height of 150 µm on a heated Teflon surface at 50 °C and kept at this temperature for *ca.* 2 h, until the composite was completely dry. The films were then detached from the surface and annealed at 105 °C for 12 h.

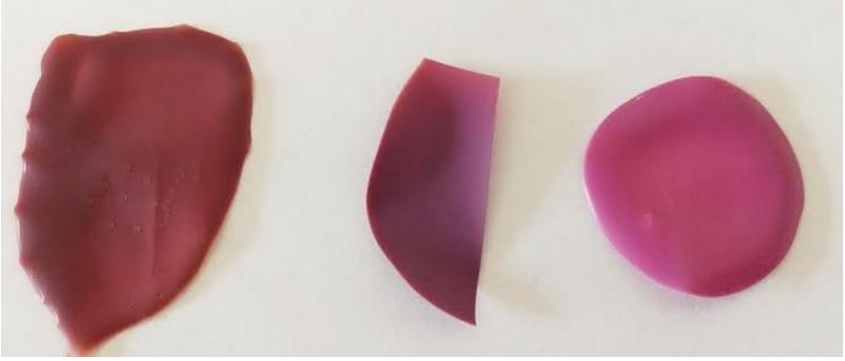

Fig 2.53) Optimized composite samples of P(VDF-TrFE) with complexes **7** (left), **6** (middle) and **8** (right).

Overall, eight new composite samples were prepared (See table 2.9) allowing us to study the influence of the concentration, composition and morphology of the particles as well as the composition of the polymer. Composite **5a** corresponds to the first-generation films and has been included in the study for the sake of comparison. In particular, the copolymer that will be used for this study is P(VDF-TrFE) 75-25. This copolymer, while slightly less piezo and pyro electric than P(VDF-TrFE) 70-30, has the advantage of having a higher Curie temperature (around 385 K on heating, see phase diagram in Fig 2.54), allowing for the SCO thermal cycles to not interfere with the polarization of the composites. Curie temperature will naturally increase with an increasing proportion of VDF in the copolymer, however above 80% there is a much greater proportion of non-ferroelectric α-phase; in this regard, the 75-25 is a good compromise.

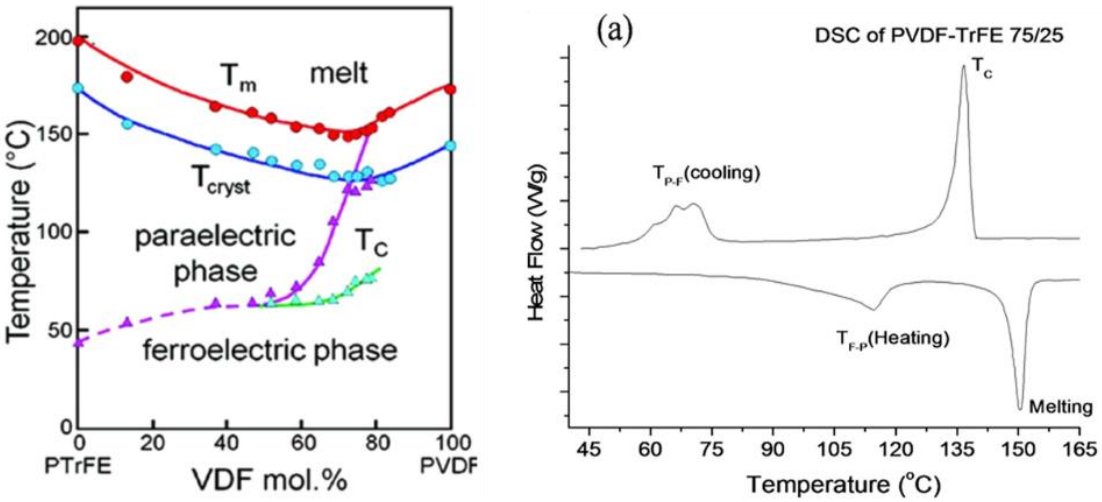

Fig 2.54) Phase diagram of P(VDF-TrFE) (left)[142] and DSC of P(VDF-TrFE) 75-25 [143] (right).

Table 2.9) Second-generation SCO@P(VDF-TrFE) composites.

Composite	**SCO sample**	**Load** wt%	**VDF:TrFE** (mol%)
3a*	**3**	15 %	75-25
5a	**5**	25 %	70-30
6a	**6**	15 %	75-25
7a	**7**	15 %	75-25
8a	**8**	33 %	75-25
8b	**8**	25 %	70-30
8c	**8**	25 %	75-25
8d	**8**	15 %	75-25
8e	**8**	5 %	75-25

***First generation sample**

Characterization of the second generation composite films will be divided in two sections. The first section details the physical and morphological characterization of the film, detailing its composition and SCO properties. The second section goes in depth into the characterization of the electroactive properties of the film, focusing on the novel arising properties from the synergy between the SCO filler and the electroactive P(VDF-TrFE) matrix.

2.3.2.5 Morphological and physical characterization of the second generation composite films.

Composites **3a** and **5a** are excluded from this characterization as composite **5a** has already been characterized as part of the first-generation study and composite **3a** is morphologically identical. Likewise, composites **8b** to **8e** are morphologically identical to **8a,** having the same SCO filler.

SEM images of composite **6a** show the anisotropic, oval-shaped particles of **6** dispersed in the polymer matrix (fig 2.55). The objects seem inhomogeneously dispersed, as expected for the relatively large microcrystalline particles.

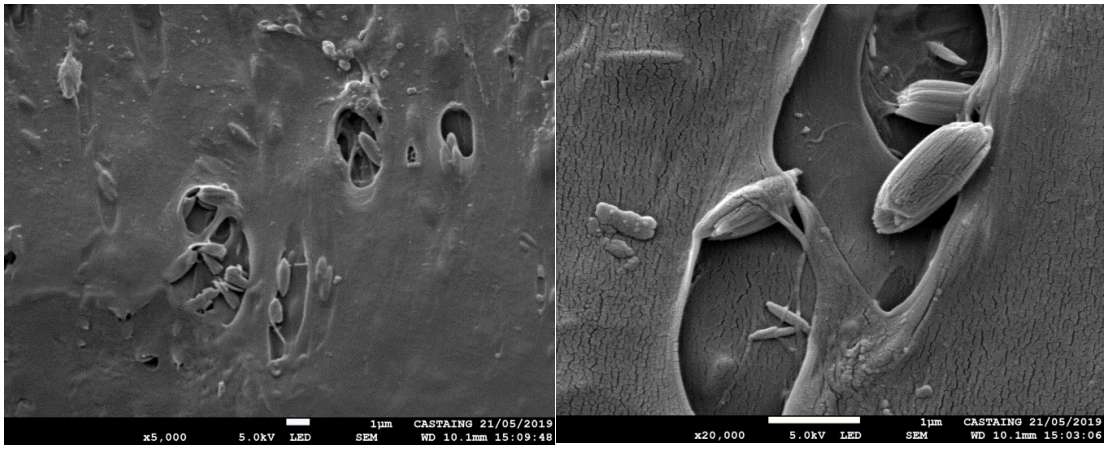

Fig 2.55) SEM Images of the cross-section of composite **6a.**

SEM images of composite **7a** reveal long, anisotropic particles in the P(VFD-TrFE) matrix (fig 2.56). The images suggest a tendency of the particles to bundle together and align over the X-Y plane, which could play a crucial role in the determination of its properties. The aligning of the particles itself could well be a result of the blade-casting technique creating flow dynamics that favor such an arrangement of particles in the polymer solution, which then solidifies as the solvent evaporates.

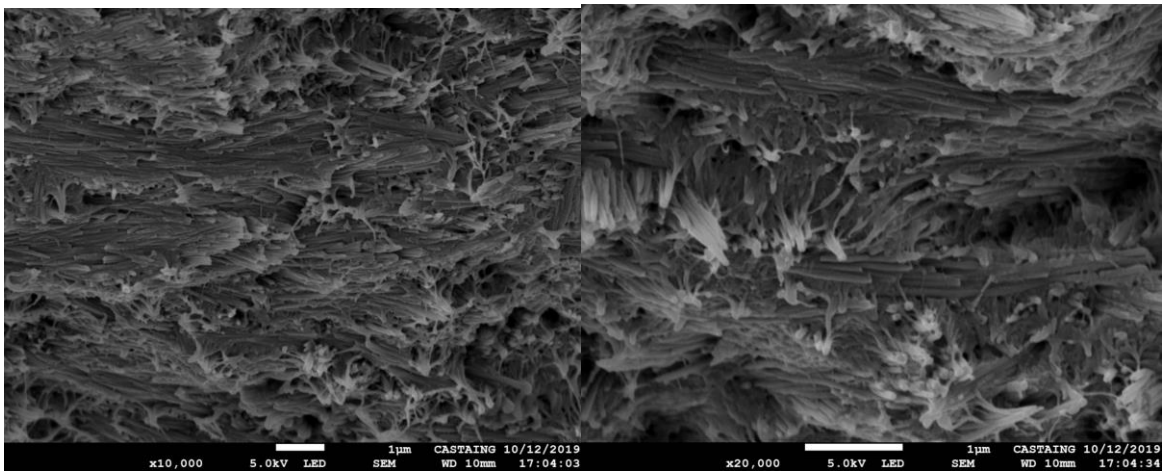

Fig 2.56) SEM Images of the cross-section of composite **7a.**

Finally, in composite **8c** the contrast can be clearly seen between the micron-sized, rectangular particles and the much smaller polymer fibres (fig 2.57). The composite seems highly inhomogeneous, with particles of different sizes unevenly distributed across the matrix. For this reason, it is surprising that composite **8a** could withstand very high polarization fields without breakdown.

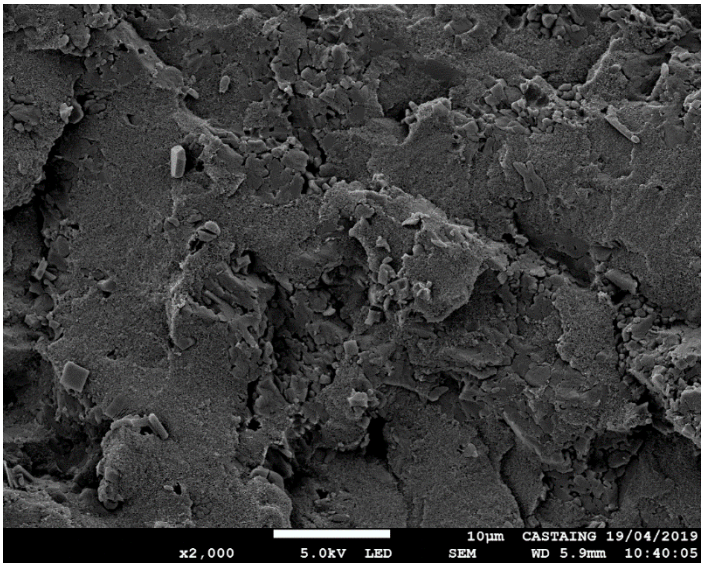

Fig 2.57) SEM image of the cross-section of composite **8c.**

To investigate the effect of the matrix on the SCO properties, variable-temperature optical reflectivity measurements were carried out on the different polymer composite materials (fig 2.58). Due to the strong optical contrast between the HS and LS forms, this technique allows us to acquire the thermally induced SCO curves. We will characterize composites **3a** to **8a**.

Variable temperature optical reflectivity of composite **3a** shows an abrupt and wide hysteresis loop, showing that the cooperativity of the SCO particles has not been affected by their inclusion in the polymer matrix. The slightly increased spin transition temperature is still well within the range needed to avoid overlap with the α-β transition of the copolymer. Composite **6a** shows an abrupt and wide hysteresis loop, showing that the cooperativity of the SCO particles has not been affected by their inclusion in the polymer matrix. This transition closely mirrors the one presented by **3a** as both complexes (**3** and **6**) have a very similar chemical composition. The slightly increased temperature range for the spin transition is still well within the range needed to avoid overlap with the α-β transition of the copolymer. For composite **7a** a more gradual behavior with also a hysteresis loop, which has been pushed towards higher temperature, is observed. The increased temperature range for the spin transition risks overlapping with the α-β transition of the copolymers. Composite **8a** shows a slightly more gradual and wider hysteresis loop compared to that of complex **8**. However this hysteresis loop is still very small when compared to the complexes of the $[Fe(Htrz)_{1+y-x}(trz)_{2-y}(NH_2trz)_x](BF_4)_y \cdot nH_2O$ family. It is interesting to note that, like in complex **8**, there is no run-in effect for composite **8a.**

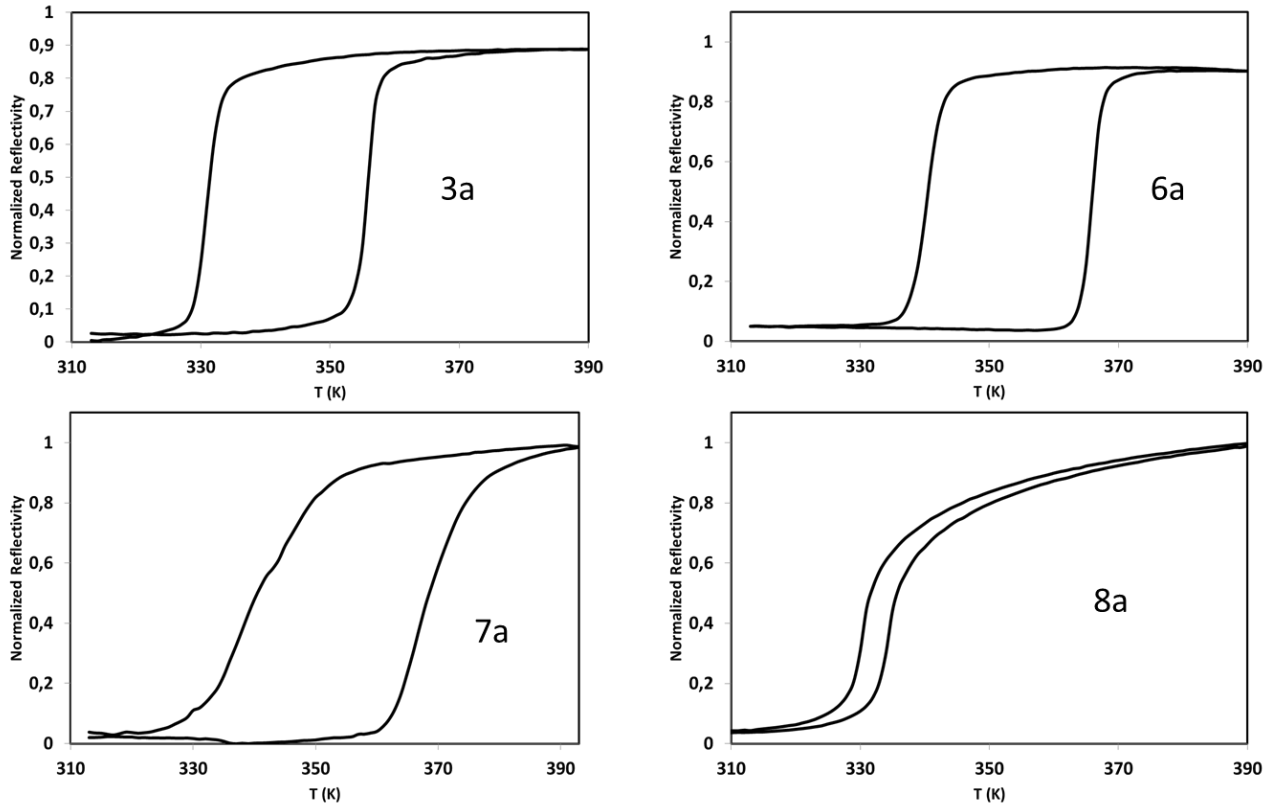

Fig 2.58) Variable temperature optical reflectivity of composites **3a, 6a-8a**.

Table 2.10) Spin transition temperatures of the neat SCO complexes and their corresponding polymer composites obtained by optical reflectivity. (All data correspond to the second thermal cycle. $T_{1/2}\uparrow$ and $T_{1/2}\downarrow$ stand for the transition temperature on heating and cooling respectively. $\Delta T = T_{1/2}\uparrow - T_{1/2}\downarrow$).

	Complex			**Composite**		
Sample	$T_{1/2}\uparrow$(K)	$T_{1/2}\downarrow$(K)	ΔT(K)	$T_{1/2}\uparrow$(K)	$T_{1/2}\downarrow$(K)	ΔT(K)
3	346	331	15	356	331	25
5	338	330	8	340	327	13
6	357	335	22	367	340	27
7	364	344	20	368	342	26
8	336	335	1	335	330	5

As it was already observed for composite **5a**, the SCO hysteresis width in each composite is noticeably increased, in comparison with that of the corresponding neat powder sample. According to theoretical works [58], it is likely that these changes of SCO properties arise from the elastic confinement of the matrix, though other reasons (*e.g.* reduced heat conduction or solvent effects) cannot be excluded either.

Raman spectra was used to detect the α and β crystalline phases in P(VDF-TrFE) [140]. Composites **3a** to **8e** as well as the pure P(VDF-TrFE) 70-30 and 75-25 were analyzed at room temperature. This analysis focuses on the 700-900cm^{-1} spectral range where the P(VDF-TrFE) crystalline phases characteristic markers are. Nevertheless, it should be noted that, compared to the pure copolymers, some of these markers seem to be shifted in the composites.

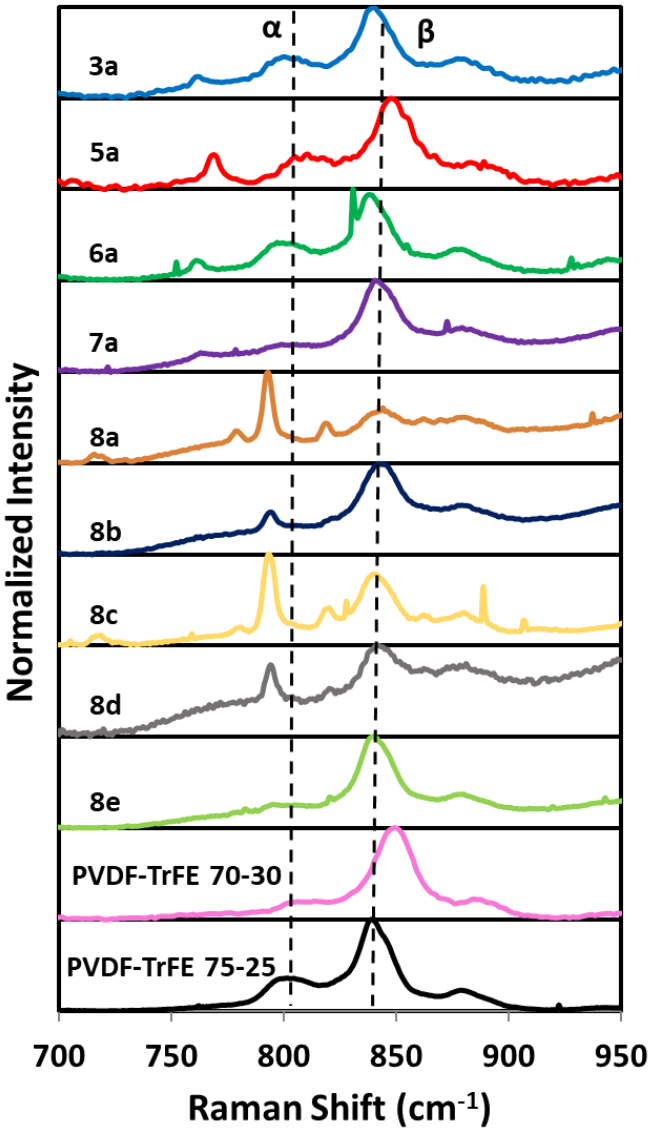

Fig 2.59) Room temperature Raman spectra of the composites and the pure copolymers.

The Raman spectra of the composites were found to be spatially homogenous at the millimeter scale, indicating good dispersion. They consist of the superposition of the spectra of the SCO compound and the P(VDF-TrFE) co-polymers (Fig 2.59). It is well-established that the β phase of the 75-25 PVDF–TrFE matrix can be clearly discerned in the Raman spectrum at 840 cm^{-1} (850 cm^{-1} for the 70–30 copolymer), whereas the signature of the α phase appears at around 800 cm^{-1} [140]. Using these characteristic Raman peaks the proportion of the α and β phases can be approximated in a qualitative manner. The pure polymer with a 75 : 25 monomer ratio appears to be a mixture of the two phases, with a majority of β form. In the case of composites **6a** and **3a** the addition of the microcrystalline particles seems to have no substantial influence on the proportion of the β phase in comparison with the pure polymer. In the case of the other composites, the proportion of the β phase appears even higher than in the pure polymer, close to 100%, suggesting that the introduction of the particles might favor the formation of the β phase.

To ascertain if the concentration of particles modulates the crystallinity of the polymer, room-temperature X-ray diffraction was performed on samples **8a**, **8c**, **8d** and **8e** (fig 2.60). This series of samples were chosen to display the effect of concentration of SCO particles on crystallinity without changing the SCO complex or the copolymer.

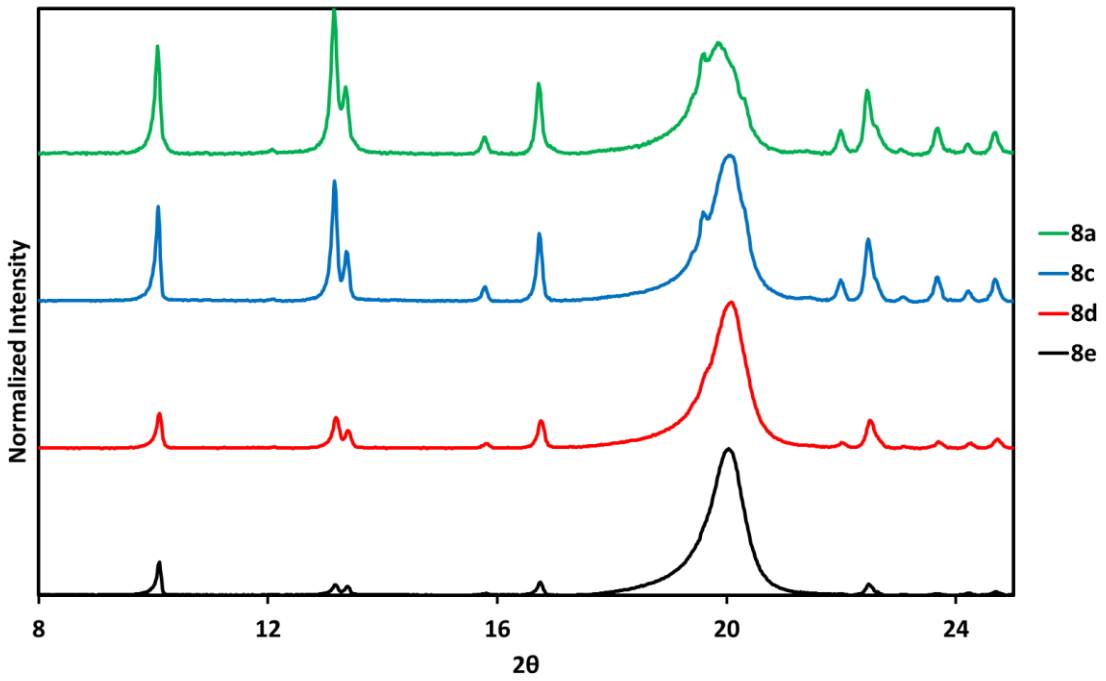

Fig 2.60) Powder X-Ray diffraction of composites **8a**, **8c, 8d** and **8e.**

In this series of composites, we can thus carry out a quantitative analysis of the relative intensities of the marker peaks of the SCO compound (at 2Θ = 15.8°, 16.8° and 19.5°) and that of the β phase of the copolymer (at 2Θ = 20.0°). It turns out that, within the experimental

uncertainty, this ratio is proportional to the nominal load of the SCO particles. This means that these composites have similar crystallinity and contain similar amounts of the β phase.

DSC measurements performed on the different composites allow us to evidence the spin transition, the para–ferroelectric phase transition and melting phenomena in a more quantitative manner (Fig A.2.4 to A.2.11 in Annex). Quantification of the melting and α-β transition allows us to ascertain the crystallinity and β phase proportion. The key result we obtain from this analysis is that for the majority of the samples we were able to achieve a good separation between the spin transition and Curie peaks in the heating mode (Table 2.11). This property is essential, because it allows one to run thermal cycles through the spin transition without affecting the β phase, which would be detrimental for the piezo/ferroelectric properties and thus the sample polarization. We stress that the DSC analysis was performed for the first thermal cycle of the samples. This is necessary because the LS to HS transition in some of the investigated complexes occurs at a slightly higher temperature on the first heating [144].

As already mentioned, the Curie temperature is dependent on the nature of the copolymer. As an example, the DSC thermogram for composite **8b** (with P(VDF-TrFE) 70-30) shows clearly the coexistence of three different separate transitions on the heating curve (fig 2.61). The first peak at 64 °C corresponds to the LS-HS transition, the following at 102 °C corresponds to the Curie Temperature and finally at 150 °C corresponds to the melting point of the polymer matrix. On the cooling process however, while the melting at 136 °C is clearly distinguishable, the Curie and HS-LS transitions overlap between 55 and 64 °C.

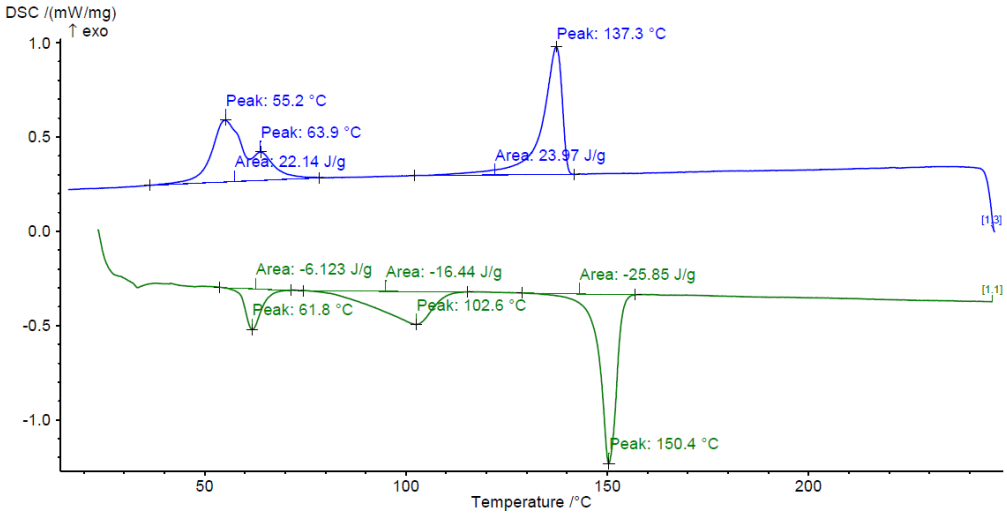

Fig 2.61) DSC thermogram for composite **8b** (heating (green) and cooling (blue)).

The DSC thermogram for composite **8c** (with P(VDF-TrFE) 75-25) shows similarly three clearly different transitions on the heating step (fig 2.62). The first peak at 61 °C corresponds to the LS-HS transition; the following at 121 °C corresponds to the Curie temperature and finally at 148 °C is the melting point of the polymer matrix. Composite **8c** uses P(VDF-TrFE) 75-25 as the

polymer matrix and as a result the Curie temperatures are higher than in the case of **8b.** This is especially interesting in the cooling step as unlike in composite **8b** it becomes possible to differentiate the SCO transition at 53 °C and the Curie transition at 71 °C.

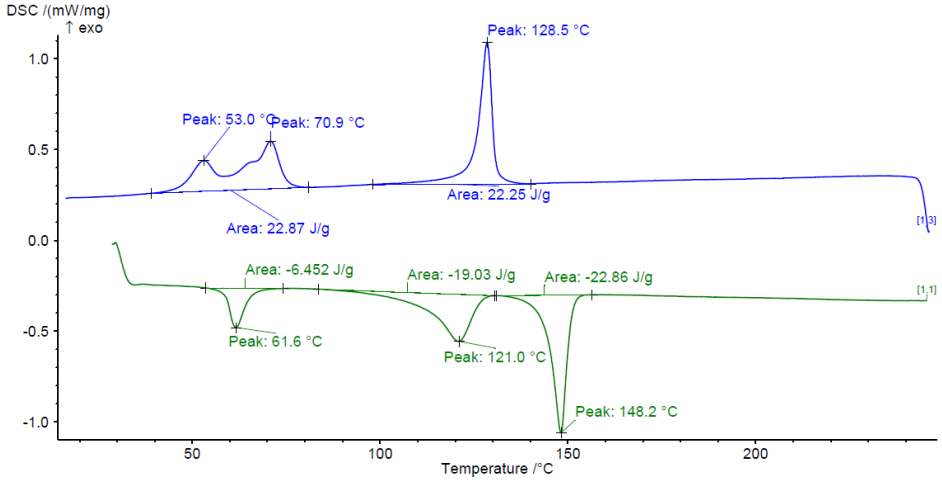

Fig 2.62) DSC thermogram for composite **8c**. Heating (green) and cooling (blue).

Table 2.11) DSC data for the composite and pure polymer samples.

Sample	T_{SCO} (K)		T_{Curie} (K)		$T_{melting}$ (K)		ΔH_{Curie}	$\Delta H_{melting}$	Crystallinity
	Heating, Cooling		Heating, Cooling		Heating, Cooling		(J/g)	(J/g)	(%)
3a	359	326	384	344	422	402	25	29	58
5a	333	317	373	330	423	408	17	28	49
6a	363	326	383	343	422	402	29	32	65
7a	365	334	383	346	422	401	29	32	65
8a	337	325	377	335	425	409	21	34	59
8b	335	328	376	337	423	410	19	34	58
8c	335	326	394	344	421	402	20	30	54
8d	334	326	395	343	422	402	25	36	65
8e	334	327	396	344	422	402	19	33	56
75-25	N/A	N/A	384	348	416	402	11	24	38
70-30	N/A	N/A	378	335	422	402	13	29	46

It is important to remark also that taking an SCO complex with a spin transition temperature below the Curie point of the chosen copolymer does not necessarily ensure the separation of the two phenomena in the composite. The reason for this is that the SCO behaviour may change upon confinement in the polymer matrix and, likewise, the phase stability of the polymer can be affected by the filler. The latter phenomenon can be clearly seen in the case of composite **8a**, whose Curie temperature suffers a very significant downshift with respect to composites **8c–8e**, which have exactly the same chemical composition, but contain a smaller amount of filler. On the other hand, the SCO temperature does not change much in this series of composites, in contrast to the SCO compounds **3–7**, which exhibit a more pronounced matrix effect and, *vice versa*, they have a more pronounced impact on the para/ferroelectric transition temperature as well.

The proportion of the polar β phase in the polymer matrix depends on the experimental conditions and the nature of the filler. It should be noted that the decrease of the TrFE monomer fraction from 30 to 25% leads to the decrease of the proportion of the β phase. The DSC data allows also for an estimation of the crystallinity of the polymer matrix, which is considered proportional to the enthalpy variation measured taking into account both the Curie and melting transitions [145]. Interestingly, the crystallinity of each composite is higher than that of the corresponding pure copolymer in particular for the copolymers, P(VDF–TrFE) 75–25 (Table 2.11). On the other hand, the latent heat associated with the para/ferroelectric transition provides information on the (relative) proportion of the β phase in the different samples. Due to the difficulties in properly determining the baseline of the DSC thermograms, the experimental uncertainty is higher here. Nevertheless, we find values of latent heat around 23 ± 6 J g^{-1} (corrected for the polymer content) (Table 2.6). While the relationship between load and crystallinity so far remained unclear, there is a tendency not only for higher crystallinity, but also for a higher proportion of the β phase in the composites – in particular in samples **6a**, **3a** and **7a**.

2.3.2.6 Electroactive properties of the second generation composite films.

In order to align the ferroelectric domains, the composite samples as well as the pure polymers were poled under a strong electrical field. It should be noted that, depending on the homogeneity of the composite film, the polarization field could cause breakdown of the material. For this reason, for each composite film there is a maximum level of polarization field it can be subjected to and a corresponding piezoelectric coefficient d_{33}.

Poling of the composite samples was undertaken at 293 K with amplitudes ranging from 20 to 50 MV m^{-1}. The resulting piezoelectric coefficient d_{33}, spans from −4.5 to −19.0 pC N^{-1} for the composites. As it can be expected, the piezoelectric coefficient has reduced values with respect to those of the pure polymers (*ca.* –20 pC N^{-1}). This can be attributed to the reduced volume fraction of the polymer as well as to the increasing sample heterogeneity, which leads to the reduction of the maximum polarization field before breakdown occurs (from *ca.* 55 MV m^{-1}

in the pure copolymers to *ca.* 20 MV m^{-1} in some of the composites). Even for a good distribution of small particles, any inclusion of a filler in the polymer will generate inhomogeneities. It is interesting to note that in some cases it was possible to maintain a piezoelectric coefficient that is not far from that of the pure polymer even for particle loads of 15%. On the other hand, the further increase of the load is concomitant with the inevitable decrease of the d_{33} coefficient.

Table 2.12) Polarization conditions for the composite samples.

Composite	**SCO sample**	**Load wt%**	**VDF:TrFE (mol%)**	**d_{33} pCN^{-1}**	**Polarization field (MV m^{-1})**
3a	3	15 %	75-25	-15	39
5a	5	25 %	70-30	-9	24
6a	6	15 %	75-25	-13	27
7a	7	15 %	75-25	-6.3	22
8a	8	33 %	75-25	-4.5	40
8b	8	25 %	70-30	-7.5	18
8c	8	25 %	75-25	-6.5	21
8d	8	15 %	75-25	-15	33
8e	8	5 %	75-25	-19	49
PVDF-TrFE	N/A	N/A	75-25	-19	54
PVDF-TrFE	N/A	N/A	70-30	-20	57

This section will focus on the characterization of the pseudo pyroelectric effect of the SCO@P(VDF-TrFE) composite material. As for the first generation composite films, in order to measure the pyroelectric response of the composite material which should arise naturally from the strong mechanical coupling between the particles and the matrix, a short-circuit setup was used. In this setup, the poled composite film is placed between two electrodes and subjected to thermal cycling, while the electrodes simply measure the electrical response of the material as an electrical current produced by the film.

Much like for the first generation films, it is expected that the volume change associated with the spin transition will have an effect on the polarized piezoelectric matrix, leading to current discharge of the material upon thermal cycling. With this generation of films, we aimed at investigating the versatility of this composite fabrication approach through the series of

samples **3a**–**8e**. In particular, we seek for the possibility of tuning simultaneously the properties of the polymer and the SCO filler – by modulating their composition, concentration and microstructure – in such a way that the pyroelectric effect of P(VDF–TrFE) and the piezoelectric effect due to the SCO appear concomitantly in the composite.

The pyroelectric discharge cycles for composites **3a**-**7a** are shown in Fig 2.63 and Fig 2.64. This series of composites uses the $[Fe(Htrz)_{1+y-x}(trz)_{2-y}(NH_2trz)_x](BF_4)_y \cdot nH_2O$ family of complexes as filler material, analogous to those used in the first generation films. The purpose of this series of composites is to determine possible effects associated to the morphology of the sample, given the wide variety of morphologies of the relatively similar complexes used.

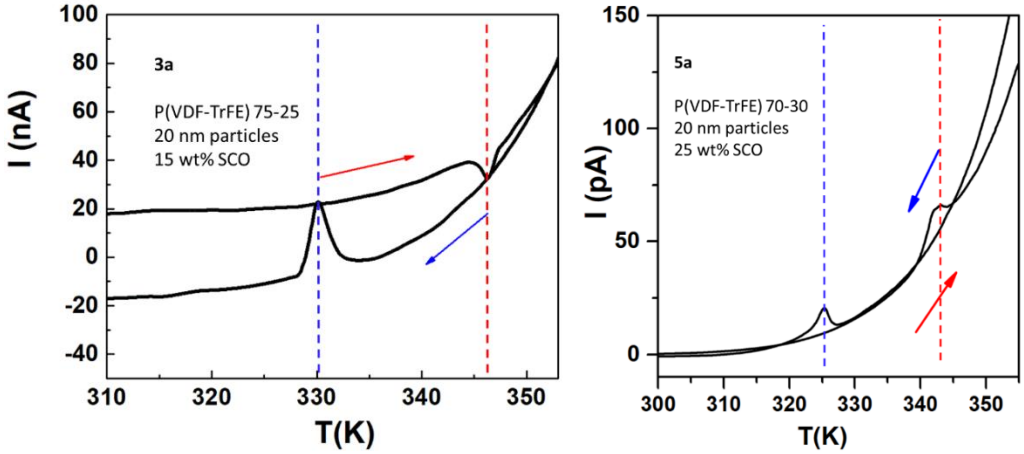

Fig 2.63) Pyroelectric discharge cycle for the polarized samples **3a** and **5a**. The arrows indicate heating and cooling. Dotted lines show the SCO-related discharge peaks for cooling (left) and heating (right)

Composite **7a** (rods) appears singular in this series of samples, as it displays neither pyroelectricity nor SCO-related discharge peaks. Indeed, this sample was particularly difficult to polarize, as it presented substantially lower d_{33} values and had a much lower polarization field tolerance (Table 2.12). In addition, in composite **7a** the spin transition in the first heating cycle strongly overlaps with the Curie transition leading eventually to the destruction of the (weak) polarization achieved. It is possible that the needle-shaped particles are disadvantageous in terms of the resistance to high applied electrical fields, due to the existence of sharp points within the dielectrics, which may lead to localized electrical discharges and treeing. Furthermore, the anisotropy of the particles, which are mostly oriented in plane, is also unfavorable because most of the SCO-related strain is produced perpendicular to the polarization direction. These effects are effectively reduced in composites **3a–6a**, which can be therefore more efficiently polarized and which should provide an increased strain component in the polarization direction. Yet, the use of the P(VDF-TrFE) 70-30 matrix in sample **5a** presents inconvenience due to the lower Curie temperature, which is overlapped with the spin transition, resulting in the (partial) erasing of the polarization during the thermal cycles. This problem was considerably reduced using the P(VDF-TrFE) 75-25 matrix, which allowed us to observe a suitable pyroelectric current (inversion of polarity upon heating and cooling) for samples **6a** and **3a**. In addition, the SCO-related discharge

peaks reach also remarkable amplitudes in these samples, to such an extent that within a restricted range of temperatures around the SCO, the pyroelectric discharge is more than for pure P(VDF-TrFE) 75-25 copolymer (see Fig 2.64 inset).

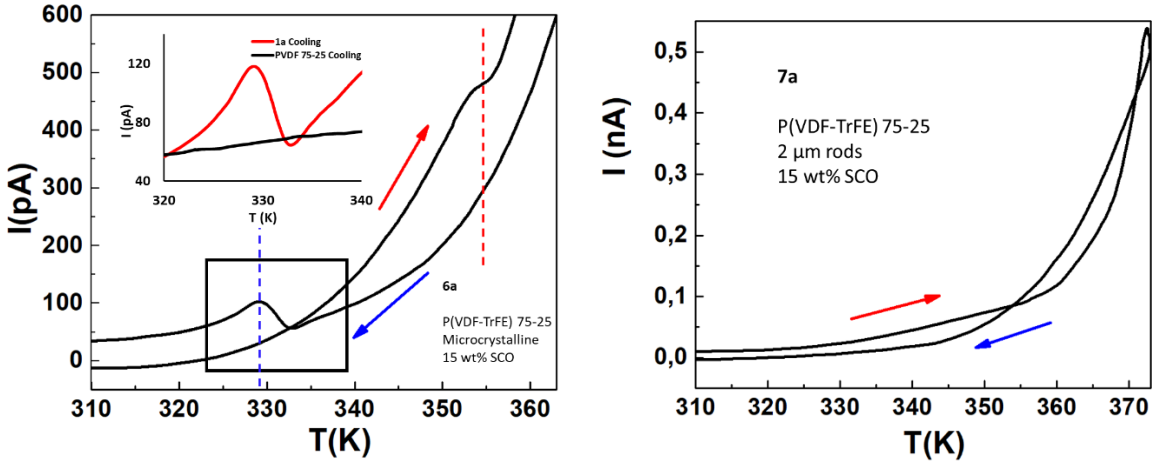

Fig 2.64) Pyroelectric discharge cycle for the polarized samples **6a** and **7a** . The arrows indicate heating and cooling. Dotted lines show the SCO-related discharge peaks for cooling (left) and heating (right). The inset shows a comparison between sample **6a** and pure PVDF–TrFE 75–25 (current corrected for the proportion of polymer).

The pyroelectric discharge cycles for composites **8a-8d** can be found in Fig 2.65 to Fig 2.67. This series of composites uses the same complex batch as filler for every sample, the highly stable and consistent $[Fe(HB(tz)_3)_2]$. The purpose of this series of composites was to evaluate the effect of concentration of the SCO complex in the matrix, as well as prove the versatility of the method by using a complex structurally very different from the $[Fe(Htrz)_{1+y-x}(trz)_{2-y}(NH_2trz)_x](BF_4)_y \cdot nH_2O$ one-dimensional coordination polymers used in the first generation of composites. Indeed, $[Fe(HB(tz)_3)_2]$ as a neutral, molecular complex is significantly different, and the inclusion of this complex in the matrix proves the possibility of using this composite fabrication method with varied different SCO fillers.

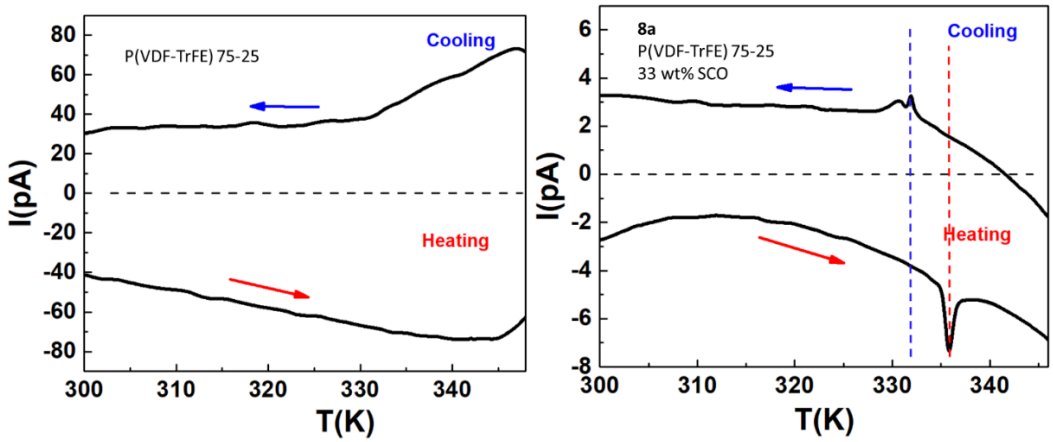

Fig 2.65) Pyroelectric discharge cycle for the polarized P(VDF-TrFE) 75-25 and **8a**.The arrows indicate

heating and cooling. Dotted lines show the SCO-related discharge peaks for cooling (left) and heating (right).

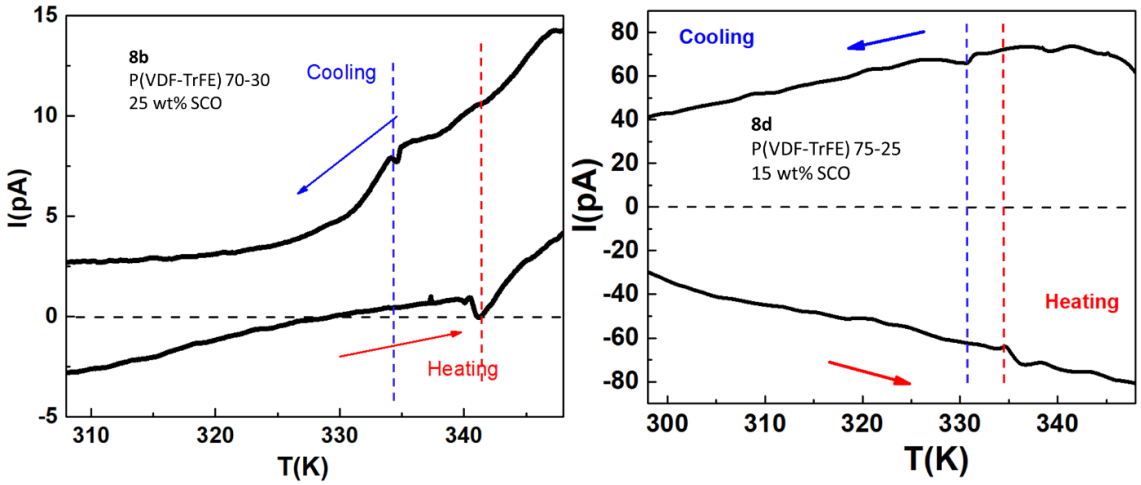

Fig 2.66) Pyroelectric discharge cycle for the composites **8b** and **8d**. The arrows indicate heating and cooling. Dotted lines show the SCO-related discharge peaks for cooling (left) and heating (right).

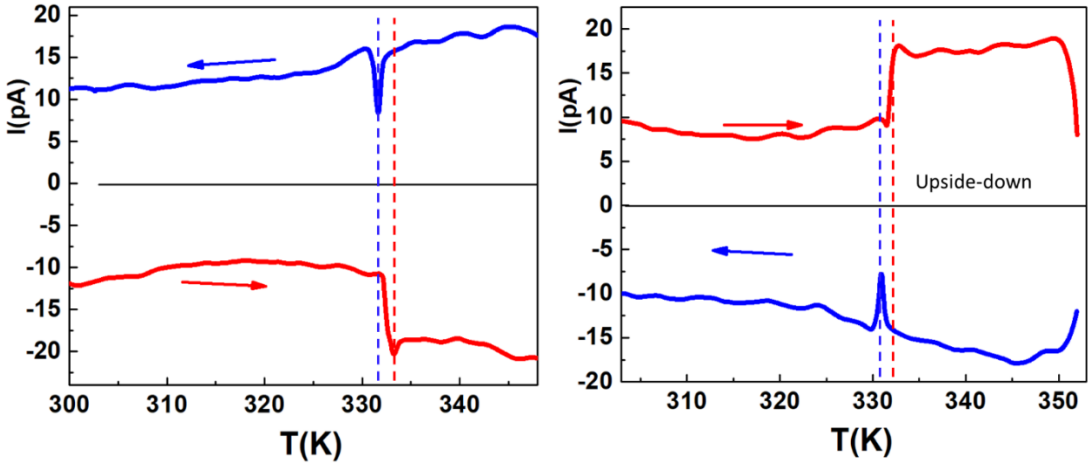

Fig 2.67) Pyroelectric discharge cycle for composite **8c** (P(VDF-TrFE) 75-25 25 wt% SCO) and the same composite turned upside down (right). The arrows indicate heating and cooling. Dotted lines show the SCO-related discharge peaks for cooling (left) and heating (right).

For SCO concentrations of 5% (**8e**) and 15% (**8d**), the pyroelectric current in the composites remains virtually unchanged in comparison with that of the pure polymer matrix. This finding is in agreement with the relatively high piezoelectric coefficients d_{33} of these composites (Table 2.12). In other words, for this concentration range, the piezoelectric properties of the composites correspond very closely to that of the pure polymer. This result proves the successful separation of the temperature regions in which the spin transition and ferro/paraelectric transition occur. In addition to the conventional pyroelectric behavior, a small discharge peak is

also discernible at the spin transition temperature even at relatively low filler concentrations. However, the intensity of these peaks remains weak. These "weakly charged" (< 15%) composites of compound **8** can be therefore considered, from an electrical point of view, nearly equivalent to the pure polymer. At the same time, however, the introduction of the SCO filler gives rise to interesting new, smart functionalities, such as pronounced thermochromism and paramagnetism (in the HS state), which are obviously not present in the neat polymer and which can enlarge therefore the scope of its applications.

As expected, for increasing SCO concentrations (samples **8a–8c**) the discharge peaks associated with the spin transition appear more clearly. However, this increase in the discharge peaks is not linked to a substantial increase of the discharge current at the SCO. Instead, the peaks emerge because the conventional pyroelectric response (*sic* "the baseline") shrinks drastically (Fig 2.68) leading to a much lower electrical yield.

It is interesting to compare the pyroelectric discharge cycles of composites **8b** and **8c**, which were synthesized with the same load (25%), but using the two different copolymers, P(VDF–TrFE) 70–30 and 75–25, respectively. Owing to the better separation between the spin transition temperature and the Curie temperature, sample **8c** exhibits discharge peaks upon spin transition with higher intensity. In addition, one can observe a more characteristic pyroelectric behavior with a clear inversion of the polarity of the pyroelectric current between heating and cooling and also when changing the orientation of the sample. This co-existence of the pyro- and piezoelectric phenomena stems from the very neat separation between the spin transition and Curie temperatures in this sample.

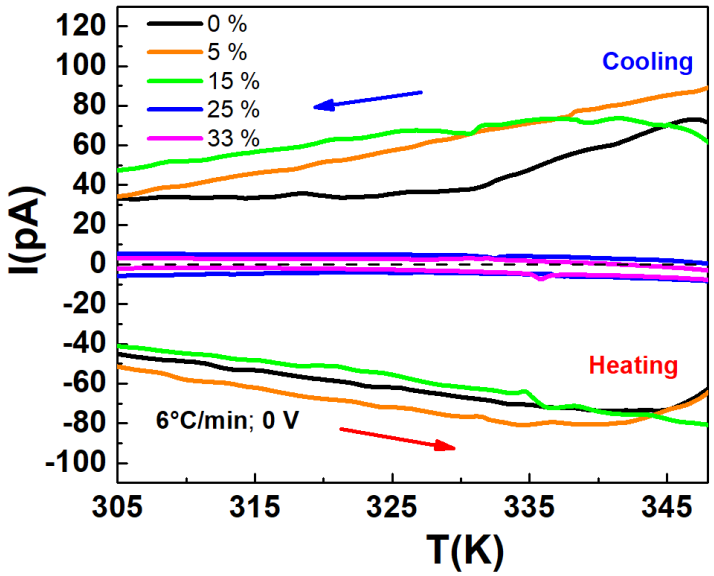

Fig 2.68) Pyroelectric discharge cycle for composites **8a-8e** as well as pure P(VDF-TrFE) 75-25. The legend indicates the concentration of complex **8** on each of the composites. The arrows indicate heating and cooling.

Another important comparison can be made between sample **8b** and the first-generation film **5a** which were made using the same copolymer and the same load (25%), but using two different SCO compounds. There is indeed a striking decrease of the intensity of the SCO-related discharge peaks in **8b**, based on compound $[Fe(HB(tz)_3)_2]$, when compared to **5a**, based on the $[Fe(Htrz)_{1+y-x}(trz)_{2-y}(NH_2trz)_x](BF_4)_y \cdot nH_2O$ chains. We believe that this difference can be attributed primarily to the fact that the volume change for the $[Fe(HB(tz)_3)_2]$ complex upon the spin transition is significantly lower, *ca.* 5% [141] when compared to that of complexes **3–7** with formulae $[Fe(Htrz)_{1+y-x}(trz)_{2-y}(NH_2trz)_x](BF_4)_y \cdot nH_2O$, which present up to 10% volume change [137].

2.4 Conclusion

The main result of this research work was the development of a flexible and reproducible fabrication technique to synthesize SCO@P(VDF-TrFE) composites. These composites retain both the SCO properties of the filler complex and the piezoelectric properties of the matrix. The resulting composite films can be polarized under an electrical field, and the polarized films show a **synergy between the volume change associated with the spin transition and the inherent piezoelectric properties of the matrix, which results in pseudo pyroelectric discharge peaks around the spin transition**.

The use of a wide variety of complexes with different morphologies and concentration as well as the use of different proportions of TrFE in the matrix allowed us to demonstrate that the mechano-electric coupling between a ferroelectric PVDF-TrFE copolymer matrix and spin crossover particles is a generic property. An important result of this work is that by tuning the Curie temperature of the copolymer (*via* the modification of the VDF : TrFE ratio) and the spin transition temperature of the particles we were able to effectively separate these two phenomena and recover thus the pyroelectric property of the neat polymer. Depending on the concentration of the SCO filler, we observed two behaviors. In the low-concentration limit (*ca.* 5–15% – depending on the experimental details), we were able to achieve electromechanical properties in the composites, which are comparable with those of the pure polymer matrix. These composites can be considered as **high performance, multifunctional, smart materials displaying interesting electromechanical, optical and magnetic properties**. On the other hand, in the high-concentration limit (*ca.* 15–33%), the sample polarization becomes increasingly difficult and the electromechanical properties are degraded. Yet, these composites remain useful for their interesting mechanical actuating properties, with the advantage that the mechano-electric coupling between the SCO phenomenon and the matrix gives rise to an additional electrical signal, which may be potentially useful for sensing and control purposes. Interestingly, in some favorable cases, we could even demonstrate an effective **sum up of the pyroelectric response of the polymer and the piezoelectric response** induced by the SCO filler. This result provides prospects for developing composite materials with enhanced thermal–electrical harvesting output.

Overall, these results provide clear proof for the possibility of combining the pyroelectric response of the polymer with the piezoelectric effect arising due to the SCO. Nevertheless, to exploit this combined effect for thermal energy harvesting the following issues will have to be considered. First, a real gain with respect to state-of-the-art pyroelectric harvesters can be expected only for small and slow temperature excursions around the spin transition temperature. Second, the ideal SCO compound should display a relatively abrupt spin transition without hysteresis in the temperature range between *ca.* 30 and 50 °C and an associated large volume change (*ca.* 10%).

The most immediate application of these composites, however, which will be explored in the next section of this research work, is the fabrication of flexible, reproducible and freestanding films that expand and contract upon the SCO. These films could therefore be used in the fabrication of actuating devices that exploit the volume change of the spin transition.

Chapter 3: Spin crossover composite actuators.

Soft robotics is a rapidly growing field of research and concerns flexible and soft materials able to twist, bend, deform themselves to move or to adapt their shape for accomplish specific tasks. This field of robotics has multiple applications in medicine and manufacturing such as: manipulators interacting with objects, robots traversing unpredictable terrain and devices working in close contact with human beings [146]. The developing of smart materials and in particular flexible actuators is crucial for the development of this field as a whole [147,148]. As an example, Fig 3.1 shows a robotic fish where the muscles that direct the caudal fin use soft flexible actuators to imitate the movement of a living fish. In fact, the caudal fin uses an artificial muscle powered by fluid elastomer actuators electrically stimulated.

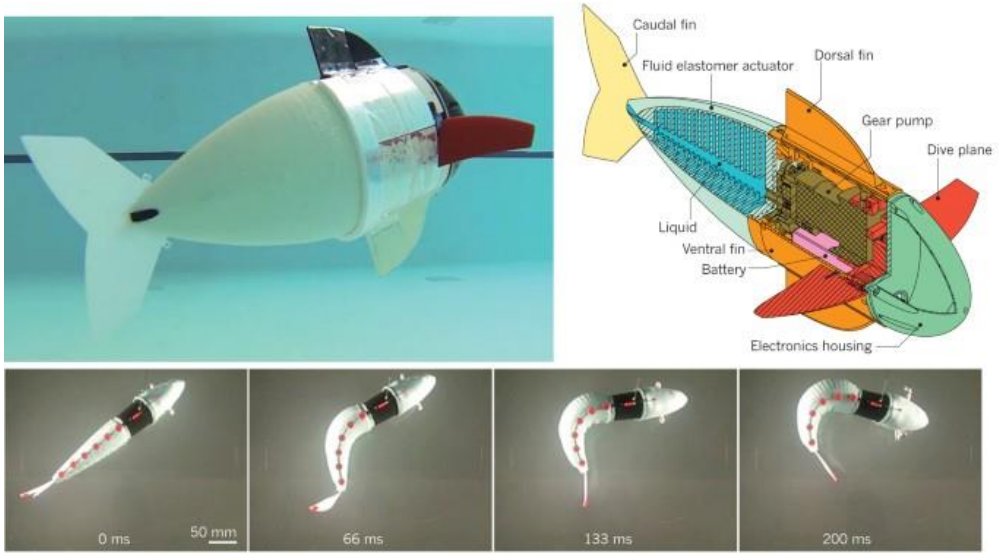

Fig 3.1) Soft robotic fish with fluid elastomer actuators [146].

SCO materials could be of great interest in the development of soft actuators, as they present a highly reversible transition that induces a significant volume change at the molecular level which can be transmitted to a matrix. Indeed, in the previous chapter, one of the key results was the possibility to use SCO materials in combination with polymer matrices to exploit the significant volume change of SCO complexes activating a piezoelectric polymer. We found that, indeed, this volume change is effectively transmitted to the matrix, which in turn shows a mechanical strain.

This volume change can also be exploited for actuation, which is the aim of this chapter. There is a wide variety of materials that have been employed for these applications, and before

delving directly into the subject of SCO composite actuators, an overview of actuating materials for soft actuators will be presented to contextualize our research. This overview will also include the developments of our research group in fabricating SCO actuators.

This chapter will focus on the two main research routes that were explored in this work for the fabrication of actuator devices. The first is the use of additive manufacturing, 3D printing, to reliably and reproducibly fabricate SCO composite actuators with a variety of geometries. This approach of using 3D printing to fabricate moving objects is often called 4D printing. The second approach we used to fabricate SCO composite actuators was solvent casting, which afforded P(VDF-TrFE) conductive bilayers to make **electrically-driven highly-controllable SCO actuators.** To properly operate these devices, a closed-loop controller system was put in place, and the actuation properties of the device were evaluated.

3.1 Materials for soft actuators.

At the core of soft robotics as a technology is the ability to effectively generate an applied force and movement using flexible and versatile materials. In this regard, flexible actuators play a crucial role in the development of soft robotics. Flexible actuators are a category of devices that respond to an external stimulation to produce a reversible shape, size or properties change. This stimulation can be induced by an electric field, temperature variation, humidity change, light irradiation, applied pressure and magnetic field [149]. The main materials used for soft actuation will be presented in table 3.1, along with their main advantages and drawbacks.

The materials needed to fabricate these actuators must present both flexibility and the ability to generate force and movement in a reversible, efficient and controllable manner**. In fact, this concomitant need for softness and force; adaptability and accuracy, is the key challenge of the field.** While there is a multitude of materials that satisfy these criteria, we present three main approaches that have been explored in depth and which represent a significant portion of the materials used for this end. These are electroactive polymers, shape memory materials and fluid-driven materials.

Electroactive polymers (EAPs) are polymeric materials that change their shape and produce movement when exposed to an applied electrical stimulus. They cover a broad range of chemical compositions ranging from natural rubber to piezoelectric PVDF. These materials can be further divided in two groups depending on the type of stimulus: ionic-activated materials and field-activated materials [150]. Among ionic-activated materials are **ionic polymer–metal composites** (IPMCs) which consist of an ion-exchange polymer membrane laminated between two electrodes. Application of a voltage to the material causes the migration of ions within the film to the oppositely charged electrode causing one side of the membrane to swell and the other to contract resulting in a bending motion (Fig 3.2). IPMCs are materials with high actuation strains and low voltage requirements, but are hindered in terms of applicability by the need of a liquid phase for ionic migration.

Table 3.1) Overview of selected families of soft actuators.

Material Family	Stimulus Type	Actuation mechanism	Advantages	Disadvantages	Ref
Dielectric Elastomers	Electrical	Maxwell Stress	Large strain, rapid response	High driven voltage	[151][152]
Ferroelectric Polymer	Electrical	Polarization induced lattice strain	High responding stress	High driven voltage, large hysteresis	[153]
Gel actuators	Electrical	Ion migration and Maxwell forces	High strain	High voltage requirement, low elastic modulus	[154]
Ionic polymer-metal composites (IPMC)	Electrical	Localized ion aggregation	Fast response, large strain, low voltage	Requirement of a liquid interface for ion mobility	[155]
Conducting polymer	Electrical	Redox-induced deformation	High output force, low voltage	Electrolyte requirement. Slow response.	[156]
Carbon materials	Electrical	Electrochemically induced deformation	High mechanical strength, high thermal conductivity	Low strain, poor stretchability	[157]
Liquid crystal polymers	Thermal, electrical or optical	Phase transition between nematic and isotropic phase.	High strain	Slow	[158–160]
Shape-memory polymers	Thermal	Mechanical strain storage after a glass transition.	Large strain. Precise tuning of the actuation.	Transition between states not continuously controllable. Slow	[10]
Photoresponsive LCPs	Optical	Light-induced isomerization	Remote nano and microscale control	Limited thickness due to light absorption	[161]

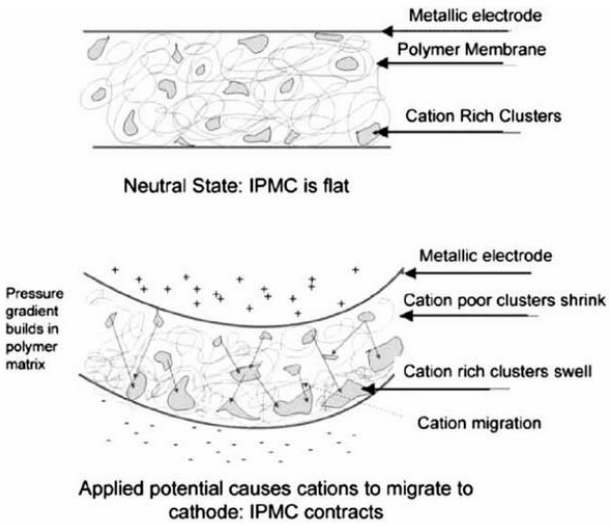

Fig 3.2) IPMC actuator principle[162].

Another commonly used group of ionic-activated EAPs are **ionic polymer gels**. Ionic polymer gels consist of a crosslinked polymer in an electrolyte solution. These materials are hydrogels, network polymers that swell in aqueous solution. These actuators can change in shape and volume by a change in the polymer–liquid interaction. This is often achieved by varying the pH of the aqueous solution [163].

Conductive polymers are another family of ionic-activated EAPs. These actuators perform actuation based on redox chemistry: as these materials undergo oxidation and reduction, their change in chemical properties leads to a significant dimensional change and corresponding deformation. The most commonly used materials in this family are polypyrrole, polyaniline and PEDOT/PSS. These materials often have excellent mechanical performance with very high output force with low voltage requirements, but require an ion-transfer medium and have slow response times [156].

Regarding field-activated EAPs, the most commonly used materials are **dielectric elastomers**. These materials perform actuation based on coulombic interactions between oppositely charged soft electrodes. Rubbers, silicones and polyurethanes and often employed for the fabrication of these dielectric films [151]. Another group of commonly used field-activated EAPs is electrostrictive **ferroelectric polymers**. These materials present a spontaneous electric polarization. Electrostriction and thus actuation result from a change in dipole density of the material when exposed to an electrical field (Fig 3.3). These polymers contain polarized domains that spontaneously arrange under an applied electrical field. The most commonly used material by far in this family is PVDF [153]. Some **liquid crystal polymers** are often used in these kinds of devices, as they present substantial alignment under an applied field, which leads to a shape variation that can be transformed into linear actuation [164]. Notably however, liquid crystal elastomers which respond to heat [159] and optical [160] stimuli have also been developed.

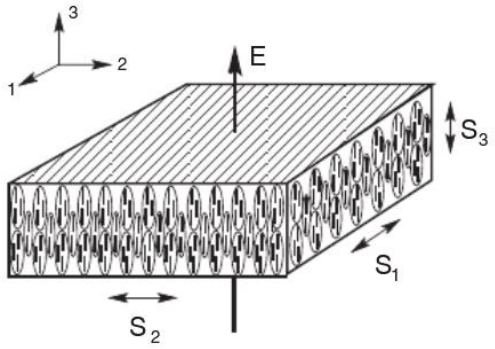

Fig 3.3) Shape variation of a liquid crystal gel film under an applied field [164].

Dielectric and ferroelectric EAPs show very interesting mechanical properties, with dielectric materials showing high actuation strains and response times and ferroelectric polymers showing very high actuation stress. However, both families of materials are hampered by very high voltage requirements that severely limit their usability.

The next family of materials often used in soft robotics applications are shape memory materials. **Shape memory materials** (SMMs) are defined by their ability to recover their original shape from a significant deformation when a particular stimulus is applied [165]. They are generally divided in two main groups: shape memory alloys (SMAs) and shape memory polymers (SMPs).

SMAs have outstanding mechanical properties as actuators. The most commonly used SMAs are NiTi based alloys that are activated by a thermal stimulus to recover from any shape deformation. These alloys, often known as Nitinol, are nickel-titanium alloys, usually in similar proportions, that naturally show both superelestacity and shape memory [166]. They can be used as electrically-driven actuators via the joule effect which translates a current passing through a resistance (in this case the NiTi alloy itself) into heat. These materials show an outstanding mechanical output due to their very high elastic modulus coupled with their relatively high actuation strains. The main drawback of SMAs is that, as a thermally-driven material, their response time is limited by the cooling step, which renders them relatively slow [167]. Fig 3.4 shows a robotic octopus arm fabricated using SMA wires as actuators.

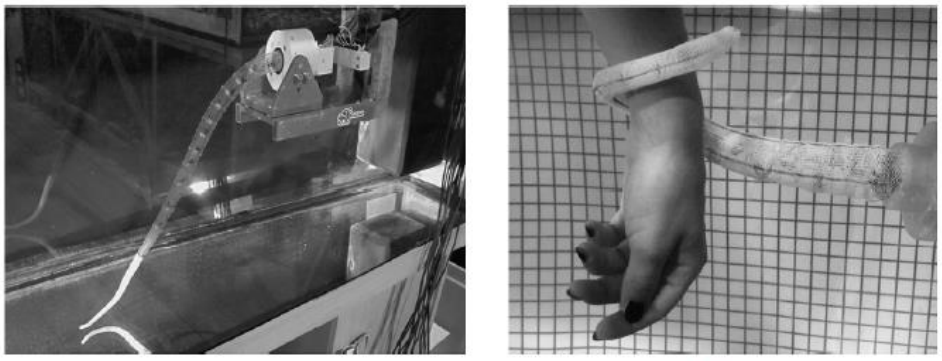

Fig 3.4) Soft robotic octopus arm based on SMA actuators. a) at rest. b) gripping a person's hand [168].

SMPs show a memory effect, which comes from a variety of physical effects, largely depending on the composition of the material. The underlying very large extensibility comes from the intrinsic elasticity of polymeric networks [169]. SMPs undergo a cycle of four steps when performing actuation: deformation, fixing, unloading and recovery. Unlike materials such as rubber, which do not present a memory effect when exposed to such a cycle, there is a fixing capacity in SMPs. This means that unlike rubbery polymers, the SMP does not naturally return to its original shape after unloading and a thermal recovery step is necessary, hence the origin of the actuation (Fig 3.5). Recently, thermally driven reversible 2-way SMPs have been developed that allow these materials to overcome this drawback. They are however relatively rare [149].

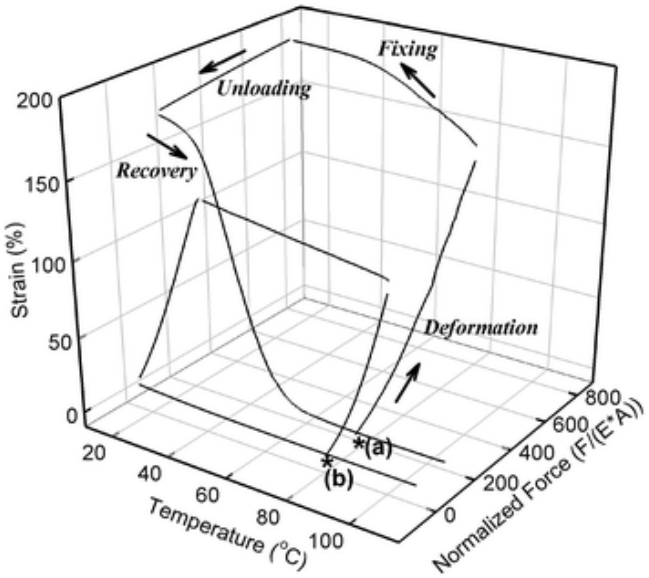

Fig 3.5) 3-D plot of the shape-memory cycle for (a) a shape-memory polymer and (b) natural rubber. The star indicates the start of the experiment [169].

Not all SMPs however are thermally activated. Recently, a new generation of reversible 2-way memory shape materials has been developed that can perform actuation in a reversible manner when activated via cyclic stimulation with UV light [170]. These are composite polymer systems, using light-sensitive materials in a cross-linked polymer matrix. As an example, Fig 3.6 shows a UV activated SMP gripper. The material is cut in the shape of a cross and bent in a shaping process to fabricate a gripper; this gripper is then reversibly actuated with a UV light stimulus.

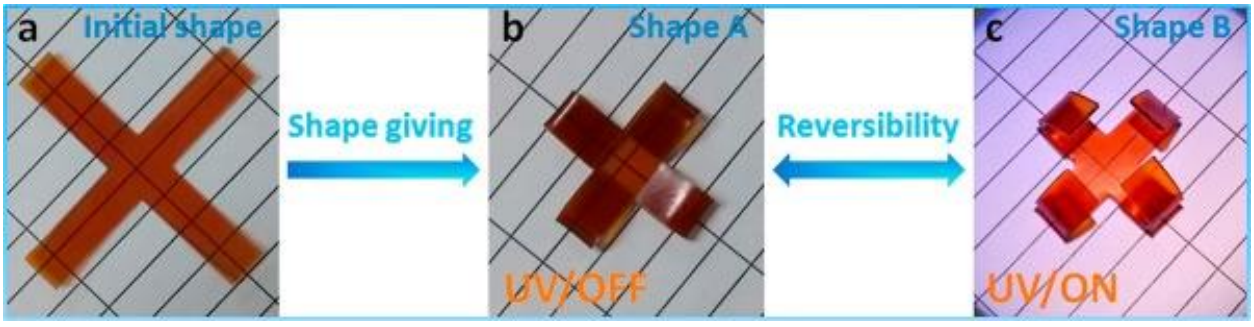

Fig 3.6) UV-activated SMP flexible mechanical gripper.

The next family of actuators we will explore are **Fluid-driven soft actuators**. Fluid-driven soft actuators are attractive in the field of soft robotics as they often simplify design and are highly compatible with humans, allowing for applications in which these devices are in close contact with human beings, such as biomedical applications [171]. They work by the displacement of pressurized fluids, allowing for highly controllable and reversible shape changes in the material. Pneumatic actuators are perhaps the most commonly employed actuators in this family.

The materials used for fluid-driven actuators are most commonly soft elastomers, such as silicones. PDMS is a flagship material in this regard. Silicones can be readily modified or adapted at the surface level to confer new properties to the material such as compatibility or adhesion to specific substrates, which makes them versatile and adaptable for robotics applications [172].

These actuators rely on pressurized fluids, and the choice of fluid plays a crucial role on the properties of the actuator. Liquids are attractive for the generation of significant force at the cost of increased weight and viscosity. Gases are lightweight and have low viscosity, but are also compressible and require more sophisticated control and sensory feedback [171]. Fig 3.7 presents a fluid driven pneumatic actuator, this actuator imitates the human muscle, performing a contraction/expansion cycle with an agonist/antagonist pair to reversibly move a skeleton arm.

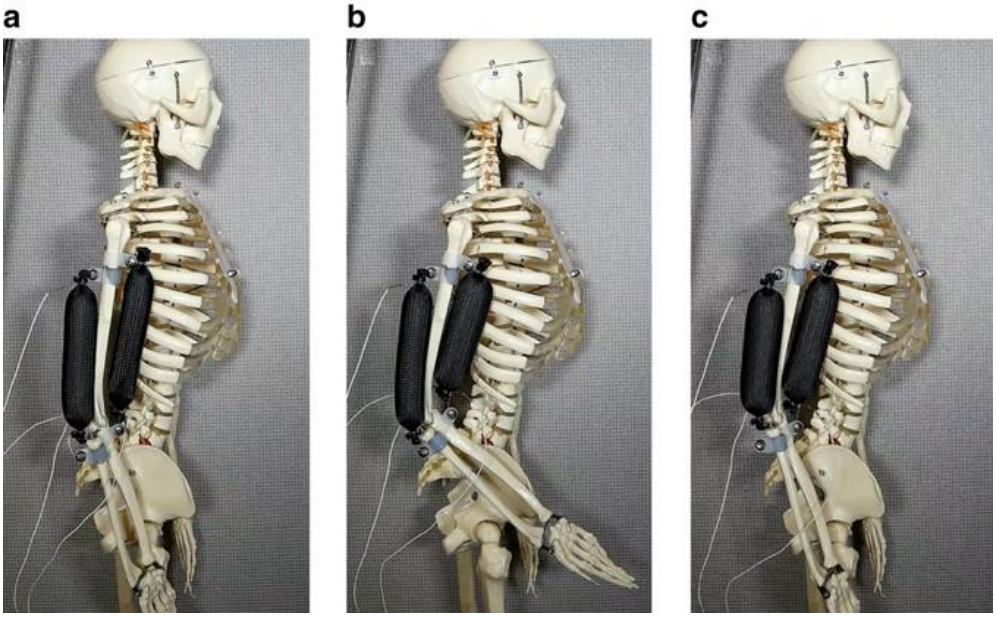

Fig 3.7) Fluid-driven actuators operating as an agonist/antagonist pair to move a skeleton model [173].

Each of these materials present their different advantages and disadvantages, such as the use of intense electrical fields for EAPs or the use of pressure generators to operate fluid-driven actuators. New materials with their own set of advantages and disadvantages could open up the

possibility for novel applications, especially in a field with hyper-specialized applications such as soft-robotics. Thus, spin crossover materials present a mostly unexplored alternative that opens the opportunity for novel applications.

3.2 Macroscopic spin crossover soft actuators.

Spin crossover materials are of interest in the subject of soft actuators because of their reversible phase transition, which can be activated from a series of different stimuli and which leads to a change in physical properties, but most importantly for these applications, a volume change. SCO complexes have a volume change upon spin transition up to 15% of the unit cell. In Fig 3.8, we compare the properties of SCO materials as actuators in comparison with other commonly used materials, showing that SCO materials are competitively placed, presenting an important strain for their high stiffness.

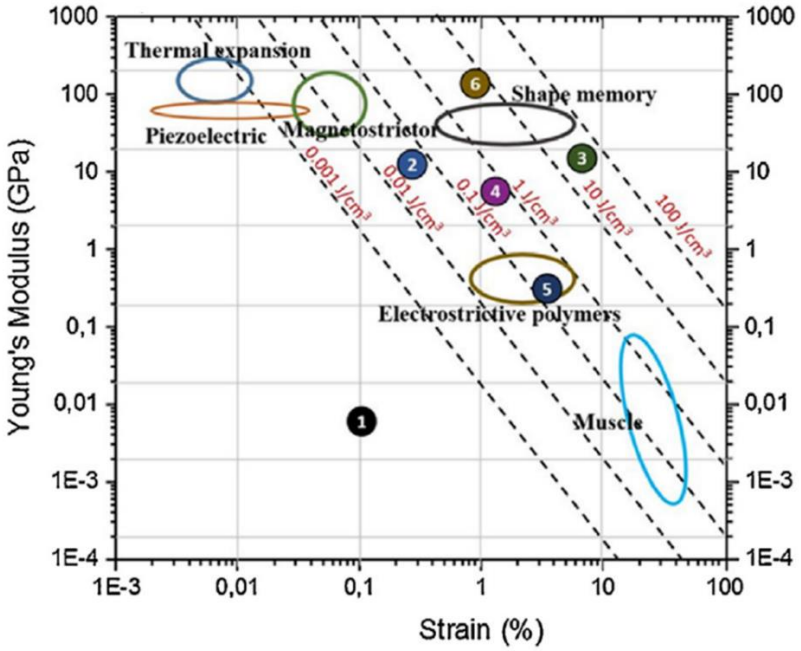

Fig 3.8) Young's modulus versus linear strain plot for selected actuation material families [7]. The contours of equal volumetric work density (in units of J cm^{-3}) are also shown by dashed lines. Encircled numbers represent compounds: (1) ruthenium sulfoxide-polymer composite [174], (2) diarylethene single crystal [175],(3) $Fe(pyrazine)[Pt(CN)_4]$ single crystal [176], (4) $\{Fe(3\text{-}CNpy)[Au(CN)_2]_2\}\cdot 2/3H_2O$ single crystal [11], (5) $[Co(NH_3)_5(NO_2)]Cl(NO_3)$ single crystal [177], (6) VO_2 single crystal [178].

In order to amplify and exploit the volume change of SCO materials, a bilayer structure is often used. **In a bilayer system, a difference in volume expansion between the two layers causes the system to deform and bend, which translates into a mechanical motion**. The active layer is thus the layer with higher strain along the beam axis, in our case the layer with SCO properties, while the inactive layer is the layer with lower strain, one without any SCO material (Fig 3.9).

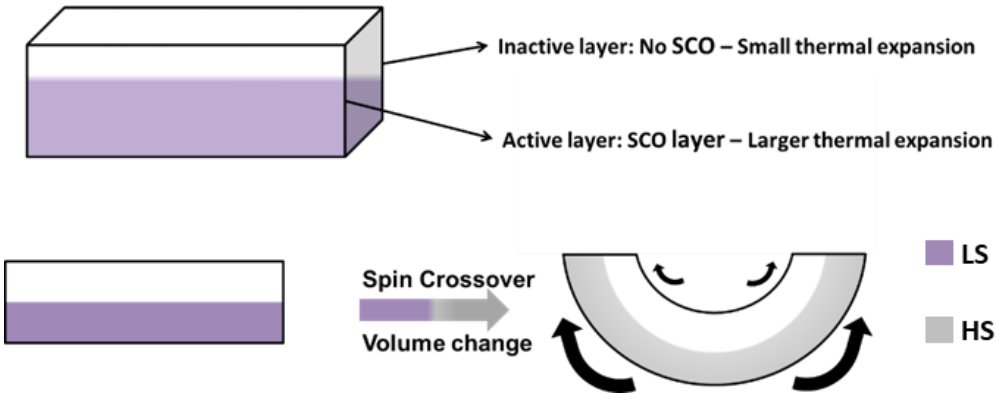

Fig 3.9) Schematic representation of a SCO bilayer material (up) and the bilayer principle for actuation (down).

Spin crossover devices that employ this actuation principle have already been developed by our research group. The first example was developed by Shepherd et al. It is an actuator based on a single crystal of {Fe(3-CNpy)[$Au(CN)_2]_2$} covered by an aluminum layer [11], which serves as both proof of concept and efficiency benchmark, by showing the mechanical potential of an actuator with an active layer composed of pure SCO material. This bilayer actuator undergoes a thermally-triggered spin transition which is then translated to a bending motion (Fig 3.10 up). The device developed by Gural'skiy et al is the first to use the composite approach and the first to perform electrically-controlled actuation via the Joule effect [179]. In this work, [Fe(trz)(H-$trz)_2$](BF_4) is dispersed in a PMMA polymer matrix as the active SCO layer. The inactive layer is a coating of a commercial silver paint, which serves also to transport electricity through the system for joule heating of the actuator, which triggers the spin transition, and thus the movement of the system (Fig 3.10 down).

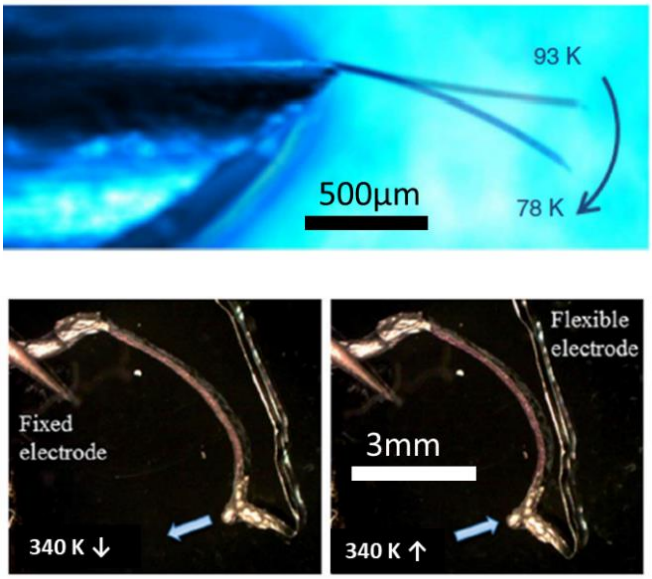

Fig 3.10) SCO bilayer actuators [11,179]. SCO Crystal/Aluminum bilayer (up) and PMMA thermal electromechanical actuator (down).

This chapter will describe the process to fabricate a new generation of SCO actuators. Usability at the macro scale, robustness, controllability and the ability to lift a charge are the main objectives of these new fabrication procedures.

Starting from the results of our research group, the objective was to go further on the fabrication and the application of such macroscopic actuator devices incorporating SCO molecules. During the development of this work, there were two main research lines for the fabrication of these composite materials. The first was the use of a high-technology, high-precision methodology, namely stereolitographic 3D printing, to fabricate bilayer actuators. The second approach was the use of highly-versatile, more artisanal, but generic casting methods to fabricate composite bilayer actuators.

The next part will thus focus on the development of stereolithographic fabrication techniques to print SCO bilayer composites. The mechanical characterization of the resulting devices will take a central role in this regard. The last part will focus on the use of 'classical' casting techniques to fabricate polymeric composite bilayers, and the control systems developed to reliably operate these devices.

3.3 3D Printing of Spin crossover actuator devices

The use of 3D printing techniques to fabricate SCO actuators opens up the possibility to reliably and reproducibly fabricate actuators with a completely controllable architecture, giving us complete control over every aspect of the device morphology. This method uses already-existing 3D printing techniques and the challenge consists in adequately incorporating SCO materials into the process and tuning the methodology to the new composition to obtain appropriate results.

This section will begin with a brief introduction to 3D printing techniques [180], in particular the stereolithographic method used in this work. Afterwards we will detail the process needed to adapt the methodology to SCO composites. Finally, we will characterize the printed materials and devices, with a focus on the actuation properties.

3.3.1 Stereolitographic 3D Printing

3D printing, also often called additive manufacturing, refers to a series of fabrication methods, which use computer-controlled devices to fabricate 3D objects via layer-by-layer addition of material. It is often defined in comparison to classical or 'subtractive' manufacturing in which 3D objects are fabricated via subtraction of material from a block of starting material [180].

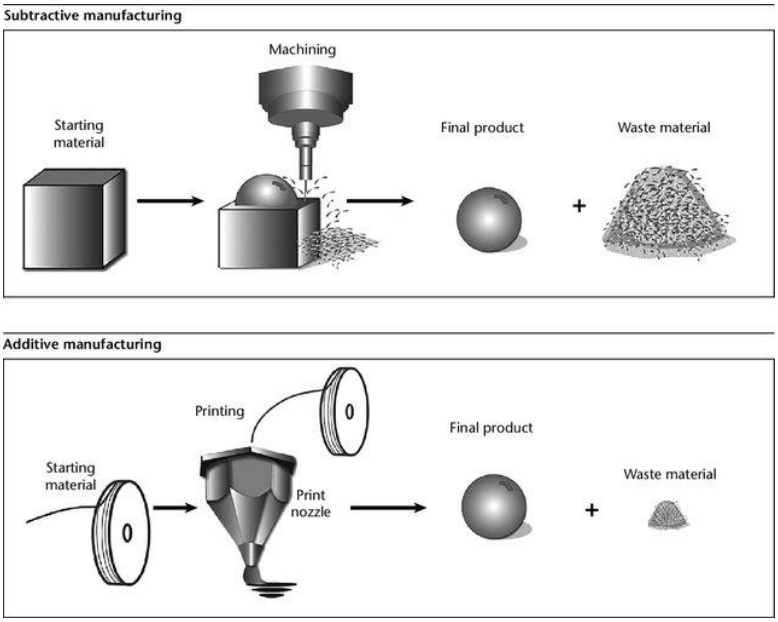

Fig 3.11) Schematic comparison of subtractive manufacturing (up) and additive manufacturing (down) [180].

3D Printing techniques have already been integrated into industrial processes for a variety of applications and materials, from the fabrication of precision mechanical equipment, orthopedic implants to jewelry and dentistry. In this work, we will focus on a specific fabrication technique, stereolithographic printing (SLA), which uses UV-sensitive resins to control the fabrication of the printed object (Fig 3.12).

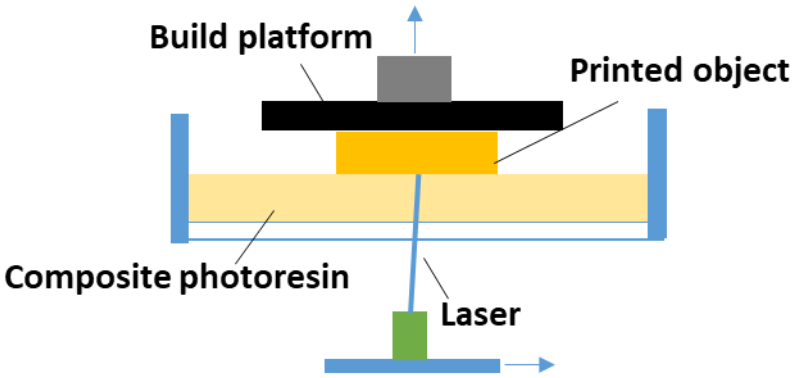

Fig 3.12) Schematic illustration of a stereolithographic 3D printing (SLA) setup.

In this experimental setup, the base printing material is a polymeric resin, DWS DS3000. The resin, which is normally liquid, becomes solid once it undergoes cross-linking, binding the polymeric chains together irreversibly via covalent bonds. Crosslinking is triggered by excitation with a 405 nm laser.

The liquid resin material is poured into a container vat, and a metallic build platform plunges into the resin vat, never touching the bottom of the vat. The laser then follows a pattern

given to it by the program, crosslinking this layer of DS3000 resin to its solid form. In this manner, the first layer of the printed object is now solidified under the desired geometry. The build platform then moves upwards, letting more liquid resin now take the place between the newly printed layer and the bottom of the vat. Once more, the laser crosslinks a layer on top of the previously printed layer, and this is how a 3D object starts to be printed on the build platform via layer-by-layer crosslinking.

3.3.2 4D Printing

Researchers developing new 3D printing technologies have coined the term 4D printing for the fabrication of 3D structures via additive manufacturing, which can perform a movement over time under a certain stimulus [181]. In this sense, it is 4D Printing as it pertains to 3D printed structures with a fourth dimension: the temporal component. Fig 3.13 shows a 4D printed linear structure using a multimaterial system containing a hydrophilic polymer. When activated, the structure bends and turns into a 3-dimensional cubic outline.

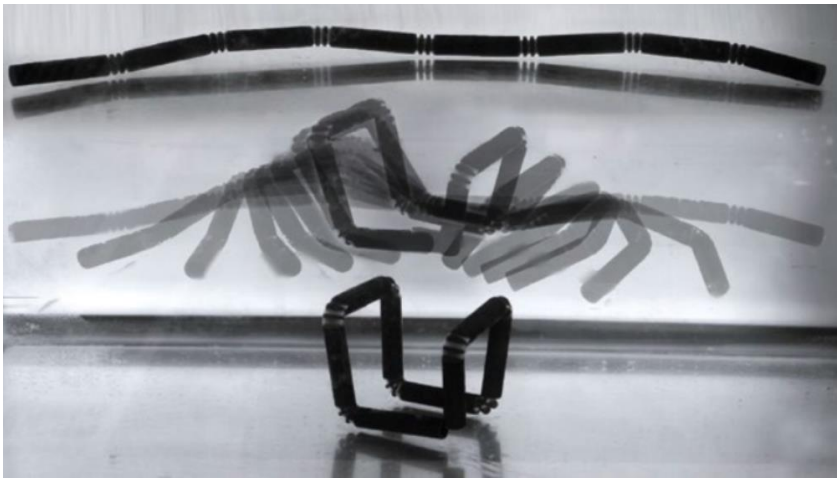

Fig 3.13) 4D Printed structure, which changes shape in response to an external stimulus [181].

Among the different materials used for 4D printing, shape memory polymers, liquid crystal elastomers and hydrogels have been the most popular. The envisioned applications of 4D printing comprise smart valves, grippers, drug delivery systems, self-healing and adaptive structures, soft robots and so forth. The composite approach has been widely used in these systems as it allows to impart new properties onto the polymeric systems often used for printing application.

The challenge thus becomes to adapt the existing printing protocols to the newly developed composite materials to achieve high levels of precision and resolution. We have a limited number of printing resins, which are compatible with our fabrication method, so the adaptation and optimization of the existing protocols becomes essential to achieve the desired results.

3.3.3 4D Printing with Spin Crossover Composites

With the end goal of successfully printing an SCO bilayer actuator, a protocol for effectively integrating the SCO complex into the matrix had to be developed. Once a resin-SCO composite system was successfully developed, the next step was to find a correct annealing procedure to print monomaterial 3D SCO objects, and finally, to further tune this procedure to fabricate 4D printed SCO bilayer actuators, which would then be characterized. Each of these research steps will be detailed before finally finishing this section with the characterization of the 4D printed SCO actuators.

3.3.3.1 Choice of the Spin crossover complex for 4D printable composites

The printing technique of choice for this study uses DWS DS3000 biocompatible resin as printing material. This resin, when cross-linked, presents the highest Young's modulus of the set of compatible printing resins that we had access to for our printing setup. This means that objects printed with DS3000 will be more rigid and exert higher force, which is ideal for an actuator. However this resin loses much of its mechanical properties at high temperatures, making it necessary to incorporate SCO systems with spin transition temperatures closer to room temperature in order to retain the attractive mechanical properties throughout the actuation process.

The SCO complex of choice for this study is $[Fe(NH_2trz)_3]SO_4$ (**9**) which belongs to the 1D triazole chain family (see Fig 2.11). This complex was chosen due to its relatively low SCO temperature and its stable thermal cycling. Practical considerations also played a crucial role in the choice of SCO complex. Due to the fact that very large amounts of material are used during the production of the composite (*ca*. 5 g of pure SCO solid for each experiment), it is necessary to choose a complex with a straightforward and highly reproducible synthesis, which can be readily scaled up. The complex, synthesized according to the procedure developed by Lavrenova et al [182], presents slightly different SCO properties (see hereafter).

$[Fe(NH_2trz)]SO_4$ (**9**) was prepared using the following method: a solution of 6 g of $FeSO_4 \cdot 7H_2O$ (21.6 mmol) in 12 ml of H_2O was added to 5,46 g of 1,2,4-4-NH_2-triazole (65 mmol) in 12 mL of H_2O. The resulting pink solution was stirred during 36 hours and the pink formed precipitate was purified by three successive ethanol washing/centrifugation cycles. Elemental analyses calculated for $Fe(NH_2trz)SO_4 \cdot 1H_2O$ ($C_6H_{14}N_{12}SO_5Fe$): C, 17.07; H, 3.32; N, 39.82%, found: C, 17.12; H, 2.60; N, 39.78% (≈ 80% yield).

3.3.3.2 Characterization of the Spin crossover complex for 3D printing

TEM image of the complex (Fig 3.14) reveals a series of microcrystalline rods with length ranging from 300 nm to 2 µm. The wide size distribution of the objects is as expected from a synthesis with no control over either the nucleation or the growth process. It is interesting to note that regardless of the size of the objects, they retain their anisotropy, suggesting the possibility of observing anisotropic effects in the actuation process.

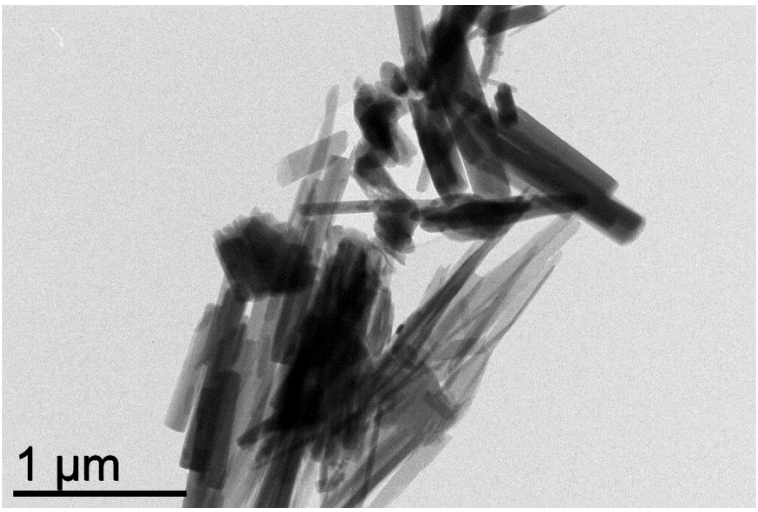

Fig 3.14) TEM image of microcrystalline sample **9** used in the fabrication of the SCO@DS3000 composite resin.

Variable temperature optical reflectivity measurements of complex **9** show a 10 K hysteresis loop centered around 335 K (second thermal cycle since the first cycle presents a run-in effect modifying irreversibly the transition temperature). This hysteresis loop is slightly narrower than the one reported by Lavrenova [182] for the same complex. This could be attributed to a different crystalline morphology as a result of the slightly different synthesis conditions. It is important to note, however, that by our synthetic procedure we obtained each time the same SCO properties, even as we scaled up the synthesis, meaning that this methodology allows for high reproducibility of the complex across multiple samples.

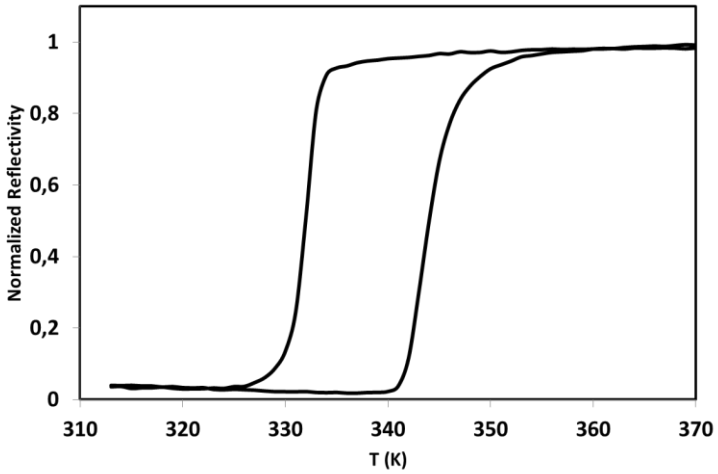

Fig 3.15) Optical reflectivity of **9** on heating and cooling (second thermal cycle).

With the choice of SCO complex clear, the next step becomes to tune the composition and preparation of the SCO(**9**)@DS3000 composite resin and later on to appropriately tune the laser crosslinking conditions to obtain appropriate 4D printed spin crossover objects.

3.3.3.3 Optimization of 4D printing conditions

The technique of choice for the fabrication of the 3D printed SCO objects was single-photon absorption stereolithographic methodology (SLA), based on the photopolymerization of a resin [183]. This technique has been used for the direct laser fabrication of 2D and 3D architectures (scalable up to 500 cm^3) with micrometric feature resolution. The effective polymerization depth in the material allows to easily write in both thick (maximum-tested 100 µm) and thin (minimum-tested 10 µm) layers as well as to realize 3D architectures including true freestanding structures without the need of sacrificial supports.

The DWS 029D printer was used in our study. The SLA setup consists of galvanometric mirrors, which move the laser beam (20 µm diameter) along the x and y directions with a maximum writing speed of 6400 mm/s. The sample holder and the tank are mounted on a z-axis moving stage, which can ensure a minimum layer thickness of 10 µm. The maximum printed object volume is 15 (x) × 15 (y) × 10 (z) cm^3. In order to avoid sticking the printed object to the surface of the vat, the bottom of the vat is covered by PDMS, which inhibits the crosslinking of the resin. All the structures produced in this work were obtained layer-by-layer using a raster scan filling procedure. Each layer in the z axis has a set thickness defined as the z-slicing distance. These layers are then fabricated by sweeping the target writing area with the laser in a pattern composed of parallel lines, the distance between these lines is the hatching distance. The shorter the z-slicing and the hatching distances, the higher the resolution of the printed object, but the printing time becomes longer. Once the printing procedure is finished, and in order to remove the unexposed materials, the samples are developed in an isopropanol bath under sonication for 15 minutes.

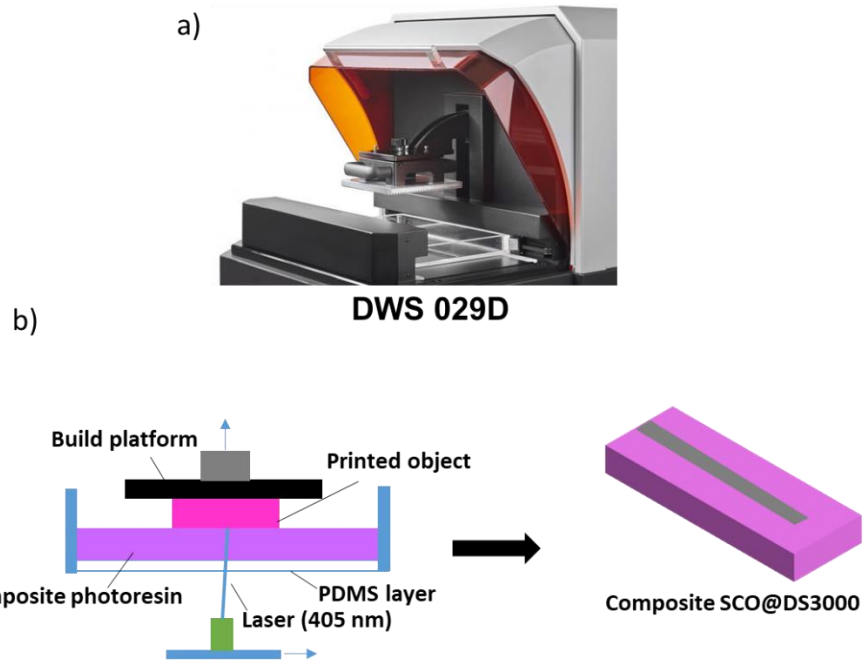

Fig 3.16) a) DWS 029D SLA 3D-printer. b) SLA printing process of the SCO(**9**)@DS3000 objects.

The first composites used for the printing essays were prepared by mechanical mixing of 0.5 g of complex **9** with 4.5 g of liquid DS3000 resin by mortar and pestle to eliminate aggregates of the SCO powder and ensure dispersion of the particles in the resin. The resulting composite liquid resin, however, was highly inhomogeneous, with aggregates clearly visible to the naked eye. 3D printed objects were fabricated with this composite resin (10 wt% SCO in DS3000). The resulting printed 2D springs (Fig 3.17) showed clear thermochromism, indicating that the SCO complexes kept their spin transition, but also show poor dispersion, which is not a desirable trait for the development of actuators.

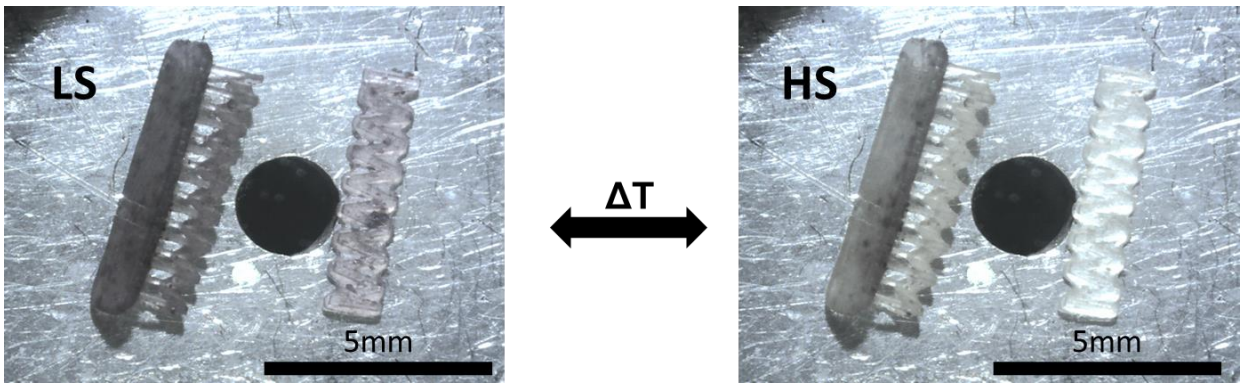

Fig 3.17) SCO(**9**)@DS3000 (10 wt% SCO) printed 2D springs prepared by manual mixing. Low spin (left) and High spin (right).

In order to obtain a homogeneous dispersion, the spin crossover complex (up to 20 wt%) was mixed and homogenised with the DS3000 resin during 30 minutes using a handheld homogenizer. This allows us to obtain a homogeneous resin even when significantly increasing the proportion of complex **9** in the composite. The optimized composite resin SCO(**9**)@DS3000 contains 15 wt% of SCO.

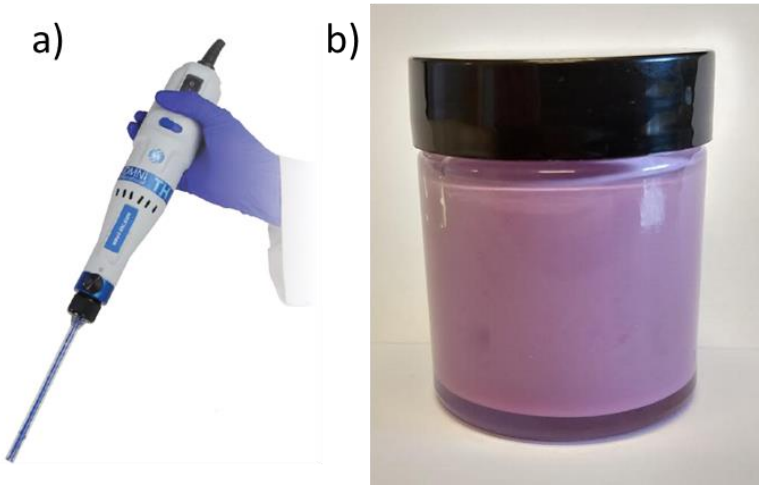

Fig 3.18) a) Handheld Homogenizer. b) Homogeneous SCO(**9**)@DS3000 composite resin (15 wt% SCO).

Using this homogeneous resin, monolithic SCO(**9**)@DS3000 objects with varied morphologies were successfully printed. These objects were printed with 5800 mm/s writing

speed, z-slicing set at 30 µm/layer and a hatching of 30 µm to avoid overexposure and reduce the overall fabrication time (15 min for a 1 mm thick pattern). The printed objects retain the thermochromic characteristic of SCO complexes, showing that the complex retains its properties even when finely and homogeneously dispersed. Using this procedure, 2D and 3D shapes (square, triangle, spring, dog bone and bowtie for tensile stage analysis, etc.) were printed with various thicknesses (from 100 to 1000 µm) and sizes (up to 3 cm long). The most complex 3D structures we fabricated are helical springs of 6.6 mm length, 4.2 mm diameter, 300 µm wire diameter, pitch size of 800 µm and coil angle of 18 degrees. These springs were fabricated with supporting bars of 500 µm, which were eventually removed. Clearly, 3D printing allows us to obtain SCO materials with shapes, which would be extremely difficult, if not impossible, to obtain by other fabrication methods (Fig 3.19).

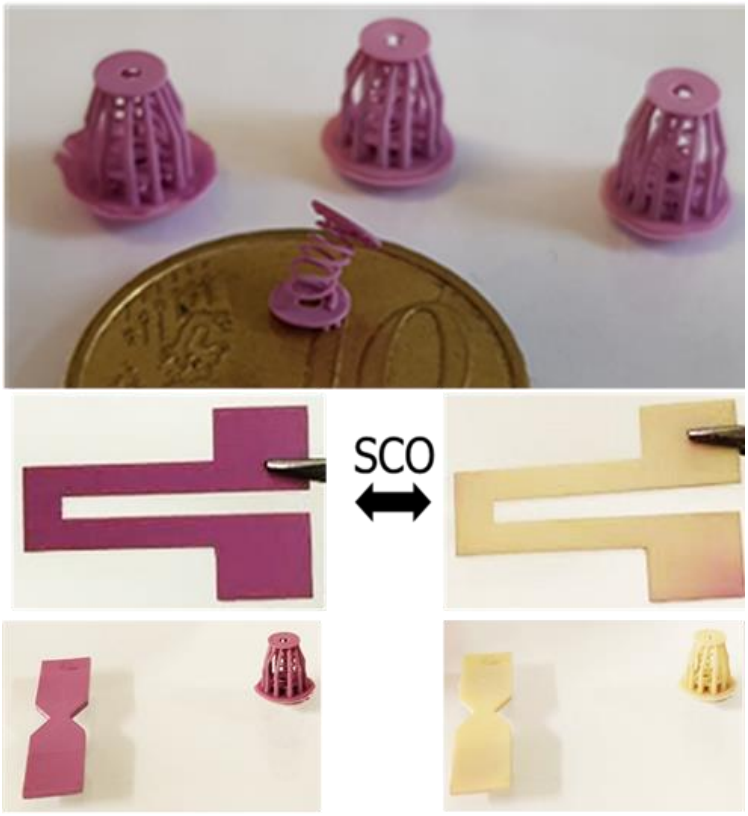

Fig 3.19) 3D printed SCO(**9**)@DS3000 (15 wt% SCO) composites. Reversible color change upon heating above 80°C due to the spin transition.

The 3D printed springs showed almost negligible strain, barring their use as standalone actuators, so it was necessary to develop a new protocol to appropriately exploit and amplify the volume change of SCO complexes. We went with a bilayer approach, as used earlier in other SCO actuators [11,179]. In order to try to increase the effect of the spin transition, a homogeneous composite resin was prepared at a higher concentration of SCO: 20 wt%.

We fabricated a 3 cm long bimorph architecture consisting of two stacks: the pure DS3000 polymer and the SCO-polymer composite. For the 3D printing of bimorphs, the tank was divided by a PDMS wall into two area. First, the pure DS3000 stack (90 µm) was printed at 200 mm/s writing speed to ensure tight adhesion with the build platform, setting the z-slicing at 30 µm/layer and 60 µm of hatching. Then the build table was removed and put into an isopropanol bath to remove the uncrosslinked polymer. The build table was then replaced into the 3D printer to continue the second part of the printing with the SCO material (thickness of 150 µm) stored in the other part of the tank. In this case, the z-slicing and the hatching parameters were fixed to 30 µm. In order to reduce the fabrication time, the writing speed was increased to 5800 mm/s. Thickness is controlled by the number of stacks, with the z-slicing determining the stack thickness.

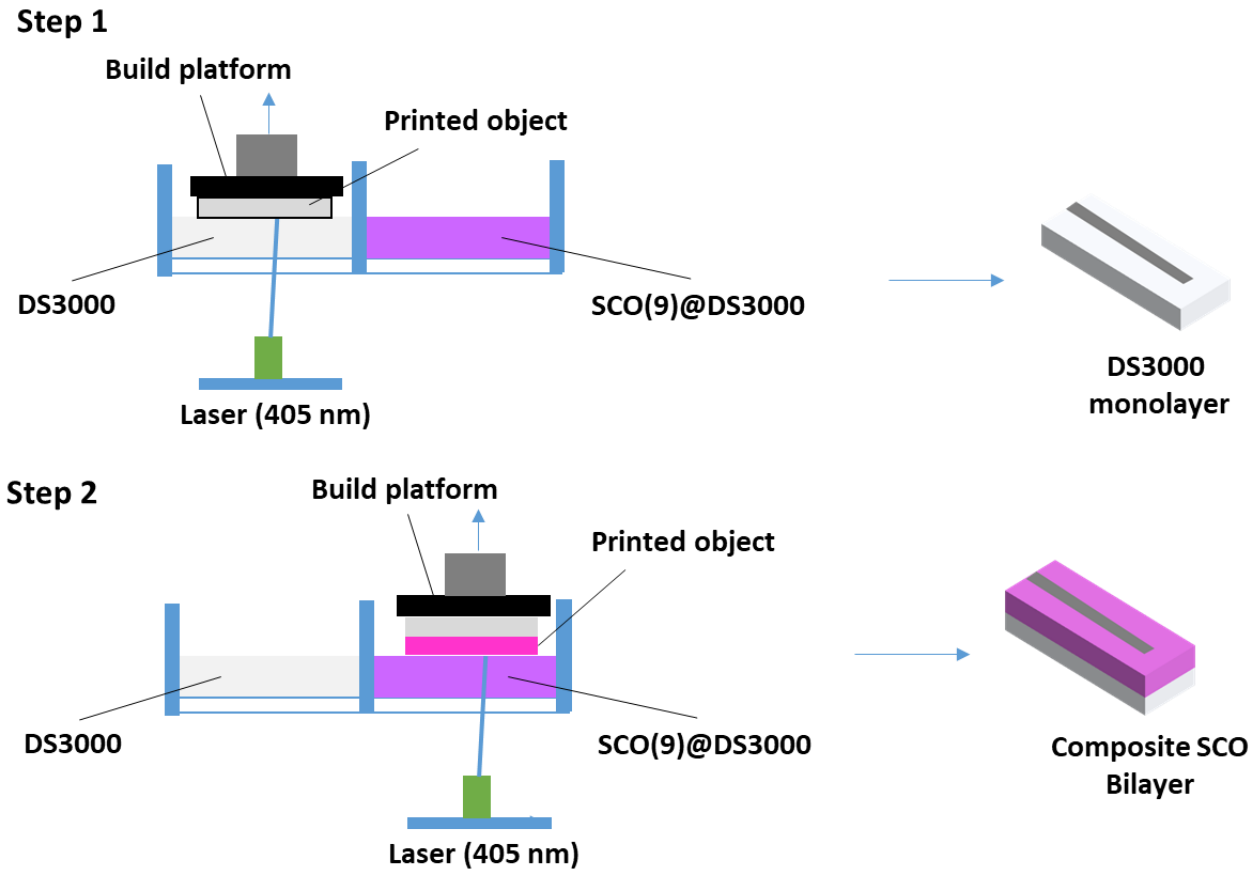

Fig 3.20) 3D printing procedure of a SCO(**9**)@DS3000/DS3000 bilayer actuator. First the pure DS3000 is printed on the platform, and then the SCO(**9**)@DS3000 layer is printed on top of the DS3000 layer.

The resulting 3D-printed bilayers suffered from two significant downsides (Fig 3.21): first, the active layer was delaminated from the inactive layer, indicating insufficient adhesion between the pure DS3000 and the SCO(**9**)@DS3000 composite. Second, the SCO(**9**)@DS3000 sublayers showed also delamination between them. This delamination had never been observed for the 15 wt% SCO(**9**)@DS3000 composites, so the implication is that SCO concentrations above

this limit do not allow the resin to crosslink properly, probably due to the absorption of the laser by the SCO complex.

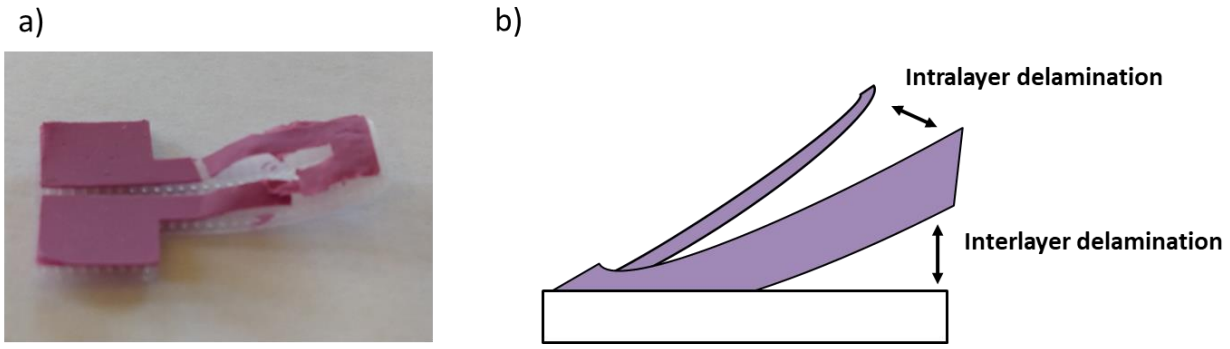

Fig 3.21) a) Delaminated SCO(**9**)@DS3000/DS3000 3D printed bilayer composite. b) Schematic representation of interlayer and intralayer delaminations.

In order to reduce delamination effects, another SCO(**9**)@DS3000/DS3000 bilayer structure was printed following the same procedure, but with a SCO concentration of 15 wt%, to ensure proper adhesion between the sublayers and between the active and inactive layers. This newly printed structure showed no intralayer delamination between the sublayers on either the pure DS3000 phase or the composite SCO(**9**)@DS3000 phase (Fig 3.22). It did however show delamination between the active and inactive layers. This shows that the adhesion between the two phases does not depend on the concentration of the active layer.

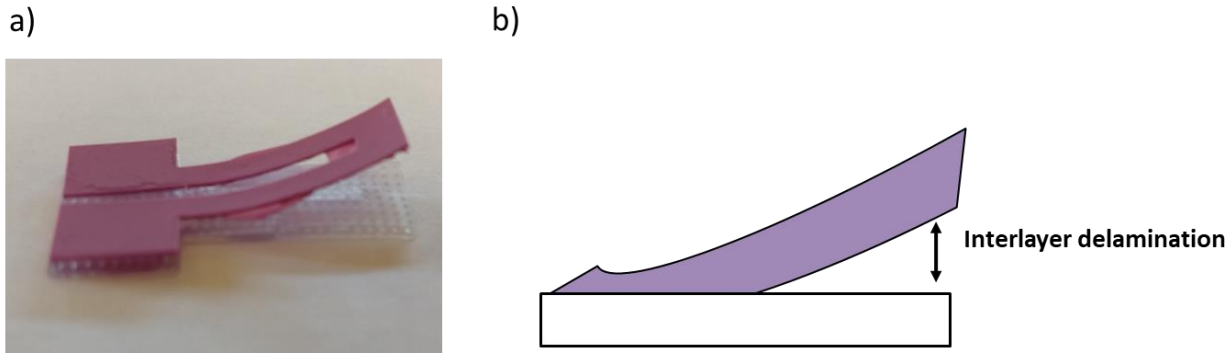

Fig 3.22) a) Delaminated SCO(**9**)@DS300 3D printed bilayer composite. b) Schematic representation of interlayer delamination.

To increase adhesion between the layers, exposure time of the interface was significantly increased, reducing the printing speed, making it match the initial exposure time used for the pure DS3000 layer to successfully adhere to the printing substrate. The new 3D printing protocol for the 3D printed SCO bilayers is as follows: first, the pure DS3000 stack (90 µm) was printed at 200 mm/s writing speed to ensure tight adhesion with the build platform, setting the z-slicing at 30 µm/layer and 60 µm of hatching, for an overall fabrication time of around 7 minutes. For the second step, printing with the SCO material (thickness of 150 µm), the z-slicing and the hatching parameters were fixed to 30 µm. In order to obtain strong adhesion between the layers of pure DS3000 and the composite layers containing SCO material it is necessary to fabricate the first SCO

composite layers under the same high-exposure conditions used for the fabrication of the pure D3000 layers. Afterwards, in order to reduce the fabrication time, the writing speed was increased to 400 mm/s. The resulting bilayer objects show no delamination, even when heated at the spin transition temperature, showing the effectiveness of the printing protocol (Fig 3.23).

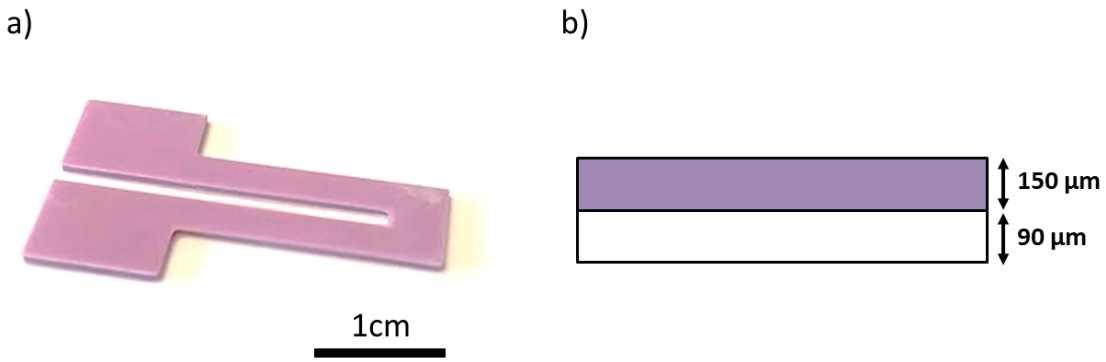

Fig 3.23) a) SCO(**9**)@DS3000/DS3000 3D printed bilayer composite. b) Schematic representation of a bilayer system with no delamination.

The following section will then delve into the characterization of these printed objects and their properties as mechanical actuators.

3.3.3.4 Morphological and physical characterization of the SCO(9)@DS3000 3D printed objects

Temperature dependent magnetic measurements of complex **9** and the SCO(**9**)@DS3000 material were performed in the 290-390 K range. The analysis shows that the composite retains the spin transition properties of the complex (Fig 3.24); the LS-HS transition remains identical at 340 K while the HS-LS transition is slightly shifted towards lower temperature and becomes more gradual (330 K for the complex and 325 K for the composite).

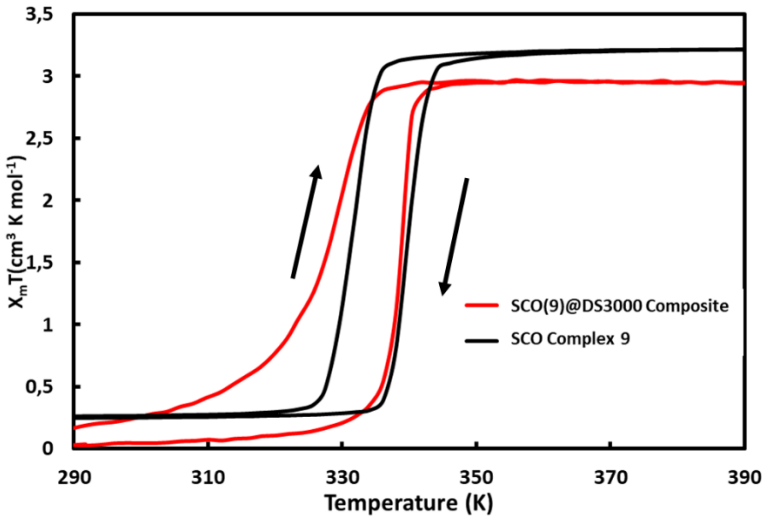

Fig 3.24) Magnetic measurements of **9** and the SCO(**9**)@DS3000 composite material (second thermal cycle).

Magnetic measurements show that the SCO properties remain relatively intact. To investigate the thermal stability of the printed devices at the actuation temperatures, differential scanning calorimetry (DSC) analysis was performed on both the composite, the pure complex and the pure DS3000 resin (see annex A3.1 to A3.3). These thermal analyses show that SCO occurs at a temperature well below any crystalline transition of the polymer matrix, and that the composite retains its stability at 120°C, thus ensuring that actuation does not interfere with the intrinsic properties of the polymer matrix.

A thermal mechanical analysis (TMA) was performed to determine the Young's Modulus (E) of the composite material. E defines the relationship between stress $\boldsymbol{\sigma}$ (force per unit area) and strain $\boldsymbol{\varepsilon}$ (relative deformation):

$$E = \frac{\sigma}{\varepsilon}$$

The thermal variation of the Young's Modulus allows us to more accurately gauge the change in mechanical properties of the material upon the spin transition. To this end, bowtie shaped samples were printed using the SCO(**9**)@DS3000 composite resin (Fig 3.25a). The printed samples were subjected to a series of constant forces and the temperature dependence of the strain was measured. From this measurement, a set of strains and stresses were determined for each temperature, and from these, we could determine the Young's modulus of the sample for each temperature.

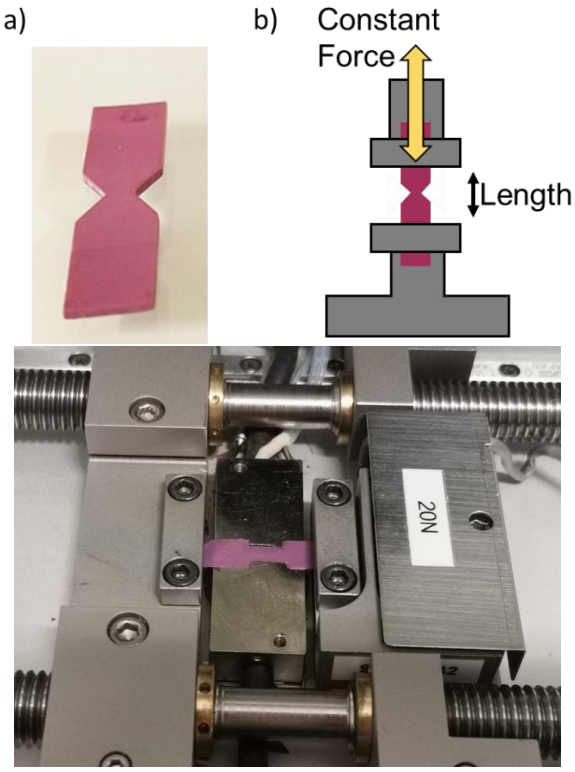

Fig 3.25) a) Printed SCO(**9**)@DS3000 bowtie. b) Schematic representation of a tensile mechanical analysis setup. c) Photo of the tensile mechanical analysis setup.

From the TMA analysis, we found that the Young's modulus of the SCO(**9**)@DS3000 composite (1.7 ± 0.2 GPa) at room temperature is comparable with that of the pure polymer matrix (1.5 ± 0.2 GPa). Upon heating, one can observe a similar decrease of the Young's modulus (*ca.* 0.2 GPa at 360 K) in the two samples, but a detailed tracking reveals in the SCO composite a discontinuity of the Young's modulus around the spin transition temperatures – the HS phase being considerably softer (Fig 3.26). This indicates that, the mechanical strain of the complex is effectively transmitted to the DS3000 matrix.

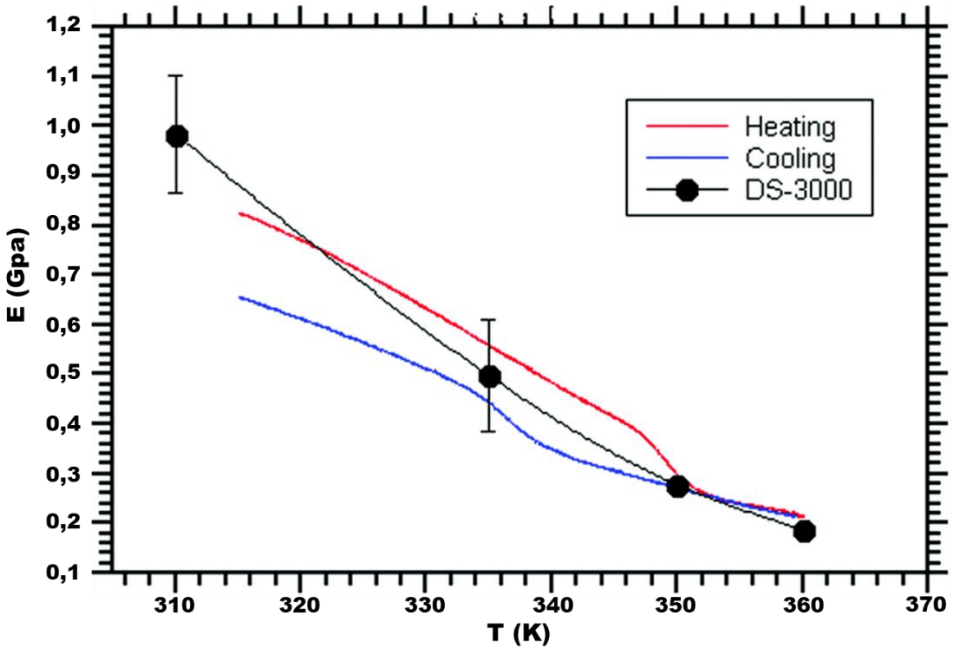

Fig 3.26) Young's Modulus (E) of the DS3000 resin (black) and the SCO(**9**)@DS3000 printed composite (blue and red).

While the magnetic, thermal and mechanical analysis give us an idea of the properties of the SCO(**9**)@DS3000 composite material, the bilayer actuators fabricated with this material remain to be characterized. To this end, the SCO(**9**)@DS3000/DS3000 printed bilayers were analysed via Scanning Electron Microscopy (SEM). Special attention was given to the interface between the pure DS3000 layer and the SCO(**9**)@DS3000 layer to confirm that the two layers show adhesion at the micrometric level. Indeed the SEM imagery allows to clearly differentiate the two phases of the bilayer. We can clearly discern the interface in between the smooth, nude DS3000 stack and the rough SCO(**9**)@DS3000 composite stack containing well dispersed particles of the SCO compound (Fig 3.27). Most important of all is the good continuity between the two layers, which is an indispensable feature to avoid the delamination and to optimise the performance of the bimorph actuator.

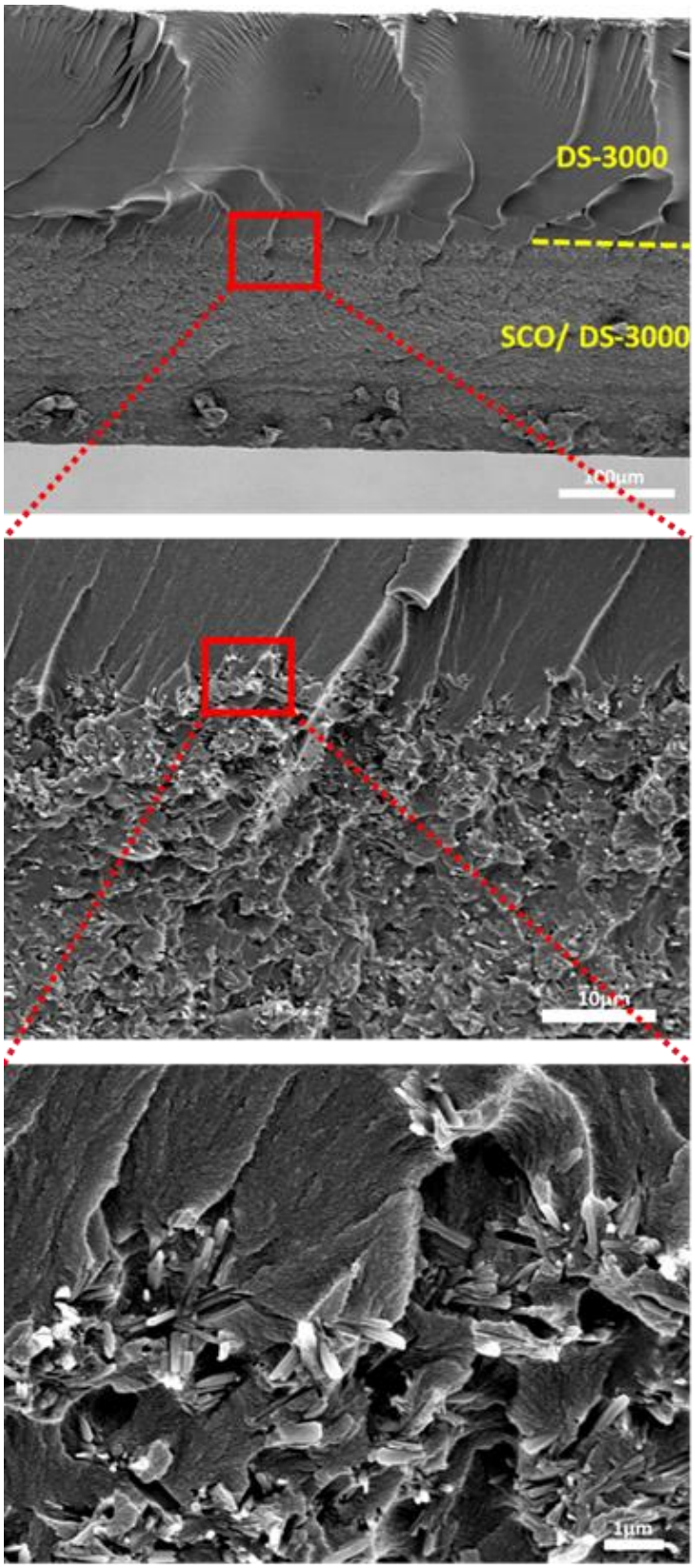

Fig 3.27) SEM images of the interface of the SCO(**9**)@DS3000/DS3000 printed bilayer system

3.3.3.5 Actuation properties of the SCO(9)@DS3000/DS3000 printed bilayer :

To assess the movement of the bilayer, the printed object was stimulated via heat to actuate with one fixed end while a non-contact distance tracker (NCDT) laser system tracked the position of the free tip.

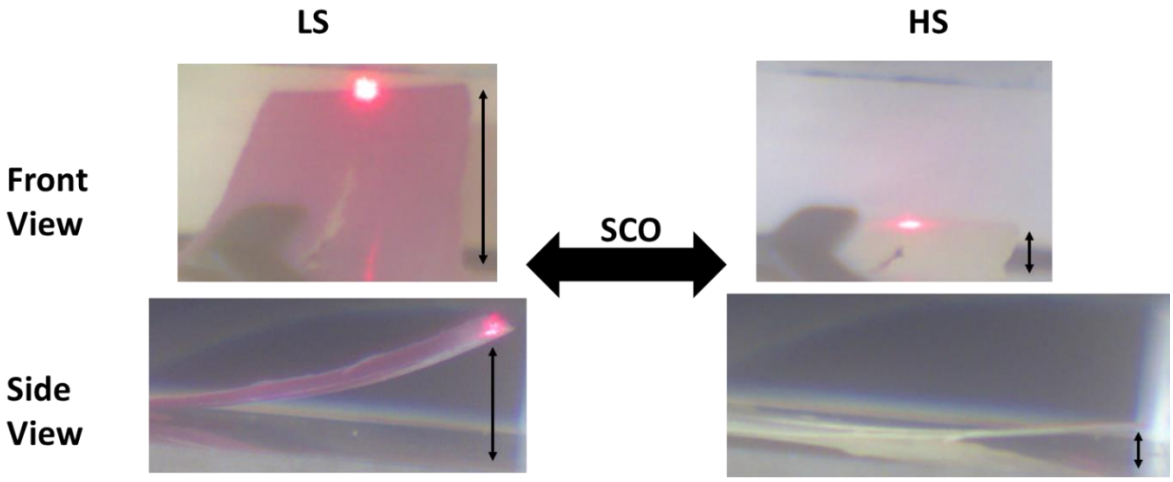

Fig 3.28) Actuation of the SCO(**9**)@DS3000/DS3000 Bilayer. Frontal view of the actuator (up) and lateral view of the actuator (down)

The tip displacement for a 240 µm thick sample upon heating and cooling between 300 and 360 K allows us to see the brusque movement associated with the spin transition. The origin of this movement is the mismatch of the expansion between the active SCO(**9**)@DS3000 layer, which undergoes spin transition and the DS3000 layer which does not. In fact, the volume change of the SCO phenomenon causes the SCO(**9**)@DS3000 layer to expand and this bends the system, creating a reversible deformation of the SCO(**9**)@DS3000/DS3000 bilayer. The tip displacement for this 30 mm long bimorph is ca. 4.5 mm, denoting a displacement (D) to length (L) ratio of D/L = 0.15.

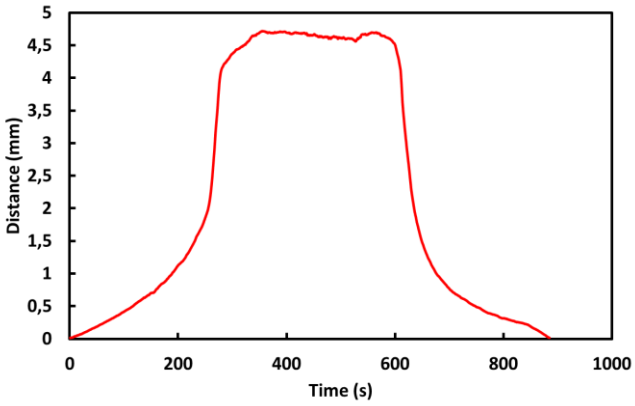

Fig 3.29) Tip displacement of the SCO(**9**)@DS3000/DS3000 sample when heated for 500 seconds and then allowed to cool down (300 – 360 K)

In order to evaluate the effect of the thickness of the sample on the actuation, an identical SCO(**9**)@DS3000/DS3000 bilayer was printed at a higher thickness (1 mm). The thickness of the inactive layer was 150 µm and the thickness of the active layer was 850 µm. This bilayer actuator showed significantly diminished actuation compared to the 240 µm thick sample (Fig. 3.30-3.31) with a tip displacement of only 1.2 mm.

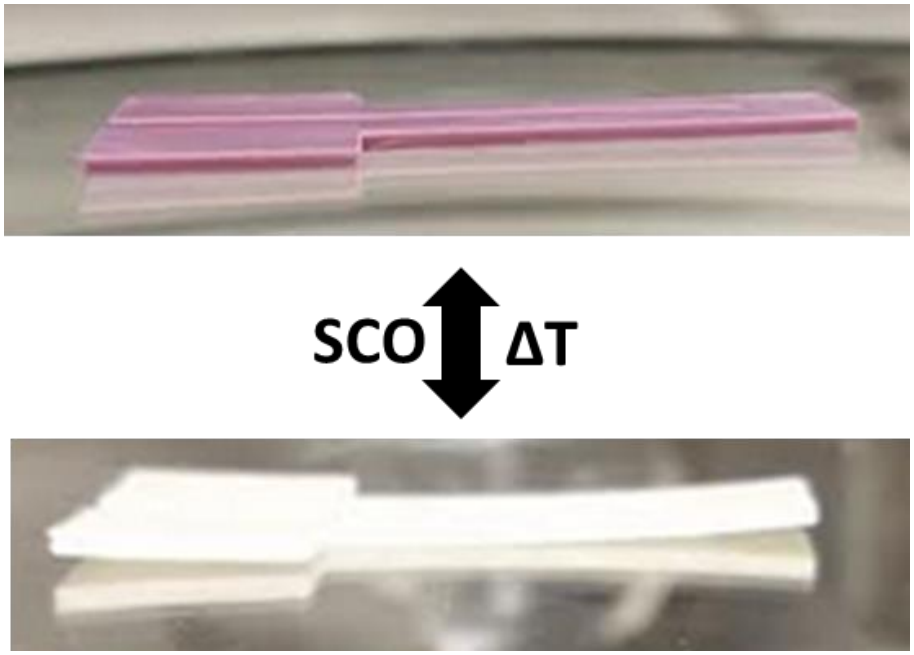

Fig 3.30) Lateral view of a 1 mm thick SCO(**9**)@DS3000/DS3000 bilayer actuator

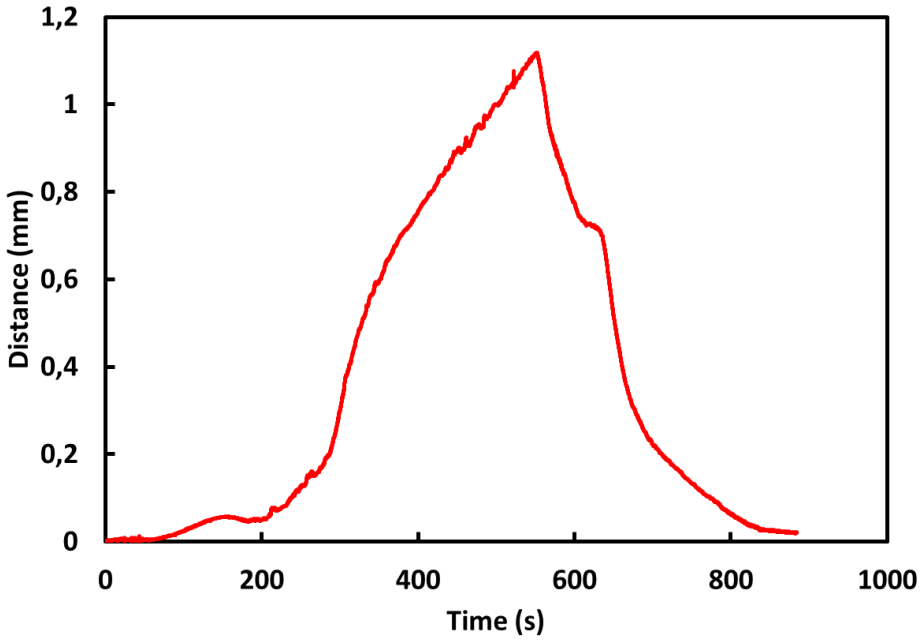

Fig 3.31) Tip displacement of a 1 mm thick SCO(**9**)@DS3000/DS3000 bilayer sample when heated for 500 seconds and then allowed to cool down (300 – 360 K)

In order to use the classical bilayer model to determine the mechanical and actuating properties of our composite, a similar simple rectangular bilayer object (2 cm x 0.4 cm x 240 µm) was also fabricated in the same experimental conditions. The actuation of this bilayer was monitored in a well-thermalized glycerol environment with no influence of gravity due to a lateral movement.

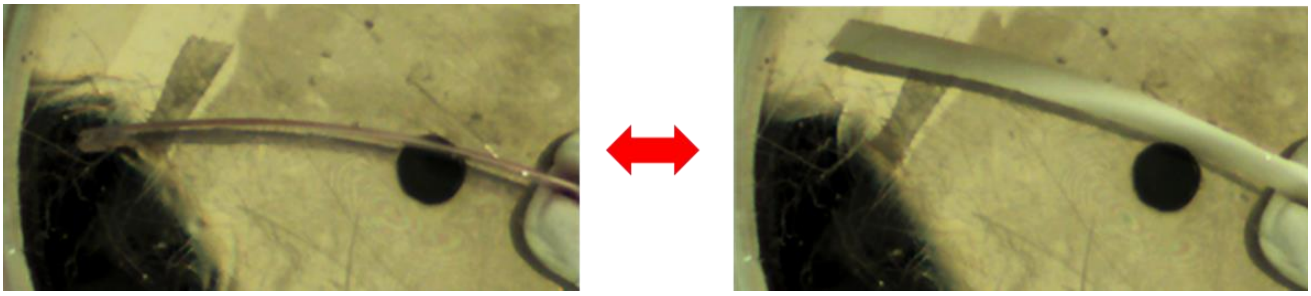

Fig 3.32) Movement of a rectangular printed SCO(**9**)@DS3000/DS3000 bilayer strip upon the spin transition

Using Timoshenko's beam theory [12], it is possible to associate the change in curvature *k* of a bilayer beam to the strain produced by the spin transition *ΔL/L*:

$$k = \frac{6(\alpha_2 \Delta T + \frac{\Delta L}{L} - \alpha_1 \Delta T)(1+m^2)}{h[3(1+m^2) + (1+mn)\left(m^2 + \frac{1}{mn}\right)]} \quad (1)$$

Where:

$$m = \frac{a_1}{a_2} \ (2)$$

$$n = \frac{E_1}{E_2} \ (3)$$

$$h = \ a_1 + a_2 \ (4)$$

In this case, a_i is the thickness of each layer. E_i is the Young's modulus of each layer, α_i is the thermal expansion coefficient of each layer, and ΔT is the temperature range of interest. In this case, the temperature range is restricted to exactly that of the SCO to isolate the effect of the spin transition from any effects caused by the natural mismatch in thermal expansion coefficient in the two layers.

The parameters a_1 and a_2 were 0.09 mm and 0.15 mm respectively. Young's modulus of each layer at the SCO temperature were obtained from tensile mechanical analysis. E_1 = 280 MPa and E_2 = 190 MPa. Linear thermal expansion coefficients were likewise obtained from temperature-controlled mechanical testing (see page 127) . $\alpha_1 = 6.5 \cdot 10^{-4}\ K^{-1}$ $\alpha_2 = 9 \cdot 10^{-4}\ K^{-1}$.

The change in curvature can be estimated from the tip deflection δ for relatively small deflections by the relationship:

$$\delta = \frac{kL^2}{2} \quad (5)$$

With these parameters, the strain of the active layer caused by the spin transition is estimated as ΔL/L = 0.0033. With the strain from the spin transition we can then calculate the volumetric work density W/V of the actuator with the following equation:

$$\frac{W}{V} = \frac{E(\frac{\Delta L}{L})^2}{2} \quad (6)$$

The obtained value of the work density 1.5 mj·cm^{-3} is in accordance with other SCO actuators in the literature [11,92,99] and highly competitive with other kinds of actuating devices proposed for artificial muscles applications [10]. Table 3.1 shows a comparison of the mechanical properties of the SCO(**9**)@DS3000/DS3000 bilayer actuators with other materials used for soft robotic actuators.

Table 3.2) Comparison of Young's modulus, strain and work density of selected polymer based bending actuators.

Active Material	**E (Gpa)**	**Strain (%)**	**Work density (mJ cm^{-3})**	**Ref**
Nylon	0,4	2,5	125	[184]
PEDOT	0,00033	0,5	0,004	[185]
Bucky gel	0,26	1,9	45	[186]
Polypyrrole	0,12	14	1180	[187]
Ru-sulfoxide polymer	0,02	0,105	0,0055	[174]
SCO/DS3000	0,28	0,33	1,5	Present work

In conclusion, using a stereolithographic approach in conjunction with spin crossover-polymer composites, we have 3D printed various stimuli-responsive mono- and bimorph architectures with sizes up to several cm and structural details down to the 80 µm scale. The objects display good thermal and mechanical properties and afford for reversible mechanical actuation generated by the volume change accompanying the spin crossover phenomenon. The fabrication process developed here is straightforward, versatile and enables the creation of arbitrary planar and three-dimensional geometries, which are otherwise not accessible using spin crossover complexes. This work widens the restricted choice of materials for 4D printing.

As far as the applicability of this material goes, there seems to be one core drawback to this approach: so far none of our attempts to confer the DS3000 resin with electrically conductive properties have been successful. We have attempted integration of silver particles into the resin

to confer it with electrical conductivity, but the addition of silver has a negative effect on the reticulation process of the resin. Electrically controlled systems are of great interest in the field of robotics, another approach might be necessary to achieve electrically controlled actuators.

This is the core issue that we will attempt to solve with our second approach to spin crossover soft actuators: SCO@P(VDF-TrFE)/P(VDF-TrFE) casted bilayer actuators.

3.4 Spin crossover/P(VDF-TrFE) electrically driven actuators

With the goal of fabricating electrically driven, highly controllable SCO actuators, we need a polymeric matrix that can be easily processed, and which can be imbued with conductive properties. The work done for the fabrication of pyroelectric SCO/P(VDF-TrFE) composites (in chapter 2) showed the versatility of using P(VDF-TrFE); it can be easily processed into SCO composites and there are multiple fabrication routes with which we can obtain macroscopic free-standing films [188].

There are two main challenges that must be overcome in order to successfully fabricate conductive bilayer actuators: the first is the fabrication of a homogeneous, stable bilayer with good adhesion at the interface to avoid delamination of the two layers. The second challenge is the integration of electrical conductivity into this bilayer system, which allows for effective Joule heating of the bilayer system to trigger and control the SCO allowing for electrically driven controllable actuation.

This section will first explain the optimization process needed to obtain conductive SCO bilayers, and it will afterwards proceed to a characterization of these bilayers as actuators, before finally highlighting their potential as highly controllable electrically driven mechanical devices.

3.4.1 Fabrication of SCO@P(VDF-TrFE)/P(VDF-TrFE) bilayer composites

The first challenge in our research was the successful fabrication of an SCO bilayer composite. Keeping the integrity of the interface is a crucial factor that determines the actuating properties of bilayer systems, and for this reason, special attention was given to the optimization of this step.

The first bilayer system that we wanted to fabricate, as a proof of concept for SCO@P(VDF-TrFE)/P(VDF-TrFE) bilayers, was a bilayer where the SCO material of choice is complex **5** with formula $[Fe(H\text{-}trz)_{1,85}(trz)_{0,85}(NH_2trz)_{0,3}](BF_4)_{1,15}\bullet 1H_2O$, whose synthesis and integration into P(VDF-TrFE) composites can be found on section 2.3.1.5. Much like in the previous work, the concentration of SCO in the P(VDF-TrFE) 70-30 copolymer matrix is 25 wt%.

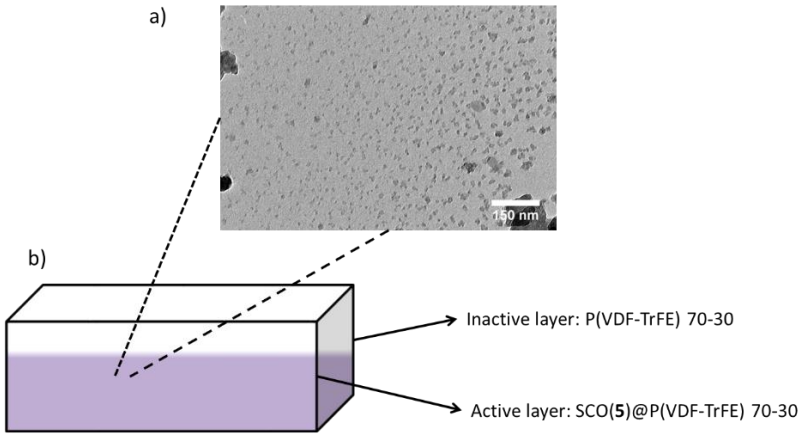

Fig 3.33) a) 20nm particles of complex **5** used in the fabrication of the composite. b) Composition of the SCO(**5**)@P(VDF-TrFE)/P(VDF-TrFE)70-30 bilayer.

As a first attempt to fabricate these bilayers, a synthesis protocol was developed where pure P(VDF-TrFE) 70-30 was drop cast on a still-drying film of the SCO(**5**)@P(VDF-TrFE) composite. This protocol intended to ensure good adhesion between the two layers by allowing them to partially mix. 90 mg of **5** was dispersed in 1.2 mL of DMF, and 270 mg of P(VDF-TrFE) 70-30 were dissolved in this dispersion. This mixture was drop cast on a glass substrate and allowed to partially dry at 378 K. Before the film was completely dry, 180 mg of P(VDF-TrFE) 70-30 dissolved in 0.8 mL of DMF were drop cast on top of the still drying composite film, and the bilayer was allowed to dry at 378 K overnight. The resulting film, however, showed that the two layers diffused completely, resulting in a single inhomogeneous composite layer.

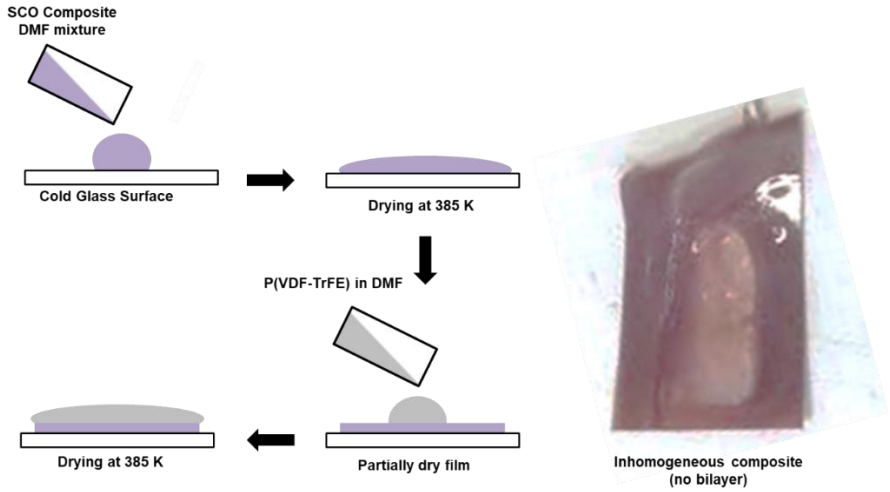

Fig 3.34) Failed fabrication procedure for a casted SCO(**5**)@P(VDF-TrFE)/P(VDF-TrFE) bilayer.

In order to avoid this layer diffusion effect, we repeated the synthesis, but we allowed the SCO(**5**)@P(VDF-TrFE) composite layer to dry completely before addition of the pure P(VDF-TrFE) 70-30. The resulting film, however, also showed layer diffusion and the resulting bilayer showed no actuation upon heating. This can be attributed to the fact that, despite the SCO(**5**)@P(VDF-TrFE) layer being already dry when the solution of P(VDF-TrFE) was added on top,

because DMF is a nonvolatile solvent with a high boiling point, the solvent took a long time to dry and attacked the initial layer, causing diffusion between the layers.

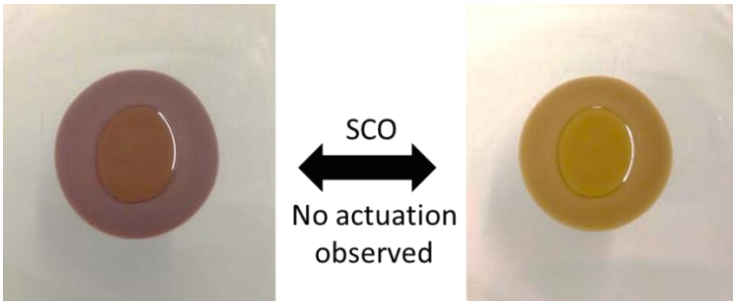

Fig 3.35) SCO(**5**)@P(VDF-TrFE)/P(VDF-TrFE) bilayer with layer diffusion. The loss of interface integrity hampers the actuation properties.

To avoid layer diffusion it then becomes necessary to use a more volatile solvent that does not readily dissolve the initial SCO(**5**)@P(VDF-TrFE) layer during the drying process. **We decided to use methyl ethyl ketone (MEK) and a blade-casting method to increase the surface area of the deposit and to ensure a more rapid evaporation**.

The active SCO(**5**)@P(VDF-TrFE) composite layers were finally prepared by dispersing complex **5** (90 mg) in MEK (1.8 mL) in an ultrasonic bath for 40 min. Then, the corresponding P(VDF-TrFE) copolymer (270 mg) was added to the mixture and dissolved at 45 °C. The resulting suspension was then blade-cast at a height of 150 µm on a heated Teflon surface at 50 °C and kept at this temperature for 10 min, until the composite was dry. The inactive layer was then prepared by dissolving the corresponding P(VDF-TrFE) copolymer (270 mg) in 1.8 mL MEK at 45 °C. The resulting solution was then blade-cast at a height of 150 µm on top of the recently dried active layer at 50 °C and kept at this temperature for ca. 2 h, until the composite was completely dry. The bilayer film was then annealed at 105°C for 12 h.

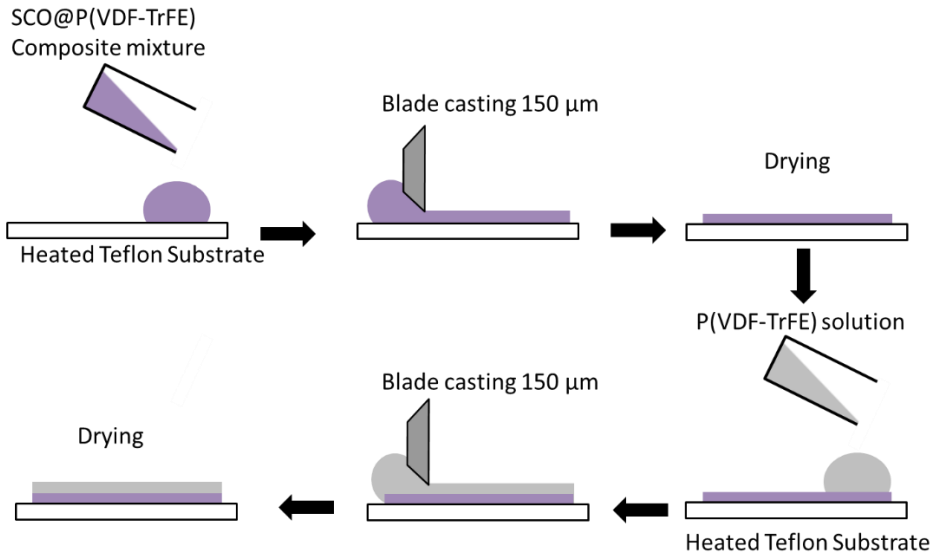

Fig 3.36) Optimized SCO@P(VDF-TrFE)/P(VDF-TrFE) bilayer fabrication procedure.

The resulting bilayer material shows no diffusion or delamination, and the integrity of the bilayer system is confirmed by the fact that it shows actuating properties upon the spin transition. This confirms the usability of this fabrication procedure to make SCO@P(VDF-TrFE)/P(VDF-TrFE) bilayer actuating systems. It is a flexible and easily tuneable procedure, so it will serve as the base for the fabrication of all conductive SCO@P(VDF-TrFE)/P(VDF-TrFE) bilayer systems presented hereafter.

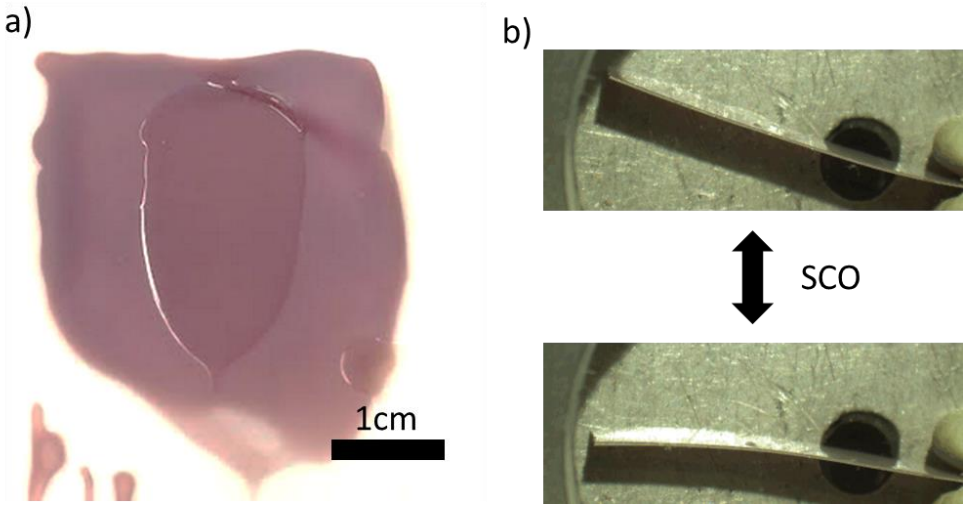

Fig 3.37) a) SCO(**5**)@P(VDF-TrFE)/P(VDF-TrFE) bilayer film. b) Actuation of a cantilever fabricated using a SCO(**5**)@P(VDF-TrFE)/P(VDF-TrFE)bilayer film.

Now that we can reliably fabricate bilayers, the next challenge is conferring our bilayer systems electrical conductivity to allow for Joule heating to drive the spin transition. The fabrication procedure of the bilayers via blade casting will have to be adjusted, but it will remain at its core the same principle of using a rapidly evaporating solvent with a wide surface area to avoid diffusion of the layers. Integration of electrical conductivity into these bilayer systems is a core goal of our work, as excitation of a device via electrical stimulus lends itself well to real applications.

3.4.2 Fabrication of SCO@P(VDF-TrFE)/P(VDF-TrFE) conductive composite bilayers

In order to confer our SCO@P(VDF-TrFE)/P(VDF-TrFE) bilayer systems electrical conductivity properties, three different approaches were attempted: the first one was a "conductive trail" approach in which a third conductive material was integrated into the bilayer system, and Joule heating of this material drove the spin transition. The second approach was the use of Carbon nanotubes (CNT) to fabricate a SCO@P(VDF-TrFE)/CNT@P(VDF-TrFE) conductive composite. The third approach was the use of micrometric silver flakes to fabricate SCO@P(VDF-TrFE)/Ag@P(VDF-TrFE) conductive composites. In this section, we will discuss these results.

With the goal of making Joule-effect driven composites, a specific geometry was needed so that the electrical current would move along the entire length of the composite, ensuring that

it heats up in a homogeneous manner. The chosen design allows for positioning two electrodes at the base (wider sections, see Fig 3.38) of the actuator and current goes through the whole cantilever. The initial square-shaped geometry was later phased-out and changed for a round shape that allows for a more homogeneous heating of the sample.

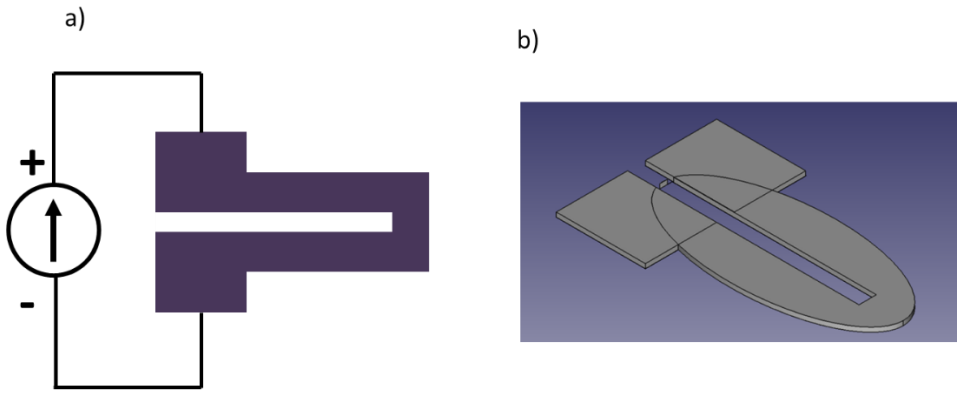

Fig 3.38) a) Conductive actuator geometry and operation in a circuit. b) Rounded actuator geometry with more homogeneous Joule heating.

The first approach to conductive bilayers was the use of a third material, technically turning the system into a trilayer system. Due to the fact that the third conductive material will be mechanically inactive, the implementation of the conductive trail has to be on top of the pure P(VDF-TrFE) 70-30 layer so as not to interfere with the actuation (Fig 3.39).

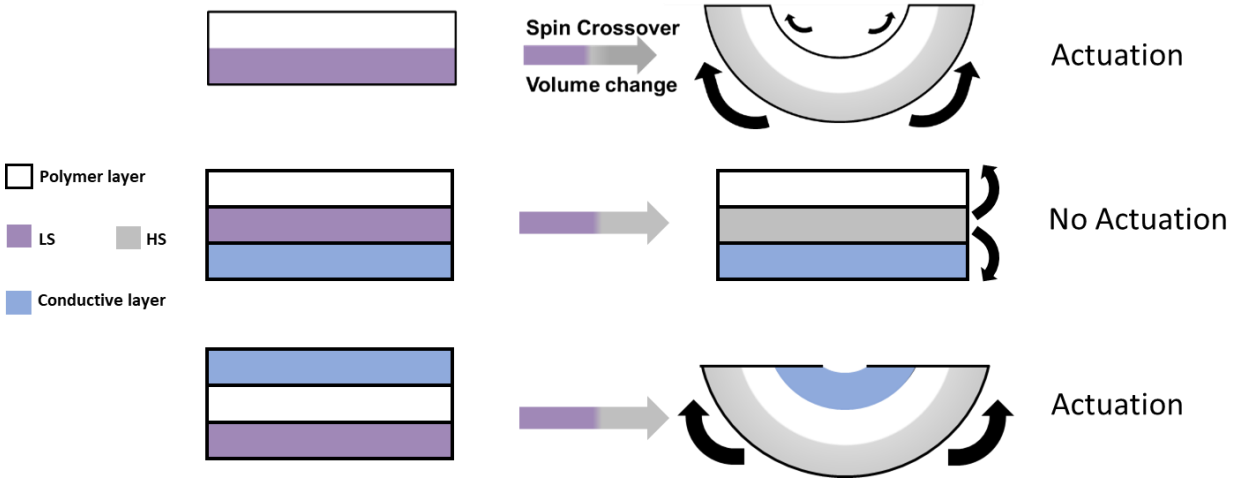

Fig 3.39) Effect of a third inactive layer on the actuation of a SCO bilayer system.

Following the first approach, three different options were implemented: the first was the use of conductive epoxy. A small trail of conductive CW2400 conductive silver epoxy was manually distributed across the length of the actuator. The epoxy resin was allowed to cure for 5 hours before its conductivity was tested. The actuator showed high conductivity (approx 3 Ω cm^{-1}) and application of an electrical current successfully allowed the composite system to be heated via Joule effect. Thermochromism of the sample confirmed the spin transition of the

composite. However, there was no actuation observed, probably due to the extremely high rigidity of the epoxy layer. The second attempt was the use of a thin conductive wire (Block 1 core constantan alloy resistive wire 0.1 mm RD 100/0.1) embedded in the P(VDF-TrFE) layer and directly connected to the circuit. The circuit showed good conductivity (0.6 Ω cm^{-1}) and successfully allowed the heating of the composite bilayer. The wire however made the system too rigid and no actuation was observed. Finally, the third attempt at adding a conductive trail was the use of silver conductive paint (RS Pro electrically conductive paint). A layer of silver paint was manually added on top of the bilayer system and subsequently dried and baked at 120°C for 10 minutes as per the manufacturers recommendation. The conductive trail showed good electrical conductivity (approx 10 Ω cm^{-1}) and application of an electrical current successfully allowed Joule heating to induce spin crossover. The system successfully showed mechanical actuation upon spin transition. However, material fatigue caused the silver trail to break after three heating cycles, eliminating the conductivity. Silver paint is mechanically too fragile for systems intended to be constantly in motion.

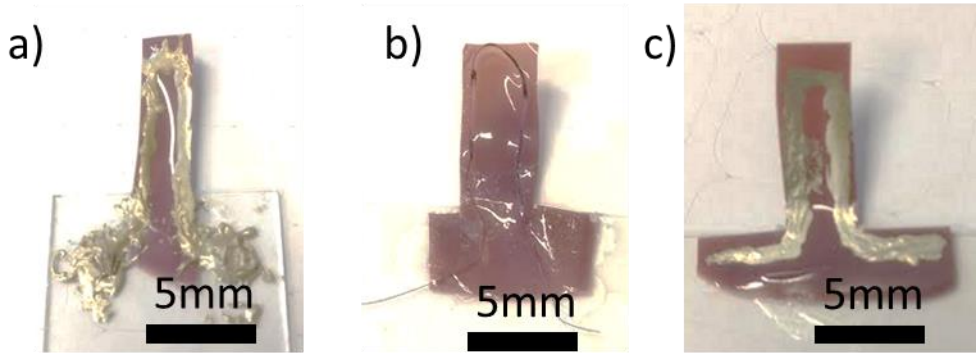

Fig 3.40) a) SCO bilayer with a conductive epoxy trail. b) SCO bilayer with an embedded resistive constantan alloy wire. c) SCO bilayer with a conductive silver paint trail.

An increased rigidity of the system and the fragility of the third layer are the main drawbacks of using the conductive trail approach. Instead, we opted for a composite material approach to avoid using a third layer. By integrating the conductive element in the inactive layer, the stability of the P(VDF-TrFE) composite becomes our main concern. To this end, we attempted to use multi-walled carbon nanotubes (MWCNTs) which have been shown before to confer conductivity to PVDF composites [189].

In order to optimize the properties of this conductive layer as a thermal heater we must first understand the principle behind it. Joule heating is governed by Joule's first law which states that the thermal power *P* generated by a resistor is proportional to the product of its resistance *R* and the square of the current *I*. For a perfect resistor this translates to the equation:

$$P = RI^2 \ (7)$$

This means that, in order to keep the required voltage relatively low, we need a system with low resistance that can thus be subject to high current. For composites fabricated with a conductive filler, the concentration threshold at which the filler forms a conductive network in

the composite is called the percolation threshold. This threshold is reported to be about 1 wt% for MWCNTs in PVDF [189], further addition of conductive filler will not significantly change the conductivity of the material after the percolation threshold.

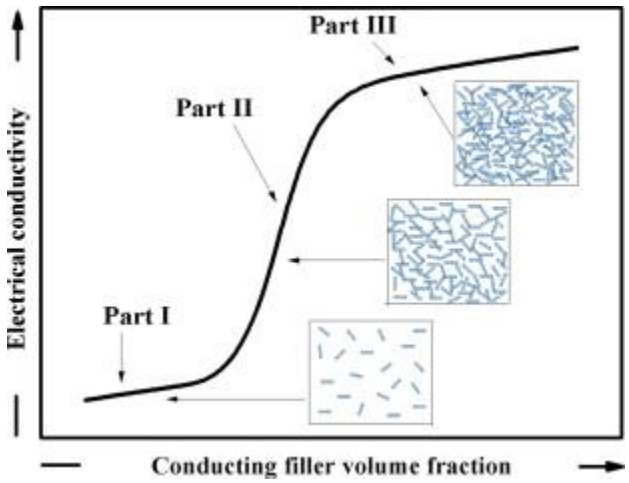

Fig 3.41) Schematic representing the relationship between electrical conductivity and conductive filler concentration in a composite material forming a percolation network.

We fabricated MWCNT@P(VDF-TrFE) composites with concentrations ranging from 0.5 wt% to 7.5 wt% of MWCNTs with 40-60 nm diameter and 5-15 µm length. The composites were fabricated by dispersing the MWCNTs in 1.8 mL MEK and then dissolving 270 mg P(VDF-TrFE) 70-30 in the dispersion. The composites were then blade cast at 150 µm and dried overnight at 105°C. Even at the highest concentration, 7.5 wt%, far above the percolation threshold, the conductivity of the synthesized composites remained too low to allow proper heating of the system via Joule heating. With 5.2 kΩ cm^{-1} the maximum current we could apply was 7 mA, not enough to appreciably heat the composite.

Regardless, to assess the mechanical properties of these composites, a bilayer composite was fabricated following the procedure detailed in page 136, using the 7.5 wt% MWCNT/P(VDF-TrFE) composite as the inactive layer. Upon heating, this composite displayed actuation, however the mechanical properties of the polymer were compromised by the addition of MWCNTs, as this actuation was irreversible.

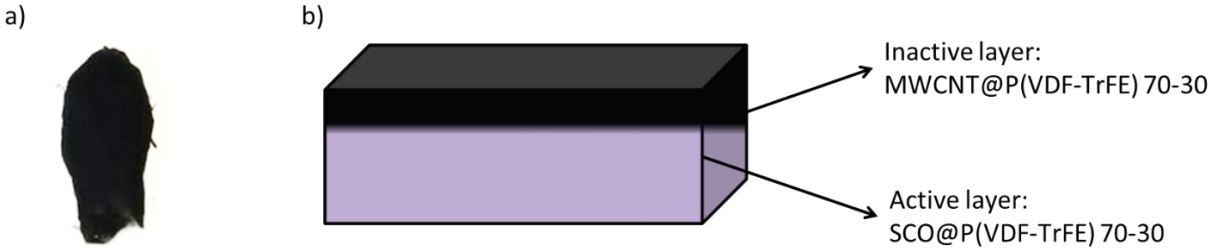

Fig 3.42) a) MWCNT/P(VDF-TrFE) 70-30 composite film. b) Schematic representation of the composition of a SCO bilayer with MWCNTs as conductive filler.

In order to fabricate a highly conductive P(VDF-TrFE) composite we opted for the use of a filler material with very high conductivity. In the end we decided to use metallic silver under the form of micro flakes which has been successfully used before to confer PVDF with conductive properties and even allow for its use as mechanical sensors [190]. Conductive Ag@P(VDF-TrFE) 70-30 composites were fabricated at 2, 4, 8, 12, and 20 v/v% of Ag. The composites at 2-8 v/v% of Ag showed no appreciable conductivity, meaning that they must be under the percolation threshold. At 12 v/v%, the conductivity abruptly increases to 10 Ω cm^{-1}. At 20 v/v% of Ag, however, there is a much more modest change in conductivity, at 6 Ω cm^{-1}. This means that the percolation threshold for this particular system is between 8 and 12 v/v%. We decided to use 20 v/v% as our working concentration of silver. Indeed, high conductivity in the system gives us more flexibility to tune the applied electrical current without overheating and burning the sample.

Table 3.3) Ag and P(VDF-TrFE) 70-30 amounts for the fabrication of the Ag@P(VDF-TrFE) composites and their resistivity.

Ag v/v%	Ag mass (mg)	P(VDF-TrFE) 70-30 mass (mg)	R (Ω cm^{-1})
2	32	265	-
4	63	259	-
8	127	248	-
12	191	237	10
20	318	216	6

SCO conductive bilayers were thus fabricated using the following procedure: the active SCO@P(VDF-TrFE) composite layers were prepared by dispersing each SCO complex (90 mg) in MEK (1.8 mL) in an ultrasonic bath for 40 min. Then, the corresponding P(VDF-TrFE) copolymer (270 mg) was added to the mixture and dissolved at 45 °C. The resulting suspensions were then blade-cast at a height of 150 µm on a heated Teflon surface at 50 °C and kept at this temperature for 10 min, until the composite was dry. The conductive Ag@P(VDF-TrFE) layer was then prepared by dispersing 10 µm Ag flakes (318mg) in of MEK (1.8mL) in an ultrasonic bath for 5 min. Then, the corresponding P(VDF-TrFE) copolymer (216 mg) was added to the mixture and dissolved at 45 °C. The resulting suspensions were then blade-cast at a height of 150 µm on top of the recently dried active layer at 50 °C and kept at this temperature for ca. 2 h, until the composite was completely dry. The bilayer films were then annealed at 105 °C for 12 h. A bilayer film was then cut into a circuit shape (page 138) using a Realmeca RV 2-SP high precision lathe by attaching the bilayer films to an aluminium support. A current of 0.7 A has induced the spin transition via Joule heating and, as a result, reversible electrically-driven actuation of the cantilever could be

performed (Fig 3.43 b). **The electrically induced movement is in itself the proof that the fabrication approach that we have been optimizing so far can indeed lead to highly controllable electromechanical devices**.

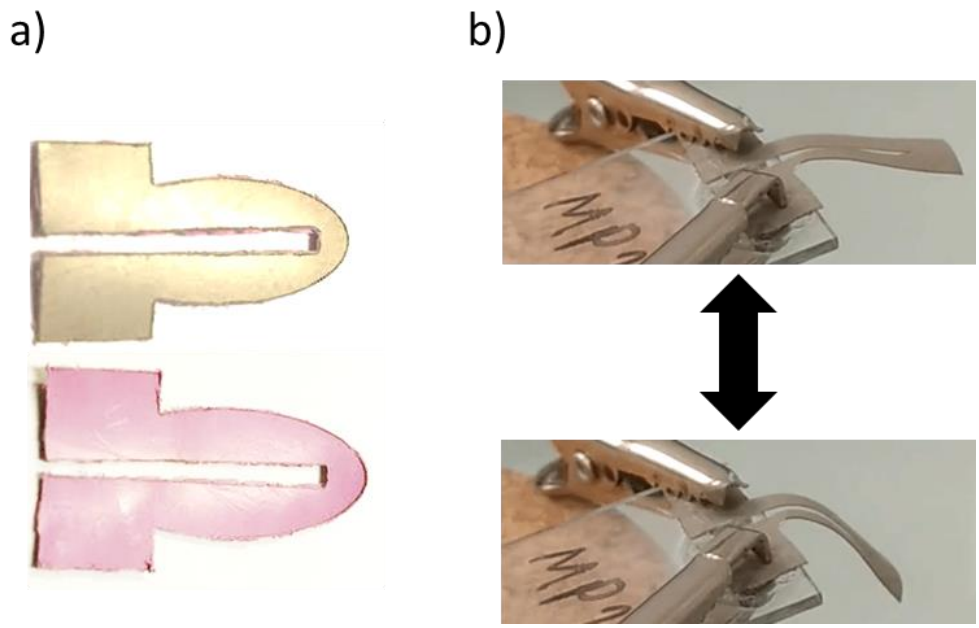

Fig 3.43) a)Ag@P(VDF-TrFE) side (up) and SCO(**5**)@P(VDF-TrFE) side (down) of the same bilayer actuator. b) Electrically driven actuation of a SCO(**5**)@P(VDF-TrFE)/Ag@P(VDF-TrFE) conductive bilayer actuator.

SEM images were taken at the interface of the bilayer, performing an elemental mapping via EDX. This analysis shows clearly differentiated layers, with the SCO(**5**)@P(VDF-TrFE) layer showing a high proportion of Iron and the Ag@P(VDF-TrFE) showing a high proportion of silver, as expected from the SCO and silver flake fillers, respectively. This shows that there is little to no diffusion between the two phases, confirming the effectiveness of this fabrication approach. A zoom-in at the interface, however, shows a continuous interface with no breaks in the polymer between the active and inactive phases, suggesting that these actuators will be resilient to delamination and efficient.

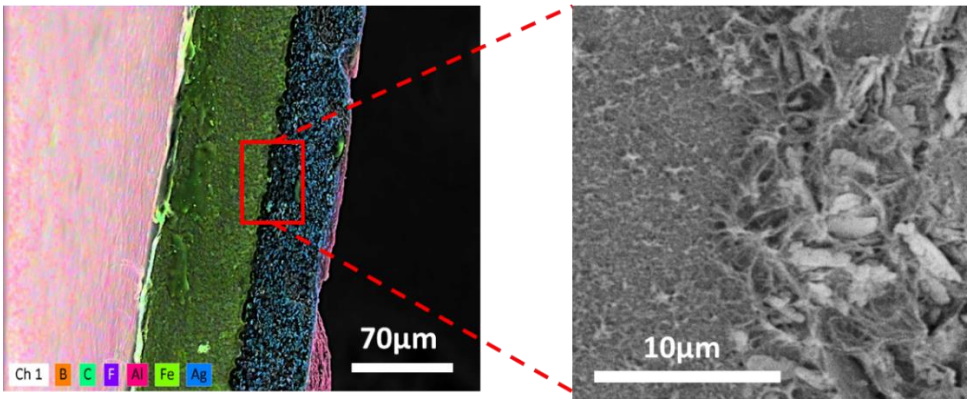

Fig 3.44) SEM images of the SCO(**5**)@P(VDF-TrFE)/Ag@P(VDF-TrFE) conductive bilayer. EDX elemental mapping (left) and zoom in at the interface (right).

We have thus successfully fabricated an electrically conductive, electrically driven bilayer SCO(**5**)@P(VDF-TrFE)/Ag@P(VDF-TrFE) bilayer actuator by incorporating micrometric Ag flakes. This flexible technique allows for the facile and reproducible fabrication of actuators with easily tuneable compositions. We will now try to develop a control system to properly exploit the controllable nature of the actuators afforded to us by the electrical conductivity.

3.4.3. Actuation control system

An actuator can be understood as a device that transforms a given input (heat, current, fluid pressure, etc) into mechanical motion. It is a dynamical system whose behaviour changes in response to an external stimulation [191]. The relationship between the input and the produced output (mechanical motion) is, however, very often unclear. This is especially true for bilayer actuators, which are complex systems with a variety of physical phenomena [192].

A control system is essentially a system which allows a user to control the input of an actuator to command it to move to a specific position or state. In our case, the input of the actuation is an electrical current, which triggers the spin transition and causes a reversible deformation of the bilayer, leading to a reversible movement.

There are two basic approaches to control a dynamical device, open-loop and closed-loop control [191]. An open-loop controller is also called a non-feedback controller; it simply sends an input to the dynamic system, which then produces an output. However, the open-loop controller cannot read the output produced by the system. In contrast, a closed-loop controller also sends an input to the system, but it recovers information from the output and through this information, it adjusts the control of the dynamic system, taking feedback from the system to optimize the output to match as closely as possible the user input.

In our case in particular, the dynamic system of choice is an electromechanical actuator. The input we will give to the system is a target position. The controller system then transforms this input into a signal that the actuator is responsive to. In our case this signal is an electrical current. This can be achieved via a digitally controlled source meter. The actuator then produces an output, a movement, which can be read by a position sensor as a position, and processed by a program, which then adjusts the electrical output of our source so that the actuator correctly moves to the target position.

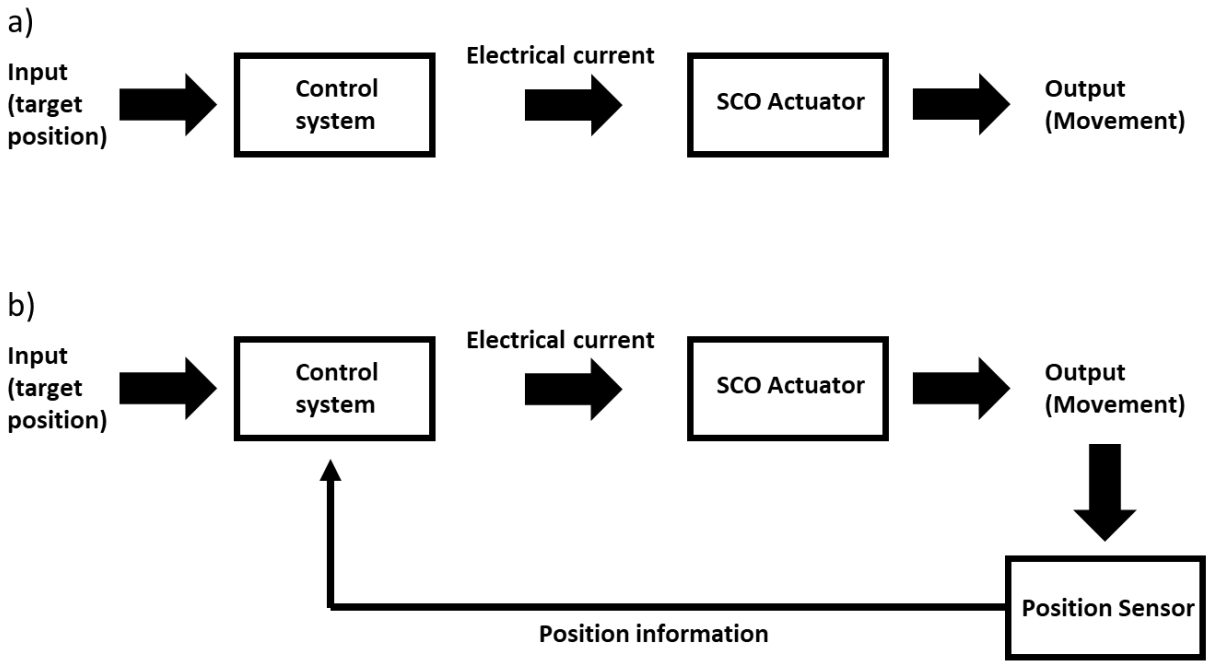

Fig 3.45) a) Schematic of an open-loop controller for an actuator. b) Schematic of a closed-loop controller for an actuator.

Closed-loop controllers offer often more accurate, without drift and faster control of a dynamic system, so with the goal of optimizing the actuating capabilities of our devices, we chose to set up a closed-loop control system. The most commonly used feedback processing method is the use of PID (Proportional Integral Derivative) controllers. These are widely used in industry, with a survey finding that 97% of regulatory controllers in the pulp industry use PID controllers [193]. PID controllers effectively adjust the input of the controller by taking into account the past behaviour of the device, the present behaviour of the device and the predicted future error.

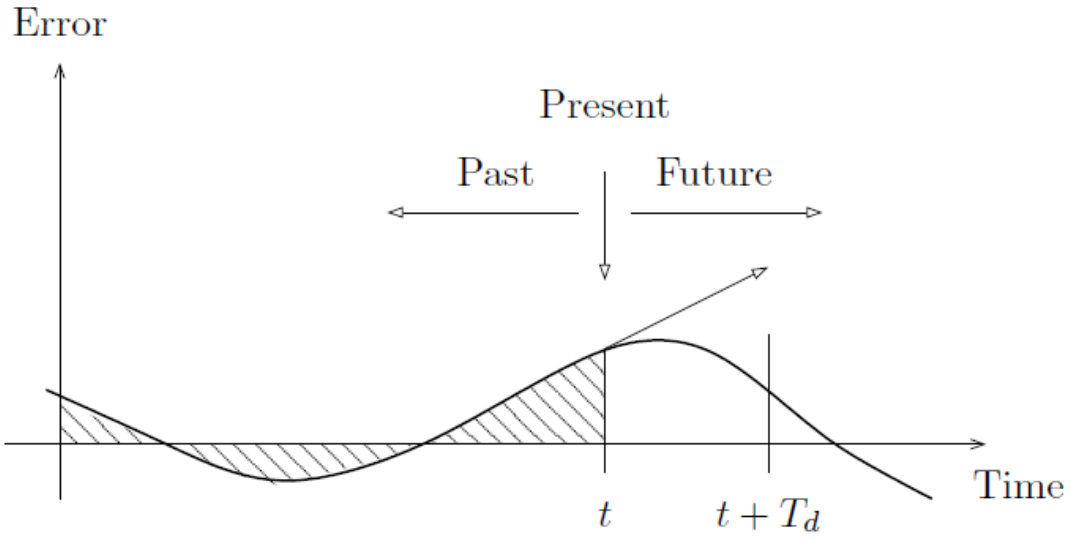

Fig 3.46) Error assessment of a PID controller [191].

The ideal PID controller is described by the formula:

$$u(t) = k_p e(t) + k_i \int_0^t e(\tau)d\tau + k_d \frac{de}{dt'} \quad (8)$$

Where u is the control signal and e is the control error. The control signal is thus the sum of three terms, one term is proportional to the error, the other term is proportional to the integral of the error and the last term is proportional to the derivative of the error, these are the proportional (P), integral (I) and derivative terms (D). Three parameters that govern the control system thus appear, k_P, the proportional gain, k_i the integral gain and k_d the derivative gain. The proportional term then acts on the present value of the error. The integral term represents an average of past errors. The derivative term can be interpreted as a prediction of future errors based on linear extrapolation. This can be seen reflected on the behavior of a PID system over time (Fig 3.46).

The ideal PID control can also be described in terms of time constants, with the proportional gain k_P playing a role on all three terms of the control signal. This is the model that we use in the present work:

$$I(t) = k_p \left(e(t) + \frac{1}{T_i} \int_0^t e(\tau)d\tau + T_d \frac{de(t)}{dt'} \right) \quad (9)$$

Where T_i and T_d are the integral and derivative time constants, respectively and I is the current, namely the input given by the controller to the actuator. It is interesting to note that there is no term directly associated with the set point target, the system is essentially being continuously driven by correction of an error. This has as a consequence that the system will never reach a zero-error state, rather it will keep oscillating around a non-zero steady state error.

In order to provide the PID controller with feedback of the position of the actuator at any given point in time, an optical non-contact displacement transducer was used (Micro Epsilon OptoNCDT 1750). With feedback from this sensor, the PID controller operates a source meter (Keithley 2400 Standard Series SMU) which then electrically triggers the spin transition of the actuator. In order for us to follow the movement and thermal variation of our devices, the setup also includes an optical CMOS camera and a Micro Epsilon infrared imaging camera.

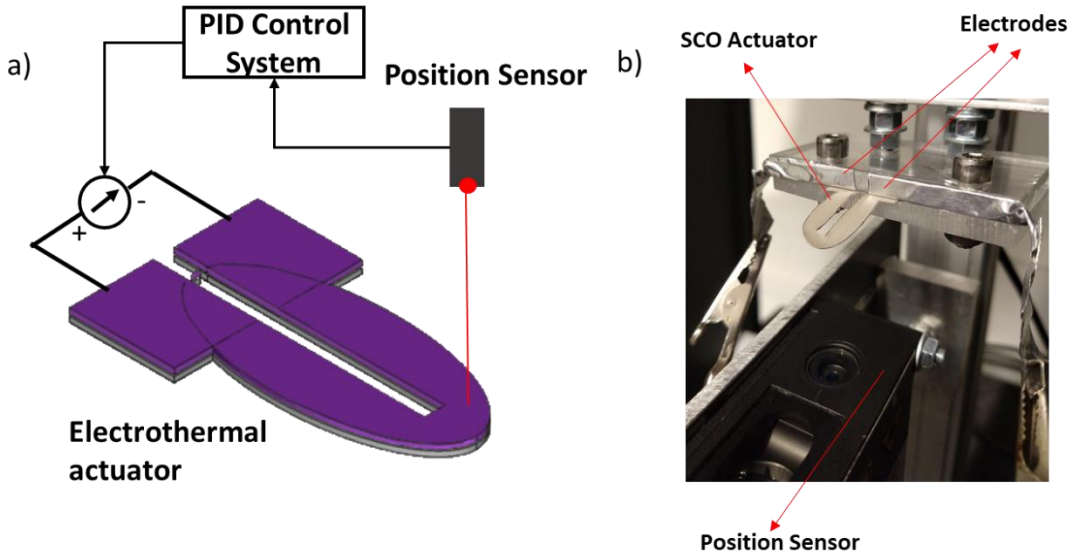

Fig 3.47) a) Scheme of SCO actuator control setup. b) Photo of the experimental setup.

The control software was developed via Labview using the PID toolkit. The flexible software allows for both closed-loop input of a given position for a set of PID parameters and open-loop input via constant current. Using this experimental setup, it becomes possible to reliably and comparably measure the actuation of a series of devices, allowing for optimization of certain fabrication parameters.

3.4.4 Optimization of electrically driven SCO bilayer actuators

The main force driving SCO actuators is the volume change of the SCO complex filler. Therefore, a first factor to consider in the optimization of these bilayer systems is how the use of different types of SCO complexes in the active layer affects the actuation of the devices.

In order to study the effect of the nature of the spin crossover complex on the actuation of our bilayer systems, a series of seven complexes was prepared. This section will thus be divided in two, first we will present the synthesis and physico-chemical characterization of the complexes, as well as the explanation as to why were these complexes chosen. The second section will detail the study of how the seven actuators fabricated with these complexes following the optimized procedure (see page 141) respond to a straightforward open-loop stimulus, to determine which complexes present a better actuation response.

3.4.4.1 Synthesis and physico-chemical characterization of the SCO complexes used to fabricate a series of SCO bilayers

The 7 complexes chosen for this study were: $[Fe(Htrz)_{1.8}(trz)_1(NH_2trz)_{0.2}](BF_4)_1 \cdot 0.7H_2O$ needle-like microparticles (**7**), $[Fe(HB(tz)_3)_2]$ (**8**), $[Fe(NH_2trz)_3]SO_4$ (**9**) $[Fe(C_5trz)_3](tosylate)_2]$ (**10),** $[Fe(C_{18}trz)_3](tosylate)_2$ (**11**), $[Fe(qsal\text{-}I)_2]$ (**12**), and $Fe(NH_2trz)_3](BF_4)_2$ (**13**) . The synthesis of complex **7** was described previously in this work on chapter 2.3.2.2. The synthesis of complex **8** is described by Rat et al [141]. The synthesis of complex **9** was described previously in this chapter

in section 3.3.3.1. Complex **12** was synthesized using the procedure described by Phonsri et al. [194].

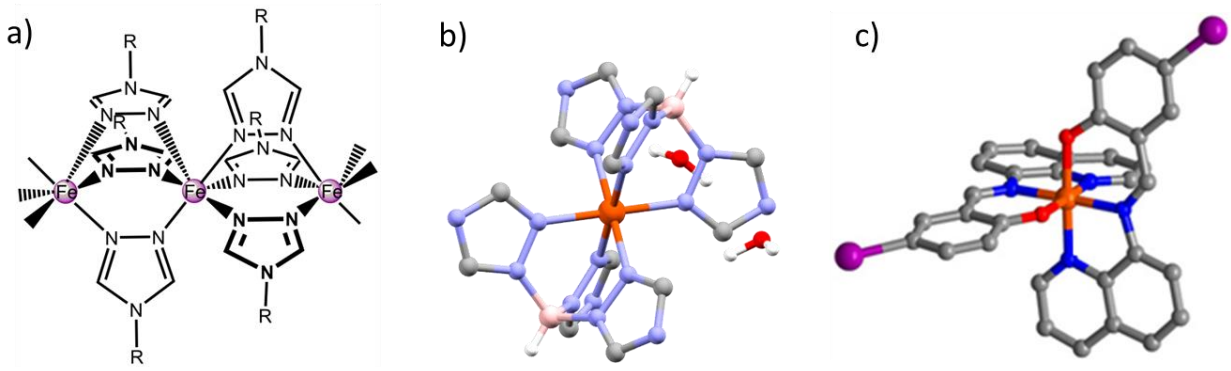

Fig 3.48) Structures of the complexes used. a) General structure of 1D triazole polymer chains. Complexes **7**, **9**, **10**, **11**, and **13** belong to this family. b) [Fe(HB(tz)$_3$)$_2$] (**8**). c) [Fe(qsal-I)$_2$] (**12**).

[Fe(C$_5$trz)$_3$](tosylate)$_2$ (10):

Synthesis of the 4-pentyl-1,2,4-triazole ligand was performed using the following procedure: 2.6 g (43.14 mmol) of monoformyl hydrazine was dissolved in 100 mL of ethanol and 7.6 mL (45.73 mmol) of triethyl orthoformate was added slowly. The mixture was refluxed for 4 h and then cooled to room temperature. 5 mL (43.14 mmol) of amylamine was added and the reaction was kept in reflux for 20 h. The product was cooled to room temperature and dried by vacuum, with a yellow oil as product. The product was diluted in 100 mL of dichloromethane and washed with 3 x 15 mL of water, then the dichloromethane was extracted with 4 x 8 mL of an HCl solution (5 mL of conc. HCl + 3mL of H_2O). The acid solution was then carefully neutralized with NaOH to pH 7-8 and then it was extracted with 4 x 20 mL of dichloromethane. The final solution of dichloromethane was then dried with $MgSO_4$ and then evaporated to dryness resulting in a slight yellow oil as a pure product (68% yield). ^{1}H NMR (300 MHz, $CDCl_3$) δ 8.13 (s, 2H), 3.99 (t, J = 7.2 Hz, 2H), 1.78 (p, J = 7.4 Hz, 2H), 1.42 – 1.17 (m, 4H), 0.86 (t, J = 7.0 Hz, 3H). ^{13}C NMR (75 MHz, $CDCl_3$) δ 142.7, 45.3, 30.4, 28.4, 22.0, 13.7.

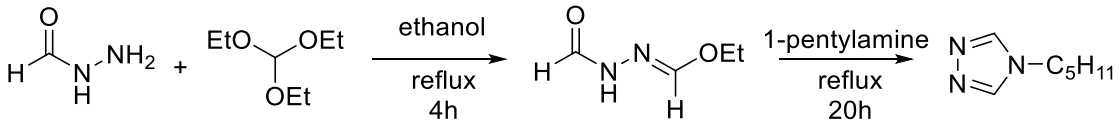

Fig 3.49) Reaction scheme of the synthesis of the 4-pentyl-1,2,4-triazol ligand.

[Fe(C$_5$trz)$_3$](tosylate)$_2$ was synthesized by the following procedure: 750 mg (5.38 mmol) of the 4-pentyl-1,2,4-triazol was dissolved in 25 mL of ethanol. In a separated flask 909 mg (1.79 mmol) of the Fe(OTs)$_2$·6H$_2$O was dissolved in 25 mL of water with some ascorbic acid. The iron solution was added slowly to the triazole solution, and it was stirred for 24 hours at room temperature resulting in a pink precipitate. The pink product was filtrated under vacuum and then washed with water, ethanol and diethyl ether; resulting in 900 mg of a pink solid (56% yield).

Elemental analyses calculated for $[Fe(C_5H_{11}trz)_3](Ots)_2 \cdot 4H_2O$: C, 47.4; H, 6.9; N, 14.2%, found: C, 47.6; H, 7.1; N, 14.2%.

$[Fe(C_{18}trz)_3](tosylate)_2$ (11):

Synthesis of the 4-octadeyl-1,2,4-triazole ligand ($C_{18}trz$) ligand (11.7 g, 82%) was performed in the same conditions using 12 g of stearylamine (82% yield). ^1H NMR (300 MHz, $CDCl_3$) δ 8.17 (s, 2H), 4.02 (t, J = 7.2 Hz, 2H), 1.82 (p, J = 6.7, 6.3 Hz, 2H), 1.41 – 1.15 (m, 30H), 1.01 – 0.76 (m, 3H). ^{13}C NMR (75 MHz, $CDCl_3$) δ 142.7, 45.4, 31.9, 30.7, 29.7, 29.6, 29.6, 29.5 29.5, 29.3, 28.9, 26.4, 22.7, 14.1.

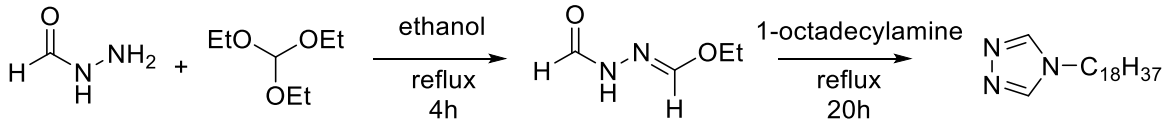

Fig 3.50) Reaction scheme of the synthesis of the 4-octadeyl-1,2,4-triazol ligand.

$[Fe(C_{18}trz)_3](tosylate)_2$ was synthesized by the following procedure: 1.5 g (4.66 mmol) of the 4-octadeyl-1,2,4-triazol was dissolved in 75 mL of ethanol, in a separated flask 787.3 mg (1.55 mmol) of the $Fe(OTs)_2 \cdot 6H_2O$ was dissolved in 75 mL of distilled water with some ascorbic acid. The iron solution was added slowly to the triazol solution, and it was stirred like this for 24 h at room temperature resulting in a pink suspension. It was filtrated under vacuum and then washed with water, ethanol and diethyl ether; resulting in 1.56 g of a pink solid (71% yield). Elemental analyses calculated for $[Fe(C_{18}H_{37}trz)_3](Ots)_2 \cdot 2H_2O$: C, 63.5; H, 9.7; N, 9.0%, found: C, 63.4; H, 9.8; N, 8.9%.

$[Fe(NH_2trz)_3](BF_4)_2$ (13):

The SCO complex $[Fe(NH_2trz)_3](BF_4)_2$ was synthesized using the following procedure: 2.5 mL of a 0.395 M solution of $Fe(BF_4)_2 \cdot 6H_2O$ in H_2O was mixed with a solution containing 727 mg of 1,2,4-4-NH_2-triazole in 2.5 mL of H_2O. The mixture was allowed to react for 24 h. The resulting white solid was cleaned multiple times by centrifugation with ethanol and dried under vacuum (54% yield). Elemental analyses calculated for $[Fe(NH_2trz)](BF_4)_2 \cdot 0{,}3H_2O$: C, 14.8; H, 2.6; N, 34.4%, found: C, 14.8; H, 2,0; N, 34.0%.

Characterization of the SCO complexes:

The transition temperatures of the complexes were characterized by variable temperature optical reflectivity. Since many of the complexes show a run-in effect on the first heating, all the analysis shown for these complexes correspond to the second thermal cycle. Ideally we are looking for complexes with a spin transition temperature just above room temperature, so that the actuators fabricated with these complexes can show a LS-HS-LS thermal cycle without the need for a cooling system. The speed at which the actuator can go from HS to LS depends on how close to room temperature the associated spin transition is. The morphologies of the complexes were determined via TEM.

Complex $[Fe(Htrz)_{1.8}(trz)_1(NH_2trz)_{0.2}](BF_4)_1 \cdot 0.7H_2O$ **7** has a relatively wide hysteresis and high transition temperature which make it less ideal for this study ($T_{1/2}\uparrow$ = 364 K $T_{1/2}\downarrow$ = 345 K). However, it was chosen for this study due to the particle morphology . Indeed, it crystallizes forming needle-like structures, which could potentially amplify the effect of the volume change of the spin crossover if correctly aligned along the beam axis of the actuator.

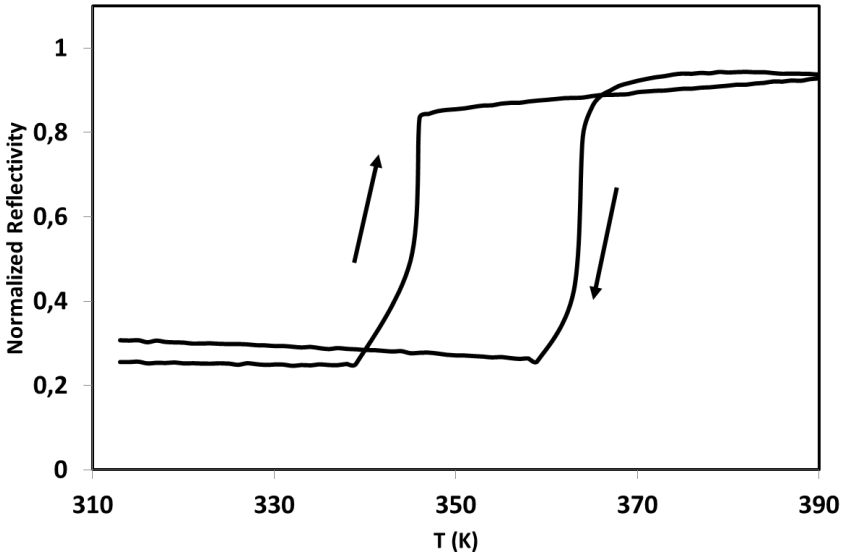

Fig 3.51) Variable temperature optical reflectivity of complex **7** (second thermal cycle).

TEM analysis of this complex reveals highly anisotropic needle-like crystals between 2 µm and 3 µm in length (Fig 3.52). Successful alignment of these particles upon the preferential axis for the actuation of the devices would significantly improve the effect of the volume change upon the spin transition, and as a result, the actuator would present significantly increased motion.

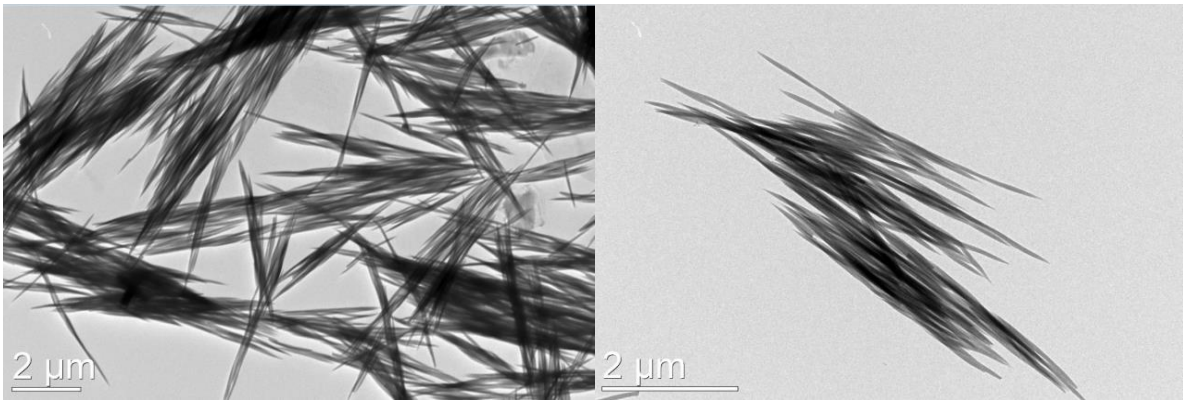

Fig 3.52) TEM images of needle-like particles of **7**.

Complex $[Fe(HB(tz)_3)_2]$ **8** is a molecular complex with a very abrupt transition and virtually no hysteresis (Fig 3.53). This complex shows a very reproducible and stable spin transition. It has been shown to be able to withstand over 10^7 thermal cycles around the spin transition with no degradation [195]. It was precisely because of this highly reliable spin transition that this complex

was chosen for the study. TEM images of the complex reveal micrometric, inhomogeneous crystals.

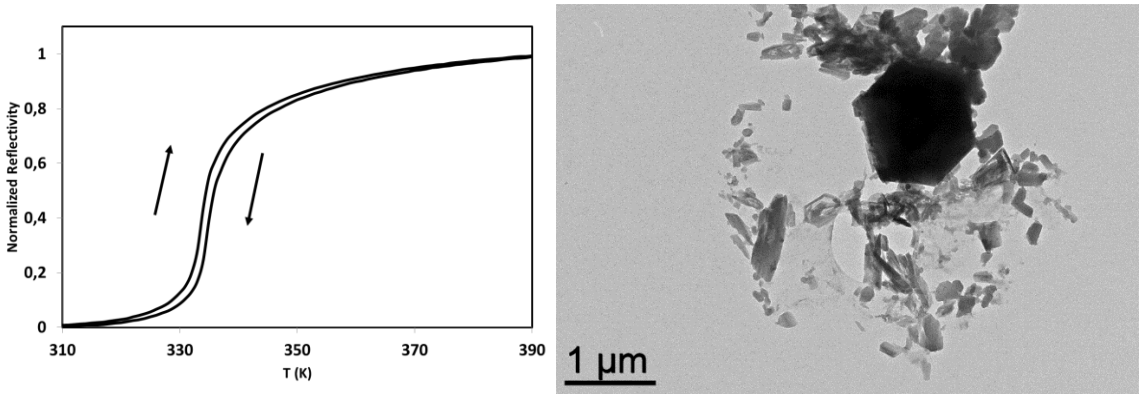

Fig 3.53) Variable temperature optical reflectivity (second thermal cycle) and TEM image of **8.**

The spin crossover complex $[Fe(NH_2trz)_3]SO_4$ **9** presents an abrupt spin transition with a relatively small hysteresis loop between 345 and 332K. It was chosen for this study for its closeness to room temperature. TEM images of the complex reveals micrometric anisotropic rods, which are relatively heterogeneous in size and shape.

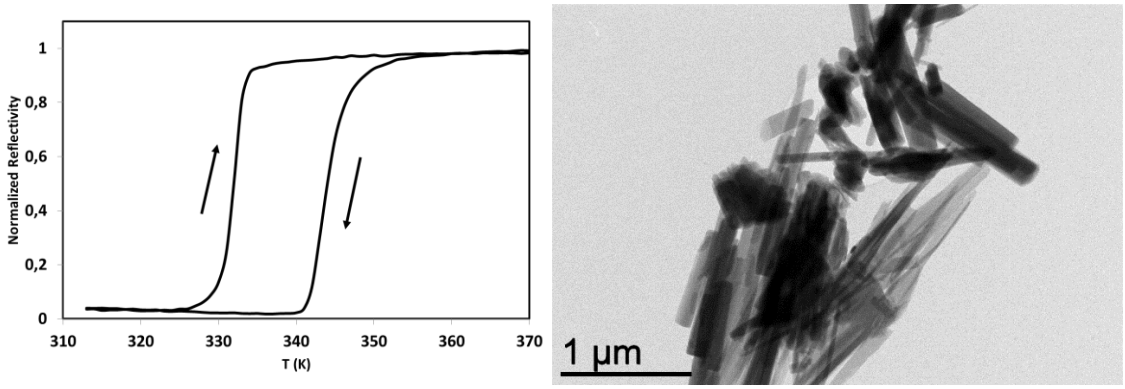

Fig 3.54) Variable temperature optical reflectivity (second thermal cycle) and TEM image of **9.**

Complex $[Fe(C_5trz)_3](tosylate)_2]$ **10** presents a hysteresis loop between 340 and 315 K (Fig 3.55). A relatively low $T_{1/2}\uparrow$ should allow the actuator to rapidly go from the LS to the HS state. This complex was mainly chosen for its transition temperature close to room temperature. TEM analysis of the complex shows a microcrystalline, heterogeneous powder.

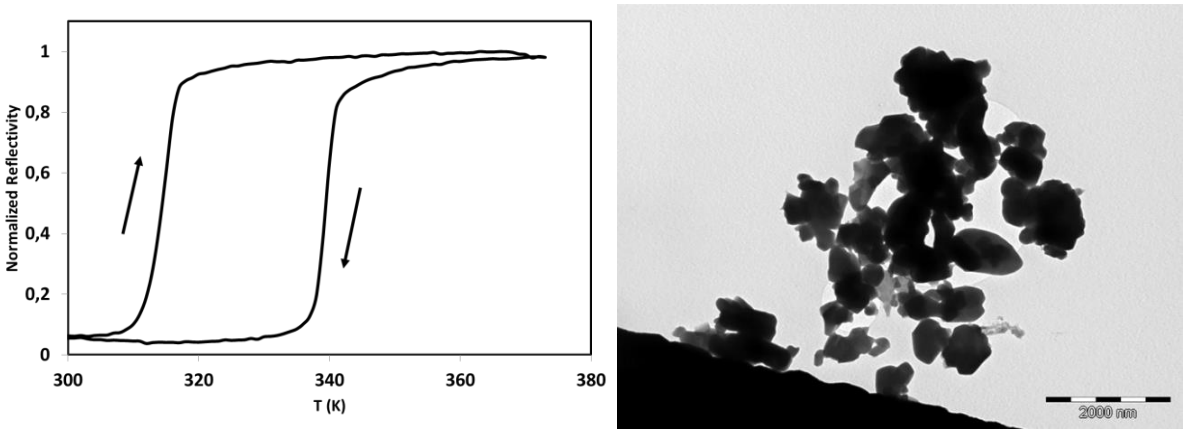

Fig 3.55) Variable temperature optical reflectivity (second thermal cycle) and TEM image of **10.**

Complex $[Fe(C_{18}trz)_3](tosylate)_2$ **11** Is a complex which shows spin transition properties very similar to those of $[Fe(C_5trz)_3](tosylate)_2$, with a more gradual transition and shifted slightly towards room temperature (Fig 3.56). It was chosen for this study to determine if the long alkyl chains have an effect on the stiffness of the SCO/P(VDF-TrFE) composite layer, and if this effect in turn is reflected on the actuation of the bilayer material.

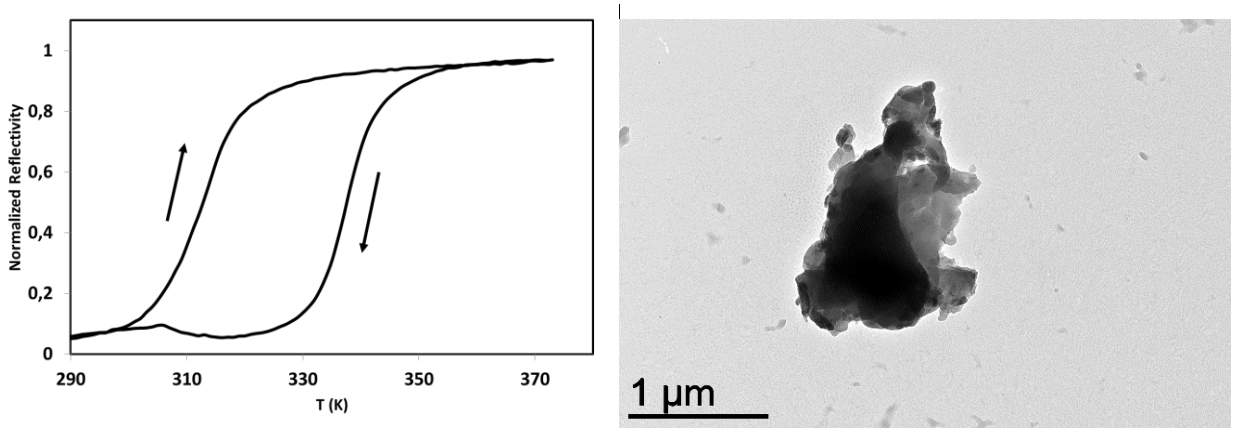

Fig 3.56) Variable temperature optical reflectivity (second thermal cycle) and TEM image of **11**

Complex $[Fe(qsal\text{-}I)_2]$ **12** is a molecular spin crossover complex with a hysteresis centered exactly around room temperature ($T_{1/2}\uparrow$ = 296 K, $T_{1/2}\downarrow$ = 291 K, Fig 3.57). It was chosen for this study to see if it would be possible to create a lock-state actuator by heating the actuator beyond the spin transition and then leaving it locked on the HS state as the temperature of the actuator goes down to room temperature but not low enough to reach the cooling branch. TEM images reveal large, multiple-microns long crystals.

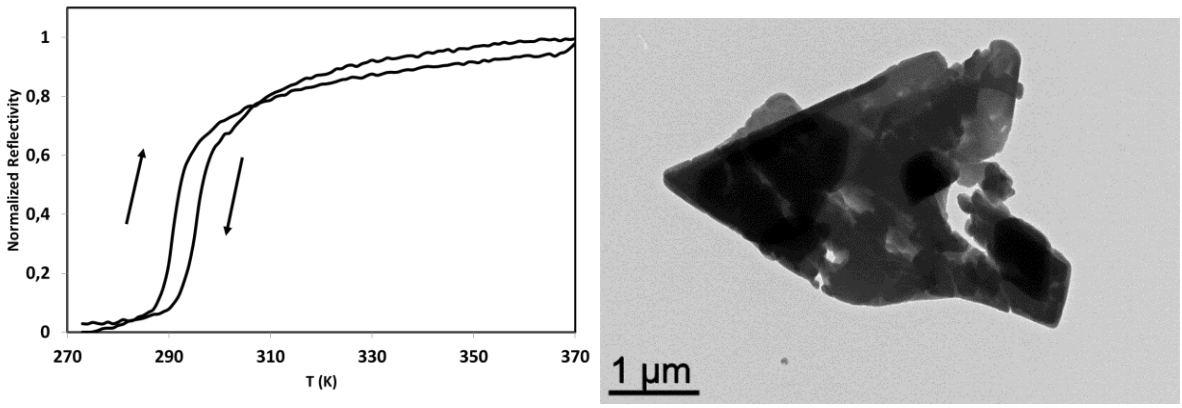

Fig 3.57) Variable temperature optical reflectivity (second thermal cycle) and TEM image of **12.**

The SCO complex $Fe(NH_2trz)_3](BF_4)_2$ **13** has a spin transition well below room temperature with $T_{1/2}\uparrow$= 284 K and $T_{1/2}\downarrow$ = 279 K (Fig 2.58). It was chosen for this study to act as a blank sample. By the inclusion of a material with physical characteristics similar to other SCO complexes, but which will show no spin transition in the considered temperature range for actuation, we can determine how much of the actuation of our bilayers is caused by the SCO phenomenon and how much of it is due simply to differences in the thermal expansion coefficient of the two layers.

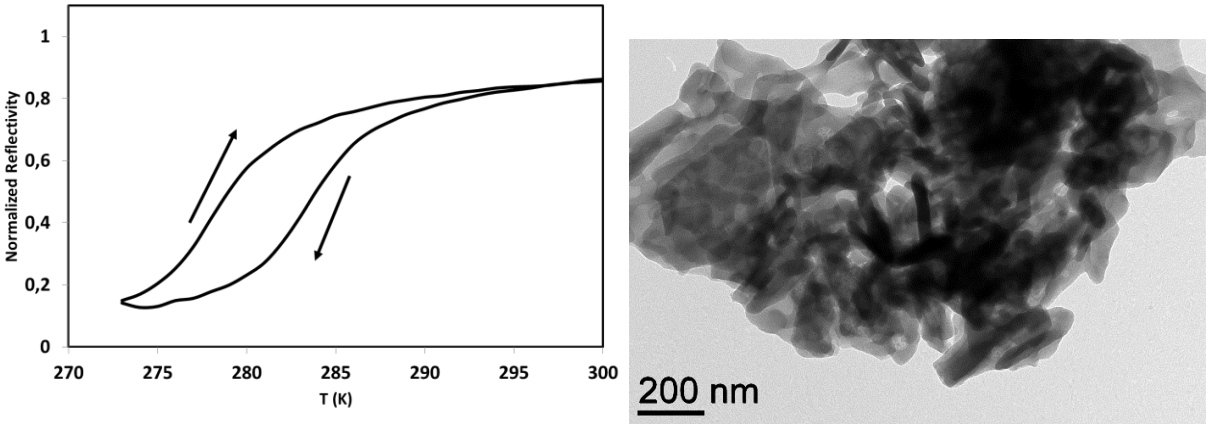

Fig 3.58) Variable temperature optical reflectivity (second thermal cycle) and TEM image of **13**.

Table 3.4) Review of the morphology and spin transition temperatures of the spin crossover complexes used for the fabrication of actuators:

Actuator	SCO complex	Morphology	$T_{1/2}\uparrow$ (K)	$T_{1/2}\downarrow$ (K)
7	$[Fe(Htrz)_{1.8}(trz)_1(NH_2trz)_{0.2}](BF_4)_1 \cdot 0.7H_2O$	2-3 µm long rods	364	345
8	$[Fe(HB(tz)_3)_2]$	Microcrystalline	336	334
9	$[Fe(NH_2trz)_3]SO_4$	Microcrystalline	345	332
10	$[Fe(C_5trz)_3](tosylate)_2$	Microcrystalline	340	315
11	$[Fe(C_{18}trz)_3](tosylate)_2$	Microcrystalline	338	311
12	$[Fe(qsal\text{-}I)_2]$	Microcrystalline	296	291
13	$[Fe(NH_2trz)_3](BF_4)_2$	Microcrystalline	284	279

3.4.4.2 Characterization of a series of actuators with different SCO complexes

Using complexes **7-13**, a series of conductive SCO@P(VDF-TrFE)/Ag@P(VDF-TrFE) bilayers were fabricated following the procedure described in page 141. Concentration of SCO in the active layer was 25 wt%. The bilayer films were then cut into a circuit shape (page 138) using a Realmeca RV 2-SP high precision lathe by attaching the bilayer films to an aluminium support.

3.4.4.2.1 Scanning electron microscopy of SCO@P(VDF-TrFE)/Ag@P(VDF-TrFE) bilayers

SEM imagery of the composite are shown in Annex A.3.4 - A.3.9. As examples, Fig 3.59 shows SEM images of samples **7** and **12**. Remarkably, for all samples analyzed, the Ag@P(VDF-TrFE) and the SCO@P(VDF-TrFE) layers were easily distinguishable and there seemed to be no diffusion between them. Yet, the interface between the layers is continuous, suggesting that there is no gap between the layers, and thus it is expected that we will not observe delamination of the samples upon repeated actuation.

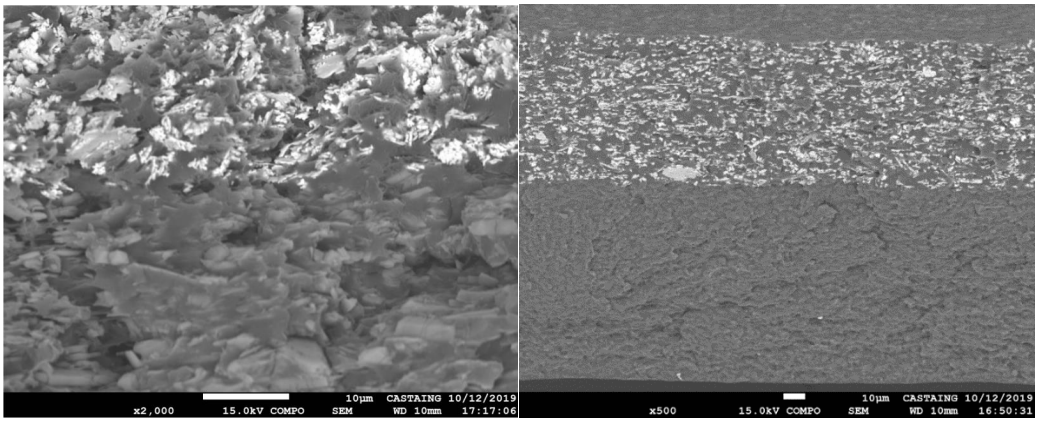

Fig 3.59) SEM images of the cross section of actuators **12** and **7**. Ag@P(VDF-TrFE) layer (up) and SCO@P(VDF-TrFE) layer (down).

In order to confirm whether the needle-like anisotropic particles in actuator **7** were aligned in the composite, we collected SEM images of its cross-section in two different orientations (Fig 3.60): one parallel to the direction of the blade-casting procedure and one perpendicular. Interestingly, the parallel orientation of the sample shows particles aligned across the length of the cross-section, whereas the perpendicular orientation shows what would seem to be particles aligned perpendicular to the cross-section, suggesting that indeed the anisotropic particles were aligned by the blade-casting process. These results are also confirmed by SEM images of the surface of the SCO@P(VDF-TrFE) layer, which clearly shows the anisotropic objects with a preferential orientation across the surface of the sample (Fig 3.61).

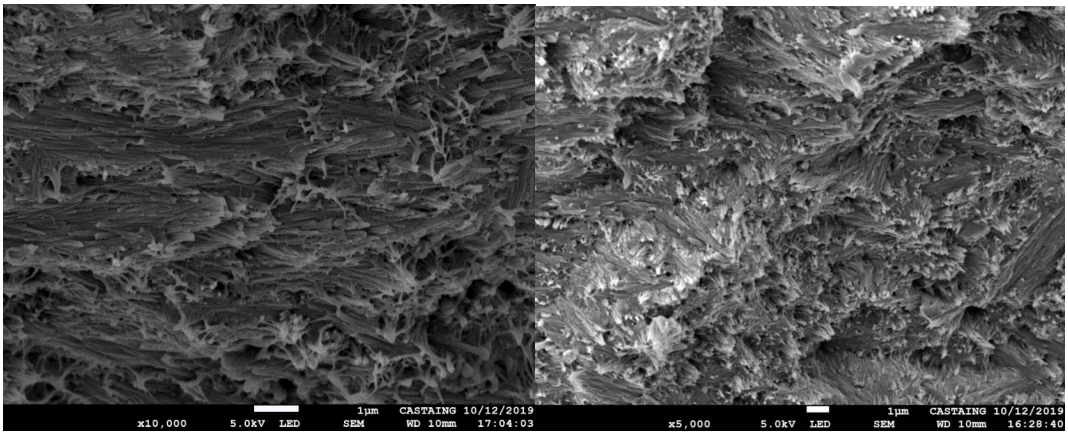

Fig 3.60) SEM images of the cross section of active SCO(**7**)@P(VDF-TrFE) layer of actuator **7:** parallel to the blade-casting direction (left), perpendicular to the blade-casting direction (right).

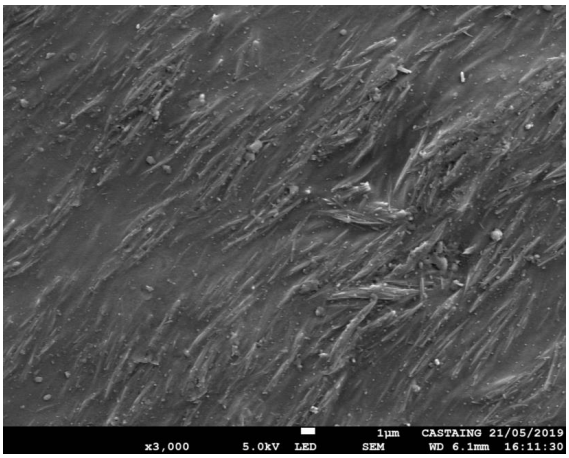

Fig 3.61) SEM image of the surface of the active SCO(**7**)@P(VDF-TrFE) layer of actuator **7**.

3.4.4.2.2 Open loop actuation properties of the bilayer samples

In order to characterize the actuating properties of each device, the samples were activated under open-loop control and their position tracked and measured. Each sample was excited by an input current sufficient to induce the maximum movement possible. The measured deflection amplitudes were thus the maximal deformation that the samples could be subjected to (Fig 3.62).

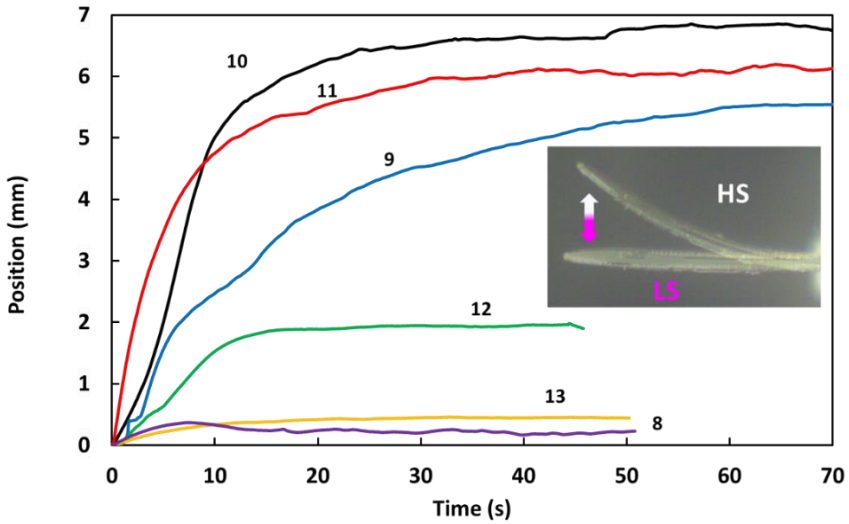

Fig 3.62) Highest amplitude open-loop actuation curves for a series of actuators using different SCO complexes. The inset shows the reversible movement of bilayer **10**.

In this study, actuator **13** is a blank, because $[Fe(NH_2trz)_3](BF_4)_2$ has a spin transition temperature well below room temperature and thus is not active in the implemented temperature range. As such, its actuation results exclusively from the thermal expansion mismatch of the two composite layers. Indeed, it shows an actuation amplitude which is an order of magnitude smaller than that of actuators **9-12**. This proves that the strain associated with the SCO phenomenon plays a crucial role in the movement of the actuators. Actuator **10** displays the most interesting properties, both in terms of the maximum actuation amplitude and in terms of the response speed. Actuators **11** and **9** show a comparable performance to that of actuator **10**, albeit with somewhat lower amplitude and slightly different response times. The good performance of the actuators **9**-**11** is likely related to the large volumetric strain (up to 10 vol% [196]) associated with the SCO in this family of Fe(II)-triazole complexes and to the abrupt nature of the spin transitions occurring at relatively low temperatures. To accurately perform the full actuation of sample **12** it was cooled down to the LS state using liquid nitrogen fumes. Nevertheless the lower deflection amplitude is in agreement with the rather low volumetric strain (ca. 4%) measured for the "molecular" active material [194]. Unfortunately, it was impossible to lock the spin state of composite **12** due to the too narrow hysteresis and the inhomogeneity of the heating of the device. Actuator **8** is a particular case. It shows an actuation amplitude which is comparable (even slightly lower) to that of the blank, despite the fact that the $[Fe(HB(tz)_3)_2]$ complex exhibits ca. 4.5 vol% strain associated with the SCO well above room temperature [197]. This intriguing observation might be related to the pronounced anisotropy of the transition strain in $[Fe(HB(tz)_3)_2]$ determined by X-ray diffraction on a single crystal [141]. Indeed, if the microcrystals are aligned in such a way that the *c*-axis of the orthorhombic unit cell is normal to the long axis of the bilayer cantilever, the bilayer curvature will be very small or even of opposite sign. Table 3.5 summarizes the deflection amplitudes and the corresponding angle of the bilayer samples.

Table 3.5) Deflection amplitudes and bending angles upon open-loop excitation of actuators **8**-**13**.

Actuator	SCO complex	Deflection amplitude (mm)[a]	Bending angle (°)[a]
8	$[Fe(HB(tz)_3)_2]$	0.2	0.6
9	$[Fe(NH_2trz)_3]SO_4$	5.5	16.0
10	$[Fe(C_5trz)_3](tosylate)_2$	6.8	19.9
11	$[Fe(C_{18}trz)_3](tosylate)_2$	6.1	17.8
12	$[Fe(qsal\text{-}I)_2]$	1.9	5.5
13	$[Fe(NH_2trz)_3](BF_4)_2$	0.4	1.1

Actuator **7** had outstanding performance under open-loop conditions (Fig 3.63). Actuator **7**, rather than bending at an angle as actuators **8**-**13**, folds over itself, showing a spiral winding reminiscent of the coiling movements of plant tendrils [198]. This however means that under our current measurement setup it becomes impossible to measure the movement of the actuator with our optical distance tracker. Operation in closed loop becomes near-impossible. Instead we are limited to recording the movement under open-loop conditions.

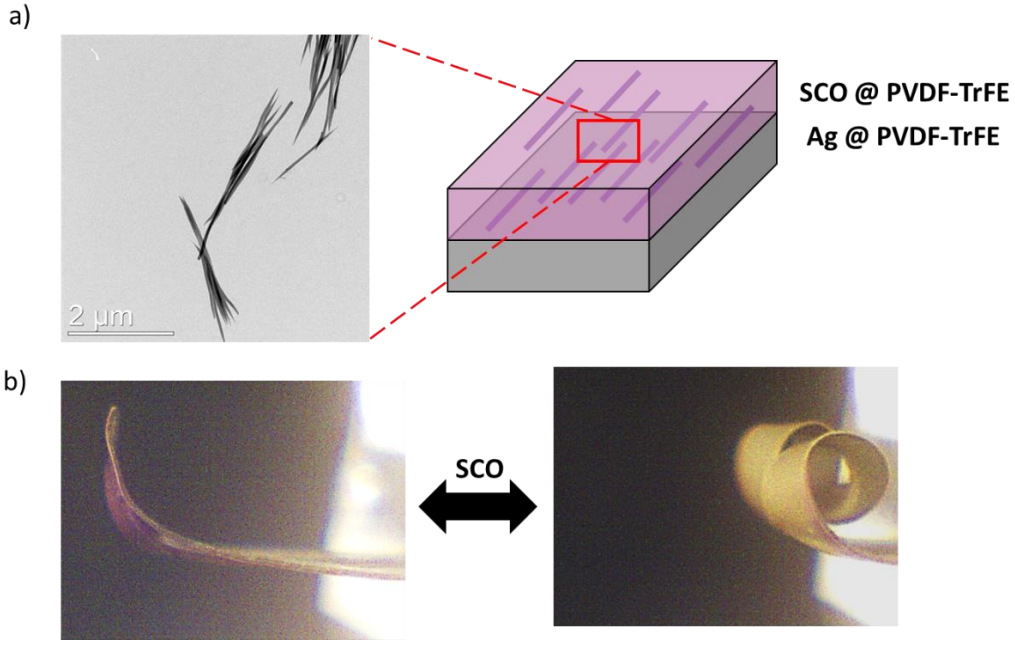

Fig 3.63) a) Scheme of the bilayer device **7** prepared using rod-like microcrystals of complex **7** with preferential orientation in the P(VDF-TrFE) matrix. A TEM image of the microcrystals is also shown b) Reversible electrothermal actuation of a bilayer device **7** under open-loop conditions at 0.7 A.

In order to test the extent of the capabilities of this device, increasing weights with the same input current were added to the actuator and its performance recorded under open-loop conditions. Actuator **7** can reversibly perform this extraordinary movement even while holding a load equivalent to 9 times of its own weight (Fig 3.64). On loads higher than that, actuation quickly becomes irreversible, leading to permanent deformation of the devices, and after a few actuation cycles, the deformation induces a breakdown of the conductive layer.

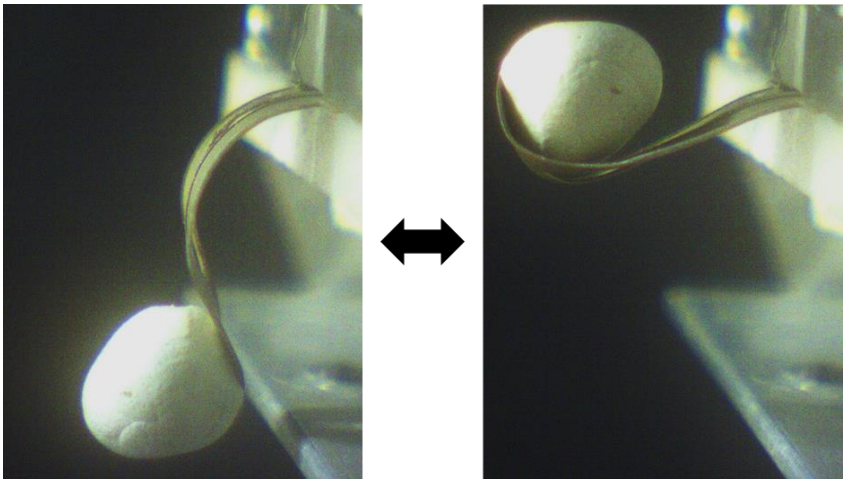

Fig 3.64) Electrothermal actuation of a bilayer device **7** under open loop conditions at 0.7 A with a load equivalent to 9 times its own weight.

In order to demonstrate the effect of the alignment of the particles, an actuator was cut with an orientation perpendicular to the direction of the blade-casting, in contrast to actuator **7** which has a parallel orientation. This new device will be referred to as Actuator **7**$_{\perp}$. Perpendicular cut bilayer actuators **7**$_{\perp}$ systematically broke down during the first cycles of actuation, suggesting that particle alignment governs not only the actuation performance, but also the fracture strength of the devices.

It is interesting to notice that in contrast to sample **7**, the anisotropic character of sample **9** does not permit to increase the performance of the actuation, perhaps because of the much lower aspect ratio and/or the inhomogeneity of the size and shape of the particles. SEM images (A.3.4) do not suggest that the SCO particles are aligned in actuator **9.**

3.4.4.2.3 Tensile analysis of the bilayer sample 7

In order to confirm the hypothesis of a particle alignment in the matrix, the active layers of actuators **7** and **7**$_{\perp}$ were subjected to tensile stage analysis under constant force. In this analysis, the sample is subjected to a constant force and thermally cycled, and the strain of the sample is measured. From this strain we can thus obtain the effective thermal expansion of the composites at a given temperature. It would be expected that if there is an alignment of the particles in the matrix in the preferential crystallographic axis of the complex, then the sample being analyzed parallel to the alignment of the particles should present a much higher effective thermal expansion coefficient at the spin crossover temperature, as a result of the associated

volume change of the spin transition. Indeed, as shown by Grosjean et al, complexes of the triazole family often show a crystallographic axis with an increased linear expansion upon the spin transition[199].

As expected, tensile analysis shows an effective thermal expansion of the composite parallel to the blade casting almost one order of magnitude greater (Fig 3.65). This confirms the alignment of the particles of the matrix, which can be explained by the fluid flow during blade casting, which results in a significant torque that aligns the anisometric particles in the casting direction [200].

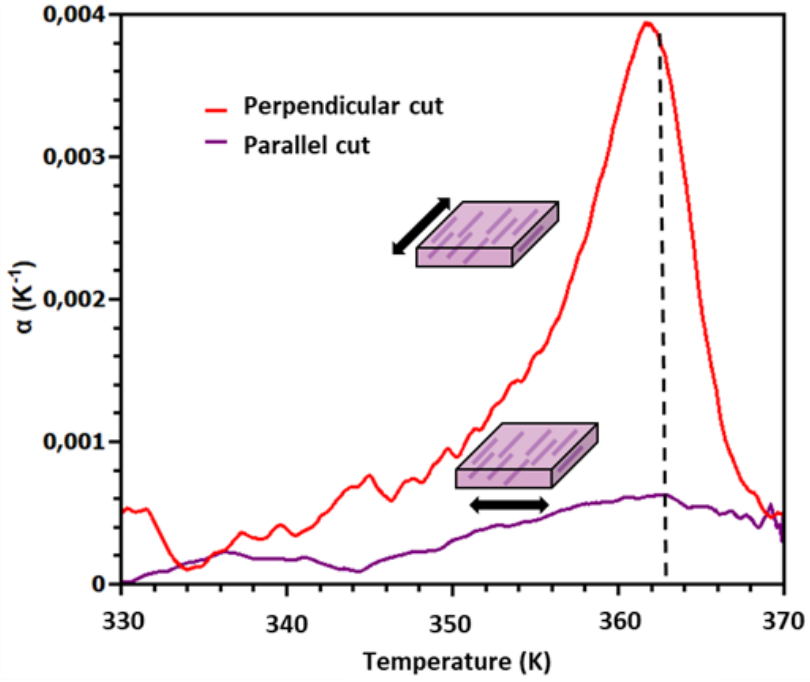

Fig 3.65) Linear thermal expansion coefficient of composite **7**$_{\perp}$ for perpendicular and **7** for parallel cut of the bilayers vs. the casting direction. Vertical dotted line indicates the spin transition temperature upon heating ($T_{1/2}\uparrow$) of the composites.

3.4.4.2.4 Actuation properties of the bilayer samples and Timoshenko beam theory

While the performance of actuator **7** is clearly extraordinary, it cannot be estimated properly by our distance tracker setup, making it difficult to compare to other devices. To quantitatively measure and compare the actuating properties of the different devices, rectangular bilayer strips were fabricated to perform a controlled temperature measurement to accurately estimate the actuation properties of the material using the Timoshenko beam theory [12] (Fig 3.66). Samples **10**, **7** and **7**$_{\perp}$ were evaluated. The different bilayer samples were submerged in glycerol to ensure homogeneous thermalization.

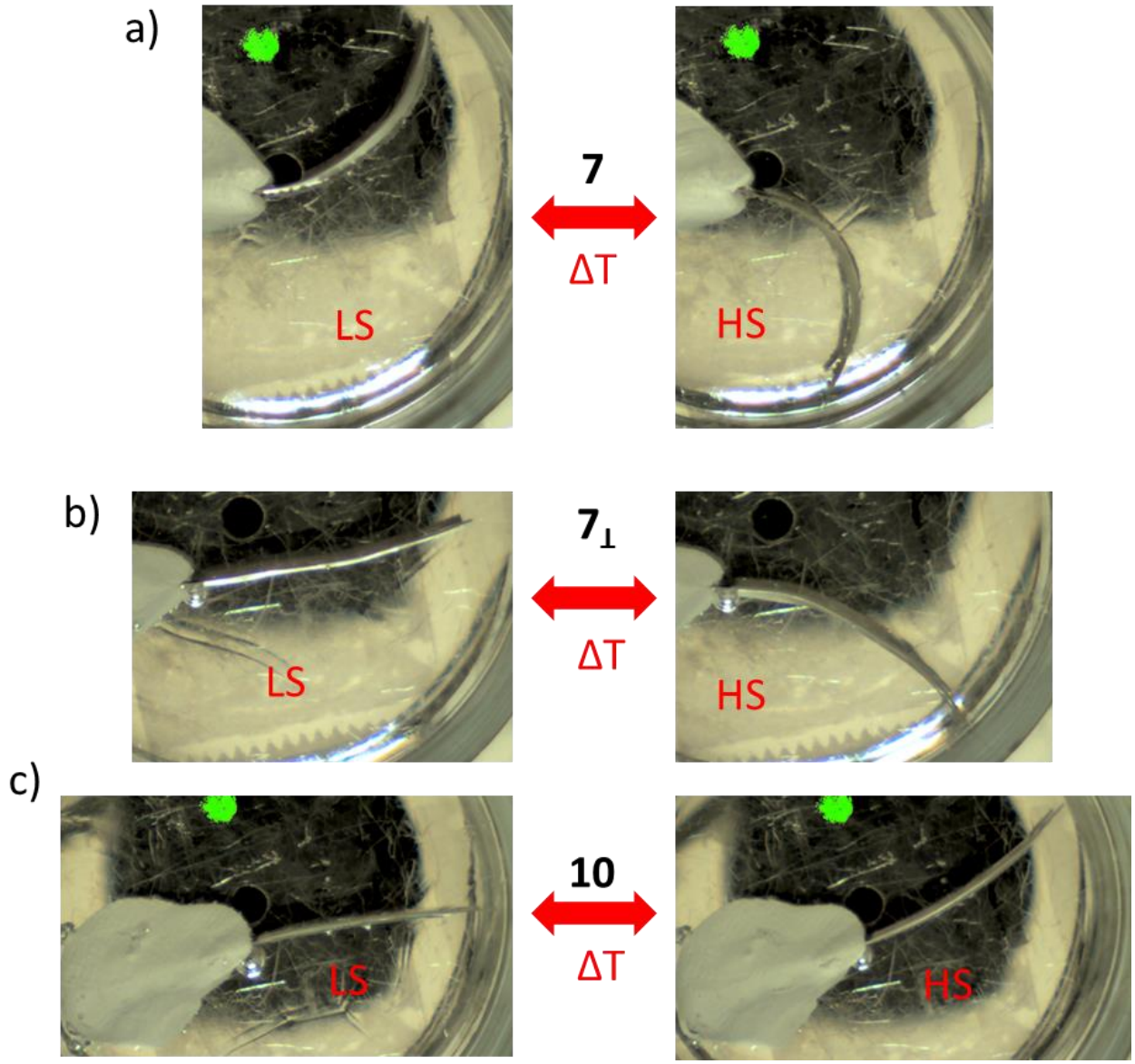

Fig 3.66) Movement of rectangular bilayer strips upon the spin transition. a) Bilayer **7**. b) Sample **7**$_{\perp}$. c) Sample **10**.

Using Timoshenko's beam theory, it is possible to associate the change in curvature *k* of a bilayer beam to the strain produced by the spin transition *ΔL/L* [11]. The Young's modulus of each layer at the SCO temperature were obtained from tensile mechanical analysis. Linear thermal expansion coefficients were likewise obtained from temperature-controlled mechanical testing. The change in curvature was calculated from the tip deflection by graphical estimation using the following principle [179]:

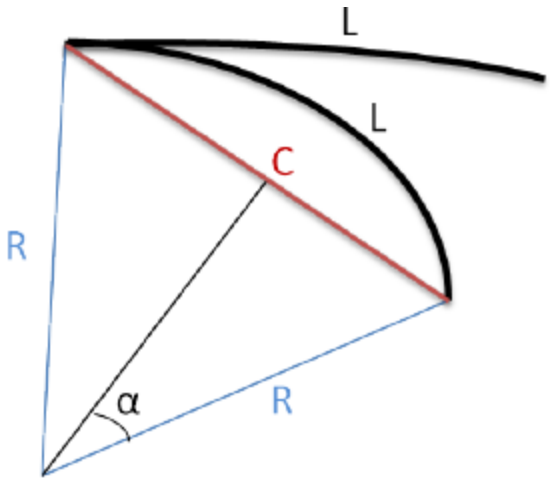

Fig 3.67) Scheme explaining how to graphically estimate the curvature of a cantilever.

Where:

$$k = 1/R \quad (10)$$

With these parameters, the strain of the active layer caused by the spin transition is estimated. With the strain from the spin transition we can then calculate the volumetric work density W/V of the actuator with the following equation:

$$\frac{W}{V} = \frac{E(\frac{\Delta L}{L})^2}{2} \quad (11)$$

The linear strain of the active layer corresponding to the percentage change in length upon excitation normalized to the initial length of the device is 2% for the actuator **7**, four times more than the corresponding sample with a perpendicular orientation of the rods. Such effect has been also reported for other classes of materials such as ceramics, hydrogels and lightweight cellular composites [200,201]. In particular, Gladman et *al.* used a 3D printing approach to obtain a hydrogel composite ink composed of cellulose fibrils embedded in a soft acrylamide matrix. The printed architectures exhibit a comparable increase of the swelling strains when passing from the transverse to longitudinal orientation of the fibrils.

Using the linear strain, the volumetric work density of the actuator **7** could be estimated as W/V = 260 mJ cm^{-3}. This value determines the maximum amount of work per unit volume that an actuator can perform.

Stress is the force generated by the artificial muscle upon excitation, normalized to its initial cross-sectional area. Stress was estimated for each sample to be 14.7 (**10**), 26.0 (**7**) and 8.0 (**7**$_{\perp}$) MPa. Comparison of these mechanical parameters with those of other polymer based soft actuators show that both composites **10** and **7** have mechanical properties that are highly competitive with other materials used in the field, with composite **7** being even in the upper range in work density (Table 3.4). This shows that these SCO bilayer actuators might be of interest in the domain of soft robotics.

Table 3.6) Comparison of SCO bilayer actuators with other polymer based soft actuators.

Active material	Actuator dimension (mm)	Young's modulus (E) (GPa)	Strain (ΔL) (%)	Work density (WV) (mJ/cm^3)	Ref.
Nylon	90 × 3 × 0.87	0.4	2.5	125	[184]
PEDOT	6 × 1 × 0.018	0.00033	0.5	0.004	[188]
Bucky gel	8 × 4 × 0.465	0.26	1.9	45	[186]
Polypyrrole	0.58 × 0.22 × 0.16	0.12	14	1180	[187]
Ru-sulfoxide polymer	5 × 1 × 0.002	0.02	0.105	0.0055	[174]
SCO@DS3000	20 × 4 × 0.24	0.28	0.33	1.5	Present work
10@P(VDF-TrFE)	30 x 20 x 0.15	1.2	1.13	76	Present work
$7_{\perp}$@P(VDF-TrFE)	30 x 20 x 0.15	1.3	0.6	24	Present work
7@P(VDF-TrFE)	30 x 20 x 0.15	1.3	2.0	260	Present work

Despite the spectacular properties of bilayer device **7** as an actuator, the fact that we cannot accurately measure its movement in real time using a distance tracker makes it impossible for it to provide feedback to the closed-loop controller, which relies on feedback from the actuator to adjust the input signal. For this reason, we will focus now on the use of the PID control system to operate actuator **10** under closed loop conditions.

3.4.5 Closed-loop control of spin crossover bilayer actuator 10:

This section will detail the closed-loop control of actuator device **10** (with complex $[Fe(C_5trz)_3](tosylate)_2$) showcasing its high controllability, stability and loading capacity. First, we will present the process of fine tuning the PID controller; then we will show the results of applying closed-loop control to actuator **10** and the dramatic increase in performance. Finally, we will present the effect that varying the concentration of the SCO complex in the active layer has on the closed-loop control of the actuators.

The first step in order to prepare the parameters of a PID system is to know the operating range of the actuator. In order to do this, actuator **10** was excited under open-loop conditions with a series of different electrical currents and its position tracked to determine the current needed to produce the maximal actuation of the sample and the minimal current needed to produce an effect on the actuator at all. This analysis showed an operating range between 0.7 and 1.2 A. The reaction time (RT) will be defined as the time needed for the actuator to reach 95% of the displacement setpoint, or in this case, the maximal displacement at a given current.

We see that for actuator **10** the RT oscillates around 20-40 s under open loop conditions. While obviously a more intense current would result in faster displacement, a constant current that is higher than the current needed for maximal actuation of the sample often leads to overheating of the sample, which in turns leads to melting of the P(VDF-TrFE) matrix and the breaking down of the actuator as the conductive layer is broken. This is thus the limit of the system under open-loop conditions.

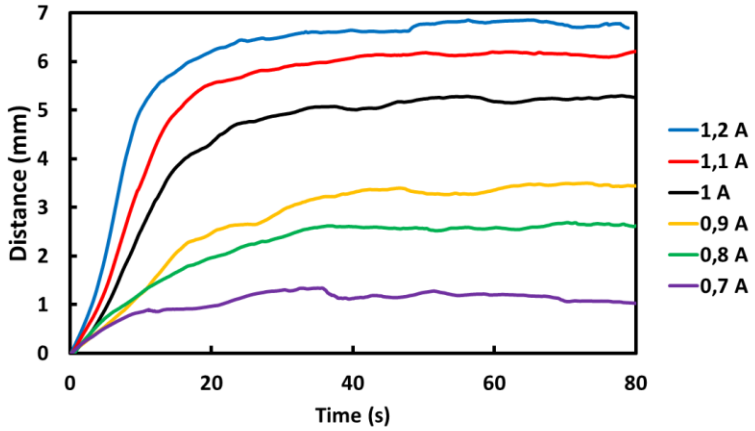

Fig 3.68) Open-loop excitation of actuator **10** under different electrical currents.

It is interesting to note that the SCO actuators clearly present a series of continuous steady states at any given current. This actuator can thus remain at equilibrium at any given position with the correct current input. This is because the thermalization of the actuator as a result of the Joule effect is inhomogeneous: the tip of the actuator has a smaller surface and higher electrical resistance, heating up more from the Joule heating while the base is wider and less heat is produced towards the base. As a result, at any given time, a portion of the device remains at the low spin state while another portion is on the high spin state. We follow the temperature of the device via an infrared camera to avoid overheating, and the thermal imaging confirms this hypothesis perfectly, showing distinct temperatures at the tip and the base of the actuator for any given thermal cycle.

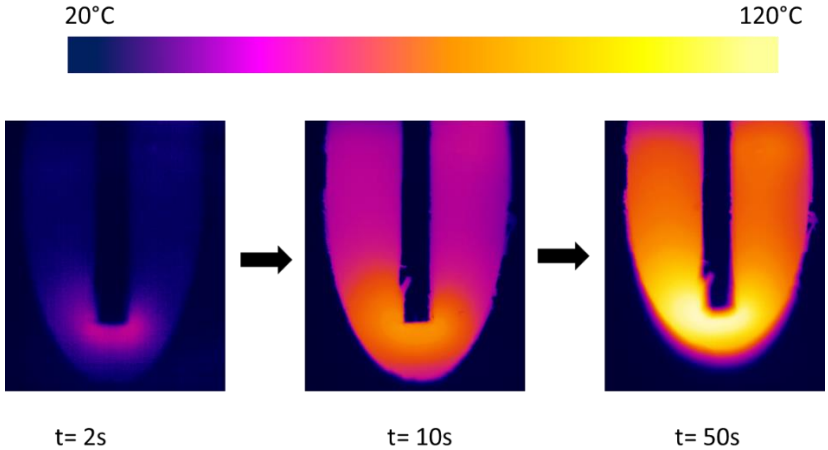

Fig 3.69) Thermal imaging of actuator **10** during an actuation cycle.

Having established the range of actuation of our device, we can manually tune the parameters K_p T_d and T_i of the PID system. These are determined by making the actuator move under closed-loop conditions and tracking its response over time. The fine-tuning is performed by trying to reduce oscillation of the actuator around the position input as much as possible while also trying to minimize the RT of the actuator. While oscillations of the actuator are unavoidable, we optimize the system by ensuring that these oscillations remain within 5% of error of the given position input.

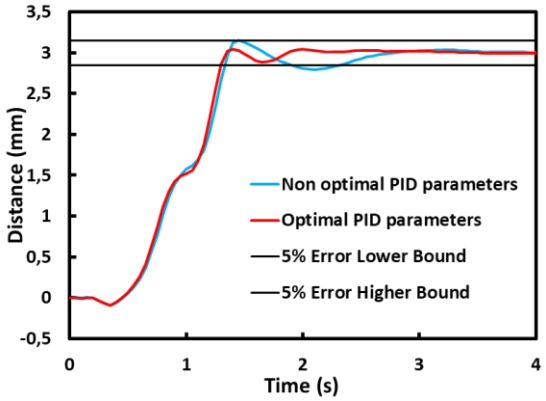

Fig 3.70) Closed loop actuation of actuator **10** under an optimized and a non-optimized set of PID parameters. Black lines indicate the region within 5% of error of the position setpoint.

It was found that this actuator operates better with a different set of PID parameters for each target distance, so the PID parameters were manually established for a set of target distances: 2 mm, 3 mm, 4 mm and 5 mm. While the actuator is capable of reaching 6 mm displacement, this is a displacement very close to the absolute maximal displacement and if used as set point it is possible that the oscillatory nature of the input, especially on unoptimized PID parameters, will cause the device to surpass maximal displacement, overheat and break down. For this reason we will avoid taking the system to its absolute limits under PID closed loop control.

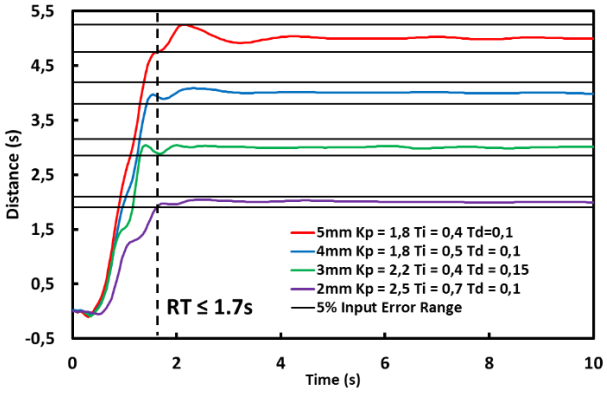

Fig 3.71) Closed loop actuation of actuator **10** with a 5, 4, 3 and 2 mm displacement input with optimized PID parameters. Black lines indicate the region within 5% of error of each input. Dotted line indicates the highest reaction time.

Interestingly, the reaction time (RT) for all distance setpoints was below 1.7 s, which is indicative of the average response time of our actuator. This is a considerable increase in performance when compared to the open-loop actuation, which presented a RT of around 20 s in the best-case scenario. This happens primarily because in open-loop actuators the current input is constant and cannot surpass 1,2 A after which the current input risks overheating and destroying the sample. Closed-loop actuation allows for a dynamic current input, which begins the actuation routine by saturating the current input at 3 A for 0.5 s to heat the sample to the spin transition temperature and bypass the latent heat of the spin transition. Once the main energetic requirement has been bypassed and the actuator starts moving, the PID then adjusts the current input to an input comparable to those of open-loop actuation. The moderate current input allows the controller to keep the system in equilibrium at the desired displacement.

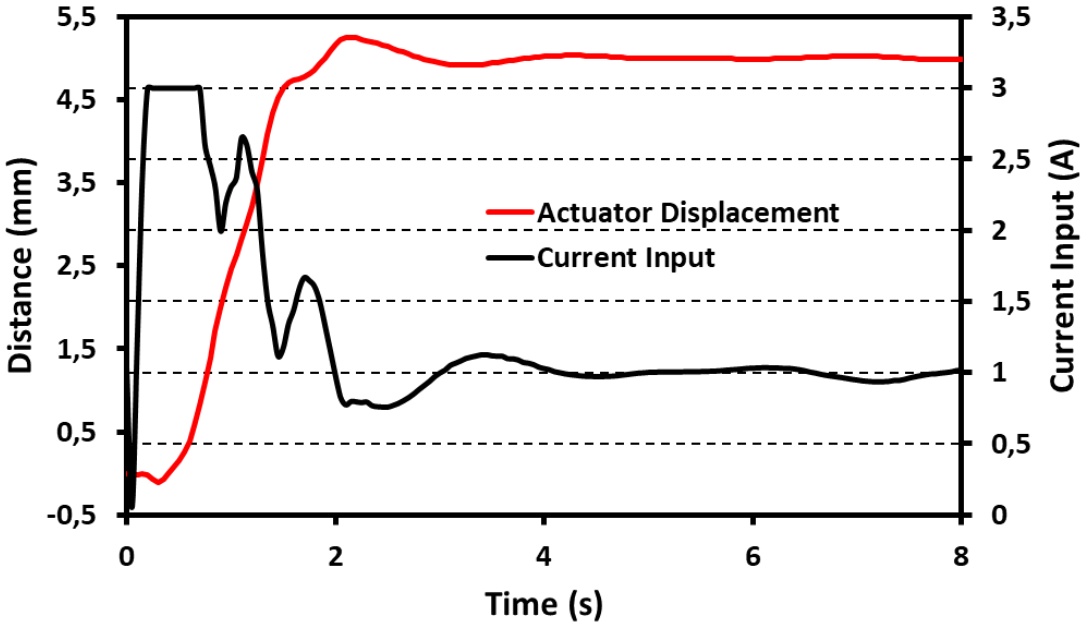

Fig 3.72) Closed loop actuation of actuator **10** with a 5 mm displacement setpoint (red). Current input of the control system during a 5 mm displacement cycle (black).

In order to confirm the ability of our actuator to perform work in a reliable manner under different working conditions, we repeated the closed-loop experiments at 2, 3, 4 and 5 mm, using the same set of PID parameters, but this time bearing a series of loads equivalent to 1, 2, 3 and 5 times the mass of the actuator (67 mg, 134 mg, 204 mg and 343 mg). Even at the highest load, and with the highest displacement, the response time remained unchanged, proving that the device can reliably perform mechanical work under a variety of conditions in a highly controllable manner. Response time for all inputs, at all loads remained virtually identical, with an average of 1.55 s (see Fig 3.73 for actuator **10**).

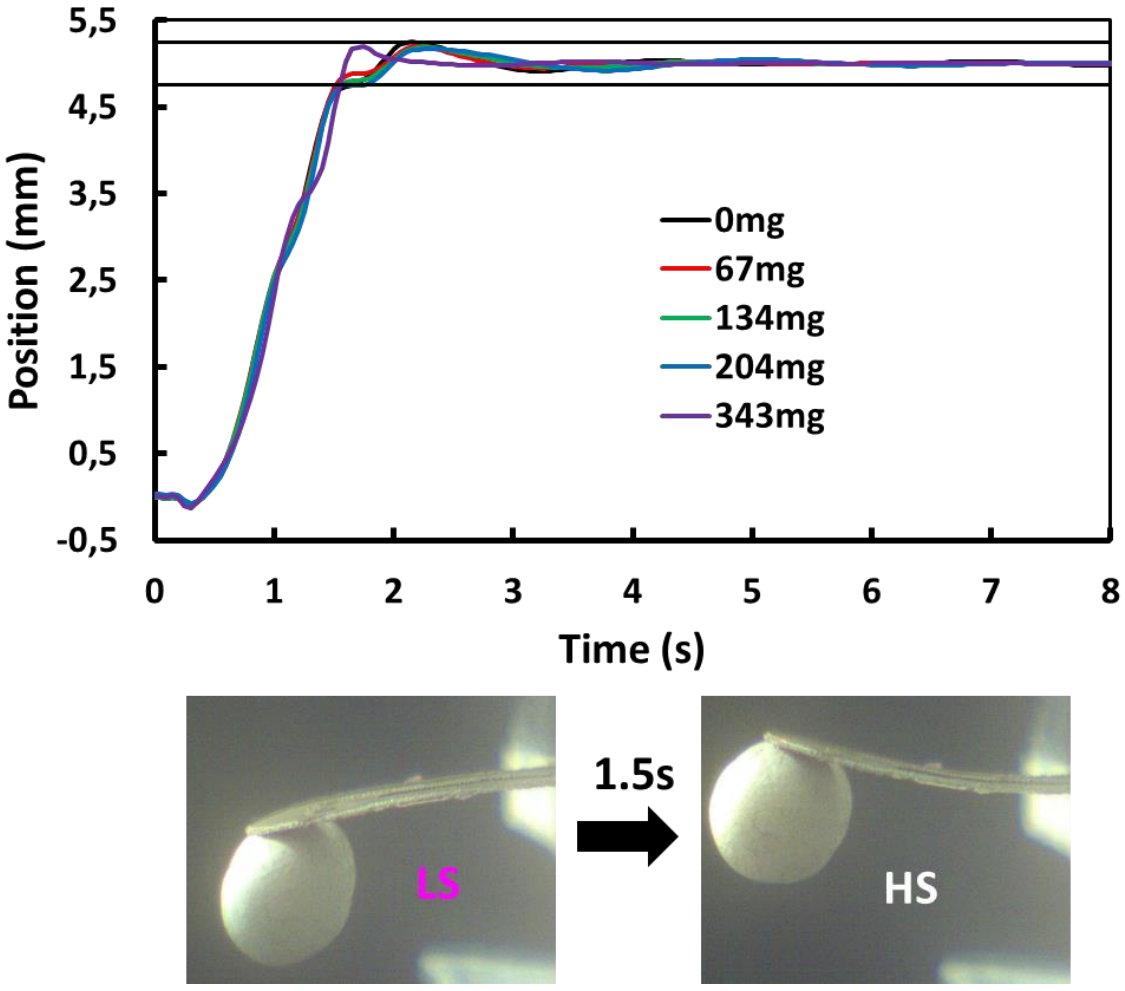

Fig 3.73) Closed-loop actuation of actuator **10** with a 5 mm displacement setpoint, bearing a series of loads equivalent to 1, 2, 3 and 5 times its own mass (up). Black lines indicate the region within 5% of error of the position input. Actuator **10** lifting a 343 mg load (down).

To further assess the controllability and reliability of the actuator under closed-loop control conditions**,** the actuator was driven using various sinusoidal waveforms of different amplitudes and frequencies. The PID parameters used for this analysis were the same as for the 4 mm setpoint (K_P = 1.8 T_i = 0.5 T_d = 0.1). Actuator **10** follows these commands with very high precision, being even able to follow a change in sinusoidal parameters with minimal shift from the target position, with an average error of 0.7% of the target position. When displacing a load of 343 mg (5 times its own mass) the sinusoidal displacement remains completely unchanged, further confirming the capability of the actuator to perform meaningful work in a reliable manner (Fig 3.74).

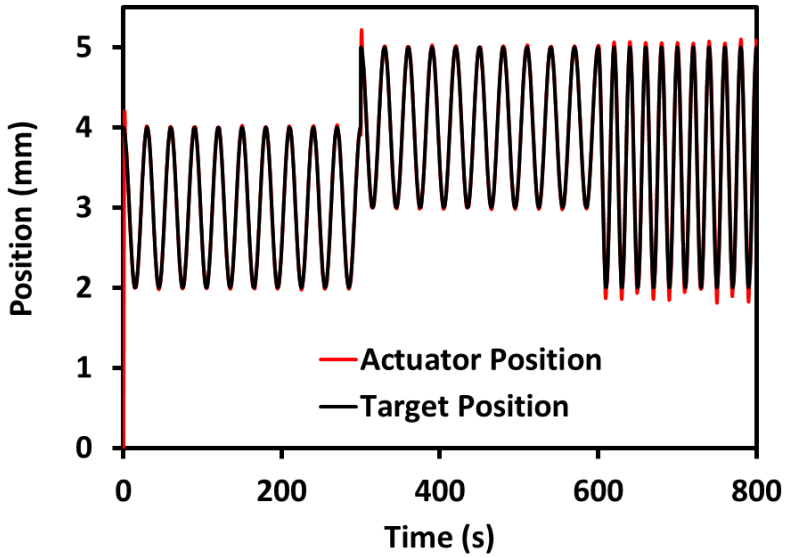

Fig 3.74) Closed-loop sinusoidal actuation of a bilayer device **10** bearing a 343 mg load (5 times its own mass) with varying control parameters (target displacements, amplitude and frequency).

To evaluate the long-term reliability of the control, actuator **10** was oscillated with a period of 30 s, at an amplitude of 3 mm, during 12 days for a total of 35000 actuation cycles. The device showed virtually no signs of fatigue and was able to pursue the command with a standard deviation of ca. 0.4 µm for the 35000 cycles, indicating an important operating life-cycle. It is important to note that, besides the obvious benefits of the close-loop control, the actuator is intrinsically fairly robust.

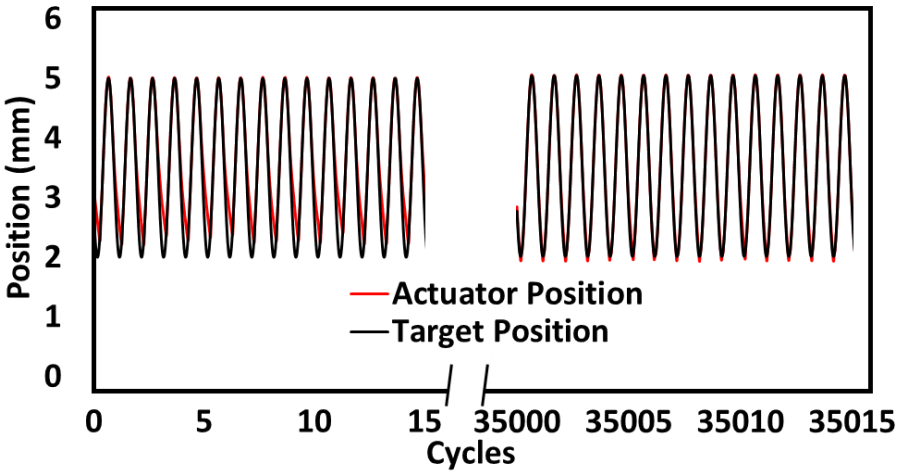

Fig 3.75) Closed-loop sinusoidal actuation of bilayer device **10** before and after performing 35000 cycles in ambient air (12 days, 0.033 Hz).

Finally, to prove that the actuator presents no drifting during the actuation process, the actuator was subjected to an open-loop constant current of 0.85 A during several hours while following its position. After 3 hours the initial position at 2.89 ± 0.04 mm (averaged for the first

20 minutes excluding the first 10 s of ramp up time) has shifted to 2.92 ± 0.02 mm (averaged for the last 20 minutes), denoting no measureable drift within the experimental uncertainty. This ensures that even at open loop conditions, where the system takes a long time to reach equilibrium, it does not drift in the long term.

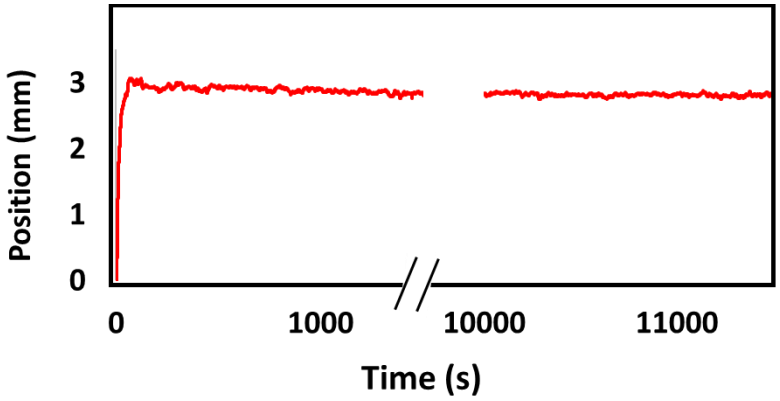

Fig 3.76) Open-loop actuation of a bilayer device **10** over a period of 3 hours (I = 0.85 A)

In an attempt to see whether by increasing the concentration of the SCO complex in the active layer we can significantly amplify the effect of the volume change, we prepared actuators **9'** and **9''**. These actuators use complex **9** as the SCO filling much like actuator **9**, however these complexes have a concentration of SCO complex in the active layer of 33 and 50 wt%, respectively. These bilayers were fabricated following the procedure detailed in page 141.

Table 3.7) Composition of actuators **9**, **9'** and **9''**

Sample	**SCO complex**	**SCO wt% in active layer**
Actuator **9**	$[Fe(NH_2trz)_3]SO_4$	25%
Actuator **9'**	$[Fe(NH_2trz)_3]SO_4$	33%
Actuator **9''**	$[Fe(NH_2trz)_3]SO_4$	50%

An open-loop characterization to determine the maximal actuation of actuators **9**, **9'** and **9''** was performed (Fig 3.77). The maximal actuation of **9** is 5.5 mm, slightly lower than the benchmark actuator **10**. The maximal actuation of **9'** is, as expected, significantly higher at 8 mm, almost a 50% increase from **9**, following a linear trend. However the maximal actuation of **9''** is actually lower than that of **9'** despite having a higher concentration of SCO complex in the active layer, suggesting that the relationship between SCO load and actuation is not directly linear and there are more factors at play. Interestingly the RT of the actuators seems to increase with the concentration, due to the fact that having a higher proportion of SCO complex means that there is a higher energetic barrier associated to the latent heat of spin transition.

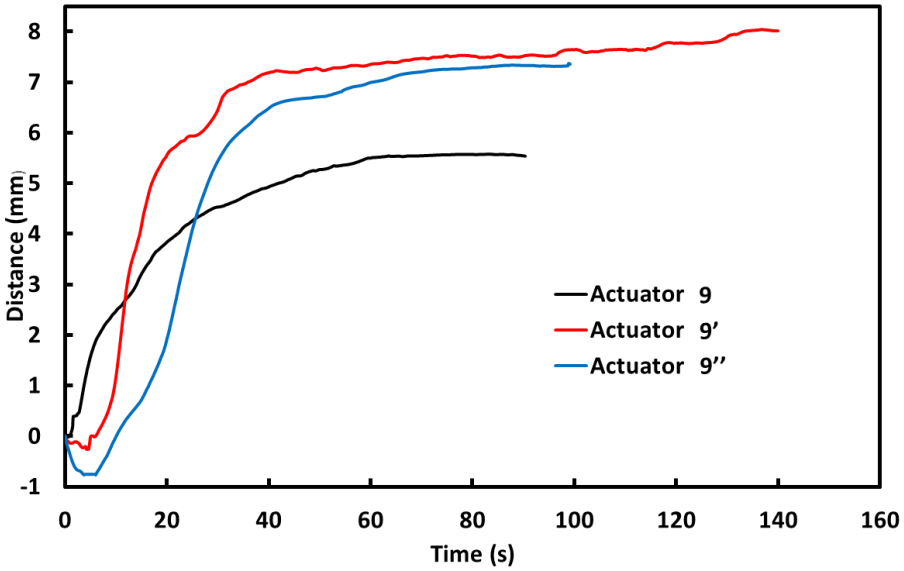

Fig 3.77) Open-loop actuation of samples **9**, **9'** and **9''**

To further compare the difference between the actuators, they were set in closed loop conditions to perform the same movement: a 3 mm displacement (Fig 3.78). PID parameters were previously optimized for each actuator at 3 mm. The RT significantly increases with the concentration of SCO complex, as expected, going from 1.6 s at 25 wt% of SCO to 5.1 s at 50 wt% of SCO. This loss in performance is exacerbated by the fact that actuation becomes more oscillatory and less stable with higher loads of SCO complex. An interesting result of this analysis however is the "reverse motion" observed for actuators **9'** and **9''** at the start of the movement. In the case of actuator **9'',** this reverse motion is significant, with the actuator moving roughly 33% of the target displacement in the opposite direction before starting the actuation in the proper direction. This reverse motion proves the mechanical instability caused by the addition of surplus SCO complex in the active SCO/P(VDF-TrFE) phase of the bilayer system.

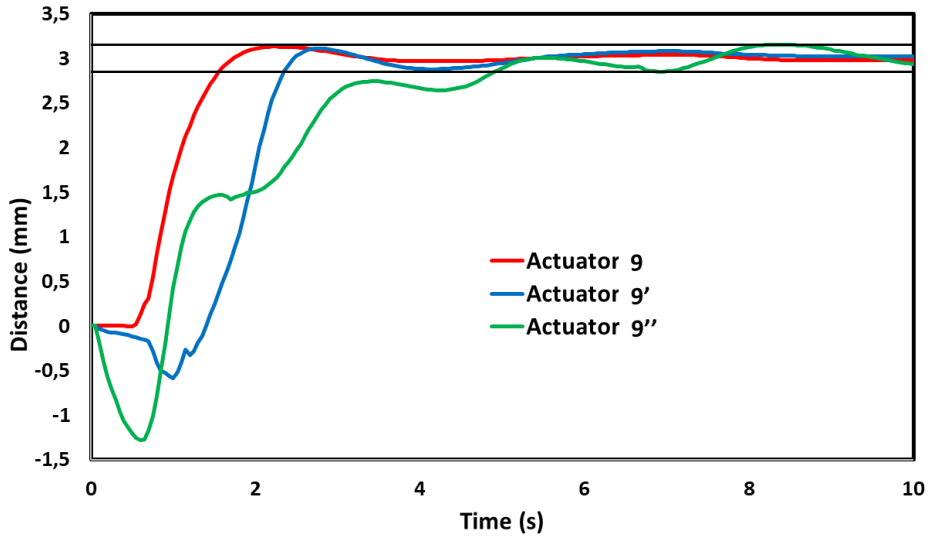

Fig 3.78) Closed loop actuation of samples **9**, **9'** and **9''** with a displacement input of 3 mm

From these results, it is clear that while increasing the proportion of the SCO complex in the active layer has a positive impact on the amplitude of the actuation of the bilayer; it comes at a cost in speed and reliability. This positive effect is also limited to a threshold after which the increased volume change of the SCO particles cannot compensate for the loss of mechanical properties of the composite and actuation amplitude does not increase. The loss of mechanical reliability in the bilayer system becomes apparent from the reverse motion performed by the actuators at the beginning of the actuation cycle.

In conclusion, we have developed a unique self-contained, electrically-driven, soft, robust composite material-actuator that combines the elastic properties of a polymeric matrix and the volume change accompanying the spin crossover material. **We have demonstrated that the material engineering and in particular the integration of oriented objects represents a serious pathway to significantly improve the amplitude of the strain.** Attempts were realized to increase the volume change of the actuator system by simply increasing the concentration of SCO complex in the active layer. The increase in actuation amplitude is significant but comes at a steep price in reaction time and is limited to a threshold.

What remains to be seen yet is how feasible it is to integrate these materials into functional, electrically-driven actuators. The next section will thus describe the fabrication of a demonstrator integrating SCO bilayer actuators into a device.

3.4.6 Demonstrator device employing electrically-driven spin crossover actuators.

In order to incorporate these SCO conductive bilayer systems into a functional device, the first step is to integrate electrical connectivity with a circuit into the composite. Due to the mostly non-adhesive nature of P(VDF-TrFE), and seeing the great success of the casting approach in adhering two layers of P(VDF-TrFE), we decided to use a drop casting approach to deposit an Ag-rich@P(VDF-TrFE) layer (22 v/v%) onto the base of the actuators to solder electrical cables to the actuators (see Fig 3.79).

117 mg of Ag flakes were dispersed in 0.9 mL of MEK. 70 mg of P(VDF-TrFE) 70-30 were dissolved at 50°C in the dispersion. The resulting dispersion was gently drop cast on top of the actuator and a copper wire to solder the wire to the bilayer, sandwiching the electrical connection between the two conductive layers. The mixture was immediately dried with a heat gun to quickly eliminate excess MEK without damaging the integrity of the device.

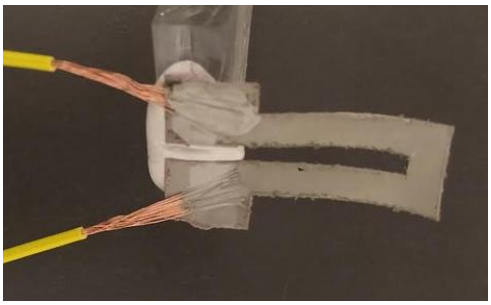

Fig 3.79) SCO bilayer device soldered to copper wiring.

The design we chose for the final device was a pincer-like gripper, as it allows us to integrate the bilayer actuators as they are into a functional device. This gripper-like structure would remain closed when on the low-spin state, and upon electrical excitation would activate and open, allowing for an object to be placed between the fingers of the device which would then be gripped as electrical excitation stops and the actuators return to the low-spin state.

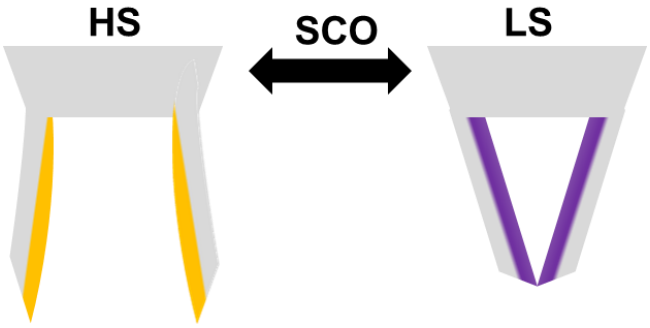

Fig 3.80) Schematic representing an SCO bilayer gripper device.

For the fabrication of this gripper, the wired actuators were glued in a triangular pattern around a PMMA support to create an electrically-driven, SCO pincer-like gripper. A soft gripper device was fabricated assembling three specimens of the actuator **10** incorporating the $[Fe(C_5trz)_3](tosylate)_2$ spin crossover complex. Each independent actuator is used as a finger of the gripper and can be electrically activated independently, but also simultaneously to catch and release an object.

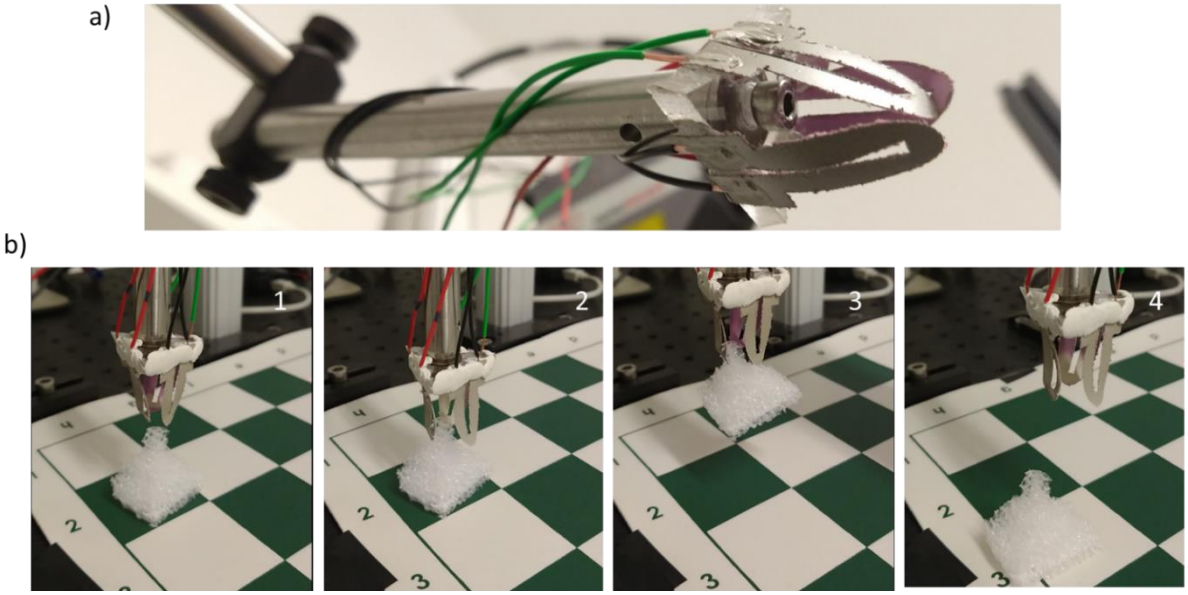

Fig 3.81) a) Image of a gripper device composed of three independent electrically active actuators **10** as finger. b) 1- without current the gripper approaches the target sample, 2- simultaneous injection of current in the actuators induces the opening of the gripper, 3- stopping the current injection allows catching the sample and the sample can be moved to a precise location, 4- new injection of current allows to release the object.

Albeit basic, this result proves that SCO actuators can be integrated into soft, flexible devices performing mechanical actuation, and can be of interest to the field of soft robotics. There are still many open questions and this is just a first approach to SCO actuators as devices, but it proves that these materials have the potential to become a very interesting addition to the repertoire of soft actuating materials.

3.5 Conclusion

With the goal of exploiting the volume change of the spin transition, we set our sights on actuation as a possible application of these materials. Throughout this chapter, we have successfully used two different types of fabrication techniques to create **SCO@Polymer soft actuators**.

First, we successfully used **3D printing technology** to fabricate SCO@DS3000 3D printed composites. Through this technique, we have access to an unprecedented capability to shape SCO materials to any geometry or morphology, opening up a wide variety of applications. Using this flexible approach, we printed spin crossover bilayer actuators, which could reversibly perform **thermally driven mechanical motion** based on the volume change of the spin crossover filler. These actuators show mechanical properties that make them competitive with other soft actuating materials. This actuator fabrication technique could be taken much further by either integrating a conductive element in the inactive layer of the actuator to make an electrically driven printed artificial muscle, or by using more advanced techniques for multimaterial 3D printing allowing us to take bilayer structures and give them 3D geometries.

The other technique that was explored was **solvent casting**. This methodology was used to create a SCO@P(VDF-TrFE)/Ag@P(VDF-TrFE) 70-30 bilayer structure, integrating conductive silver particles in the inactive layer. We successfully fabricated **electrically-driven, highly controllable SCO actuators**. Through the use of a closed-loop controller, the performance of these actuators was enormously increased, leading to short response times (1.5 s) and very high reproducibility and controllability of their motion (0.7 % average error when following a sinusoidal position input). **These actuators proved to be not only mechanically robust, capable of lifting a mass of 5 times their weight with no change in the response time, but also extremely resilient, withstanding 35000 thermal cycles with constant movement and showing no sign of degradation**.

The mechanical properties of these SCO@P(VDF-TrFE)/Ag@P(VDF-TrFE) actuators could be further improved via intelligent design. By incorporating **anisotropic SCO particles** aligned along both the preferential axis of actuation and the crystallographic axis of maximum thermal expansion, we obtained actuators which showed twice the linear strain and almost four times the work density, an unprecedented result with great potential, proving that there are ways to capitalize on the anisotropic volume expansion of SCO composites. Finally, using these conductive bilayer composites we fabricated a **gripping device** able to move an object, showcasing the potential of SCO materials in the field of soft robotics.

As a general conclusion for this chapter, we have shown the potential for SCO-based polymer composites to be used as actuators of great interest in the field of robotics. We have shown not only their performance, but their versatility and flexibility by using multiple fabrication techniques and SCO complexes to obtain highly attractive results.

General Conclusion:

This PhD work is centered on **the use of spin crossover (SCO) composite materials to exploit their inherent volume change** with two differrent applications as objectives: **energy harvesting** via incorporation of SCO materials into a P(VDF-TrFE) matrix and **artificial muscles** using a **composite bilayer approach**. The goal of this work in both cases was the realization of SCO devices that synergistically exploit the spin transition properties.

Regarding the work undertaken to achieve SCO composites for thermal harvesting applications, the strategy used to achieve the goal of a synergistic SCO material exploiting the piezoelectric effect was a composite approach using P(VDF-TrFE) copolymer as the matrix. Indeed, under this approach, particles of SCO complex would be dispersed in a P(VDF-TrFE) matrix and the thermal excitation of the resulting composite would trigger the piezoelectric effect in the copolymer matrix, producing a current discharge. In order to observe such an effect, it is necessary to use a SCO complex that can undergo spin transition within the thermal stability window set by the copolymer, more specifically below the Curie temperature of the ferroelectric P(VDF-TrFE) copolymer.

In order to find the correct SCO sample and analyze the solid-state properties of the complex, a study was undertaken where a series of **nanoparticles of iron complexes** with general formula $[Fe(Htrz)_{1+y-x}(trz)_{2-y}(NH_2trz)_x](BF_4)_y \cdot nH_2O$ were prepared by the **ligand dilution method,** using the benchmark $[Fe(Htrz)_2(trz)](BF_4)$ and NH_2trz ligand. These complexes were then analyzed via variable temperature magnetic measurement, TEM, TGA, DSC, powder XRD, and Mossbauer spectroscopy. As a core result of this study, a surfactant-free method for the fabrication of SCO nanoparticles was used to synthesize a series of SCO complexes while varying the ligand substitution rate. Investigation of the ligand substitution effects by XRD revealed a pronounced change of the structural organisation associated with a dramatic drop of the **lattice stiffness** when introducing only a very small amount of NH_2trz ligand (3.3 %), confirmed by Mossbauer spectrometry.

The study on the physical properties of $[Fe(Htrz)_{1+y-x}(trz)_{2-y}(NH_2trz)_x](BF_4)_y \cdot nH_2O$ mixed complexes allowed us to solidify our choice of complex. A **drop casting** method for the fabrication of SCO(**5**)@P(VDF-TrFE) 70-30 was thus developed (first generation films). The morphology of the films was characterized and their electroactive properties were evaluated. We found that indeed, the films can be polarized, can retain their polarization and electroactive β phase upon the spin transition. When the polarized films are subjected to a thermal cycle triggering the spin transition, they show **current discharge peaks at the spin transition temperatures**, presumably linked to a piezoelectric effect caused by the volume change of the SCO filler.

In summary we succeeded in synthesizing high quality, homogenous SCO@P(VDF-TrFE) 70-30 in a reproducible manner allowing us to **obtain flexible, freestanding, macroscopic objects displaying novel electro–mechanical synergies between the two components**. This coupling leads to concomitant macroscopic thermal expansion and electrical discharge peaks at the spin transition.

A second, follow-up study was developed, to fabricate and characterize a second generation of electroactive SCO@P(VDF-TrFE) composites with the goal of determining the effect of particle morphology, filler composition and copolymer composition on the electromechanical properties of the composites. A series of SCO@P(VDF-TrFE) composite films were thus fabricated using a **blade-casting** approach following an optimized procedure using five different complexes with different morphologies, concentrations and even copolymer compositions.

As a core result of this work, the versatility of our fabrication method demonstrates that the mechano-electric coupling between a ferroelectric PVDF-TrFE copolymer matrix and spin crossover particles is a generic property. Additionally we were able to effectively separate these two phenomena and recover the pyroelectric property of the neat polymer. Depending on the concentration of the SCO filler, we observed two behaviors. In the low-concentration limit (*ca.* 5–15% – depending on the experimental details) we were able to achieve pyroelectrical properties in the composites, which are comparable with those of the pure polymer matrix. On the other hand, in the high-concentration limit (*ca.* 15–33%), the sample polarization is reduced, but we observe an additional **pseudo pyroelectric discharge peak**.

In conclusion, we developed a versatile and generic method to fabricate SCO@P(VDF-TrFE) films. Through proper tuning of the composition of these films, we were able to separate the spin crossover phenomenon from the Curie transition of the copolymer matrix without compromising the inherent electroactive properties of the copolymer, allowing us to observe a synergistic effect of the volume change of the spin crossover phenomenon and the piezoelectric properties of the copolymer, leading to current discharge upon the spin transition. The morphology of the particles might play a crucial role, as there was no pseudo pyroelectric discharge observed when anisotropic particles were used as filler, however, further studies are needed.

A perspective concerning the use of SCO@P(VDF-TrFE) materials for thermal harvesting applications would be further **tuning of the SCO filler properties**. Indeed, it would be ideal to use a complex with a significant volume change which has an abrupt transition with a small hysteresis between 35 – 50°C. An abrupt transition within a small temperature window is ideal for this application as it means that we can observe the full effect of the spin transition on the piezoelectric matrix with very small temperature changes. This is in fact one of the main advantages of SCO@P(VDF-TrFE) materials as pyroelectric harvesters. Another interesting perspective would be the use of more advanced fabrication techniques such as spray-coating to obtain thinner films of the SCO@P(VDF-TrFE) material which can be more easily polarized and

integrated into microelectronic harvester devices and should enhance the piezoelectrical response.

Regarding the use of **SCO composites for artificial muscles**, the core strategy used throughout this work was the use of a **bilayer approach** to exploit the volume change of SCO composites and transform it into a significant bending motion. There were two fabrication methods used to obtain these bilayer actuator systems: **3D Printing and solvent casting**.

A stereolithographic 3D printing setup was used, using DS3000 as printing material, in order to obtain SCO@DS3000 composites. It was necessary to adapt the fabrication process normally used by this setup in order to obtain SCO@DS3000 4D printed objects, and through fine tuning of the printing procedure it was even possible to obtain SCO@DS3000/DS3000 bilayers. The printed objects retain the SCO properties of the filler complex, as evidenced by the thermochromic effect and the optical reflectivity analysis. It was found that the **integrity of the interface between the two layers** plays a crucial role in the stability of the printed bilayers, and through careful tuning of the printing procedure, a continuous interface can be guaranteed between the layers. The printed bilayers were characterized and their mechanical properties evaluated. Indeed, they show actuation, deforming in a reversible manner when thermally activated and this actuation is highly dependent on the morphology of the printed object. Mechanical properties of these actuators show comparable properties to those of other commonly used materials in the development of artificial muscles.

As a general conclusion of our work using 3D printing techniques to fabricate SCO artificial muscles, we have 3D printed various stimuli-responsive mono- and bimorph architectures with sizes up to several cm and structural details down to the 80 μm scale. The objects display good thermal and mechanical properties and afford for reversible mechanical actuation thermally generated by the volume change accompanying the spin crossover phenomenon. The fabrication process developed here is straightforward, versatile and enables the creation of arbitrary planar and three-dimensional geometries.

The core perspective of our work in 3D printed SCO composites is the integration of electrical conductivity into the bilayer system. Indeed, by allowing electrical control of these actuators a series of technological applications of this technology would become available. The second perspective is the tuning of this technology to use SCO complexes with a lower transition temperature and flexible resins that are resilient to temperature changes. In fact, the loss of stiffness of the DS3000 resin at high temperature is one of the main factors limiting its mechanical properties.

Solvent casting methods were also employed to fabricate SCO composite actuators. The matrix of choice for these composites was P(VDF-TrFE) 70-30 due to its good mechanical properties, flexibility and solubility lending itself well to this technique. In order to obtain SCO@P(VDF-TrFE)/P(VDF-TrFE) bilayers it was necessary to develop a new methodology employing a doctor blade to control the thickness of the layers and ensuring the integrity of the

interface. This methodology is versatile and generic and through a tuning process it was possible to grant electrical conductivity to the fabricated bilayers. Indeed, by using silver microflakes, we successfully fabricated a SCO@P(VDF-TrFE)/Ag@P(VDF-TrFE) bilayer, which was then used to fabricate actuator devices.

These **conductive actuator devices, electrically triggered via joule effect** to undergo spin transition, show reversible deformation when activated. Further analysis of the bilayer integrity shows both clear separation and yet a continuous interface between the two layers, suggesting the **resilience of the actuators against delamination phenomena**. In order to fully exploit the actuation potential of these bilayer devices, a **PID control** system was put in place, using a distance tracker to provide feedback to the software.

To optimize the fabrication process of these bilayers, a series of SCO complexes with different morphology, dimensionality and transition temperature were used, and the actuation of each of the corresponding devices was evaluated to find the optimal SCO complex for this application. Once the composition of these bilayers had been optimized, an evaluation of the actuation of this device using the PID control system took place. It was found that, under closed-loop control, the devices show a rapid response time, an order of magnitude smaller than for the open-loop control. The actuator showed attractive mechanical properties, being able to follow a sinusoidal command with minimal error and being able to perform 35000 actuation cycles over two weeks of continuous actuation, it was also capable of lifting a mass equivalent to five times the mass of the actuator with no effect on response time or reliability. This means that **we successfully fabricated a reliable, controllable, resilient and robust actuator.**

To take the actuation properties one step further, and through smart material design, we incorporated and aligned anisotropic SCO particles in the polymer matrix, exploiting the natural anisotropy of the spin crossover to direct the volume change towards the beam axis of the actuators, multiplying the effect of the actuation. Indeed we found that the **actuator devices fabricated with anisotropic aligned objects show significantly larger actuation amplitudes**, with the bending deformation so large that it causes the actuator to coil around itself. The mechanical properties of the actuators fabricated in this manner are vastly improved, and the poor properties of actuators fabricated perpendicular to the particle alignment axis prove the anisotropic effect present in these devices. Unfortunately, the wide movement of these devices makes them hard to control under closed loop conditions. Finally, as a proof of concept of the applicability of this technology in soft robotic devices **we fabricated a gripper demonstrator device using three actuator "fingers" that can be independently or simultaneously triggered to catch and release an object**.

In summary, we have developed an electrically-driven, controllable, robust composite material actuator. We have demonstrated that the material engineering and in particular the integration of oriented objects represents a serious pathway to significantly improve the amplitude of the strain. Thus the measured performance compare well with other class of polymer based soft materials. Other characteristics like the response speed of 1 second, the

controllability in open and closed loop and also the resilience of the actuation for several tens of thousands of cycles makes these materials compatible for future applications. In particular, we have demonstrated the ability of these materials to carry significant loads and to move objects using a fully electric gripper device. The possibility to adapt the transition temperature of these materials in a large range of temperature between -150 and + 150°C prove the high versatility of the spin crossover materials which is a significant advantage compare to other class of active compounds. Ultimately, we have demonstrated that these modular actuators present simultaneously flexibility and the ability to generate force in a reversible, efficient and controllable manner, which is a key challenge of the field.

An important perspective for these devices is the integration of internal movement sensors in the material, thus allowing for **self-sensing artificial muscle devices**. This strategy would also allow us to readily control the actuators fabricated with anisotropic particles. Another important perspective is the exploration of different morphologies and geometries to better respond to the needs of soft robotics. Indeed, linear and rotational actuation are highly in demand in the field of robotics, and the adaptation of our materials to **fiber-like morphologies** would allow us to better respond to those needs. Creating biomimetic electrically responsive actuating issue is another perspective that we could explore by having access to a wider variety of morphologies. The implementation, on one hand, of other SCO materials with spin transition temperatures closer to room temperature and directly bonded to the organic polymer matrix, and on the other hand, the use of other polymer matrices and in particular conductive polymers could multiply the possibility of application of these devices.

As a general conclusion of this PhD work, we successfully managed to fabricate SCO composite materials, which, synergistically exploiting the volume change of the SCO phenomenon allow us to obtain electromechanical responses which can be thus integrated into functional devices for either thermal energy harvesting or artificial muscle applications.

Résumé de thèse:

Introduction:

La science des matériaux suscite un grand intérêt pour les matériaux intelligents commutables [1]**.** Les matériaux qui peuvent changer leurs propriétés intrinsèques en réponse à un stimulus externe sont très recherchés, de même que les matériaux multifonctionnels qui changent de propriétés de manière réversible. L'élaboration de dispositifs intelligents utilisant ces matériaux reste l'application la plus directe et la plus intéressante selon ce principe.

Les matériaux à transition de spin (TS) peuvent être particulièrement intéressants dans ce domaine en raison de leur capacité à moduler leurs propriétés physiques de manière réversible [2]. En effet, les matériaux à transition de spin peuvent passer d'un état haut spin (HS) à un état bas spin (BS) de manière réversible lorsqu'ils sont soumis à une série de stimulii externes : température, pression, lumière, champs magnétiques et adsorption d'un composé chimique. Cette commutation réversible entre les deux états moléculaires du matériau, qui peut être effectuée à une température contrôlable, entraîne un changement des propriétés magnétiques, optiques et diélectriques [3]. Cependant, ce qui est le plus intéressant pour le présent travail de recherche de doctorat, c'est que ces matériaux peuvent également modifier de manière réversible le volume de leur réseau cristallin jusqu'à 15 % [4]. Ce changement de volume est très intéressant car ces matériaux ont également une rigidité relativement élevée, ce qui leur permet d'exercer une force importante. Néanmoins, les matériaux à transition de spin sont des matériaux cristallins, rigides et diélectriques, ce qui signifie qu'une mise en forme est nécessaire afin de les intégrer dans des dispositifs électriques fonctionnels.

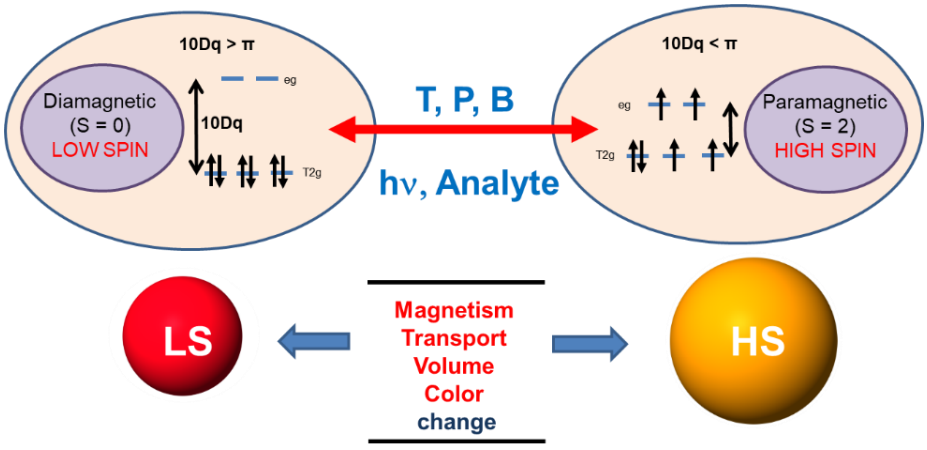

Fig 1) Aperçu général du phénomène de transition de spin dans le cas du Fe(II).

Une approche commune qui a été utilisée avec succès auparavant pour intégrer efficacement les matériaux à transition de spin dans des dispositifs fonctionnels est l'approche composite [5]. Selon cette approche, ces matériaux sont incorporés dans une matrice, ce qui

confère au matériau final à la fois la commutation intrinsèque du matériau et les propriétés de la matrice. L'utilisation de matrices polymères pour conférer aux matériaux à transition de spin des propriétés plus adaptées à l'intégration dans des dispositifs souples, à savoir la flexibilité et la stabilité mécanique, nous intéresse tout particulièrement. Les composites polymères à transition de spin ont déjà été utilisés auparavant et il existe une grande variété d'exemples dans la littérature qui ont été proposés pour une variété d'applications différentes [6], cependant très peu de travail a été fait vers l'exploitation du changement de volume de la transition de spin [7].

Le premier chapitre de ce manuscrit de thèse portera sur une brève explication du phénomène de transition de spin, un examen sur l'élaboration de nanoparticules à transition de spin, bien adaptés à l'élaboration de matériaux composites, et un état de l'art sur les matériaux composites et nanocomposites associant polymères et matériaux à transition de spin. Nous évoquons également les applications envisagées avec ces matériaux dans des dispositifs fonctionnels.

Dans ces travaux de thèse, nous concentrerons notre attention sur le développement de matériaux composites qui utilisent de manière synergique le changement de volume des matériaux à transition de spin pour différentes applications. Les deux principales applications sur lesquelles nous travaillerons sont l'économie d'énergie et l'actionnement électromécanique. En fait, l'objectif final de ce travail est la fabrication de dispositifs de récupération d'énergie et de muscles artificiels qui utilisent le changement de volume associé au phénomène de transition de spin.

L'économie d'énergie consiste à récupérer l'énergie ambiante perdue dans divers processus pour alimenter des dispositifs électriques. Un exemple courant est une montre thermoélectrique [8] qui utilise la chaleur du corps comme source d'énergie. Dans le présent travail, nous utiliserons l'effet piézoélectrique couplé au changement de volume des composés à transition de spin pour élaborer des matériaux qui génèrent des décharges électriques à partir d'un stimulus thermique. En effet, en couplant le changement de volume de la transition de spin avec un matériau piézoélectrique qui produit une décharge électrique lorsqu'il est activé mécaniquement, nous pouvons transformer le changement de volume du phénomène de transition de spin en une source d'énergie électrique. Pour y parvenir, nous couplerons différents matériaux de transition de spin avec des matériaux copolymères piézoélectriques P(VDF-TrFE), via l'approche composite.

Ainsi, le deuxième chapitre de ce travail de doctorat couvrira d'abord une brève introduction sur la récupération d'énergie, avant d'approfondir les stratégies choisies pour coupler de manière synergique l'effet piezoélectrique [9] au phénomène de transition de spin. Après cette introduction, le chapitre se penchera sur le choix des matériaux à transition de spin pour cette application et la caractérisation de deux générations de films composites fabriqués.

Le troisième chapitre concerne l'utilisation de matériaux à transition de spin comme éléments de base pour l'élaboration de muscles artificiels [10]. Un muscle artificiel est un

dispositif qui peut effectuer un travail et exercer une force de manière réversible et de façon autonome, simplement par la stimulation d'un matériau qui effectue intrinsèquement un mouvement lorsqu'il est activé. Des matériaux à transition de spin ont déjà été utilisés par le groupe dans des applications électromécaniques comme preuve de concept [11]. Cependant, dans le cadre du présent travail, nous avons l'intention d'aller plus loin, en passant d'un actionnement micromécanique stimulé thermiquement à des actionneurs macroscopiques stimulés électriquement, en utilisant des matériaux à transition de spin pour effectuer des mouvement sous contraintes de manière contrôlable, fiable et robuste.

Pour atteindre cet objectif, nous avons utilisé une approche bicouche [12], en utilisant la différence d'expansion thermique entre deux couches d'un matériau composite pour provoquer une déformation et un mouvement réversibles. Deux approches de fabrication ont été utilisées pour élaborer ces dispositifs bicouches : l'impression 3D et le moulage de polymères. D'une part, l'impression 3D permet l'incorporation de matériaux à TS dans des composites à morphologie hautement contrôlable et, grâce à ce contrôle de la morphologie, d'élaborer des dispositifs bicouches à actionnement thermique. La méthode de moulage par solvant permet, d'autre part, d'élaborer des dispositifs d'actionnement conducteurs et par conséquent, de contrôler électriquement les dispositifs fabriqués, ce qui permet un actionnement fiable et résilient. Cette technique très générique et adaptable se prête bien à un processus d'optimisation où, grâce à une conception intelligente des matériaux, l'intégration de particules à TS anisotropes multiplie l'effet de l'actionnement. L'utilisation d'une commande électrique facilite également l'intégration de ces muscles dans un dispositif de démonstration.

Chapitre 2: Matériaux composites à transition de spin électro-actifs pour une application de récupération d'énergie :

La récupération d'énergie est le processus par lequel les sources d'énergie ambiantes telles que l'énergie cinétique, les gradients ioniques, les gradients de température ou les radiations électromagnétiques peuvent être captées, stockées et utilisées comme énergie électrique pour le fonctionnement de diverses appareils [9]. Il est important de noter que l'objectif de ces technologies n'est pas de remplacer la production d'énergie à grande échelle, mais de contribuer à l'alimentation de petits appareils sans fil, qui sont censés être autonomes.

Les matériaux piézo-électriques sont un exemple classique de récupérateurs d'énergie [113]. Ces dispositifs transforment les perturbations mécaniques ou les changements de pression en énergie électrique. Les matériaux piézoélectriques génèrent une charge électrique lorsqu'ils sont exposés à une contrainte mécanique, souvent due à la perturbation d'un réseau cristallin chargé de façon anisotrope. Ces matériaux, bien que souvent utilisés dans des applications telles que les capteurs et les actionneurs micromécaniques pour des dispositifs tels que les AFM, les STM et les microbalances, ont également un potentiel de récupération d'énergie.

Les piézoélectriques sont des matériaux qui peuvent être polarisés non seulement par l'application d'un champ électrique, mais aussi par une contrainte mécanique. Ce phénomène peut être compris à l'aide d'un modèle moléculaire simple, comme illustré ci-dessous (fig 2) : lorsqu'une unité polaire neutre comportant des domaines clairement différenciés chargés positivement et négativement subit une déformation, ces domaines s'alignent, donnant naissance à de petits dipôles. Les pôles opposés à l'intérieur du matériau s'annulent et des charges fixes apparaissent à la surface. Cela signifie que pour un matériau dont les unités polaires sont bien alignées, les petits dipôles internes du matériau auront moins de chances de s'annuler et les charges apparaissant à la surface du matériau seront plus importantes [112].

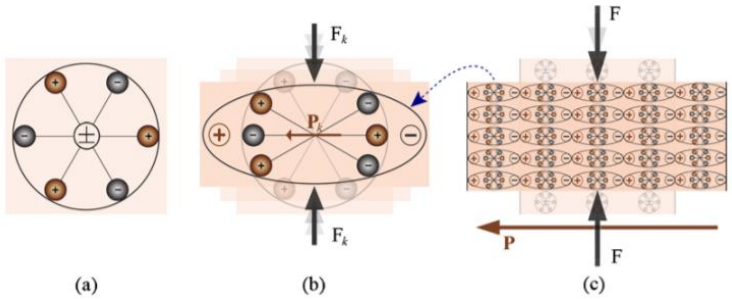

Fig 2) Modèle moléculaire simple de l'effet piézoélectrique. a) Une unité polaire neutre au repos. b) L'application d'une force externe F_k a généré une polarisation P_k dans le matériau. c) L'alignement des dipôles internes du matériau génère une charge à la surface [112].

L'une des possibilités les plus intéressantes pour la récupération d'énergie est la récupération thermique, qui exploite de petits gradients ou décalages de température pour générer de l'énergie électrique afin d'alimenter des appareils légers. Les générateurs thermiques sont limités dans leur rendement, le flux de chaleur étant le principal facteur limitant. Cependant, le corps humain fournit un gradient thermique et une source de chaleur presque constants, qui peuvent être exploités pour alimenter de manière totalement autonome des appareils à très faible besoin énergétique, tels que des capteurs. C'est pourquoi l'intégration de récupérateurs d'énergie thermique en tant qu'électronique souple et portable est un sujet de recherche très intéressant.

Il existe deux principaux types de collecteurs d'énergie thermique : les dispositifs thermoélectriques et les dispositifs pyroélectriques (fig. 3). Les dispositifs thermoélectriques transforment les gradients thermiques en électricité par l'effet Seebeck [114]. Les dispositifs thermoélectriques ont fait l'objet d'une grande attention en tant que récupérateurs d'énergie. Cependant, ils ne peuvent pas toujours fonctionner efficacement, car un dispositif thermoélectrique nécessite un gradient thermique spatial, et ne peut pas fonctionner sur des gradients thermiques temporels.

Le deuxième type de dispositifs thermiques est basé sur des matériaux pyroélectriques, qui s'appuient sur un changement de température dans le temps pour générer des courants électriques. ils se distinguent des dispositifs thermoélectriques en utilisant un gradient thermique temporel plutôt que spatial. Cela permet à ces dispositifs de couvrir des applications

que les dispositifs thermoélectriques ne peuvent pas couvrir. Le principe de fonctionnement de la pyroélectricité provient du changement de polarisation spontanée dans un solide, résultant d'une fluctuation de température.

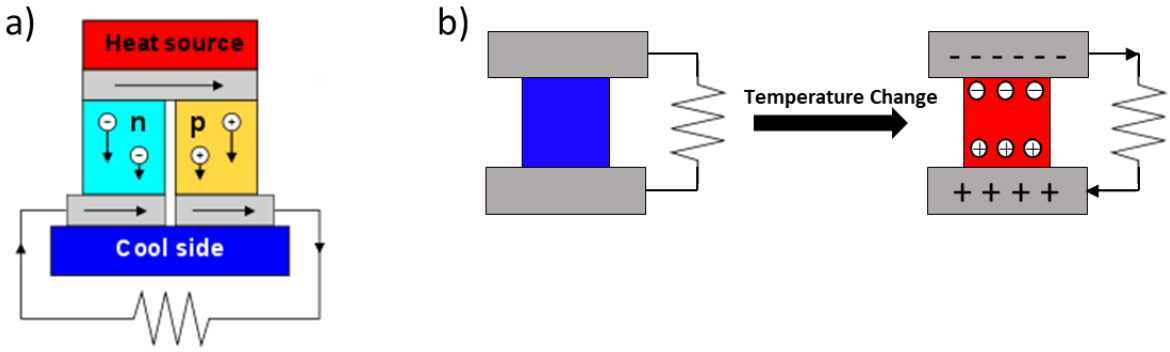

Fig 3) Représentation schématique des deux types de récupérateurs d'énergie thermique : a) thermoélectrique. b) pyroélectrique.

Le PVDF est un polymère linéaire thermoplastique (fig 4). Il est facilement soluble dans une variété de solvants et peut être facilement transformé en films et en dispositifs. C'est un polymère chimiquement stable, flexible et mécaniquement résistant. Plus important encore, le PVDF possède une phase cristalline (phase β) dans laquelle il présente des propriétés ferroélectriques, qui donnent lieu à leur tour à des propriétés piézoélectriques et pyroélectriques.

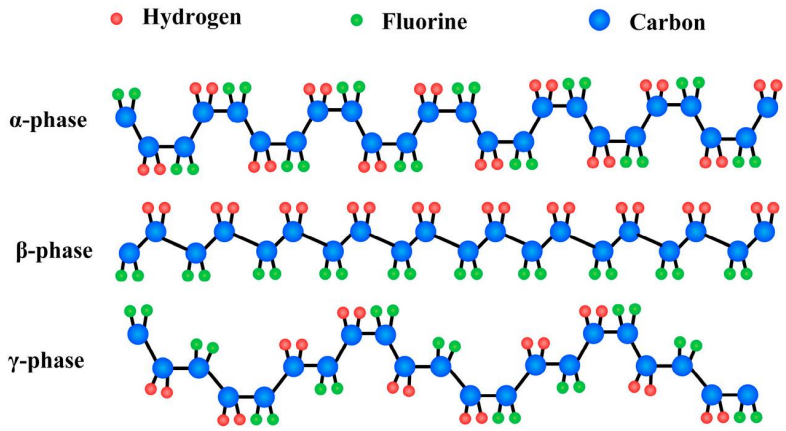

Fig 4) Conformations cristallines du PVDF [116].

Une approche couramment utilisée pour améliorer les propriétés électroactives du PVDF et du P(VDF-TrFE) est l'utilisation de matériaux composites [122]. Il existe un important corpus de recherche sur l'incorporation de charges dans la matrice polymère du PVDF ou de son copolymère. Par exemple, des chercheurs ont tenté d'intégrer des nanoparticules et des nano-fils piézoélectriques, montrant une augmentation de la production électrique due aux effets de synergie entre les nanoobjets piézoélectriques et la matrice polymère piézoélectrique [121].

Cela suggère la possibilité d'utiliser les matériaux à TS de la même manière : le stimulus thermique induirait la transition de phase du matériau a TS ce qui impliquerait un changement de volume. Ce changement de volume interagirait à son tour avec la matrice piézoélectrique P(VDF-TrFE) pour générer des courants de décharge autour des températures de transition de spin, créant ainsi un composite synergique. Le phénomène de TS est particulièrement intéressant pour cette application car il permet un changement de volume important dans une fenêtre de température étroite de manière réversible.

La matrice choisie pour cette étude, P(VDF-TrFE) 70-30 (70% PVDF, 30% TrFE), a une température de travail délimitée par la température de transition vitreuse et la température de Curie. En dessous de la température de transition vitreuse (238 K), le P(VDF-TrFE) perd ses propriétés ferroélectriques [119], et au-dessus de la température de Curie du polymère (370 K), il est incapable de conserver la phase cristalline β nécessaire pour que le polymère montre ses propriétés électroactives.

Étant donné les propriétés de la matrice polymère précédemment établies comme étant P(VDF-TrFE), il est nécessaire d'utiliser un complexe à TS avec une température de transition bien dans les limites déterminées par la matrice polymère. En plus de cette condition, il est nécessaire d'utiliser un composé présentant un changement de volume significatif lors de la transition de spin pour déclencher la synergie entre le matériau à TS et la matrice piézoélectrique. Enfin, il est également important d'utiliser un complexe pouvant former des nanoparticules, afin de permettre une dispersion adéquate du complexe dans la matrice.

Avec toutes ces considérations, un complexe modèle a été choisi pour l'étude : le complexe de coordination polymérique 1-D à TS $[Fe(Htrz)_2(trz)](BF_4)$ (trz = 1,2,4-Triazole), voir Fig 5. Ce complexe a montré à la fois un degré élevé de changement de volume lors de la transition de spin (≈11%) [129] et la capacité à être fabriqué sous forme de nanoparticules. Cependant, la température de transition lors du chauffage (380 K) est trop proche de la température de Curie du polymère. Afin d'abaisser la température de TS, l'approche «ligands mixtes» a été choisie. Grâce à cette technique, le complexe est préparé avec un mélange de ligands, en remplaçant spécifiquement une fraction du ligand original (dans ce cas le ligand triazole (trz) par un ligand qui correspond à un complexe ayant une température de transition de spin considérablement réduite. Dans ce cas, le complexe est $[Fe(NH_2trz)_3](BF_4)_2$ (NH_2trz=1,2,4-4-NH_2-triazole) qui a une température de transition à environ 280 K.

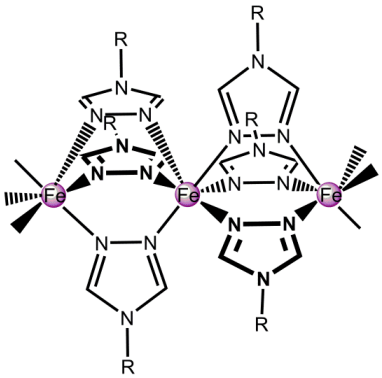

Fig 5) Structure chimique des complexes de la famille Fe-triazole à chaîne polymère 1D.

Cette technique a permis de synthétiser le complexe [Fe(H-trz)$_{1,85}$(trz)$_{0,85}$(NH_2trz)$_{0,3}$](BF_4)$_{1,15}$-1H_2O et, grâce à l'optimisation d'un protocole de fabrication basé sur la technique du dépôt de gouttes, un film composite SCO@P(VDF-TrFE) 70-30 a été fabriqué avec succès. Le film flexible et autonome présente un thermochromisme comme prévu par l'inclusion des particules à TS.

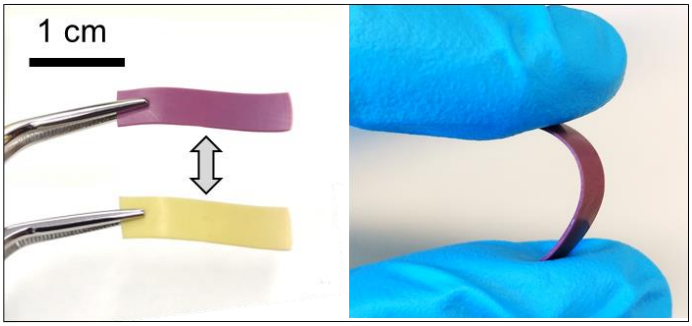

Fig 6) Composite SCO@P(VDF-TrFE) 70-30, autoportant et homogène.

Afin de mesurer la réponse pyroélectrique du matériau composite, qui devrait résulter naturellement du fort couplage mécanique entre les particules et la matrice, un dispositif court-circuit a été utilisé (Fig 7). Dans ce dispositif, le film composite polarisé est placé entre deux électrodes et soumis à des cycles thermiques, tandis que les électrodes mesurent simplement la réponse électrique du matériau sous la forme d'un courant électrique produit par le film.

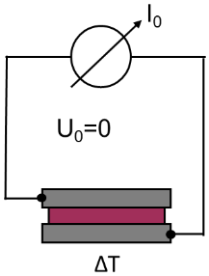

Fig 7) Représentation schématique d'un dispositif expérimental pyroélectrique en court-circuit.

Dans une première analyse, un échantillon composite polarisé à 13 MV m^{-1} a été chauffé au-delà de la température de Curie, refroidi à température ambiante puis chauffé à nouveau au-

delà de la température de Curie (Fig 8a). L'étape 1 montre une décharge pyroélectrique du composite lors du chauffage, en raison de la transition de spin provoquant un changement de volume dans la matrice piézoélectrique. L'étape 2 montre un refroidissement dans lequel le composite produit une décharge pyroélectrique de signe opposé à la décharge de chauffage de l'étape 1, avec une intensité similaire. L'étape 3 montre ensuite une étape finale de chauffage, avec un pic de décharge beaucoup plus faible. Cette analyse montre le comportement du composite polarisé lorsqu'il est dépolarisé par la suite. Une fois la polarisation perdue, on observe une réponse pyroélectrique significativement réduite, avec un petit pic correspondant à la température de transition. Cette analyse donne deux résultats intéressants : premièrement, l'échantillon dépolarisé montre toujours des pics de décharge associés à la transition de spin, et deuxièmement l'inversion du signe du pyrocourant après le processus de dépolarisation.

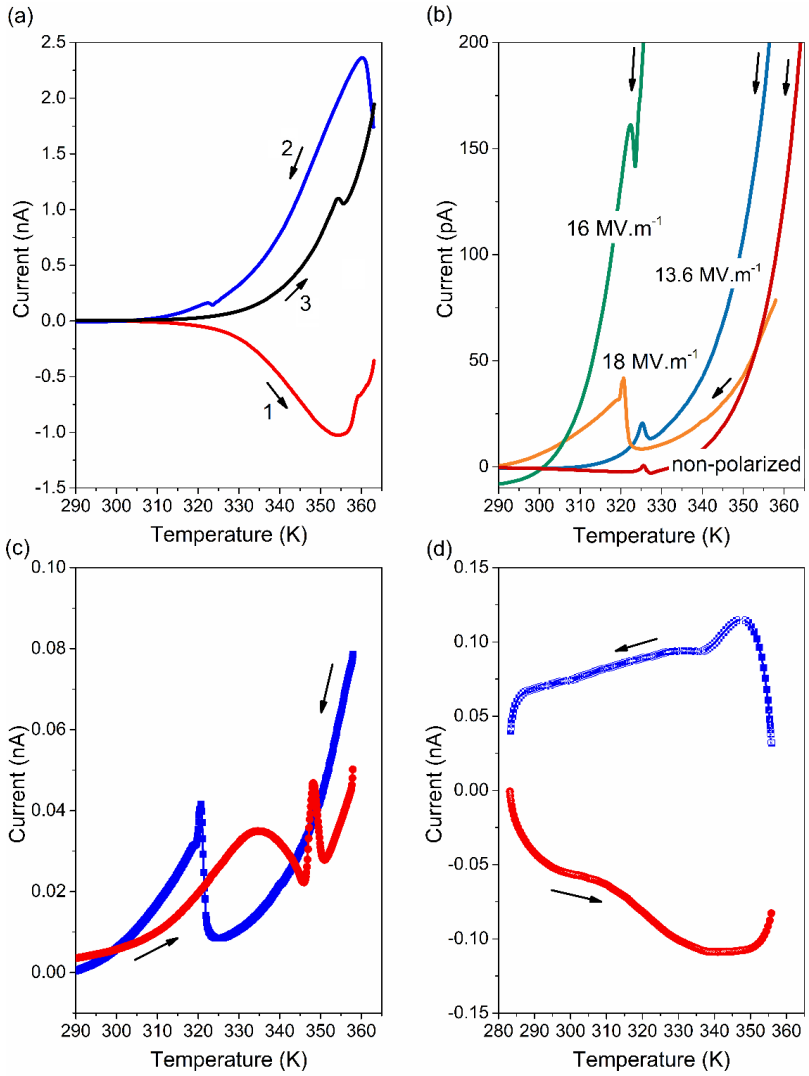

Fig 8) Mesures en court-circuit d'un film TS@P(VDF-TrFE). (a) Courant de court-circuit enregistré à 7 K min^{-1} révélant l'inversion du signe du courant suite à une polarisation de 13 MV m^{-1}. Etape 1) chauffage, 2) refroidissement, 3) chauffage après avoir perdu la polarisation initiale (b) Mesures de courant en mode

refroidissement, échantillon non polarisé, échantillons polarisés à 16 et 18 MV m^{-1} (c) Cycle de courant avec un échantillon polarisé à 18 MV m^{-1}. (d) Données de référence avec le P(VDF-TrFE) pur 70-30 polarisé à 57 MV m^{-1} sans pics de décharge.

Dans une seconde analyse, une série d'échantillons composites a été polarisée sous différentes intensités de champ électrique (13,6, 16 et 18 MV m^{-1}) et chacun des échantillons composites a été soumis à un cycle entre 260 et 360 K sans aucune tension appliquée. Les courbes de courant stimulé thermiquement qui en résultent révèlent des pics de courant de décharge prononcés autour des températures de transition de spin, qui sont nettement améliorés par rapport à l'échantillon non polarisé (Fig 8b). L'intensité du pic de décharge augmente avec le champ électrique utilisé pour polariser l'échantillon, ce qui confirme encore le rôle clé du processus de polarisation.

Il est intéressant de noter qu'il semble y avoir de petits changements dans la température de transition de spin entre les échantillons. Ceci est simplement attribué à une erreur expérimentale, provenant du fait que pour obtenir des réponses pyroélectriques intenses qui peuvent être mesurées avec précision, les changements de température doivent être relativement rapides (10 K min^{-1}) ce qui laisse place à l'incertitude de la thermalisation. En d'autres termes, la polarisation de l'échantillon ne semble pas avoir d'impact significatif sur la température de transition.

Le résultat expérimental qui prouve les propriétés électro-actives du composite est l'observation expérimentale répétée de l'effet "pseudo-pyroélectrique" dans les matériaux composites sous la forme de pics de courant de décharge lorsqu'ils sont soumis à des changements de température autour des températures de transition de spin (Fig 8c).

Une étude comparative a été réalisée, avec une série de nano-composites TS@P(VDF-TrFE), en faisant varier la composition du polymère ainsi que la composition, la concentration et la morphologie des particules à transition de spin. L'objectif était de montrer qu'en ajustant la matrice et les propriétés des particules, il est possible d'observer simultanément l'effet piézoélectrique du à la transition de spin et la réponse pyroélectrique du polymère. Un autre objectif était de déterminer comment chacune de ces caractéristiques joue un rôle dans les propriétés électromécaniques du composite.

Dans ce travail, les composés à TS utilisés appartiennent à la famille des $[Fe(Htrz)_{1+y-x}(trz)_{2-y}(NH_2trz)_x](BF_4)_y\text{-}nH_2O$ présentant des transitions de spin thermique entre 50°C et 100°C (selon la stœchiométrie) ainsi que le complexe mononucléaire $[Fe(HB(tz)_3)_2]$ (tz = 1,2,4-triazol-1-yl) présentant une transition de spin abrupte et très stable autour de 60°C. L'effet de la composition du copolymère est également étudié. Dans les films de première génération, le copolymère de choix était le P(VDF-TrFE) 70-30. Ce copolymère affiche une température de Curie à 105°C, alors que pour le dérivé 75-25 %, la température de Curie passe à 115°C. Ce dernier copolymère, bien que légèrement moins piézoélectrique, semble donc plus intéressant pour nos travaux car il offre une "fenêtre de température" plus large pour le choix du complexe à TS.

Une nouvelle méthode d'élaboration de films composites plus flexible, basée sur la technique du dépôt de gouttes, a été optimisée pour obtenir une seconde génération de composites TS@P(VDF-TrFE) de compositions variables. Ces films ont également été caractérisés par la mesure en court-circuit de leurs propriétés électromécaniques.

L'utilisation de la matrice P(VDF-TrFE) 75-25 nous a permis d'observer un courant pyroélectrique approprié (inversion de polarité lors du chauffage et du refroidissement) pour l'échantillon 6a, élaboré en utilisant des microparticules de formule $[Fe(H\text{-}trz)_{1,85}(trz)_{0,95}(NH_2trz)_{0,2}](BF_4)_{1,05}\text{-}0.6H_2O$. En outre, les pics de décharge liés au matériau à TS atteignent également des amplitudes remarquables dans cet échantillon, à tel point que dans une plage de températures restreinte autour de la TS, la décharge pyroélectrique est plus importante que pour le copolymère P(VDF-TrFE) 75-25 pur (voir Fig 9 en encadré).

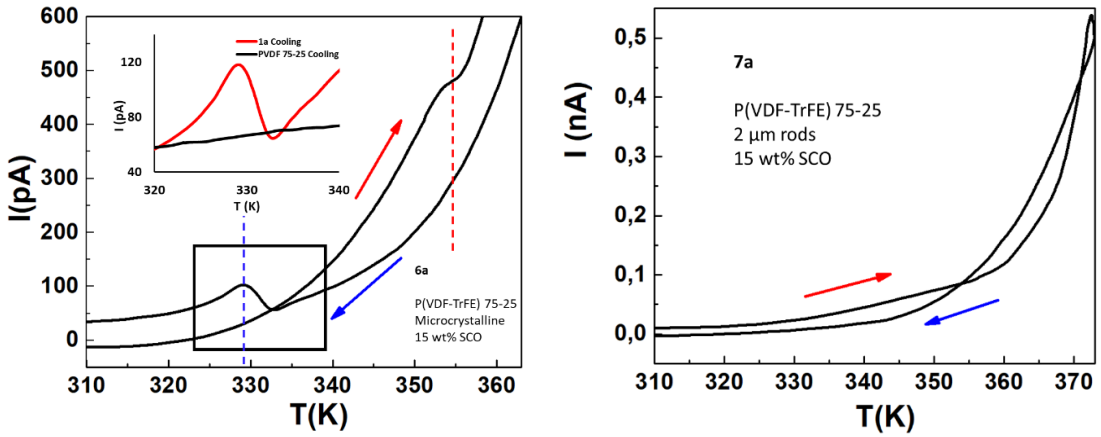

Fig 9) Cycle de décharge pyroélectrique pour les échantillons polarisés **6a** et **7a** . Les flèches indiquent le chauffage et le refroidissement. Les lignes en pointillés indiquent les pics de décharge liés à la TS pour le refroidissement (à gauche) et le chauffage (à droite). L'encadré montre une comparaison entre l'échantillon 6a et le PVDF-TrFE 75-25 pur (courant corrigé par la proportion de polymère).

Le composite **7a**, élaboré à partir de particules anisotropes en forme d'aiguille de $[Fe(H\text{-}trz)_{1.8}(trz)_1(NH_2trz)_{0.2}](BF_4)_1\text{-}0.7H_2O$, apparaît singulier dans cette série d'échantillons, car il ne présente ni pyroélectricité ni pics de décharge liés à la transition de spin. En effet, cet échantillon était particulièrement difficile à polariser, car il présentait des valeurs de d_{33} nettement inférieures et avait une tolérance de champ de polarisation beaucoup plus faible. En outre, dans le composite **7a**, la transition de spin du premier cycle de chauffage chevauche fortement la température de Curie, ce qui conduit finalement à la destruction de la (faible) polarisation obtenue. Il est possible que les particules en forme d'aiguille soient désavantagées en termes de résistance aux champs électriques élevés appliqués, en raison de l'existence de pointes aiguës dans les diélectriques, ce qui peut conduire à des décharges électriques localisées. En outre, l'anisotropie des particules, qui sont pour la plupart orientées dans le plan, est également

défavorable car la plupart des contraintes liées à la TS sont produites perpendiculairement à la direction de polarisation.

Comme prévu, pour les concentrations croissantes de matériau à TS (échantillons **8a-8c,** de 5 a 33%), les pics de décharge associés à la transition de spin apparaissent de plus en plus clairement. Cependant, cette augmentation des pics de décharge n'est pas liée à une augmentation substantielle du courant de décharge à la transition de spin. Au contraire, les pics apparaissent parce que la réponse pyroélectrique classique se réduit considérablement (Fig 10), ce qui entraîne un rendement électrique beaucoup plus faible.

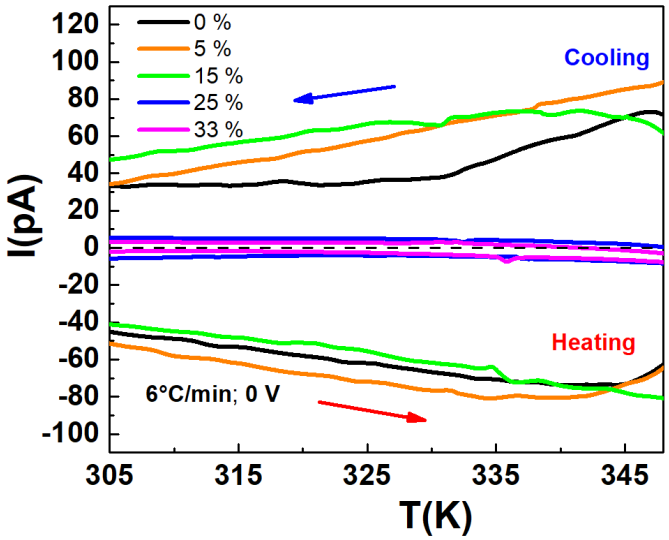

Fig 10) Cycle de décharge pyroélectrique pour les composites **8a-8e** ainsi que pour le P(VDF-TrFE) pur 75-25. La légende indique la concentration du complexe **8** dans chacun des composites. Les flèches indiquent le chauffage et le refroidissement.

Le principal résultat de ces travaux de recherche a été la mise au point d'une technique d'élaboration versatile et reproductible pour fabriquer les composites TS@P(VDF-TrFE). Ces composites conservent à la fois les propriétés de TS du complexe de coordination et les propriétés piézoélectriques de la matrice. Les films composites résultants peuvent être polarisés sous un champ électrique, et les films polarisés montrent une synergie entre le changement de volume associé à la transition de spin et les propriétés piézoélectriques inhérentes de la matrice, ce qui entraîne des pics de décharge pseudo-pyroélectrique autour de la transition de spin.

L'utilisation d'une grande variété de complexes, de morphologies et de concentrations ainsi que l'utilisation de différentes proportions de TrFE dans la matrice nous ont permis de démontrer que le couplage mécano-électrique entre une matrice de copolymère PVDF-TrFE ferroélectrique et les particules à transition de spin est une propriété générique. Un résultat important de ce travail est qu'en réglant la température de Curie du copolymère (via la

modification du rapport VDF : TrFE) et la température de transition de spin des particules, nous avons pu séparer efficacement ces deux phénomènes et récupérer ainsi la propriété pyroélectrique du polymère pur. En fonction de la concentration de la charge de matériau à TS, nous avons observé deux comportements. Dans la limite de faible concentration (environ 5-15 % - selon les détails expérimentaux), nous avons pu obtenir des propriétés électromécaniques dans les composites, qui sont comparables à celles de la matrice polymère pure. Ces composites peuvent être considérés comme des matériaux intelligents, multifonctionnels et à hautes performances, présentant des propriétés électromécaniques, optiques et magnétiques intéressantes.

Chapter 3: Actionneurs composites à transition de spin.

La robotique souple est un domaine de recherche en pleine expansion et concerne les matériaux relativement mous capables de se tordre, de se plier, de se déformer pour se déplacer ou d'adapter leur forme pour accomplir des tâches spécifiques. Ce domaine de la robotique a de multiples applications en médecine et dans l'industrie manufacturière, telles que : des manipulateurs interagissant avec des objets, des robots traversant des terrains imprévisibles et des dispositifs travaillant en contact étroit avec des êtres humains [146]. Le développement de matériaux intelligents et en particulier d'actionneurs flexibles est crucial pour le développement de ce domaine dans son ensemble [147,148].

Les matériaux à TS pourraient être d'un grand intérêt pour le développement d'actionneurs souples, car ils présentent une transition hautement réversible qui induit un changement de volume important au niveau moléculaire, qui peut être transmis à une matrice. En effet, dans le chapitre précédent, un des résultats clés a été la possibilité d'utiliser des matériaux à TS en combinaison avec des matrices polymères pour exploiter le changement de volume significatif des complexes en activant un polymère piézoélectrique. Nous avons constaté qu'en effet, ce changement de volume est effectivement transmis à la matrice qui, à son tour, présente une contrainte mécanique.

Afin d'amplifier et d'exploiter le changement de volume des matériaux à TS, une structure bicouche est souvent utilisée. Dans un système bicouche, la différence d'expansion volumique entre les deux couches provoque la déformation et la flexion du système, ce qui se traduit par un mouvement mécanique. La couche active est donc la couche avec une contrainte plus élevée le long de l'axe du dispositif, dans notre cas la couche avec des propriétés de TS, tandis que la

couche inactive est la couche avec une contrainte plus faible, une couche sans matériau à TS (Fig 11).

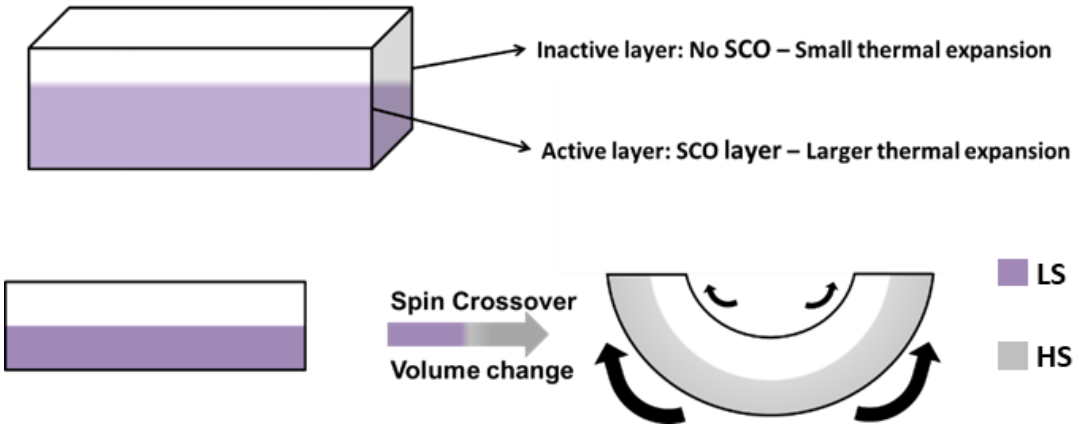

Fig 11) Représentation schématique d'un matériau bicouche SCO (en haut) et du principe bicouche pour l'actionnement (en bas).

Notre groupe de recherche a déjà mis au point des dispositifs à TS qui utilisent ce principe d'actionnement. Le premier exemple a été développé par Shepherd et al. Il s'agit d'un actionneur basé sur un monocristal de {Fe(3-CNpy)[Au(CN)$_2$]$_2$} recouvert d'une couche d'aluminium [11], qui sert à la fois de preuve de concept et de référence d'efficacité, en montrant le potentiel mécanique d'un actionneur avec une couche active composée de matériau à TS. Cet actionneur bicouche subit une transition de spin déclenchée thermiquement qui est ensuite traduite en un mouvement de flexion (Fig 12 ci-dessus). Le dispositif développé par Gural'skiy et al est le premier à utiliser l'approche composite et le premier à effectuer un actionnement contrôlé électriquement par effet Joule [179]. Dans ce travail, le composé [Fe(trz)(H-trz)$_2$](BF$_4$) est dispersé dans une matrice polymère PMMA comme couche active à TS. La couche inactive est un une peinture argentée commerciale, qui sert également à transporter l'électricité à travers le système pour le chauffage par effet Joule de l'actionneur, qui déclenche la transition de spin, et donc le mouvement du système (Fig 12 en bas).

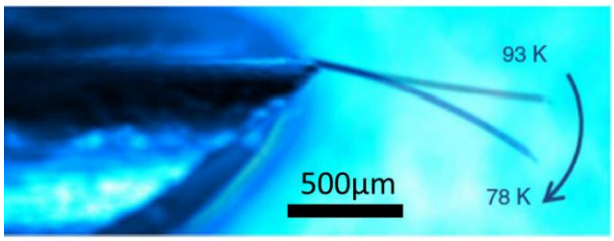

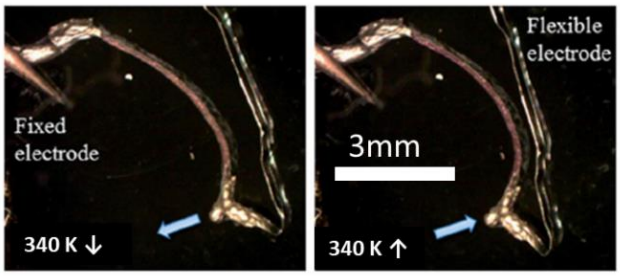

Fig 12) Actionneurs bicouches à TS [11,179]. Bicouche crystal/Aluminium (en haut) et actionneur électro thermomécanique en PMMA (en bas).

Ce chapitre décrit le processus d'élaboration d'une nouvelle génération d'actionneurs à base de matériaux à TS. La facilité d'utilisation à l'échelle macro, la robustesse, la contrôlabilité et la capacité à lever une charge sont les principaux objectifs de ces nouvelles procédures d'élaboration.

En partant des résultats de notre groupe de recherche, l'objectif était d'aller plus loin dans l'élaboration et l'application de tels dispositifs d'actionneurs macroscopiques incorporant des molécules à TS. Au cours du développement de ce travail, il y avait deux lignes de recherche principales pour l'élaboration de ces matériaux composites. Le premier consistait à utiliser une méthodologie de haute technologie et de haute précision, à savoir l'impression stéréolitographique 3D, pour fabriquer des actionneurs bicouches. La seconde approche consistait à utiliser des méthodes de moulage très polyvalentes, plus artisanales mais génériques, pour fabriquer des actionneurs bicouches composites.

L'utilisation de techniques d'impression 3D pour élaborer des actionneurs SCO ouvre la possibilité d'élaborer de manière fiable et reproductible des actionneurs avec une architecture entièrement contrôlable, nous donnant un contrôle complet sur chaque aspect de la morphologie du dispositif. Cette méthode utilise des techniques d'impression 3D déjà existantes et le défi consiste à incorporer de manière adéquate les matériaux à TS dans le processus et à adapter la méthodologie à la nouvelle composition pour obtenir des résultats appropriés.

La technique de choix pour l'élaboration des objets SCO imprimés en 3D était la méthodologie stéréo-lithographique par absorption mono-photonique (SLA), basée sur la photo-polymérisation d'une résine [183]. Cette technique a été utilisée pour la fabrication directe, sous éclairement laser, d'architectures 2D et 3D (extensibles jusqu'à 500 cm^3) avec une résolution micrométrique. La profondeur de polymérisation effective dans le matériau permet d'écrire facilement dans des couches épaisses (maximum testé 100 µm) et minces (minimum testé 10 µm) ainsi que de réaliser des architectures 3D comprenant de véritables structures autoportantes sans avoir besoin de supports sacrificiels.

L'imprimante DWS 029D a été utilisée dans notre étude. Le dispositif SLA est constitué de miroirs galvanométriques qui déplacent le faisceau laser (20 µm de diamètre) dans les directions x et y. Le porte-échantillon et le réservoir sont montés sur une platine mobile sur l'axe z, ce qui

permet d'assurer une épaisseur de couche minimale de 10 µm. Toutes les structures produites dans ce travail ont été obtenues couche par couche en utilisant une procédure de remplissage par balayage de trame. Chaque couche dans l'axe z a une épaisseur définie comme la distance de tranchage en z. Ces couches sont ensuite élaborées en balayant la zone d'écriture cible avec le laser selon un motif composé de lignes parallèles, la distance entre ces lignes étant la distance de hachure. Plus les distances de découpage en z et de hachurage sont courtes, plus la résolution de l'objet imprimé est élevée, mais le temps d'impression est plus long. Une fois la procédure d'impression terminée, et afin d'éliminer les matériaux non exposés, les échantillons sont développés dans un bain d'isopropanol sous sonication pendant 15 minutes.

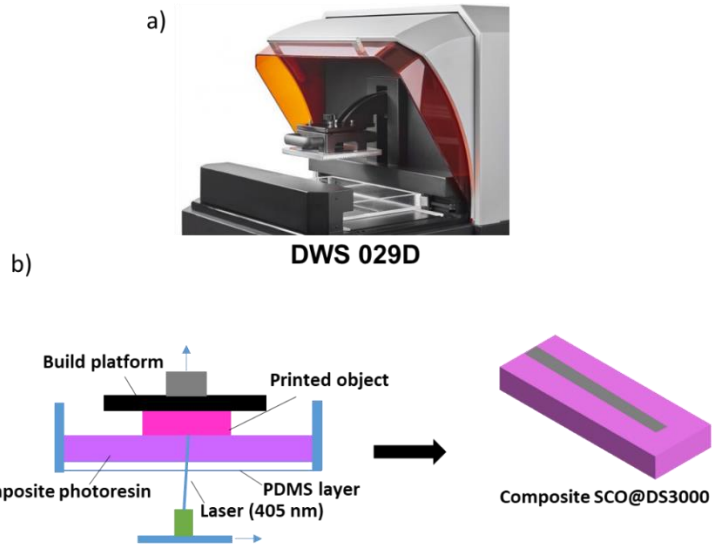

Fig 13) a) Imprimante 3D DWS 029D SLA. b) Procédé d'impression SLA des objets TS@DS3000.

Une matériau composite homogène a été élaborée en utilisant du $[Fe(NH_2trz)]SO_4$ comme complexe à TS dispersé dans la résine d'impression 3D DS3000. En utilisant cette résine homogène, des objets monolithiques TS@DS3000 de morphologies variées ont été imprimés avec succès. Les objets imprimés conservent la caractéristique thermochromique de complexe à TS, ce qui montre que le complexe conserve ses propriétés de transition même lorsqu'il est finement et uniformément dispersé. Les structures 3D les plus complexes que nous avons fabriquées sont des ressorts hélicoïdaux. Il est clair que l'impression 3D nous permet d'obtenir des matériaux à TS avec des formes spécifiques, ce qui serait extrêmement difficile, voire impossible, à obtenir par d'autres méthodes de fabrication (Fig 14).

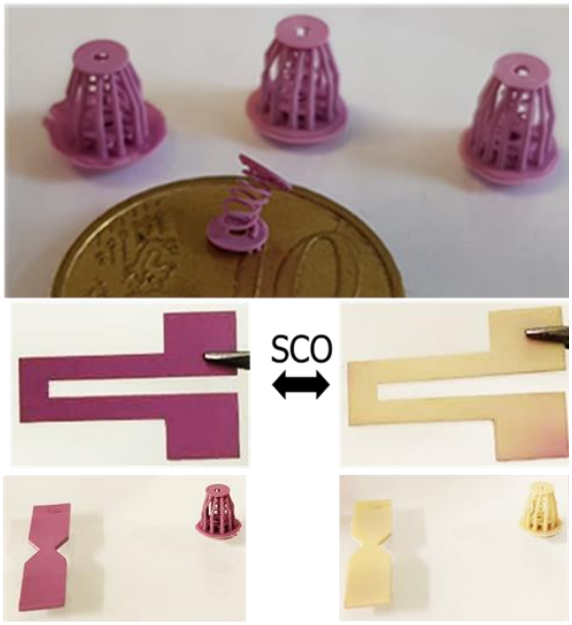

Fig 14) Composites TS@DS3000 (15 % en poids de matériau à TS) imprimés en 3D. Changement de couleur réversible lors du chauffage au-dessus de 80°C en raison de la transition de spin.

Pour une utilisation comme actionneurs autonomes, les ressorts imprimés en 3D présentent une déformation très insuffisante. Il était donc nécessaire de développer un nouveau protocole pour exploiter et amplifier de manière appropriée le changement de volume des complexes à TS. Nous avons opté pour une approche bicouche, comme celle utilisée précédemment dans l'équipe, pour d'autres actionneurs à TS.

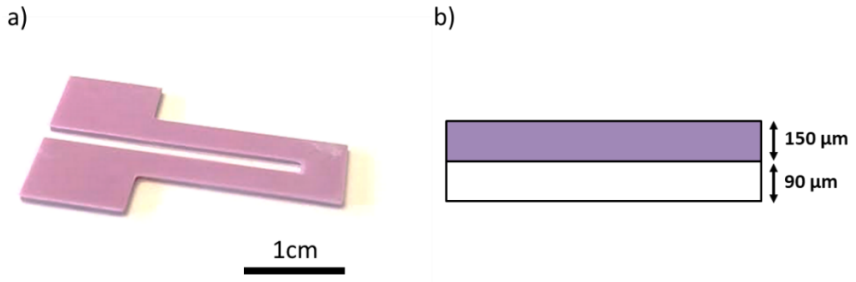

Fig 15) a) Composite bicouche imprimé en 3D TS@DS3000/DS3000. b) Représentation schématique d'un système bicouche sans délaminage.

Pour évaluer le mouvement de la bicouche, l'objet imprimé avec une extrémité fixe a été stimulé par la chaleur tandis qu'un système laser de suivi de distance sans contact (NCDT) suivait la position de la pointe libre.

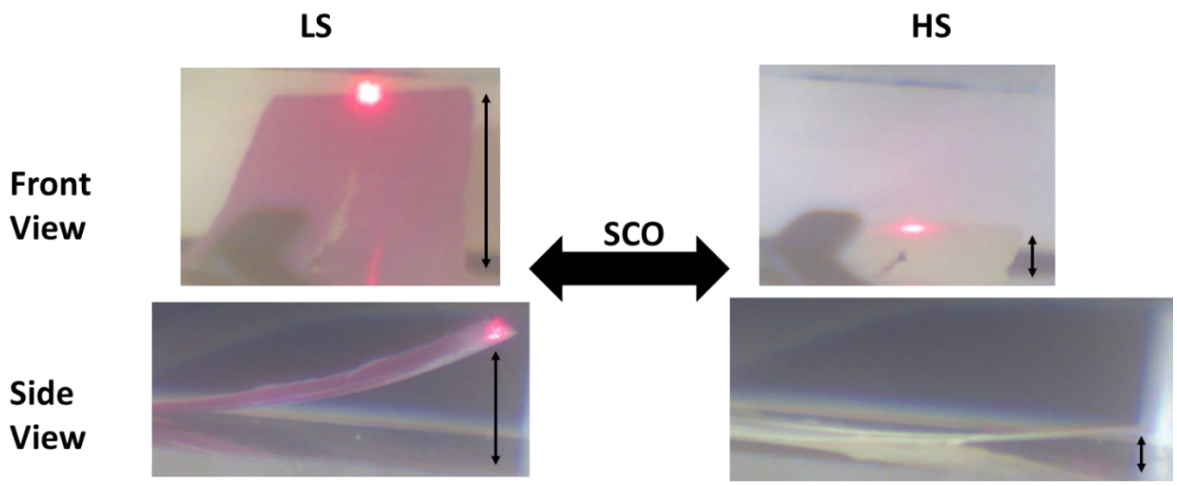

Fig 16) Actionnement de la bicouche TS@DS3000/DS3000. Vue frontale de l'actionneur (en haut) et vue latérale de l'actionneur (en bas)

Le déplacement de la pointe pour un échantillon de 240 µm d'épaisseur lors du chauffage et du refroidissement entre 300 et 360 K nous permet de voir le mouvement brusque associé à la transition de spin.

En conclusion, en utilisant une approche stéréolithographique en conjonction avec des polymères composites à transition de spin, nous avons imprimé en 3D diverses architectures mono- et bimorphes répondant à des stimuli, avec des tailles allant jusqu'à plusieurs cm et des détails structurels jusqu'à l'échelle de 80 µm. Les objets présentent de bonnes propriétés thermiques et mécaniques et permettent un actionnement mécanique réversible généré par le changement de volume accompagnant le phénomène de transition de spin. Le procédé de fabrication développé ici est simple, polyvalent et permet de créer des géométries planes et tridimensionnelles arbitraires, qui ne sont pas accessibles par d'autres techniques. Ce travail élargit le choix restreint de matériaux pour l'impression 4D. En ce qui concerne l'applicabilité de ce matériau, il semble y avoir un inconvénient majeur à cette approche : jusqu'à présent, aucune de nos tentatives pour conférer à la résine DS3000 des propriétés de conductivité électrique n'a abouti. Nous avons tenté d'intégrer des particules d'argent dans la résine pour lui conférer une conductivité électrique, mais l'ajout d'argent a un effet négatif sur le processus de réticulation de la résine. Les systèmes à commande électrique présentent un grand intérêt dans le domaine de la robotique, une autre approche est nécessaire pour réaliser des actionneurs à commande électrique. C'est le problème central que nous tenterons de résoudre avec notre deuxième approche pour l'élaboration d'actionneurs bicouches souples à transition de spin TS@P(VDF-TrFE)/P(VDF-TrFE) obtenus par moulage.

Les bicouches conductrices à TS composite ont donc été élaborées en utilisant une technique de moulage par racle. La matrice choisie pour ces actionneurs est le P(VDF-TrFE) 70-30 en raison de sa bonne stabilité mécanique et de sa facilité de mise en œuvre. Les actionneurs

fabriqués, découpés en forme de circuit pour permettre à un courant appliqué d'agir comme stimulus thermique, présentent un actionnement électrique. L'utilisation d'un stimulus électrique permet une commande autonome des dispositifs via un contrôleur PID. Cette technique de fabrication permet l'élaboration et le réglage polyvalent de ces actionneurs bicouches composites, offrant également la possibilité de fabriquer une série de matériaux pour explorer l'effet de la composition sur les propriétés d'actionnement de ces dispositifs.

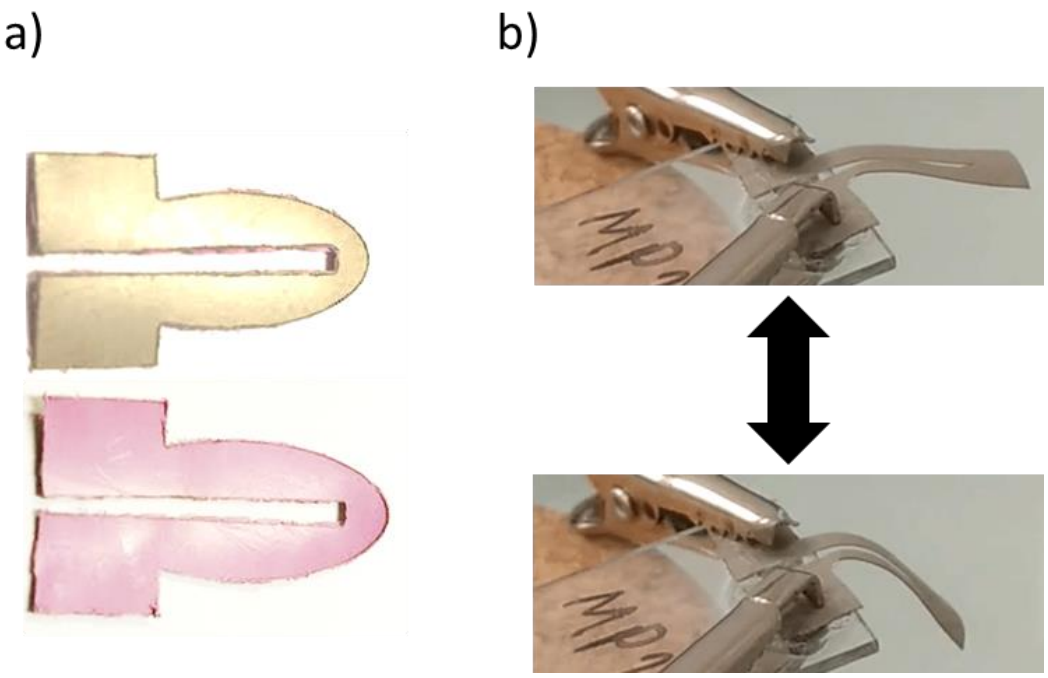

Fig 17) a) coté Ag@P(VDF-TrFE) (haut) et coté TS(**5**)@P(VDF-TrFE) (bas) du même actionneur bicouche. b) Actionnement électrique d'un bicouche conducteur TS@P(VDF-TrFE)/Ag@P(VDF-TrFE).

En utilisant une série de complexes à TS, une série de bicouches conductrices TS@P(VDF-TrFE)/Ag@P(VDF-TrFE) a été élaborée. Afin de caractériser les propriétés d'actionnement de chaque dispositif, les échantillons ont été activés sous contrôle en boucle ouverte et leur position a été suivie et mesurée. Chaque échantillon a été excité par un courant d'entrée suffisant pour induire le plus grand mouvement possible. Les amplitudes de déflexion mesurées représentent donc la déformation maximale à laquelle les échantillons peuvent être soumis (Fig 18).

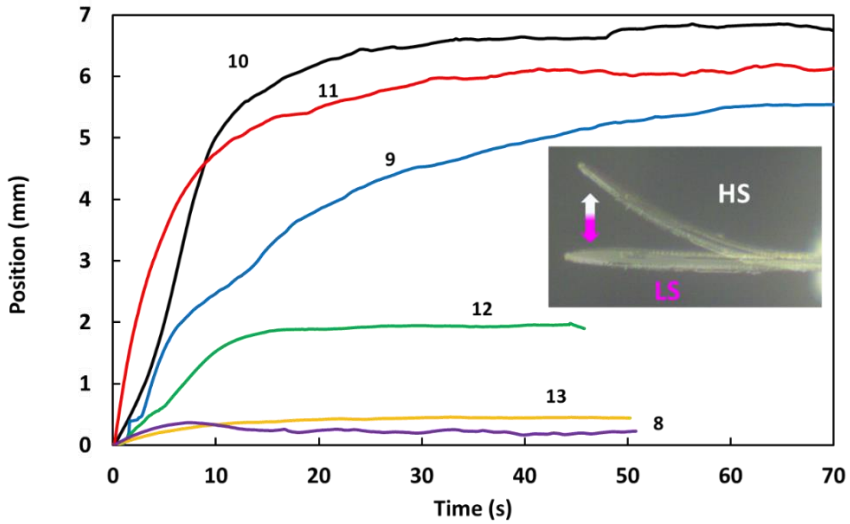

Fig 18) Courbes d'actionnement maximal en boucle ouverte pour une série d'actionneurs utilisant différents complexes à TS (**8** = $[Fe(HB(tz)_3)_2]$, **9** = $[Fe(NH_2trz)_3]SO_4$, **10** = $[Fe(C_5trz)_3](tosylate)_2$, **11** = $[Fe(C_{18}trz)_3](tosylate)_2$, **12** = $[Fe(qsal\text{-}I)_2]$, **13** = $[Fe(NH_2trz)_3](BF_4)_2$). L'encadré montre le mouvement réversible de la bicouche **10**.

Dans cette étude, l'actionneur **13** est une référence, car le composé $[Fe(NH_2trz)_3](BF_4)_2$ qui le compose présente une température de transition de spin bien inférieure à la température ambiante et n'est donc pas actif dans la plage de température mise en œuvre. En tant que tel, son actionnement résulte exclusivement du décalage de la dilatation thermique des deux couches composites. En effet, il présente une amplitude d'actionnement qui est d'un ordre de grandeur inférieur à celle des actionneurs **9-12**. Cela prouve que la contrainte associée au phénomène de TS joue un rôle crucial dans le mouvement des actionneurs. L'actionneur **10** présente les propriétés les plus intéressantes, tant en termes d'amplitude d'actionnement maximale qu'en termes de vitesse de réponse. Les actionneurs **11** et **9** présentent une performance comparable à celle de l'actionneur **10**, bien qu'avec une amplitude un peu plus faible et des temps de réponse légèrement différents. La bonne performance des actionneurs **9** à **11** est probablement liée à la grande contrainte volumétrique (jusqu'à 10 % en volume [196]) associée à la TS dans cette famille de complexes Fe(II)-triazole et à la nature abrupte des transitions de spin se produisant à des températures relativement basses. Afin d'effectuer avec précision l'actionnement complet de l'échantillon **12**, il a été refroidi dans l'état LS à l'aide de fumées d'azote liquide. Néanmoins, l'amplitude de déflexion plus faible est en accord avec la contrainte volumétrique plutôt faible (environ 4%) mesurée pour ce matériau "moléculaire" [194]. Malheureusement, il a été impossible de verrouiller l'état de spin (effet mémoire) du composite **12** en raison de son hystérésis trop étroite et de l'inhomogénéité du chauffage du dispositif. L'actionneur **8** est un cas particulier. Il présente une amplitude d'actionnement comparable (même légèrement inférieure) à celle de l'échantillon référence, malgré le fait que le complexe $[Fe(HB(tz)_3)_2]$ présente une contrainte d'environ 4,5 % en volume associée à la TS

bien au-dessus de la température ambiante [197]. Cette observation intrigante pourrait être liée à l'anisotropie prononcée de la contrainte lors de la transition de spin dans le composé $[Fe(HB(tz)_3)_2]$ déterminée par diffraction des rayons X sur un monocristal [141]. En effet, si les microcristaux sont alignés de telle manière que l'axe c de la maille cristallographique orthorhombique est normal par rapport à l'axe du dispositif bicouche, la courbure de la bicouche sera très faible ou même de signe opposé.

Afin d'optimiser les propriétés d'actionnement de ces dispositifs grâce à une conception intelligente des matériaux, une bicouche a été fabriquée à l'aide de particules anisotropes à TS. Cet actionneur (**7**) devrait avoir un actionnement nettement amélioré grâce à l'alignement du matériau à TS dans la matrice, en orientant le changement de volume des particules dans une direction donnée. L'actionneur **7** a eu une performance exceptionnelle dans des conditions de boucle ouverte (Fig 19). L'actionneur **7**, au lieu de se plier à un certain angle comme les actionneurs **8-13**, se replie sur lui-même, montrant un enroulement en spirale rappelant les mouvements d'enroulement de certaines plantes [198]. Cela signifie cependant que dans notre système de mesure optique de la distance actuel, il devient impossible de mesurer le mouvement de l'actionneur.

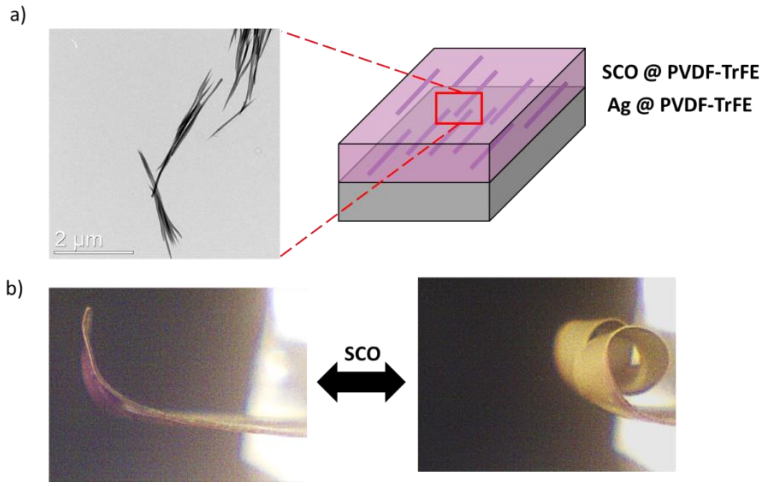

Fig 19) a) Schéma du dispositif bicouche **7** préparé en utilisant des microcristaux en forme de bâtonnets du complexe 7 avec orientation préférentielle dans la matrice P(VDF-TrFE). Une image TEM des microcristaux est également présentée. b) Actionnement électrothermique réversible d'un dispositif bicouche **7** dans des conditions de boucle ouverte à 0,7 A.

Afin de tester l'étendue des capacités de ce dispositif avec le même courant d'entrée, des poids croissants ont été ajoutés à l'actionneur et ses performances ont été enregistrées dans des conditions de boucle ouverte. L'actionneur **7** peut effectuer ce mouvement extraordinaire de manière réversible, même en maintenant une charge équivalente à 9 fois son propre poids (Fig 20). Pour des charges supérieures, l'actionnement devient rapidement irréversible, entraînant

une déformation permanente du dispositif, et après quelques cycles d'actionnement, la déformation induit une rupture de la couche conductrice.

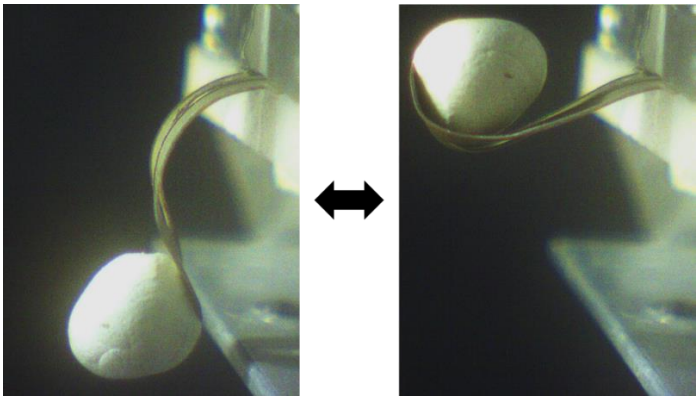

Fig 20) Actionnement électrothermique d'un dispositif bicouche **7** dans des conditions de boucle ouverte à 0,7 A avec une charge équivalente à 9 fois son propre poids.

Afin d'évaluer la contrôlabilité et la fiabilité de nos actionneurs dans des conditions de contrôle en boucle fermée, l'actionneur **10** a été piloté en utilisant diverses formes d'ondes sinusoïdales de différentes amplitudes et fréquences. L'actionneur **10** suit ces commandes avec une très grande précision, étant même capable de suivre un changement de paramètres sinusoïdaux avec un décalage minimal par rapport à la position cible, avec une erreur moyenne de 0,7% de la position cible. Lors du déplacement d'une charge de 343 mg (5 fois sa propre masse), le déplacement sinusoïdal reste totalement inchangé, ce qui confirme encore la capacité de l'actionneur à effectuer un travail significatif de manière fiable (Fig 21).

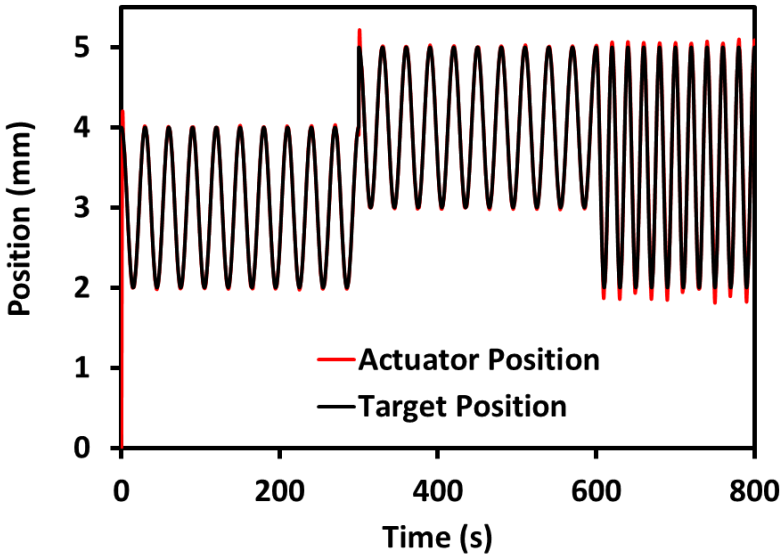

Fig 21) Actionnement sinusoïdal en boucle fermée d'un dispositif bicouche **10** supportant une charge de 343 mg (5 fois sa propre masse) avec des paramètres de contrôle variables (déplacements de la cible, amplitude et fréquence).

Pour évaluer la fiabilité à long terme de la commande, l'actionneur **10** a été mis en oscillation pendant une période de 30 s, avec une amplitude de 3 mm, pendant 12 jours pour un total de 35000 cycles d'actionnement. L'appareil n'a montré pratiquement aucun signe de fatigue et a pu poursuivre la commande avec un écart-type d'environ 0,4 µm pour les 35000 cycles, ce qui indique un cycle de fonctionnement important. Il est important de noter que, outre les avantages évidents de la commande en boucle fermée, l'actionneur est intrinsèquement assez robuste.

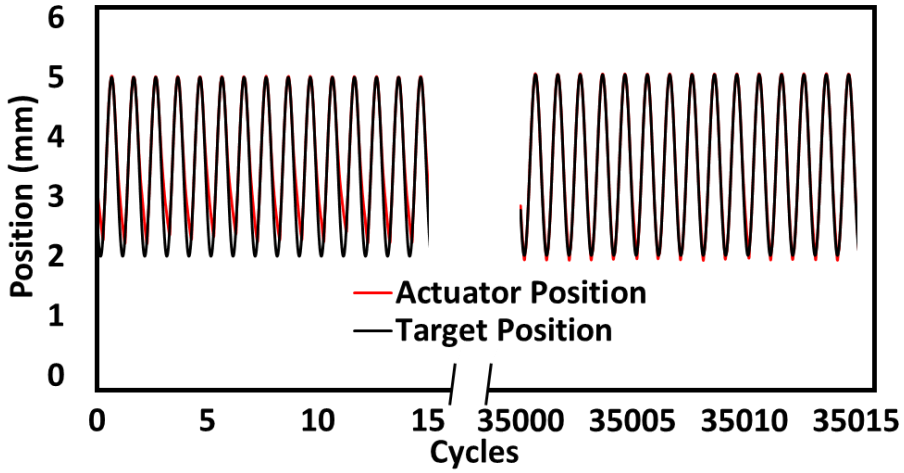

Fig 22) Actionnement sinusoïdal en boucle fermée du dispositif bicouche **10** avant et après avoir effectué 35000 cycles à l'air ambiant (12 jours, 0,033 Hz).

Il reste à voir dans quelle mesure il est possible d'intégrer ces matériaux dans des actionneurs électriques fonctionnels. Nous avons donc entrepris de fabriquer un démonstrateur intégrant des actionneurs bicouches à TS dans un dispositif plus avancé : un dispositif de préhension (figure 23).

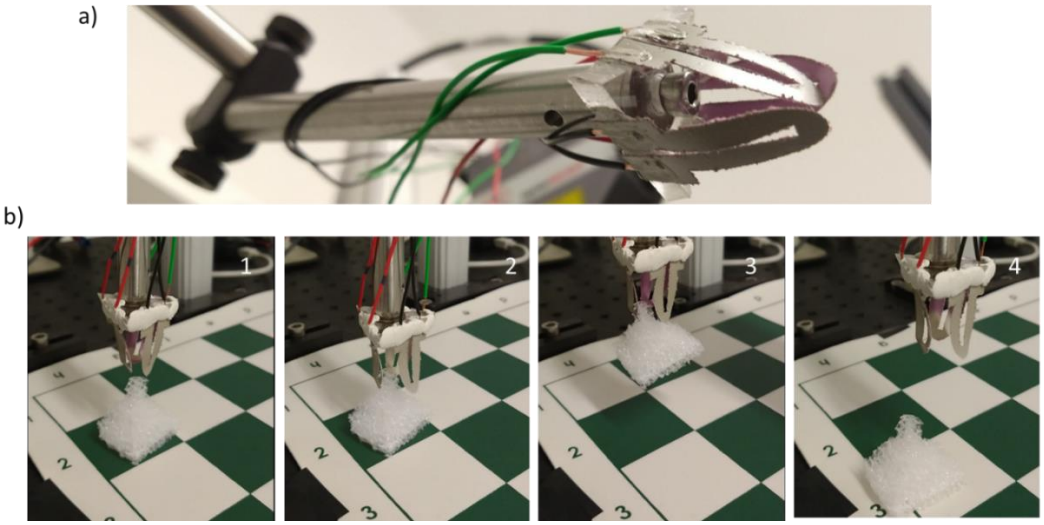

Fig 23 a) Image d'un dispositif de préhension (pince à 3 doigts) composé de trois actionneurs actifs

électriquement indépendants **10** b) 1- sans courant, la pince s'approche de l'échantillon cible, 2- l'injection simultanée de courant dans les actionneurs provoque l'ouverture de la pince, 3- l'arrêt de l'injection de courant permet d'attraper l'échantillon et de le déplacer à un endroit précis, 4- une nouvelle injection de courant permet de libérer l'objet.

Bien qu'élémentaire, ce résultat prouve que les actionneurs à TS peuvent être intégrés dans des dispositifs souples et flexibles effectuant un actionnement mécanique, et qu'ils peuvent présenter un intérêt pour le domaine de la robotique douce. Il reste de nombreuses questions en suspens et ce n'est qu'une première approche des actionneurs à TS en tant que dispositifs, mais cela prouve que ces matériaux ont le potentiel de devenir un ajout très intéressant au répertoire des matériaux d'actionnement souples.

En conclusion générale de ce chapitre, nous avons montré le potentiel des composites polymères à base de matériaux à TS pour être utilisés comme actionneurs avec un fort intérêt dans le domaine de la robotique. Nous avons montré non seulement leurs performances, mais aussi leur polyvalence et leur flexibilité en utilisant de multiples techniques d'élaboration et différents complexes à TS.

General conclusion:

Ce travail de thèse est centré sur l'utilisation de matériaux composites à transition de spin pour exploiter leur changement de volume inhérent avec deux applications différentes visées : la récupération d'énergie via l'incorporation de matériaux à TS dans une matrice piezoelectrique P(VDF-TrFE) et les muscles artificiels en utilisant une approche composite bicouche. Dans les deux cas, l'objectif de ce travail était la réalisation de dispositifs bistables qui exploitent de manière synergique les propriétés de transition de spin.

En conclusion générale de ce travail de thèse, nous avons réussi à fabriquer des matériaux composites à TS qui, en exploitant de manière synergique le changement de volume associé au phénomène de TS, nous permettent d'obtenir des réponses électromécaniques. Ainsi ces matériaux composites peuvent être intégrés dans des dispositifs fonctionnels pour la récupération d'énergie thermique ou pour le mimétisme de muscles.

References

[1] G. Molnár, S. Rat, L. Salmon, W. Nicolazzi, A. Bousseksou, Spin Crossover Nanomaterials: From Fundamental Concepts to Devices, Adv. Mater. 30 (2018) 1703862. https://doi.org/10.1002/adma.201703862.

[2] M.A. Halcrow, Spin-Crossover Materials: Properties and Applications, Spin-Crossover Mater. Prop. Appl. (2013). https://doi.org/10.1002/9781118519301.

[3] A. Bousseksou, G. Molnár, L. Salmon, W. Nicolazzi, Molecular spin crossover phenomenon: recent achievements and prospects, Chem. Soc. Rev. 40 (2011) 3313. https://doi.org/10.1039/c1cs15042a.

[4] P.D. Southon, L. Liu, E.A. Fellows, D.J. Price, G.J. Halder, K.W. Chapman, B. Moubaraki, K.S. Murray, J.-F. Létard, C.J. Kepert, Dynamic Interplay between Spin-Crossover and Host−Guest Function in a Nanoporous Metal−Organic Framework Material, J. Am. Chem. Soc. 131 (2009) 10998–11009. https://doi.org/10.1021/ja902187d.

[5] L. Salmon, L. Catala, Spin-crossover nanoparticles and nanocomposite materials, Comptes Rendus Chim. 21 (2018) 1230–1269. https://doi.org/10.1016/j.crci.2018.07.009.

[6] A. Enriquez-Cabrera, A. Rapakousiou, M. Piedrahita Bello, G. Molnár, L. Salmon, A. Bousseksou, Spin crossover polymer composites, polymers and related soft materials, Coord. Chem. Rev. 419 (2020) 213396. https://doi.org/10.1016/j.ccr.2020.213396.

[7] M.D. Manrique-Juárez, S. Rat, L. Salmon, G. Molnár, C.M. Quintero, L. Nicu, H.J. Shepherd, A. Bousseksou, Switchable molecule-based materials for micro- and nanoscale actuating applications: Achievements and prospects, Coord. Chem. Rev. 308 (2016) 395–408. https://doi.org/10.1016/j.ccr.2015.04.005.

[8] A. Thakre, A. Kumar, H.-C. Song, D.-Y. Jeong, J. Ryu, Pyroelectric Energy Conversion and Its Applications—Flexible Energy Harvesters and Sensors, Sensors. 19 (2019) 2170. https://doi.org/10.3390/s19092170.

[9] S. Priya, D.J. Inman, eds., Energy Harvesting Technologies, Springer US, Boston, MA, 2009. https://doi.org/10.1007/978-0-387-76464-1.

[10] S.M. Mirvakili, I.W. Hunter, Artificial Muscles: Mechanisms, Applications, and Challenges, Adv. Mater. 30 (2018) 1704407. https://doi.org/10.1002/adma.201704407.

[11] H.J. Shepherd, I.A. Gural'Skiy, C.M. Quintero, S. Tricard, L. Salmon, G. Molnár, A. Bousseksou, Molecular actuators driven by cooperative spin-state switching, Nat. Commun. 4 (2013) 1–9. https://doi.org/10.1038/ncomms3607.

[12] S. Timoshenko, Analysis of Bi-Metal Thermostats, J. Opt. Soc. Am. 11 (1925) 233. https://doi.org/10.1364/JOSA.11.000233.

[13] P. Gütlich, H.A. Goodwin, eds., Spin Crossover in Transition Metal Compounds I, 1st ed., Springer Berlin Heidelberg, Berlin, Heidelberg, 2004. https://doi.org/10.1007/b40394-9.

[14] P. Gütlich, H.A. Goodwin, eds., Spin Crossover in Transition Metal Compounds II, 1st ed., Springer Berlin Heidelberg, Berlin, Heidelberg, 2004. https://doi.org/10.1007/b93641.

[15] P. Gütlich, H.A. Goodwin, eds., Spin Crossover in Transition Metal Compounds III, 1st ed., Springer Berlin Heidelberg, Berlin, Heidelberg, 2004. https://doi.org/10.1007/b96439.

[16] H.G. Drickamer, Elektronische Umwandlungen in Übergangsmetallverbindungen bei hohem Druck, Angew. Chemie. 86 (1974) 61–70. https://doi.org/10.1002/ange.19740860202.

[17] S. Decurtins, P. Gütlich, C.P. Köhler, H. Spiering, A. Hauser, Light-induced excited spin state trapping in a transition-metal complex: The hexa-1-propyltetrazole-iron (II) tetrafluoroborate spin-crossover system, Chem. Phys. Lett. 105 (1984) 1–4. https://doi.org/10.1016/0009-2614(84)80403-0.

[18] G.J. Halder, Guest-Dependent Spin Crossover in a Nanoporous Molecular Framework Material, Science (80-.). 298 (2002) 1762–1765. https://doi.org/10.1126/science.1075948.

[19] A. Bousseksou, K. Boukheddaden, M. Goiran, C. Consejo, M.-L. Boillot, J.-P. Tuchagues, Dynamic response of the spin-crossover solid CoH2(fsa)2en)(py)2 to a pulsed magnetic field, Phys. Rev. B. 65 (2002) 172412. https://doi.org/10.1103/PhysRevB.65.172412.

[20] P. Gütlich, A. Hauser, H. Spiering, Thermal and Optical Switching of Iron(II) Complexes, Angew. Chemie Int. Ed. English. 33 (1994) 2024–2054. https://doi.org/10.1002/anie.199420241.

[21] M. Mikolasek, M.D. Manrique-Juarez, H.J. Shepherd, K. Ridier, S. Rat, V. Shalabaeva, A.-C. Bas, I.E. Collings, F. Mathieu, J. Cacheux, T. Leichle, L. Nicu, W. Nicolazzi, L. Salmon, G. Molnár, A. Bousseksou, Complete Set of Elastic Moduli of a Spin-Crossover Solid: Spin-State Dependence and Mechanical Actuation, J. Am. Chem. Soc. 140 (2018) 8970–8979. https://doi.org/10.1021/jacs.8b05347.

[22] A. Hauser, Ligand Field Theoretical Considerations, in: P. Gütlich, H.A. Goodwin (Eds.), Spin Crossover Transit. Met. Compd. I, Springer Berlin Heidelberg, Berlin, Heidelberg, 2004: pp. 49–58. https://doi.org/10.1007/b13528.

[23] E. König, K.J. Watson, The Fe□N bond lengths, the “ionic radii” of iron (II), and the crystal field parameters (10Dq) in a high-spin and low-spin [FeII-N6] complex, Chem. Phys. Lett. 6 (1970) 457–459. https://doi.org/10.1016/0009-2614(70)85191-0.

[24] S.K. Kulshreshtha, R.M. Iyer, E. König, G. Ritter, The nature of spin-state transitions in Fe(II) complexes, Chem. Phys. Lett. 110 (1984) 201–204. https://doi.org/10.1016/0009-2614(84)80175-X.

[25] H. Spiering, Elastic Interaction in Spin-Crossover Compounds, in: Spin Crossover Transit.

Met. Compd. III, Springer Berlin Heidelberg, Berlin, Heidelberg, 2004: pp. 171–195. https://doi.org/10.1007/b95427.

[26] Y. Garcia, O. Kahn, L. Rabardel, B. Chansou, L. Salmon, J.P. Tuchagues, Two-Step Spin Conversion for the Three-Dimensional Compound Tris(4,4‘-bis-1,2,4-triazole)iron(II) Diperchlorate, Inorg. Chem. 38 (1999) 4663–4670. https://doi.org/10.1021/ic990511q.

[27] J.A. Real, H. Bolvin, A. Bousseksou, A. Dworkin, O. Kahn, F. Varret, J. Zarembowitch, Two-step spin crossover in the new dinuclear compound [Fe(bt)(NCS)2]2bpym, with bt = 2,2’-bi-2-thiazoline and bpym = 2,2’-bipyrimidine: experimental investigation and theoretical approach, J. Am. Chem. Soc. 114 (1992) 4650–4658. https://doi.org/10.1021/ja00038a031.

[28] L. Salmon, A. Bousseksou, B. Donnadieu, J.-P. Tuchagues, Two Novel Iron(II) Materials Based on Dianionic N 4 O 2 Schiff Bases: Structural Properties and Spin-Crossover Characteristics in the Series [Fe(3-X,5-NO 2 -sal-N(1,4,7,10)] (X = H, 3-MeO, 3-EtO), Inorg. Chem. 44 (2005) 1763–1773. https://doi.org/10.1021/ic048387k.

[29] L. Salmon, L. Catala, Spin-crossover nanoparticles and nanocomposite materials, Comptes Rendus Chim. 21 (2018) 1230–1269. https://doi.org/10.1016/j.crci.2018.07.009.

[30] J.G. Moore, E.J. Lochner, C. Ramsey, N.S. Dalal, A.E. Stiegman, Transparent, Superparamagnetic KCo[FeIII(CN)6]–Silica Nanocomposites with Tunable Photomagnetism, Angew. Chemie Int. Ed. 42 (2003) 2741–2743. https://doi.org/10.1002/anie.200250409.

[31] C. Faulmann, J. Chahine, I. Malfant, D. de Caro, B. Cormary, L. Valade, A facile route for the preparation of nanoparticles of the spin-crossover complex [Fe(Htrz)2(trz)](BF4) in xerogel transparent composite films, Dalt. Trans. 40 (2011) 2480. https://doi.org/10.1039/c0dt01586e.

[32] A. Tokarev, J. Long, Y. Guari, J. Larionova, F. Quignard, P. Agulhon, M. Robitzer, G. Molnár, L. Salmon, A. Bousseksou, Spin crossover polysaccharide nanocomposites, New J. Chem. 37 (2013) 3420–3432. https://doi.org/10.1039/c3nj00534h.

[33] P.N. Martinho, T. Lemma, B. Gildea, G. Picardi, H. Müller-Bunz, R.J. Forster, T.E. Keyes, G. Redmond, G.G. Morgan, Template Assembly of Spin Crossover One-Dimensional Nanowires, Angew. Chemie Int. Ed. 51 (2012) 11995–11999. https://doi.org/10.1002/anie.201205122.

[34] S. Vaucher, M. Li, S. Mann, Synthesis of Prussian Blue Nanoparticles and Nanocrystal Superlattices in Reverse Microemulsions, Angew. Chemie Int. Ed. 39 (2000) 1793–1796. https://doi.org/10.1002/(SICI)1521-3773(20000515)39:10<1793::AID-ANIE1793>3.0.CO;2-Y.

[35] F.J. Valverde-Muñoz, A.B. Gaspar, S.I. Shylin, V. Ksenofontov, J.A. Real, Synthesis of Nanocrystals and Particle Size Effects Studies on the Thermally Induced Spin Transition of

the Model Spin Crossover Compound [Fe(phen) 2 (NCS) 2], Inorg. Chem. 54 (2015) 7906–7914. https://doi.org/10.1021/acs.inorgchem.5b00978.

[36] V. Martínez, I. Boldog, A.B. Gaspar, V. Ksenofontov, A. Bhattacharjee, P. Gütlich, J.A. Real, Spin Crossover Phenomenon in Nanocrystals and Nanoparticles of [Fe(3-Fpy) 2 M(CN) 4] (M II = Ni, Pd, Pt) Two-Dimensional Coordination Polymers, Chem. Mater. 22 (2010) 4271–4281. https://doi.org/10.1021/cm101022u.

[37] Y. Raza, F. Volatron, S. Moldovan, O. Ersen, V. Huc, C. Martini, F. Brisset, A. Gloter, O. Stéphan, A. Bousseksou, L. Catala, T. Mallah, Matrix-dependent cooperativity in spin crossover Fe(pyrazine)Pt(CN)4 nanoparticles, Chem. Commun. 47 (2011) 11501. https://doi.org/10.1039/c1cc14463d.

[38] H. Peng, S. Tricard, G. Félix, G. Molnár, W. Nicolazzi, L. Salmon, A. Bousseksou, Re-Appearance of Cooperativity in Ultra-Small Spin-Crossover [Fe(pz){Ni(CN) 4 }] Nanoparticles, Angew. Chemie. 126 (2014) 11074–11078. https://doi.org/10.1002/ange.201406710.

[39] T. Forestier, S. Mornet, N. Daro, T. Nishihara, S. Mouri, K. Tanaka, O. Fouché, E. Freysz, J.-F. Létard, Nanoparticles of iron(ii) spin-crossover, Chem. Commun. (2008) 4327. https://doi.org/10.1039/b806347h.

[40] E. Coronado, J.R. Galán-Mascarós, M. Monrabal-Capilla, J. García-Martínez, P. Pardo-Ibáñez, Bistable Spin-Crossover Nanoparticles Showing Magnetic Thermal Hysteresis near Room Temperature, Adv. Mater. 19 (2007) 1359–1361. https://doi.org/10.1002/adma.200700559.

[41] I.A. Gural'Skiy, C.M. Quintero, G. Molnár, I.O. Fritsky, L. Salmon, A. Bousseksou, Synthesis of spin-crossover nano- and micro-objects in homogeneous media, Chem. - A Eur. J. 18 (2012) 9946–9954. https://doi.org/10.1002/chem.201201063.

[42] O. Klimm, C. Göbel, S. Rosenfeldt, F. Puchtler, N. Miyajima, K. Marquardt, M. Drechsler, J. Breu, S. Förster, B. Weber, Synthesis of [Fe(L)(bipy)] n spin crossover nanoparticles using blockcopolymer micelles, Nanoscale. 8 (2016) 19058–19065. https://doi.org/10.1039/C6NR06330F.

[43] L. Catala, D. Brinzei, Y. Prado, A. Gloter, O. Stéphan, G. Rogez, T. Mallah, Core-Multishell Magnetic Coordination Nanoparticles: Toward Multifunctionality on the Nanoscale, Angew. Chemie Int. Ed. 48 (2009) 183–187. https://doi.org/10.1002/anie.200804238.

[44] G. Chastanet, N. Daro, S. Marre, C. Aymonier, T. Vaudel, L. Afindouli, One-Step Synthesis of Spin Crossover Nanoparticles Using Flow Chemistry and Supercritical CO2, Chem. – A Eur. J. (2020) chem.202002322. https://doi.org/10.1002/chem.202002322.

[45] H. Peng, G. Molnár, L. Salmon, A. Bousseksou, Matrix-free synthesis of spin crossover micro-rods showing a large hysteresis loop centered at room temperature, Chem. Commun. 51 (2015) 9346–9349. https://doi.org/10.1039/C5CC02949J.

[46] H. Peng, G. Molnár, L. Salmon, A. Bousseksou, Spin-Crossover Nano- and Micrometric

Rod-Shaped Particles Synthesized in Homogeneous Acid Media, Eur. J. Inorg. Chem. 2015 (2015) 3336–3342. https://doi.org/10.1002/ejic.201500486.

[47] H. Constant-Machado, J. Linares, F. Varret, J.G. Haasnoot, J.P. Martin, J. Zarembowitch, A. Dworkin, A. Bousseksou, Dilution Effects in a Spin Crossover System, Modelled in Terms of Direct and Indirect Intermolecular Interactions, J. Phys. I. 6 (1996) 1203–1216. https://doi.org/10.1051/jp1:1996124.

[48] A. Rotaru, J. Linares, E. Codjovi, J. Nasser, A. Stancu, Size and pressure effects in the atom-phonon coupling model for spin crossover compounds, J. Appl. Phys. 103 (2008) 07B908. https://doi.org/10.1063/1.2832674.

[49] A. Muraoka, K. Boukheddaden, J. Linarès, F. Varret, Two-dimensional Ising-like model with specific edge effects for spin-crossover nanoparticles: A Monte Carlo study, Phys. Rev. B. 84 (2011) 054119. https://doi.org/10.1103/PhysRevB.84.054119.

[50] A. Rotaru, F. Varret, A. Gindulescu, J. Linares, A. Stancu, J.F. Létard, T. Forestier, C. Etrillard, Size effect in spin-crossover systems investigated by FORC measurements, for surfacted [Fe(NH2-trz)3](Br)2·3H2O nanoparticles: reversible contributions and critical size, Eur. Phys. J. B. 84 (2011) 439–449. https://doi.org/10.1140/epjb/e2011-10903-x.

[51] J. Larionova, L. Salmon, Y. Guari, A. Tokarev, K. Molvinger, G. Molnár, A. Bousseksou, Towards the ultimate size limit of the memory effect in spin-crossover solids, Angew. Chemie - Int. Ed. 47 (2008) 8236–8240. https://doi.org/10.1002/anie.200802906.

[52] E.K. Akdogan, M. Allahverdi, A. Safari, Piezoelectric composites for sensor and actuator applications, IEEE Trans. Ultrason. Ferroelectr. Freq. Control. 52 (2005) 746–775. https://doi.org/10.1109/TUFFC.2005.1503962.

[53] C.L. Xie, D.N. Hendrickson, Mechanism of spin-state interconversion in ferrous spin-crossover complexes: direct evidence for quantum mechanical tunneling, J. Am. Chem. Soc. 109 (1987) 6981–6988. https://doi.org/10.1021/ja00257a013.

[54] A. Hauser, J. Adler, P. Gütlich, Light-induced excited spin state trapping (LIESST) in [Fe(2-mephen)3]2+ embedded in polymer matrices, Chem. Phys. Lett. 152 (1988) 468–472. https://doi.org/10.1016/0009-2614(88)80443-3.

[55] O. Kahn, J. Kröber, C. Jay, Spin Transition Molecular Materials for displays and data recording, Adv. Mater. 4 (1992) 718–728. https://doi.org/10.1002/adma.19920041103.

[56] O. Kahn, C.J. Martinez, Spin-transition polymers: From molecular materials toward memory devices, Science (80-.). 279 (1998) 44–48. https://doi.org/10.1126/science.279.5347.44.

[57] K. Senthil Kumar, M. Ruben, Emerging trends in spin crossover (SCO) based functional materials and devices, Coord. Chem. Rev. 346 (2017) 176–205. https://doi.org/10.1016/j.ccr.2017.03.024.

[58] L. Stoleriu, P. Chakraborty, A. Hauser, A. Stancu, C. Enachescu, Thermal hysteresis in spin-

crossover compounds studied within the mechanoelastic model and its potential application to nanoparticles, Phys. Rev. B. 84 (2011) 134102. https://doi.org/10.1103/PhysRevB.84.134102.

[59] A. Tissot, C. Enachescu, M.L. Boillot, Control of the thermal hysteresis of the prototypal spin-transition Fe II(phen)2(NCS)2 compound via the microcrystallites environment: Experiments and mechanoelastic model, J. Mater. Chem. 22 (2012) 20451–20457. https://doi.org/10.1039/c2jm33865c.

[60] C. Enachescu, W. Nicolazzi, Elastic models, lattice dynamics and finite size effects in molecular spin crossover systems, Comptes Rendus Chim. 21 (2018) 1179–1195. https://doi.org/10.1016/j.crci.2018.02.004.

[61] R. Tanasa, J. Laisney, A. Stancu, M.-L. Boillot, C. Enachescu, Hysteretic behavior of Fe(phen) 2 (NCS) 2 spin-transition microparticles vs. the environment: A huge reversible component resolved by first order reversal curves, Appl. Phys. Lett. 104 (2014) 031909. https://doi.org/10.1063/1.4862748.

[62] A. Slimani, H. Khemakhem, K. Boukheddaden, Structural synergy in a core-shell spin crossover nanoparticle investigated by an electroelastic model, Phys. Rev. B. 95 (2017) 174104. https://doi.org/10.1103/PhysRevB.95.174104.

[63] H. Oubouchou, A. Slimani, K. Boukheddaden, Interplay between elastic interactions in a core-shell model for spin-crossover nanoparticles, Phys. Rev. B. 87 (2013) 104104. https://doi.org/10.1103/PhysRevB.87.104104.

[64] G. Félix, M. Mikolasek, G. Molnár, W. Nicolazzi, A. Bousseksou, Control of the Phase Stability in Spin-Crossover Core-Shell Nanoparticles through the Elastic Interface Energy, Eur. J. Inorg. Chem. 2018 (2018) 435–442. https://doi.org/10.1002/ejic.201700121.

[65] G. Félix, M. Mikolasek, G. Molnár, W. Nicolazzi, A. Bousseksou, Tuning the spin crossover in nano-objects: From hollow to core–shell particles, Chem. Phys. Lett. 607 (2014) 10–14. https://doi.org/10.1016/j.cplett.2014.05.049.

[66] M. Mikolasek, G. Félix, G. Molnár, F. Terki, W. Nicolazzi, A. Bousseksou, Role of surface vibrational properties on cooperative phenomena in spin-crossover nanomaterials, Phys. Rev. B. 90 (2014) 075402. https://doi.org/10.1103/PhysRevB.90.075402.

[67] S. Park, H. Kim, M. Vosgueritchian, S. Cheon, H. Kim, J.H. Koo, T.R. Kim, S. Lee, G. Schwartz, H. Chang, Z. Bao, Stretchable energy-harvesting tactile electronic skin capable of differentiating multiple mechanical stimuli modes, Adv. Mater. 26 (2014) 7324–7332. https://doi.org/10.1002/adma.201402574.

[68] Y.-S. Koo, J.R. Galán-Mascarós, Spin Crossover Probes Confer Multistability to Organic Conducting Polymers, Adv. Mater. 26 (2014) 6785–6789. https://doi.org/10.1002/adma.201402579.

[69] S. Rat, M. Piedrahita-Bello, L. Salmon, G. Molnár, P. Demont, A. Bousseksou, Coupling Mechanical and Electrical Properties in Spin Crossover Polymer Composites, Adv. Mater.

30 (2018) 1705275. https://doi.org/10.1002/adma.201705275.

[70] A. Hauser, J. Adler, P. Gütlich, Light-induced excited spin state trapping (LIESST) in [Fe(2-mephen)3]2+ embedded in polymer matrices, Chem. Phys. Lett. 152 (1988) 468–472. https://doi.org/10.1016/0009-2614(88)80443-3.

[71] S.W. Lee, J.W. Lee, S.H. Jeong, I.W. Park, Y.M. Kim, J.I. Jin, Processable magnetic plastics composites - Spin crossover of PMMA/Fe(II)-complexes composites, Synth. Met. 142 (2004) 243–249. https://doi.org/10.1016/j.synthmet.2003.09.011.

[72] S.H. Jeong, K.N. Kim, J.S. Kang, C.S. Hong, D.H. Choi, J. Il Jin, I.W. Park, M.G. Kim, Storing spin-crossover and LC phase transitions information by hybridizing spin-crossover complexes with a thermotropic polymer matrix - A novel case of multiple switching, Mol. Cryst. Liq. Cryst. 471 (2007) 3–10. https://doi.org/10.1080/15421400701544422.

[73] Y. Chen, J.G. Ma, J.J. Zhang, W. Shi, P. Cheng, D.Z. Liao, S.P. Yan, Spin crossover-macromolecule composite nano film material, Chem. Commun. 46 (2010) 5073–5075. https://doi.org/10.1039/b927191k.

[74] M. Rubio, R. Hernández, A. Nogales, A. Roig, D. López, Structure of a spin-crossover Fe(II)–1,2,4-triazole polymer complex dispersed in an isotactic polystyrene matrix, Eur. Polym. J. 47 (2011) 52–60. https://doi.org/10.1016/j.eurpolymj.2010.10.029.

[75] C. Echeverria, M. Rubio, G.R. Mitchell, A. Roig, D. Lõpez, Hybrid polystyrene based electrospun fibers with spin-crossover properties, J. Polym. Sci. Part B Polym. Phys. 53 (2015) 814–821. https://doi.org/10.1002/polb.23702.

[76] M. Baumgartner, R. Schaller, P. Smith, I. Weymuth, W. Caseri, Co-Processing of [Fe(NH2trz)3](2ns)2 and UHMWPE into Materials Combining (Spin Crossover and High Mechanical Strength, Sci. 2 (2020) 66. https://doi.org/10.3390/sci2030066.

[77] S. Basak, P. Hui, R. Chandrasekar, Flexible and optically transparent polymer embedded nano/micro scale spin crossover Fe(II) complex patterns/arrays, Chem. Mater. 25 (2013) 3408–3413. https://doi.org/10.1021/cm401058s.

[78] N. Kojima, S. Toyazaki, M. Itoi, Y. Ono, W. Aoki, Y. Kobayashi, M. Seto, T. Yokoyama, Search on Multi-Functional Properties of Spin-Crossover System, Mol. Cryst. Liq. Cryst. 376 (2002) 567–574. https://doi.org/10.1080/713738447.

[79] A. Nakamoto, Y. Ono, N. Kojima, D. Matsumura, T. Yokoyama, Spin crossover complex film, [FeII(H-trz)3]-Nafion, with a spin transition around room temperature, Chem. Lett. 32 (2003) 336–337. https://doi.org/10.1246/cl.2003.336.

[80] X.J. Liu, Y. Moritomo, A. Nakamura, T. Hirao, S. Toyazaki, N. Kojima, Photoinduced phase transition and relaxation behavior in a spin-crossover Fe (II) complex Nafion-[Fe(Htrz)3] film, J. Phys. Soc. Japan. 70 (2001) 2521–2524. https://doi.org/10.1143/JPSJ.70.2521.

[81] A. Nakamoto, N. Kojima, L. Xiaojun, Y. Moritomo, A. Nakamura, Demonstration of the thermally induced high spin-low spin transition for a transparent spin crossover complex

film [Fe(II)(H-trz)3]-Nafion (trz = triazole), Polyhedron. 24 (2005) 2909–2912. https://doi.org/10.1016/j.poly.2005.03.040.

[82] A. Nakamoto, Y. Ono, N. Kojima, D. Matsumura, T. Yokoyama, X.J. Liu, Y. Moritomo, Spin transition and its photo-induced effect in spin crossover complex film based on [Fe(II)(trz)3], Synth. Met. 137 (2003) 1219–1220. https://doi.org/10.1016/S0379-6779(02)01058-5.

[83] A. Nakamoto, H. Kamebuchi, M. Enomoto, N. Kojima, Study on the spin crossover transition and glass transition for Fe(II) complex film, [Fe(II)(H-triazole) 3]@Nafion, by means of Mössbauer spectroscopy, Hyperfine Interact. 205 (2012) 41–45. https://doi.org/10.1007/s10751-011-0477-3.

[84] T.D. Gierke, G.E. Munn, F.C. Wilson, The morphology in nafion perfluorinated membrane products, as determined by wide- and small-angle x-ray studies, J. Polym. Sci. Polym. Phys. Ed. 19 (1981) 1687–1704. https://doi.org/10.1002/pol.1981.180191103.

[85] C. Heitner-Wirguin, Recent advances in perfluorinated ionomer membranes: structure, properties and applications, J. Memb. Sci. 120 (1996) 1–33. https://doi.org/10.1016/0376-7388(96)00155-X.

[86] H. Kamebuchi, T. Jo, H. Shimizu, A. Okazawa, M. Enomoto, N. Kojima, Development of pH-sensitive spin-crossover iron(II) complex films, [FeII(diAMsar)] Nafion: Manipulation of the spin state by proton concentration, Chem. Lett. 40 (2011) 888–889. https://doi.org/10.1246/cl.2011.888.

[87] G.P. Vishnevskaya, E.N. Frolova, I. V. Ovchinnikov, I.G. Pervova, Z.G. Rezinskikh, The spin-transition properties of Fe(III) complexes with hetarylformazan in an ion-exchange polymer: An EPR study, Russ. J. Phys. Chem. A. 84 (2010) 1388–1394. https://doi.org/10.1134/S0036024410080200.

[88] P. Durand, S. Pillet, E.E. Bendeif, C. Carteret, M. Bouazaoui, H. El Hamzaoui, B. Capoen, L. Salmon, S. Hébert, J. Ghanbaja, L. Aranda, D. Schaniel, Room temperature bistability with wide thermal hysteresis in a spin crossover silica nanocomposite, J. Mater. Chem. C. 1 (2013) 1933–1942. https://doi.org/10.1039/c3tc00546a.

[89] Y.X. Wang, D. Qiu, Z.H. Li, Z.G. Gu, X. Ren, Z. Li, Resin-Assisted Constructive Synthesis of Spin-Crossover Nanorod Arrays, Eur. J. Inorg. Chem. 2016 (2016) 4581–4585. https://doi.org/10.1002/ejic.201600774.

[90] H. Voisin, C. Aimé, A. Vallée, A. Bleuzen, M. Schmutz, G. Mosser, T. Coradin, C. Roux, Preserving the spin transition properties of iron-triazole coordination polymers within silica-based nanocomposites, J. Mater. Chem. C. 5 (2017) 11542–11550. https://doi.org/10.1039/c7tc04194b.

[91] H. Voisin, C. Aimé, A. Vallée, T. Coradin, C. Roux, A flexible polymer–nanoparticle hybrid material containing triazole-based Fe(<scp>ii</scp>) with spin crossover properties for magneto-optical applications, Inorg. Chem. Front. 5 (2018) 2140–2147.

https://doi.org/10.1039/C8QI00494C.

[92] I.A. Gural'Skiy, C.M. Quintero, J.S. Costa, P. Demont, G. Molnár, L. Salmon, H.J. Shepherd, A. Bousseksou, Spin crossover composite materials for electrothermomechanical actuators, J. Mater. Chem. C. 2 (2014) 2949–2955. https://doi.org/10.1039/c4tc00267a.

[93] Y.C. Chen, Y. Meng, Z.P. Ni, M.L. Tong, Synergistic electrical bistability in a conductive spin crossover heterostructure, J. Mater. Chem. C. 3 (2015) 945–949. https://doi.org/10.1039/c4tc02580f.

[94] A. Lapresta-Fernández, M.P. Cuéllar, J.M. Herrera, A. Salinas-Castillo, M.D.C. Pegalajar, S. Titos-Padilla, E. Colacio, L.F. Capitán-Vallvey, Particle tuning and modulation of the magnetic/colour synergy in Fe(ii) spin crossover-polymer nanocomposites in a thermochromic sensor array, J. Mater. Chem. C. 2 (2014) 7292–7303. https://doi.org/10.1039/c4tc00969j.

[95] A. Lapresta-Fernández, S. Titos-Padilla, J.M. Herrera, A. Salinas-Castillo, E. Colacio, L.F. Capitán Vallvey, Photographing the synergy between magnetic and colour properties in spin crossover material [Fe(NH 2 trz) 3](BF 4) 2 : a temperature sensor perspective, Chem. Commun. 49 (2013) 288–290. https://doi.org/10.1039/C2CC36320H.

[96] M.P. Cuéllar, A. Lapresta-Fernández, J.M. Herrera, A. Salinas-Castillo, M.D.C. Pegalajar, S. Titos-Padilla, E. Colacio, L.F. Capitán-Vallvey, Thermochromic sensor design based on Fe(II) spin crossover/polymers hybrid materials and artificial neural networks as a tool in modelling, Sensors Actuators B Chem. 208 (2015) 180–187. https://doi.org/10.1016/j.snb.2014.11.025.

[97] K.A. Vinogradova, D.P. Pishchur, I. V. Korolkov, M.B. Bushuev, Magnetic properties and vapochromism of a composite on the base of an iron(II) spin crossover complex, Inorg. Chem. Commun. 105 (2019) 82–85. https://doi.org/10.1016/j.inoche.2019.04.035.

[98] W. Hellel, A. Ould Hamouda, J. Degert, J.F. Létard, E. Freysz, Switching of spin-state complexes induced by the interaction of a laser beam with their host matrix, Appl. Phys. Lett. 103 (2013) 143304. https://doi.org/10.1063/1.4824028.

[99] M.D. Manrique-Juárez, F. Mathieu, A. Laborde, S. Rat, V. Shalabaeva, P. Demont, O. Thomas, L. Salmon, T. Leichle, L. Nicu, G. Molnár, A. Bousseksou, Micromachining-Compatible, Facile Fabrication of Polymer Nanocomposite Spin Crossover Actuators, Adv. Funct. Mater. 28 (2018) 1801970. https://doi.org/10.1002/adfm.201801970.

[100] A. Suzuki, M. Fujiwara, M. Nishijima, High spin/low spin phase transitions of a spin-crossover complex in the emulsion polymerization of trifluoroethylmethacrylate (TFEMA) using PVA as a protective colloid, Colloid Polym. Sci. 286 (2008) 525–534. https://doi.org/10.1007/s00396-007-1796-4.

[101] Y.S. Koo, J.R. Galán-Mascarós, Spin crossover probes confer multistability to organic conducting polymers, Adv. Mater. 26 (2014) 6785–6789. https://doi.org/10.1002/adma.201402579.

[102] S. Ahoulou, N. Vilà, S. Pillet, D. Schaniel, A. Walcarius, Coordination Polymers as Template for Mesoporous Silica Films: A Novel Composite Material Fe(Htrz)3@SiO2 with Remarkable Electrochemical Properties, Chem. Mater. 31 (2019) 5796–5807. https://doi.org/10.1021/acs.chemmater.9b01879.

[103] M. Sawczak, R. Jendrzejewski, D. Maskowicz, Y. Garcia, A.C. Ghosh, M. Gazda, J. Czechowski, G. Śliwiński, Nanocrystalline Polymer Impregnated [Fe(pz)Pt(CN)4] Thin Films Prepared by Matrix-Assisted Pulsed Laser Evaporation, Eur. J. Inorg. Chem. 2019 (2019) 3249–3255. https://doi.org/10.1002/ejic.201900231.

[104] Y. Maeda, M. Miyamoto, Y. Takashima, H. Oshio, Spin-crossover behaviour of iron(III) complexes with pendant type polymeric ligands, Inorganica Chim. Acta. 204 (1993) 231–237. https://doi.org/10.1016/S0020-1693(00)82930-8.

[105] W.P. Wang, Z.Q. Zhang, B.B. Ji, H.H. Zhao, G.Q. Li, L.X. Ma, H.X. Zhao, Synthesis and characterization of novel coordination spin crossover poly(glycidyl methacrylate) with pendant iron(II)-4-amino-1,2,4-triazole groups, Inorg. Chem. Commun. 56 (2015) 125–128. https://doi.org/10.1016/j.inoche.2015.04.005.

[106] W. Wang, B. Ji, C. Zhang, X. Cao, New spin crossover polymeric composite and another way to describe the result, Inorg. Chem. Commun. 67 (2016) 55–59. https://doi.org/10.1016/j.inoche.2016.03.007.

[107] G. Schwarzenbacher, M.S. Gangl, M. Goriup, M. Winter, M. Grunert, F. Renz, W. Linert, R. Saf, Preparation and Radical Oligomerization of anFe(II) Complex without Loss of Spin-Crossover Properties, Monatshefte Fuer Chemie/Chemical Mon. 132 (2001) 519–529. https://doi.org/10.1007/s007060170114.

[108] B. Djukic, M.T. Lemaire, Hybrid spin-Crossover conductor exhibiting unusual variable-temperature electrical conductivity, Inorg. Chem. 48 (2009) 10489–10491. https://doi.org/10.1021/ic9015542.

[109] B. Djukic, M.A. Singh, M.T. Lemaire, Formation of hybrid spin crossover polymer microspheres, Synth. Met. 160 (2010) 825–828. https://doi.org/10.1016/j.synthmet.2009.12.009.

[110] T.J. O'Sullivan, B. Djukic, P.A. Dube, M.T. Lemaire, A conducting metallopolymer featuring valence tautomerism, Chem. Commun. (2009) 1903–1905. https://doi.org/10.1039/b818952h.

[111] A. Benchohra, Switchable Spin-CrossOver complexes based Metallo-polymers a new class of functional molecular materials, Sorbonne University, 2019.

[112] R.S. Dahiya, M. Valle, Robotic Tactile Sensing: Technologies and System, Springer Netherlands, 2012.

[113] M. Safaei, H.A. Sodano, S.R. Anton, A review of energy harvesting using piezoelectric materials: state-of-the-art a decade later (2008–2018), Smart Mater. Struct. 28 (2019) 113001. https://doi.org/10.1088/1361-665X/ab36e4.

[114] J.-H. Lee, J. Kim, T.Y. Kim, M.S. Al Hossain, S.-W. Kim, J.H. Kim, All-in-one energy harvesting and storage devices, J. Mater. Chem. A. 4 (2016) 7983–7999. https://doi.org/10.1039/C6TA01229A.

[115] C.R. Bowen, J. Taylor, E. LeBoulbar, D. Zabek, A. Chauhan, R. Vaish, Pyroelectric materials and devices for energy harvesting applications, Energy Environ. Sci. 7 (2014) 3836–3856. https://doi.org/10.1039/C4EE01759E.

[116] X. Wang, F. Sun, G. Yin, Y. Wang, B. Liu, M. Dong, Tactile-Sensing Based on Flexible PVDF Nanofibers via Electrospinning: A Review, Sensors. 18 (2018) 330. https://doi.org/10.3390/s18020330.

[117] L. Li, M. Zhang, M. Rong, W. Ruan, Studies on the transformation process of PVDF from α to β phase by stretching, RSC Adv. 4 (2014) 3938–3943. https://doi.org/10.1039/C3RA45134H.

[118] Y. Liu, H. Aziguli, B. Zhang, W. Xu, W. Lu, J. Bernholc, Q. Wang, Ferroelectric polymers exhibiting behaviour reminiscent of a morphotropic phase boundary, Nature. 562 (2018) 96–100. https://doi.org/10.1038/s41586-018-0550-z.

[119] G. Teyssèdre, C. Lacabanne, Study of the thermal and dielectric behavior of P(VDF-TrFE) copolymers in relation with their electroactive properties, Ferroelectrics. 171 (1995) 125–144. https://doi.org/10.1080/00150199508018427.

[120] N.A. Shepelin, A.M. Glushenkov, V.C. Lussini, P.J. Fox, G.W. Dicinoski, J.G. Shapter, A. V. Ellis, New developments in composites, copolymer technologies and processing techniques for flexible fluoropolymer piezoelectric generators for efficient energy harvesting, Energy Environ. Sci. 12 (2019) 1143–1176. https://doi.org/10.1039/C8EE03006E.

[121] P. Martins, A.C. Lopes, S. Lanceros-Mendez, Electroactive phases of poly(vinylidene fluoride): Determination, processing and applications, Prog. Polym. Sci. 39 (2014) 683–706. https://doi.org/10.1016/j.progpolymsci.2013.07.006.

[122] N.A. Shepelin, A.M. Glushenkov, V.C. Lussini, P.J. Fox, G.W. Dicinoski, J.G. Shapter, A. V. Ellis, New developments in composites, copolymer technologies and processing techniques for flexible fluoropolymer piezoelectric generators for efficient energy harvesting, Energy Environ. Sci. 12 (2019) 1143–1176. https://doi.org/10.1039/C8EE03006E.

[123] A. Tamang, S.K. Ghosh, S. Garain, M.M. Alam, J. Haeberle, K. Henkel, D. Schmeisser, D. Mandal, DNA-Assisted β-phase Nucleation and Alignment of Molecular Dipoles in PVDF Film: A Realization of Self-Poled Bioinspired Flexible Polymer Nanogenerator for Portable Electronic Devices, ACS Appl. Mater. Interfaces. 7 (2015) 16143–16147. https://doi.org/10.1021/acsami.5b04161.

[124] D. Mandal, K.J. Kim, J.S. Lee, Simple Synthesis of Palladium Nanoparticles, β-Phase Formation, and the Control of Chain and Dipole Orientations in Palladium-Doped

Poly(vinylidene fluoride) Thin Films, Langmuir. 28 (2012) 10310–10317. https://doi.org/10.1021/la300983x.

[125] W. Wang, S. Zhang, L. Srisombat, T.R. Lee, R.C. Advincula, Gold-Nanoparticle- and Gold-Nanoshell-Induced Polymorphism in Poly(vinylidene fluoride), Macromol. Mater. Eng. 296 (2011) 178–184. https://doi.org/10.1002/mame.201000271.

[126] Y. Zhu, C. Li, B. Na, R. Lv, B. Chen, J. Zhu, Polar phase formation and competition in the melt crystallization of poly (vinylidene fluoride) containing an ionic liquid, Mater. Chem. Phys. 144 (2014) 194–198. https://doi.org/10.1016/j.matchemphys.2013.12.042.

[127] R. Mejri, J.C. Dias, S.B. Hentati, M.S. Martins, C.M. Costa, S. Lanceros-Mendez, Effect of anion type in the performance of ionic liquid/poly(vinylidene fluoride) electromechanical actuators, J. Non. Cryst. Solids. 453 (2016) 8–15. https://doi.org/10.1016/j.jnoncrysol.2016.09.014.

[128] B. Gusarov, E. Gusarova, B. Viala, L. Gimeno, S. Boisseau, O. Cugat, E. Vandelle, B. Louison, Thermal energy harvesting by piezoelectric PVDF polymer coupled with shape memory alloy, Sensors Actuators A Phys. 243 (2016) 175–181. https://doi.org/10.1016/j.sna.2016.03.026.

[129] P. Guionneau, Crystallography and spin-crossover. A view of breathing materials, Dalt. Trans. 43 (2014) 382–393. https://doi.org/10.1039/C3DT52520A.

[130] N. Ould Moussa, D. Ostrovskii, V.M. Garcia, G. Molnár, K. Tanaka, A.B. Gaspar, J.A. Real, A. Bousseksou, Bidirectional photo-switching of the spin state of iron(II) ions in a triazol based spin crossover complex within the thermal hysteresis loop, Chem. Phys. Lett. 477 (2009) 156–159. https://doi.org/10.1016/j.cplett.2009.06.065.

[131] I. Suleimanov, J.S. Costa, G. Molnár, L. Salmon, I. Fritsky, A. Bousseksou, Effect of ligand substitution in [Fe(H-trz)2(trz)]BF4 spin crossover nanoparticles, French-Ukrainian J. Chem. 3 (2015) 66–72. https://doi.org/10.17721/fujcV3I1P66-72.

[132] N.N. Greenwood, T.C. Gibb, Mössbauer Spectroscopy, Springer Netherlands, Dordrecht, 1971. https://doi.org/10.1007/978-94-009-5697-1.

[133] K. Boukheddaden, F. Varret, A simple formula for the thickness correction of symmetrical mössbauer doublets. Application to spin cross-over systems, Hyperfine Interact. 72 (1992) 349–356. https://doi.org/10.1007/BF02397688.

[134] M. Mikolasek, K. Ridier, D. Bessas, V. Cerantola, G. Félix, G. Chaboussant, M. Piedrahita-Bello, E. Angulo-Cervera, L. Godard, W. Nicolazzi, L. Salmon, G. Molnár, A. Bousseksou, Phase Stability of Spin-Crossover Nanoparticles Investigated by Synchrotron Mössbauer Spectroscopy and Small-Angle Neutron Scattering, J. Phys. Chem. Lett. 10 (2019) 1511–1515. https://doi.org/10.1021/acs.jpclett.9b00335.

[135] K. Boukheddaden, F. Varret, A simple formula for the thickness correction of symmetrical mössbauer doublets. Application to spin cross-over systems, Hyperfine Interact. 72 (1992) 349–356. https://doi.org/10.1007/BF02397688.

[136] V.A. Varnek, L.G. Lavrenova, Mössbauer study of the influence of ligands and anions of the second coordination sphere in Fe(II) complexes with 1,2,4-triazole and 4-amino-1,2,4-triazole on the temperature of the 1A 1⇆5 T 2 spin transitions, J. Struct. Chem. 36 (1995) 104–111. https://doi.org/10.1007/BF02577756.

[137] P. Guionneau, Crystallography and spin-crossover. A view of breathing materials, Dalt. Trans. 43 (2014) 382–393. https://doi.org/10.1039/C3DT52520A.

[138] P. Eaton, P. West, Atomic Force Microscopy, Oxford University Press, 2010. https://doi.org/10.1093/acprof:oso/9780199570454.001.0001.

[139] L.G. Lavrenova, O.G. Shakirova, Spin Crossover and Thermochromism of Iron(II) Coordination Compounds with 1,2,4-Triazoles and Tris(pyrazol-1-yl)methanes, Eur. J. Inorg. Chem. 2013 (2013) 670–682. https://doi.org/10.1002/ejic.201200980.

[140] K. Tashiro, M. Kobayashi, Vibrational spectroscopic study of the ferroelectric phase transition in vinylidene fluoride-trifluoroethylene copolymers: 1. Temperature dependence of the Raman spectra, Polymer (Guildf). 29 (1988) 426–436. https://doi.org/10.1016/0032-3861(88)90359-X.

[141] S. Rat, K. Ridier, L. Vendier, G. Molnár, L. Salmon, A. Bousseksou, Solvatomorphism and structural-spin crossover property relationship in bis[hydrotris(1,2,4-triazol-1-yl)borate]iron(<scp>ii</scp>), CrystEngComm. 19 (2017) 3271–3280. https://doi.org/10.1039/C7CE00741H.

[142] W. Xia, Z. Zhang, PVDF-based dielectric polymers and their applications in electronic materials, IET Nanodielectrics. 1 (2018) 17–31. https://doi.org/10.1049/iet-nde.2018.0001.

[143] K. Ren, R.S. Bortolin, Q.M. Zhang, An investigation of a thermally steerable electroactive polymer/shape memory polymer hybrid actuator, Appl. Phys. Lett. 108 (2016) 062901. https://doi.org/10.1063/1.4941802.

[144] M. Piedrahita-Bello, K. Ridier, M. Mikolasek, G. Molnár, W. Nicolazzi, L. Salmon, A. Bousseksou, Drastic lattice softening in mixed triazole ligand iron(<scp>ii</scp>) spin crossover nanoparticles, Chem. Commun. 55 (2019) 4769–4772. https://doi.org/10.1039/C9CC01619H.

[145] G. Teyssèdre, C. Lacabanne, Study of the thermal and dielectric behavior of P(VDF-TrFE) copolymers in relation with their electroactive properties, Ferroelectrics. 171 (1995) 125–144. https://doi.org/10.1080/00150199508018427.

[146] D. Rus, M.T. Tolley, Design, fabrication and control of soft robots, Nature. 521 (2015) 467–475. https://doi.org/10.1038/nature14543.

[147] G.M. Whitesides, Soft Robotics, Angew. Chemie Int. Ed. 57 (2018) 4258–4273. https://doi.org/10.1002/anie.201800907.

[148] L. Hines, K. Petersen, G.Z. Lum, M. Sitti, Soft Actuators for Small-Scale Robotics, Adv.

Mater. 29 (2017) 1603483. https://doi.org/10.1002/adma.201603483.

[149] Y. Yang, Y. Wu, C. Li, X. Yang, W. Chen, Flexible Actuators for Soft Robotics, Adv. Intell. Syst. 2 (2020) 1900077. https://doi.org/10.1002/aisy.201900077.

[150] P. Brochu, Q. Pei, Advances in Dielectric Elastomers for Actuators and Artificial Muscles, Macromol. Rapid Commun. 31 (2010) 10–36. https://doi.org/10.1002/marc.200900425.

[151] T. Mirfakhrai, J.D.W. Madden, R.H. Baughman, Polymer artificial muscles, Mater. Today. 10 (2007) 30–38. https://doi.org/10.1016/S1369-7021(07)70048-2.

[152] S. Shian, D.R. Clarke, Electrically-tunable surface deformation of a soft elastomer, Soft Matter. 12 (2016) 3137–3141. https://doi.org/10.1039/C6SM00090H.

[153] Q.M. Zhang, Giant Electrostriction and Relaxor Ferroelectric Behavior in Electron-Irradiated Poly(vinylidene fluoride-trifluoroethylene) Copolymer, Science (80-.). 280 (1998) 2101–2104. https://doi.org/10.1126/science.280.5372.2101.

[154] H. Xia, M. Takasaki, T. Hirai, Actuation mechanism of plasticized PVC by electric field, Sensors Actuators A Phys. 157 (2010) 307–312. https://doi.org/10.1016/j.sna.2009.11.028.

[155] L. Chang, H. Chen, Z. Zhu, B. Li, Manufacturing process and electrode properties of palladium-electroded ionic polymer–metal composite, Smart Mater. Struct. 21 (2012) 065018. https://doi.org/10.1088/0964-1726/21/6/065018.

[156] K. Kaneto, Research Trends of Soft Actuators based on Electroactive Polymers and Conducting Polymers, J. Phys. Conf. Ser. 704 (2016) 012004. https://doi.org/10.1088/1742-6596/704/1/012004.

[157] C. Li, E.T. Thostenson, T.-W. Chou, Sensors and actuators based on carbon nanotubes and their composites: A review, Compos. Sci. Technol. 68 (2008) 1227–1249. https://doi.org/10.1016/j.compscitech.2008.01.006.

[158] T.J. White, D.J. Broer, Programmable and adaptive mechanics with liquid crystal polymer networks and elastomers, Nat. Mater. 14 (2015) 1087–1098. https://doi.org/10.1038/nmat4433.

[159] L.T. de Haan, C. Sánchez-Somolinos, C.M.W. Bastiaansen, A.P.H.J. Schenning, D.J. Broer, Engineering of Complex Order and the Macroscopic Deformation of Liquid Crystal Polymer Networks, Angew. Chemie Int. Ed. 51 (2012) 12469–12472. https://doi.org/10.1002/anie.201205964.

[160] M.E. McConney, A. Martinez, V.P. Tondiglia, K.M. Lee, D. Langley, I.I. Smalyukh, T.J. White, Topography from Topology: Photoinduced Surface Features Generated in Liquid Crystal Polymer Networks, Adv. Mater. 25 (2013) 5880–5885. https://doi.org/10.1002/adma.201301891.

[161] S. Iamsaard, S.J. Aßhoff, B. Matt, T. Kudernac, J.J.L.M. Cornelissen, S.P. Fletcher, N. Katsonis, Conversion of light into macroscopic helical motion, Nat. Chem. 6 (2014) 229–

235. https://doi.org/10.1038/nchem.1859.

[162] J.D.W. Madden, N.A. Vandesteeg, P.A. Anquetil, P.G.A. Madden, A. Takshi, R.Z. Pytel, S.R. Lafontaine, P.A. Wieringa, I.W. Hunter, Artificial Muscle Technology: Physical Principles and Naval Prospects, IEEE J. Ocean. Eng. 29 (2004) 706–728. https://doi.org/10.1109/JOE.2004.833135.

[163] T. Tanaka, Phase transitions in gels and a single polymer, Polymer (Guildf). 20 (1979) 1404–1412. https://doi.org/10.1016/0032-3861(79)90281-7.

[164] C. Huang, Q.M. Zhang, A. Jákli, Nematic Anisotropic Liquid-Crystal Gels—Self-Assembled Nanocomposites with High Electromechanical Response, Adv. Funct. Mater. 13 (2003) 525–529. https://doi.org/10.1002/adfm.200304322.

[165] W.M. Huang, Z. Ding, C.C. Wang, J. Wei, Y. Zhao, H. Purnawali, Shape memory materials, Mater. Today. 13 (2010) 54–61. https://doi.org/10.1016/S1369-7021(10)70128-0.

[166] G.B. KAUFFMAN, I. MAYO, The Story of Nitinol: The Serendipitous Discovery of the Memory Metal and Its Applications, Chem. Educ. 2 (1997) 1–21. https://doi.org/10.1007/s00897970111a.

[167] K. Otsuka, X. Ren, Physical metallurgy of Ti–Ni-based shape memory alloys, Prog. Mater. Sci. 50 (2005) 511–678. https://doi.org/10.1016/j.pmatsci.2004.10.001.

[168] C. Laschi, M. Cianchetti, B. Mazzolai, L. Margheri, M. Follador, P. Dario, Soft Robot Arm Inspired by the Octopus, Adv. Robot. 26 (2012) 709–727. https://doi.org/10.1163/156855312X626343.

[169] C. Liu, H. Qin, P.T. Mather, Review of progress in shape-memory polymers, J. Mater. Chem. 17 (2007) 1543. https://doi.org/10.1039/b615954k.

[170] W. Li, Y. Liu, J. Leng, Light-actuated reversible shape memory effect of a polymer composite, Compos. Part A Appl. Sci. Manuf. 110 (2018) 70–75. https://doi.org/10.1016/j.compositesa.2018.04.019.

[171] P. Polygerinos, N. Correll, S.A. Morin, B. Mosadegh, C.D. Onal, K. Petersen, M. Cianchetti, M.T. Tolley, R.F. Shepherd, Soft Robotics: Review of Fluid-Driven Intrinsically Soft Devices; Manufacturing, Sensing, Control, and Applications in Human-Robot Interaction, Adv. Eng. Mater. 19 (2017) 1700016. https://doi.org/10.1002/adem.201700016.

[172] M.A. Rose, J.M. Taylor, S.A. Morin, Adhesion of Morphologically Distinct Crystals to and Selective Release from Elastomeric Surfaces, Chem. Mater. 28 (2016) 8513–8522. https://doi.org/10.1021/acs.chemmater.6b02575.

[173] A. Miriyev, K. Stack, H. Lipson, Soft material for soft actuators, Nat. Commun. 8 (2017) 596. https://doi.org/10.1038/s41467-017-00685-3.

[174] Y. Jin, S.I.M. Paris, J.J. Rack, Bending Materials with Light: Photoreversible Macroscopic Deformations in a Disordered Polymer, Adv. Mater. 23 (2011) 4312–4317. https://doi.org/10.1002/adma.201102157.

[175] M. Morimoto, M. Irie, A Diarylethene Cocrystal that Converts Light into Mechanical Work, J. Am. Chem. Soc. 132 (2010) 14172–14178. https://doi.org/10.1021/ja105356w.

[176] G. Félix, M. Mikolasek, H. Peng, W. Nicolazzi, G. Molnár, A.I. Chumakov, L. Salmon, A. Bousseksou, Lattice dynamics in spin-crossover nanoparticles through nuclear inelastic scattering, Phys. Rev. B. 91 (2015) 024422. https://doi.org/10.1103/PhysRevB.91.024422.

[177] P. Naumov, S.C. Sahoo, B.A. Zakharov, E. V. Boldyreva, Dynamic Single Crystals: Kinematic Analysis of Photoinduced Crystal Jumping (The Photosalient Effect), Angew. Chemie Int. Ed. 52 (2013) 9990–9995. https://doi.org/10.1002/anie.201303757.

[178] K. Liu, C. Cheng, Z. Cheng, K. Wang, R. Ramesh, J. Wu, Giant-Amplitude, High-Work Density Microactuators with Phase Transition Activated Nanolayer Bimorphs, Nano Lett. 12 (2012) 6302–6308. https://doi.org/10.1021/nl303405g.

[179] I.A. Gural'skiy, C.M. Quintero, J.S. Costa, P. Demont, G. Molnár, L. Salmon, H.J. Shepherd, A. Bousseksou, Spin crossover composite materials for electrothermomechanical actuators, J. Mater. Chem. C. 2 (2014) 2949–2955. https://doi.org/10.1039/C4TC00267A.

[180] J.N. Levesque, A. Shah, S. Ekhtiari, J.R. Yan, P. Thornley, D.S. Williams, Three-dimensional printing in orthopaedic surgery: a scoping review, EFORT Open Rev. 5 (2020) 430–441. https://doi.org/10.1302/2058-5241.5.190024.

[181] S. Tibbits, 4D Printing: Multi-Material Shape Change, Archit. Des. 84 (2014) 116–121. https://doi.org/10.1002/ad.1710.

[182] L.G. Lavrenova, O.G. Shakirova, V.N. Ikorskii, V.A. Varnek, L.A. Sheludyakova, S. V Larionov, 1A1 ⇄ 5T2 Spin Transition in New Thermochromic Iron(II) Complexes with 1,2,4-Triazole and 4-Amino-1,2,4-Triazole, Russ. J. Coord. Chem. 29 (2003) 22–27. https://doi.org/10.1023/A:1021834715674.

[183] P. Jusková, L. Matthys, J.-L. Viovy, L. Malaquin, 3D deterministic lateral displacement (3D-DLD) cartridge system for high throughput particle sorting, Chem. Commun. 56 (2020) 5190–5193. https://doi.org/10.1039/C9CC05858C.

[184] S.M. Mirvakili, I.W. Hunter, Multidirectional Artificial Muscles from Nylon, Adv. Mater. 29 (2017) 1604734. https://doi.org/10.1002/adma.201604734.

[185] T.N. Nguyen, K. Rohtlaid, C. Plesse, G.T.M. Nguyen, C. Soyer, S. Grondel, E. Cattan, J.D.W. Madden, F. Vidal, Ultrathin electrochemically driven conducting polymer actuators: fabrication and electrochemomechanical characterization, Electrochim. Acta. 265 (2018) 670–680. https://doi.org/10.1016/j.electacta.2018.02.003.

[186] K. Mukai, K. Asaka, K. Kiyohara, T. Sugino, I. Takeuchi, T. Fukushima, T. Aida, High performance fully plastic actuator based on ionic-liquid-based bucky gel, Electrochim. Acta. 53 (2008) 5555–5562. https://doi.org/10.1016/j.electacta.2008.02.113.

[187] G. Alici, V. Devaud, P. Renaud, G. Spinks, Conducting polymer microactuators operating in air, J. Micromechanics Microengineering. 19 (2009) 025017.

https://doi.org/10.1088/0960-1317/19/2/025017.

[188] C. Ribeiro, C.M. Costa, D.M. Correia, J. Nunes-Pereira, J. Oliveira, P. Martins, R. Gonçalves, V.F. Cardoso, S. Lanceros-Méndez, Electroactive poly(vinylidene fluoride)-based structures for advanced applications, Nat. Protoc. 13 (2018) 681–704. https://doi.org/10.1038/nprot.2017.157.

[189] R. Ram, M. Rahaman, D. Khastgir, Electrical properties of polyvinylidene fluoride (PVDF)/multi-walled carbon nanotube (MWCNT) semi-transparent composites: Modelling of DC conductivity, Compos. Part A Appl. Sci. Manuf. 69 (2015) 30–39. https://doi.org/10.1016/j.compositesa.2014.11.003.

[190] J. Audoit, L. Laffont, A. Lonjon, E. Dantras, C. Lacabanne, Percolative silver nanoplates/PVDF nanocomposites: Bulk and surface electrical conduction, Polymer (Guildf). 78 (2015) 104–110. https://doi.org/10.1016/j.polymer.2015.09.062.

[191] K.J. Åström, R.M. Murray, Feedback Systems, Princeton University Press, 2010. https://doi.org/10.2307/j.ctvcm4gdk.

[192] P. Du, X. Lin, X. Zhang, A multilayer bending model for conducting polymer actuators, Sensors Actuators A Phys. 163 (2010) 240–246. https://doi.org/10.1016/j.sna.2010.06.002.

[193] L. Desborough, Y. Miller, Increasing Customer Value of Industrial Control Performance Monitoring— Honeywell Experience, in: 6th Int. Conf. Chem. Process Control. AIChE Symp., Ser. 326, 2002.

[194] W. Phonsri, D.S. Macedo, K.R. Vignesh, G. Rajaraman, C.G. Davies, G.N.L. Jameson, B. Moubaraki, J.S. Ward, P.E. Kruger, G. Chastanet, K.S. Murray, Halogen Substitution Effects on N 2 O Schiff Base Ligands in Unprecedented Abrupt Fe II Spin Crossover Complexes, Chem. - A Eur. J. 23 (2017) 7052–7065. https://doi.org/10.1002/chem.201700232.

[195] K. Ridier, A.-C. Bas, Y. Zhang, L. Routaboul, L. Salmon, G. Molnár, C. Bergaud, A. Bousseksou, Unprecedented switching endurance affords for high-resolution surface temperature mapping using a spin-crossover film, Nat. Commun. 11 (2020) 3611. https://doi.org/10.1038/s41467-020-17362-7.

[196] A. Grosjean, P. Négrier, P. Bordet, C. Etrillard, D. Mondieig, S. Pechev, E. Lebraud, J.-F. Létard, P. Guionneau, Crystal Structures and Spin Crossover in the Polymeric Material [Fe(Htrz) 2 (trz)](BF 4) Including Coherent-Domain Size Reduction Effects, Eur. J. Inorg. Chem. 2013 (2013) 796–802. https://doi.org/10.1002/ejic.201201121.

[197] S. Rat, K. Ridier, L. Vendier, G. Molnár, L. Salmon, A. Bousseksou, Solvatomorphism and structural-spin crossover property relationship in bis[hydrotris(1,2,4-triazol-1-yl)borate]iron(<scp>ii</scp>), CrystEngComm. 19 (2017) 3271–3280. https://doi.org/10.1039/C7CE00741H.

[198] Q. Li, X. Wang, L. Dong, C. Liu, S. Fan, Spirally deformable soft actuators and their

designable helical actuations based on a highly oriented carbon nanotube film, Soft Matter. 15 (2019) 9788–9796. https://doi.org/10.1039/C9SM01966A.

[199] A. Grosjean, Matériaux polymériques 1D à transition de spin : investigations structurales multi-échelles, 2013.

[200] G. Besendörfer, A. Roosen, Particle Shape and Size Effects on Anisotropic Shrinkage in Tape-Cast Ceramic Layers, J. Am. Ceram. Soc. 91 (2008) 2514–2520. https://doi.org/10.1111/j.1551-2916.2008.02510.x.

[201] A. Sydney Gladman, E.A. Matsumoto, R.G. Nuzzo, L. Mahadevan, J.A. Lewis, Biomimetic 4D printing, Nat. Mater. 15 (2016) 413–418. https://doi.org/10.1038/nmat4544.

Annex:

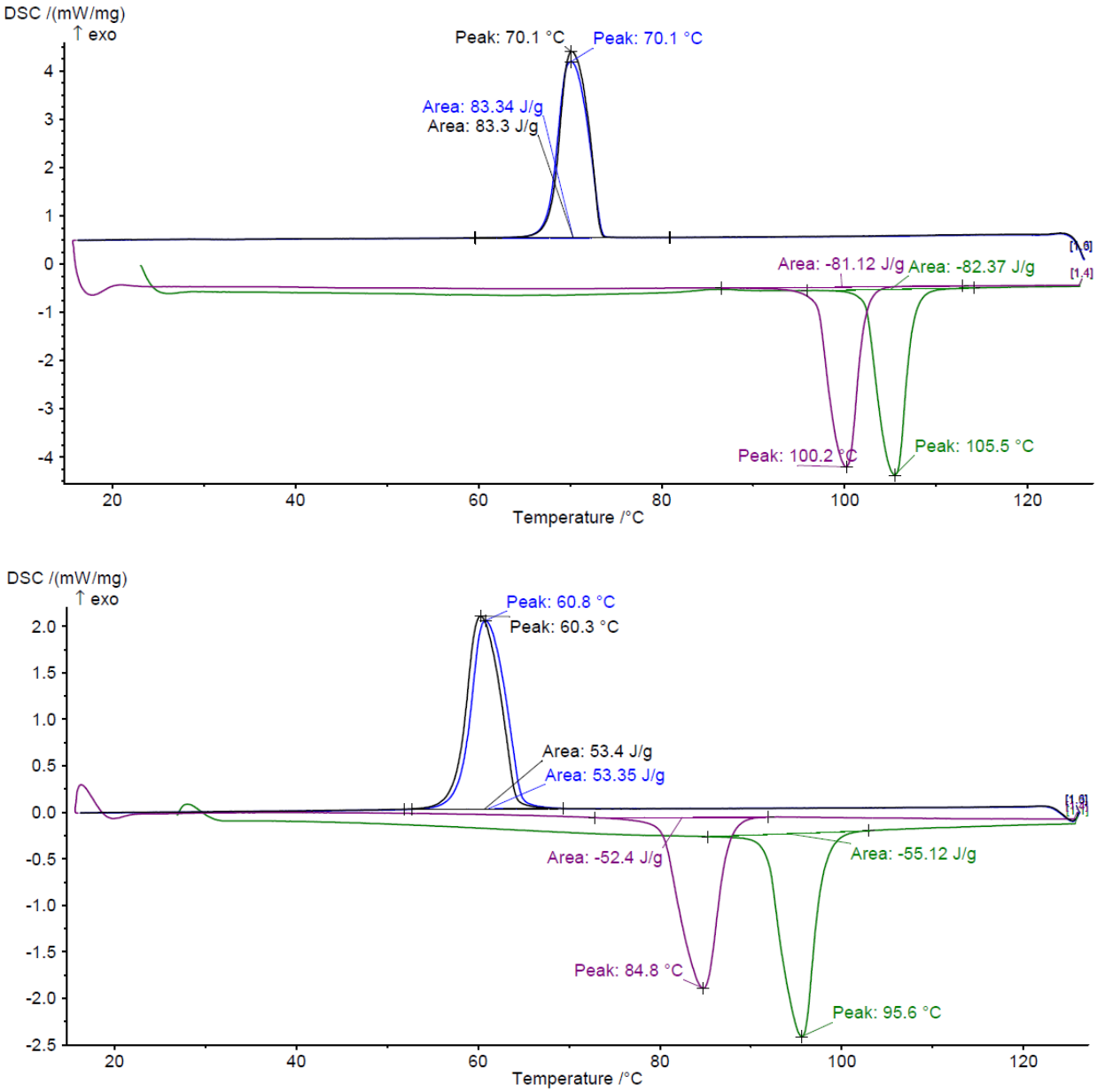

Fig A.2.1 DSC Thermograms for complexes **1** (up) and **2** (down). First heating cycle in green.

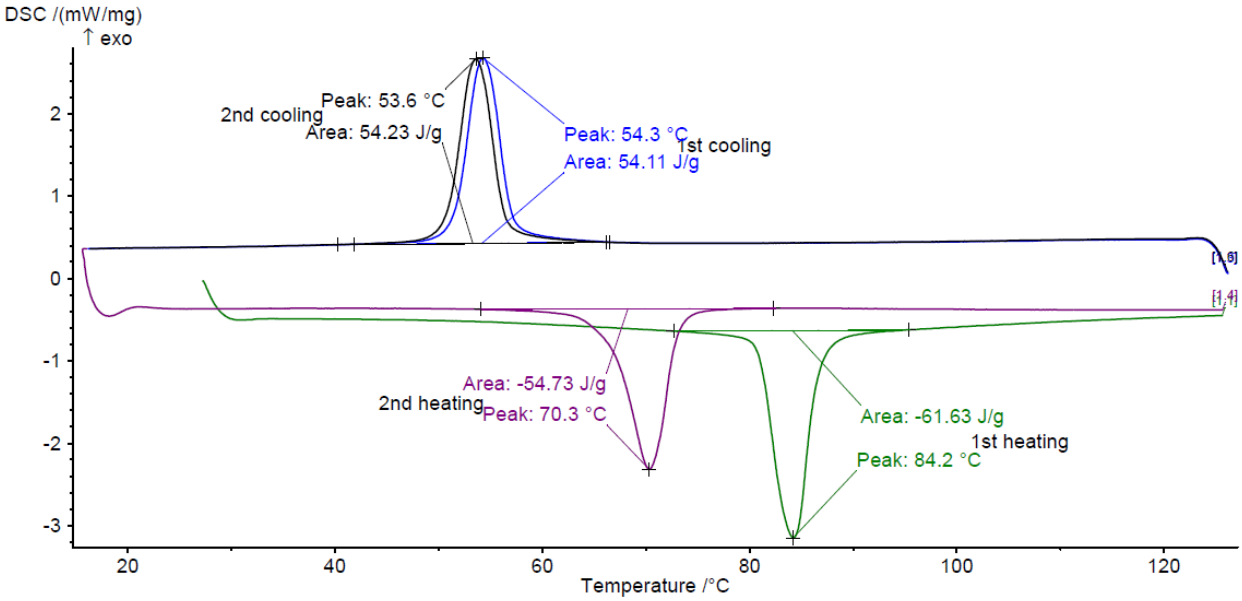

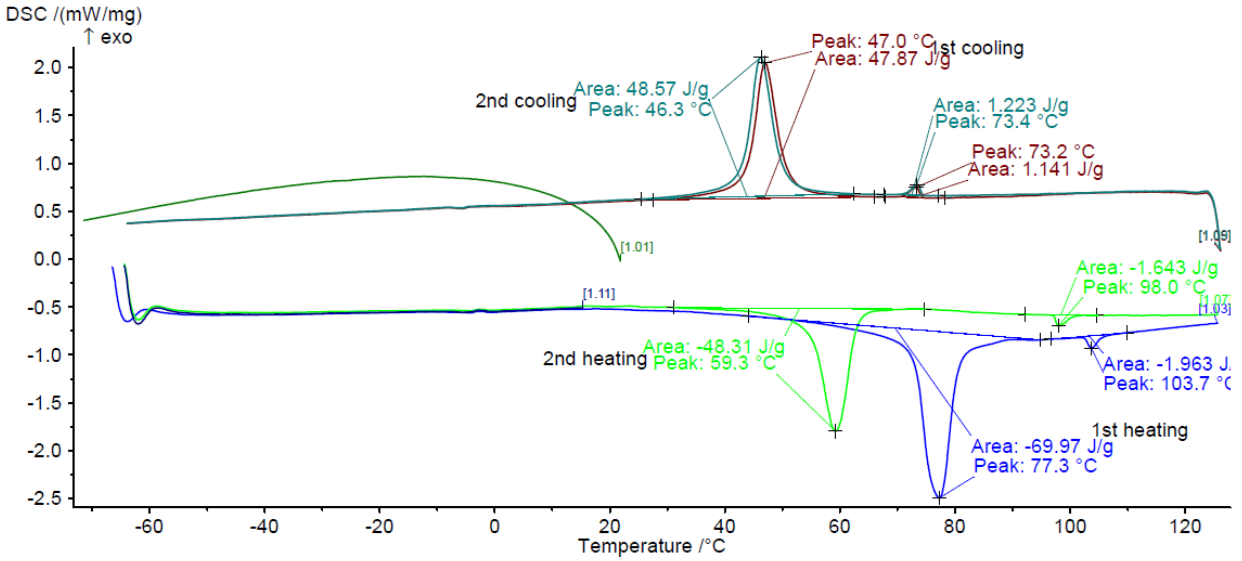

Fig A.2.2 DSC Thermograms for complexes **3** (up) and **4** (down).

Table A.2.3 Selected least-squares fitted Mössbauer data for samples **1**-**4**. δ, Δ_{EQ} and Γ stand for the isomer shift vs metallic α-Fe at room temperature, the quadrupole splitting and the half-height line width, respectively. Values in parentheses are the error bars of statistical origin. Underlined values without error bars were fixed during the fitting procedure.

T (K)	HS doublet			LS doublet			Area
	δ	ΔE$_Q$	Γ/2	δ	ΔE$_Q$	Γ/2	LS/HS
300	0.86	3.2	0.3(3)	0.438(3)	0.279(4)	0.145(4)	94/6
250	0.96(9)	3.2(2)	0.3(2)	0.456(2)	0.277(3)	0.146(3)	94/6
200	1.05(6)	3.2(1)	0.3(1)	0.477(1)	0.273(2)	0.145(1)	93/7
150	1.19(5)	3.31(9)	0.23(8)	0.491(2)	0.269(3)	0.148(3)	94/7
80	1.15(3)	3.51(5)	0.27(4)	0.501(1)	0.264(2)	0.151(2)	92/8

Sample **1**

T (K)	HS doublet			LS doublet			Area
	δ	ΔE$_Q$	Γ/2	δ	ΔE$_Q$	Γ/2	LS/HS
300	0.86	3.1	0.3	0.443(2)	0.244(4)	0.153(3)	96/4
250	0.99	3.12	0.3(1)	0.463(2)	0.246(3)	0.153(3)	96/4
200	1.15	3.2	0.27	0.483(5)	0.24	0.167(7)	97/3
150	1.19	3.31	0.27	0.494(6)	0.23(2)	0.21(2)	98/2
80	1.2(2)	3.5(3)	0.28	0.506(3)	0.229(8)	0.195(7)	96/4

Sample **2**

T (K)	HS doublet			LS doublet			Area
	δ	ΔE$_Q$	Γ/2	δ	ΔE$_Q$	Γ/2	LS/HS
300	1.05(4)	2.81(9)	0.25	0.441(1)	0.240(2)	0.153(2)	96/4
250	1	3.1(5)	0.27	0.461(3)	0.240(6)	0.152(5)	97/3
200	1.1	3.2(2)	0.27	0.481(1)	0.238(2)	0.167(3)	97/3
150	1.19	3.4(3)	0.27	0.491(3)	0.237(4)	0.173(5)	97/3
80	1.2	3.4(2)	0.27	0.504(1)	0.243(2)	0.161(2)	97/3

Sample **3**

T (K)	HS doublet			LS doublet			Area
	δ	ΔE$_Q$	Γ/2	δ	ΔE$_Q$	Γ/2	
320	0.99(4)	2.56(8)	0.21(6)	0.427(4)	0.238(8)	0.162(7)	87/13
300	1.04(4)	2.72(7)	0.20(6)	0.443(2)	0.241(4)	0.157(4)	93/7
250	1	2.9(1)	0.27	0.466(1)	0.241(3)	0.157(2)	94/6
200	1.18(7)	3.2(2)	0.27	0.486(2)	0.246(4)	0.160(3)	95/5
150	1.12(6)	3.4	0.27	0.497(1)	0.247(2)	0.161(2)	96/4
80	1.16(5)	3.33(9)	0.27	0.508(9)	0.247(2)	0.181(2)	96/4

Sample **4**

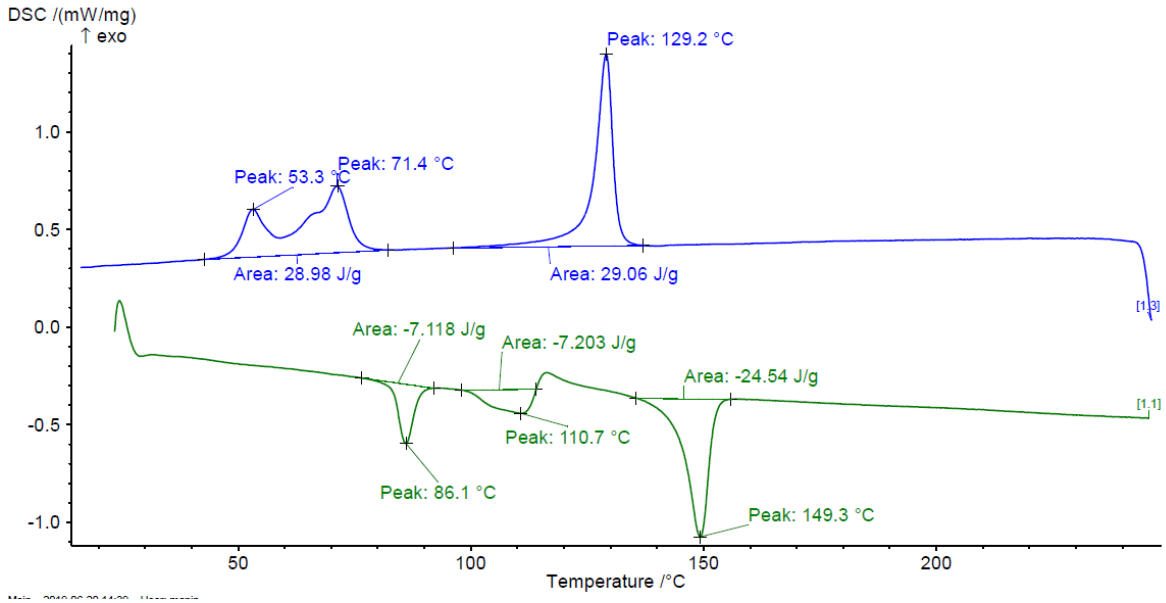

Fig A.2.4 DSC thermogram for composite **3a.**

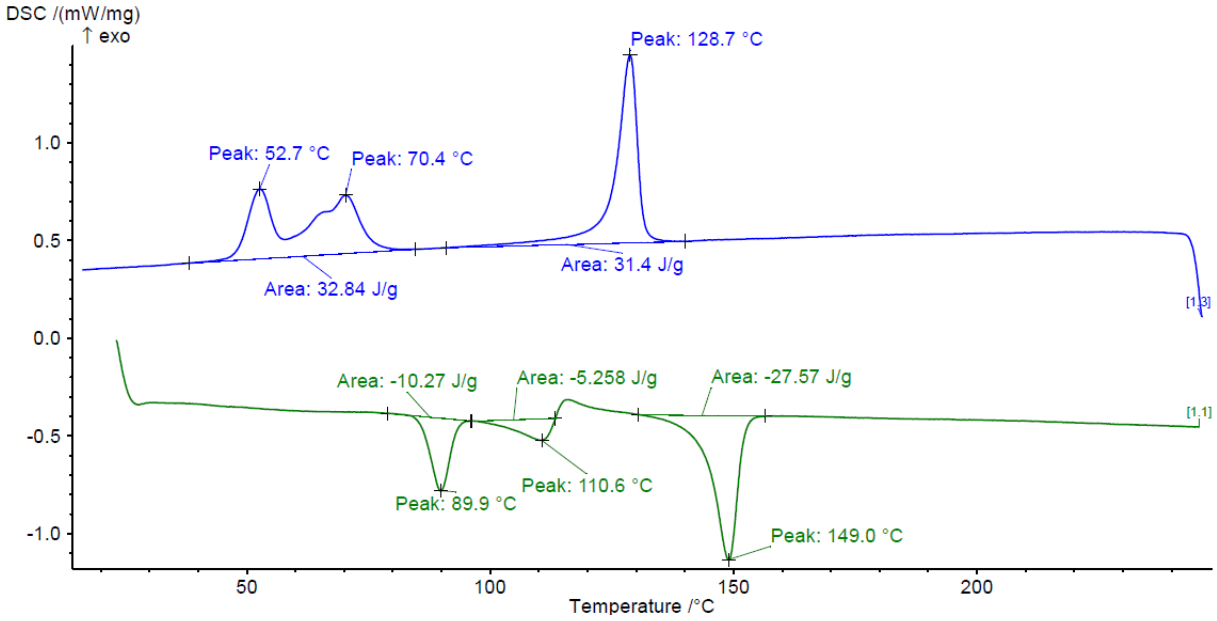

Fig A.2.5 DSC thermogram for composite **6a.**

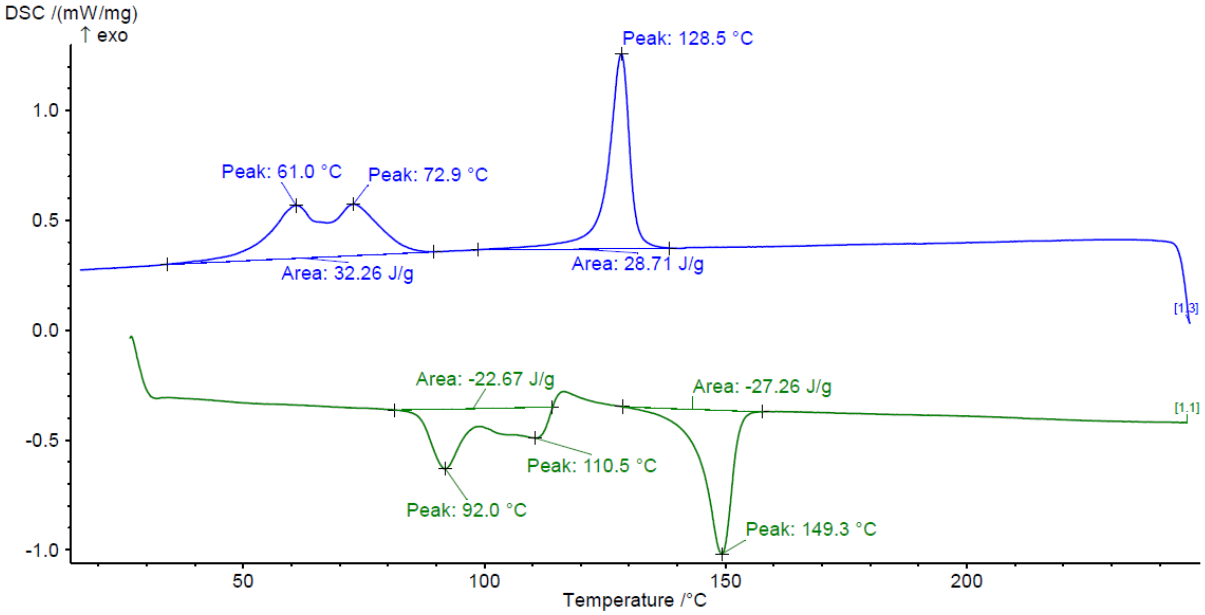

Fig A.2.6 DSC thermogram for composite **7a.**

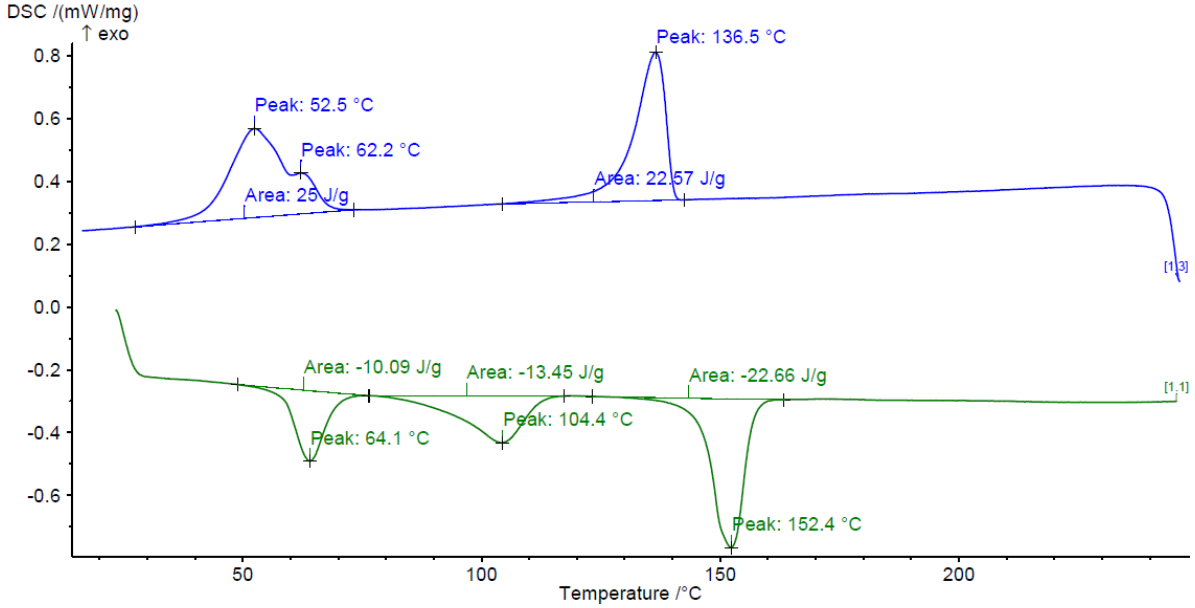

Fig A.2.7 DSC thermogram for composite **8a.**

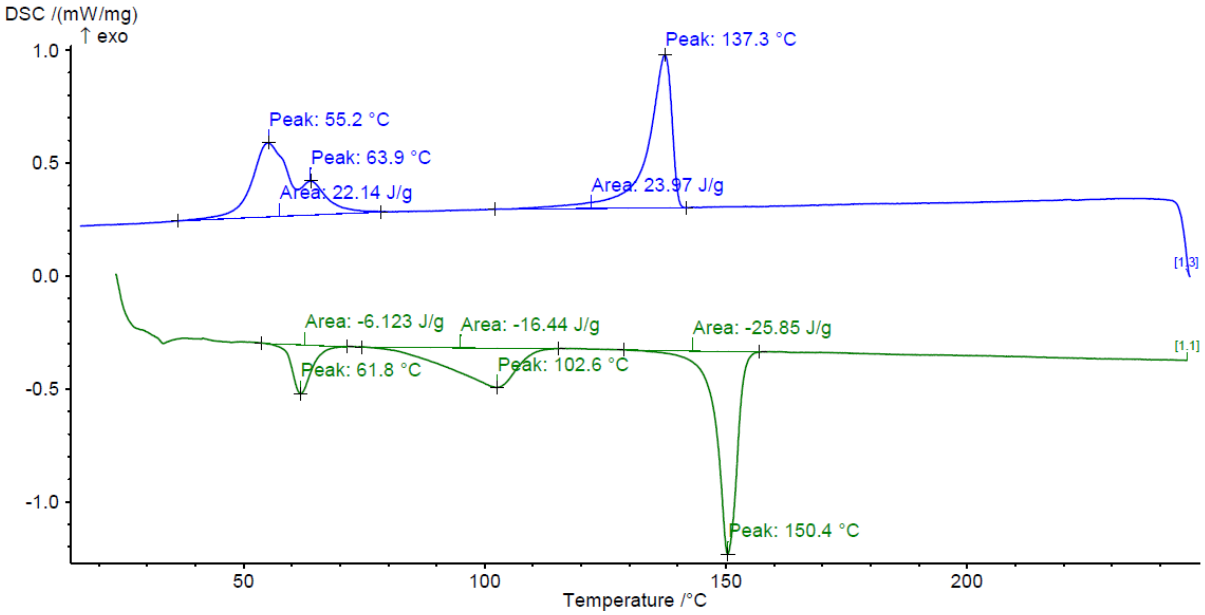

Fig A.2.8 DSC thermogram for composite **8b.**

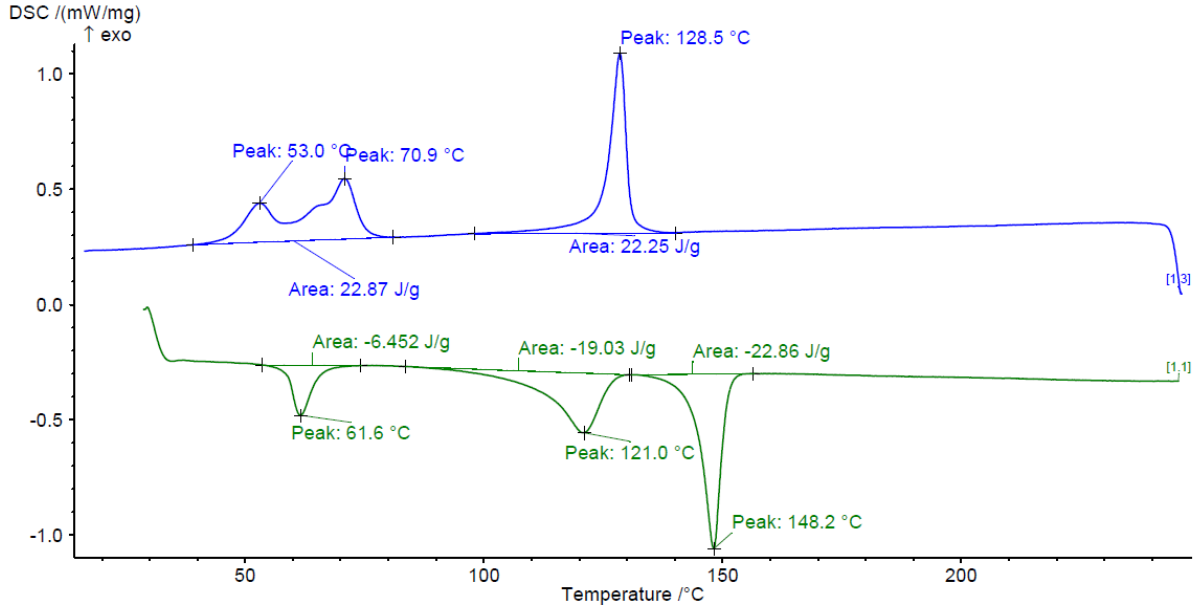

Fig A.2.9 DSC thermogram for composite **8c.**

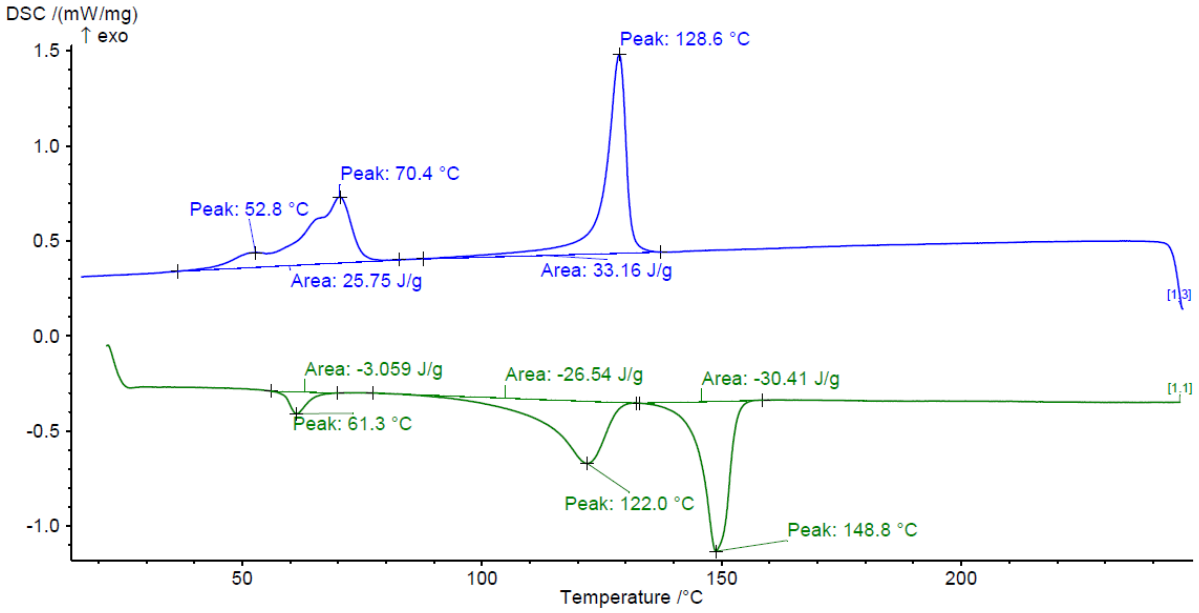

Fig A.2.10 DSC thermogram for composite **8d.**

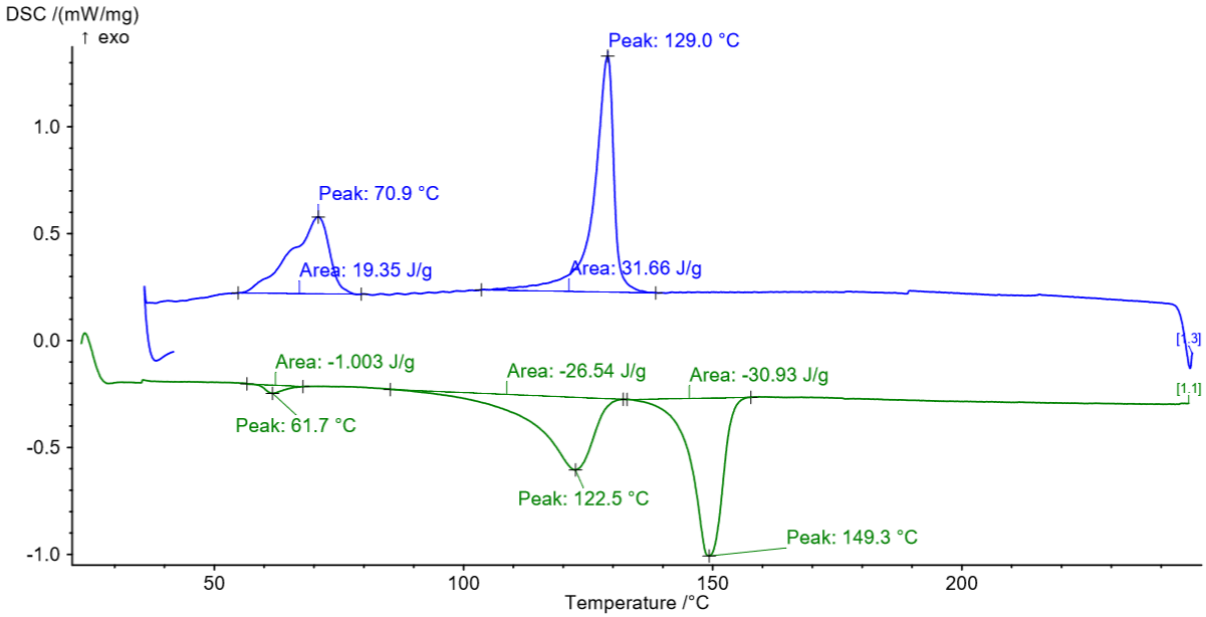

Fig A.2.11 DSC thermogram for composite **8e.**

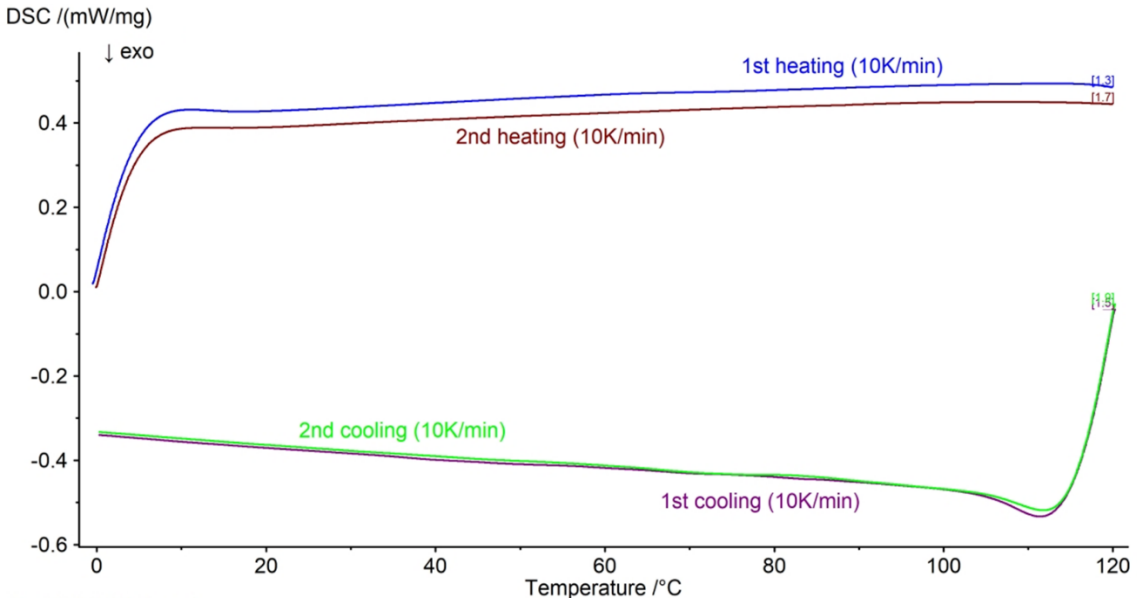

A.3.1 DSC measurements of the pure DS3000 resin.

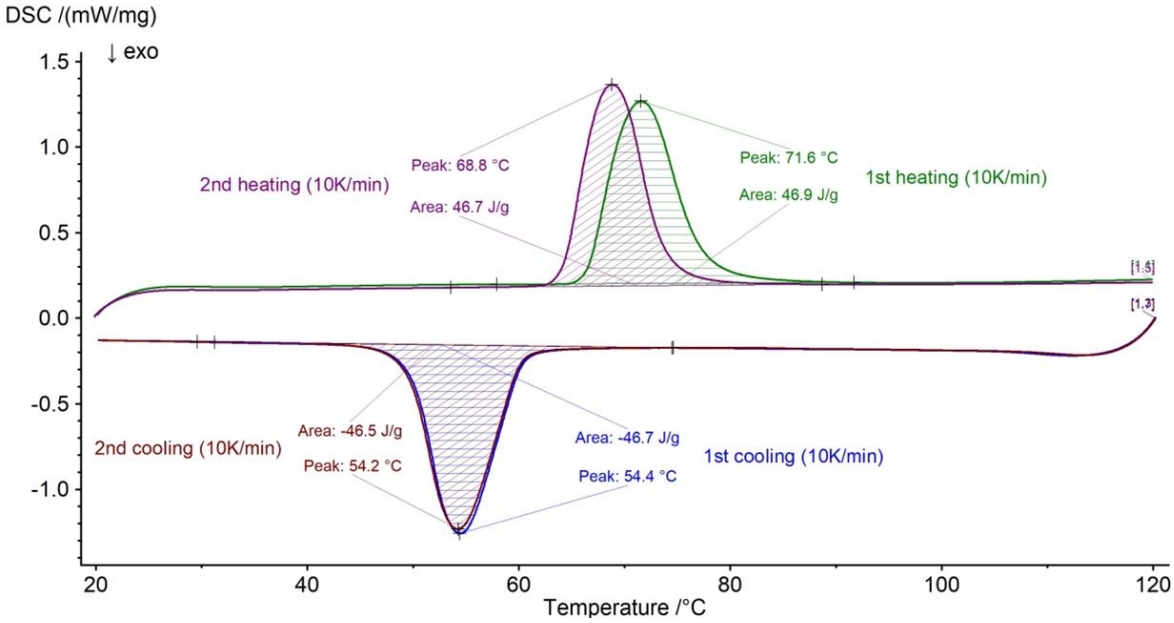

A.3.2 DSC measurement of complex **9**.

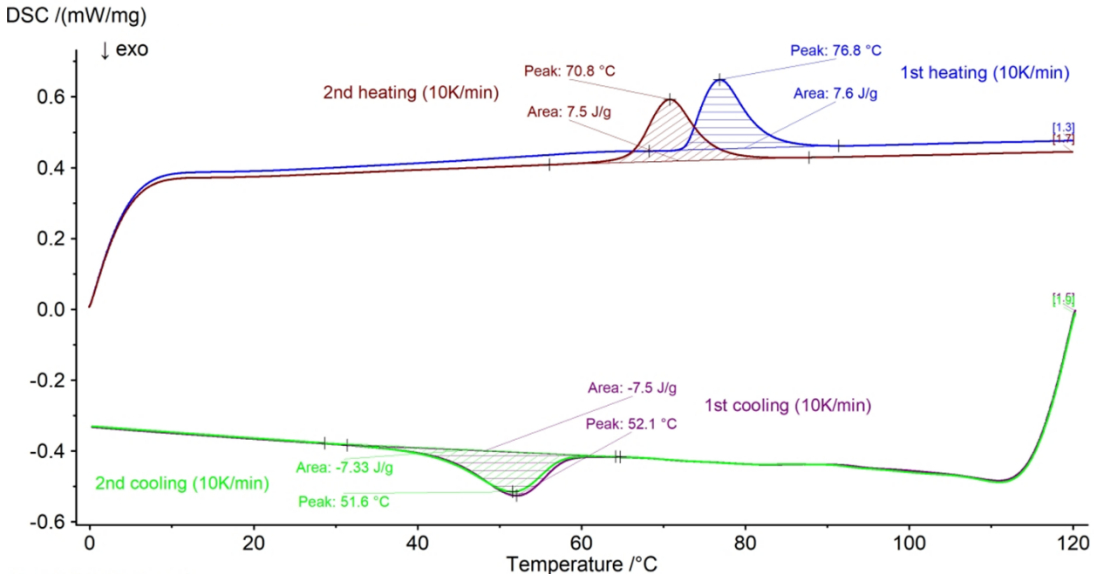

A.3.3 DSC measurements of the SCO(**9**)@DS3000 composite.

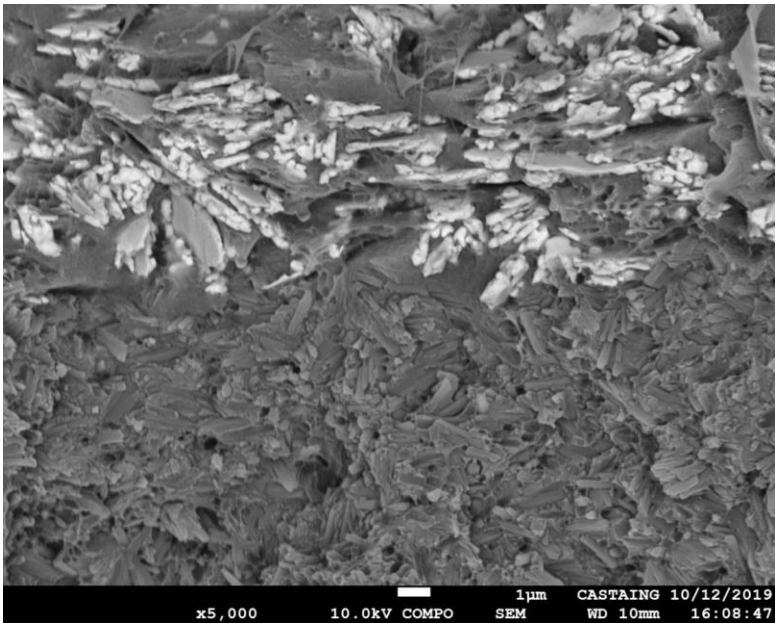

A.3.4 SEM image of the cross section of bilayer actuator **9.** Ag@P(VDF-TrFE) layer (up) and SCO(**9**)@P(VDF-TrFE) layer (down).

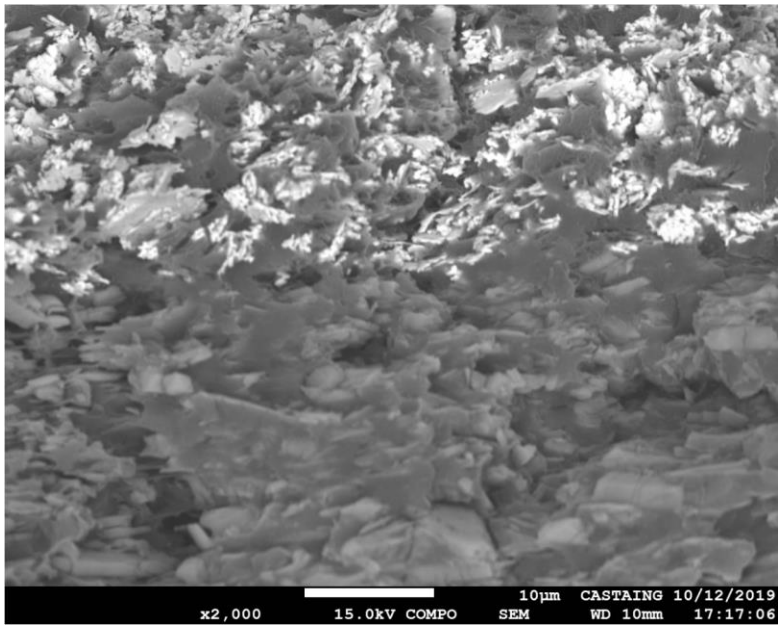

A.3.5 SEM image of the cross section of bilayer actuator **12.** Ag@P(VDF-TrFE) layer (up) and SCO(**12**)@P(VDF-TrFE) layer (down).

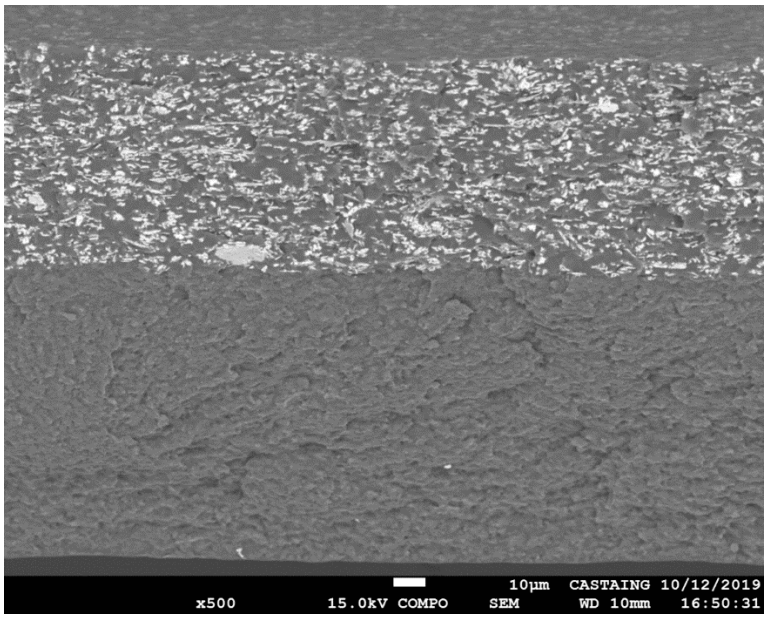

A.3.6 SEM image of the cross section of bilayer actuator **7.** Ag@P(VDF-TrFE) layer (up) and SCO(7)@P(VDF-TrFE) layer (down).

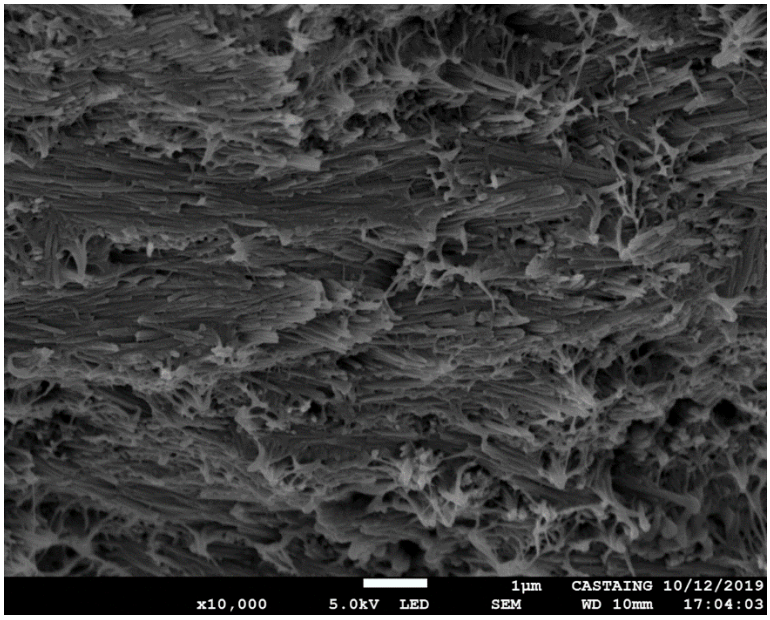

A.3.7 SEM image of the cross section of bilayer actuator **7.** SCO(**7**)@P(VDF-TrFE) layer. Cross-section parallel to the blade-casting direction.

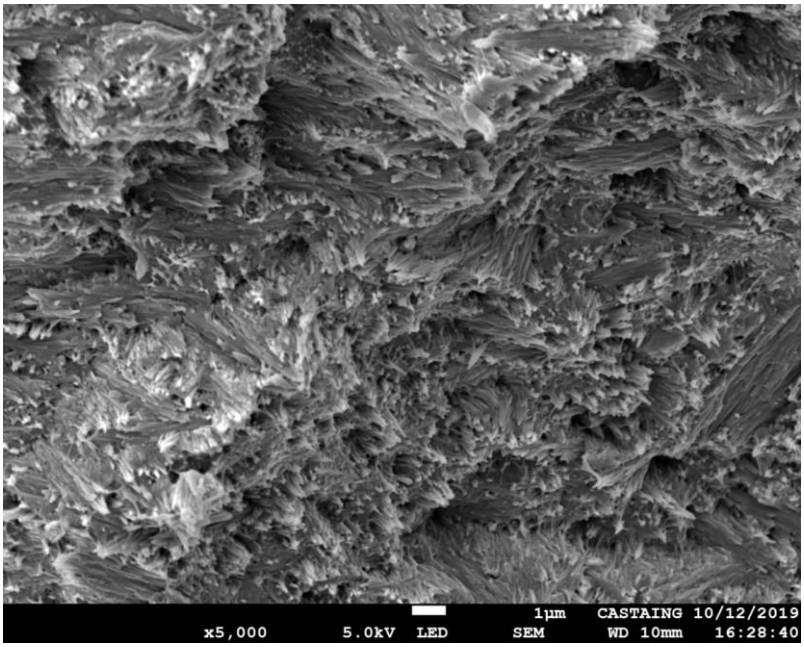

A.3.8 SEM image of the cross section of bilayer actuator **7.** SCO(**7**)@P(VDF-TrFE) layer. Cross-section perpendicular to the blade-casting direction.

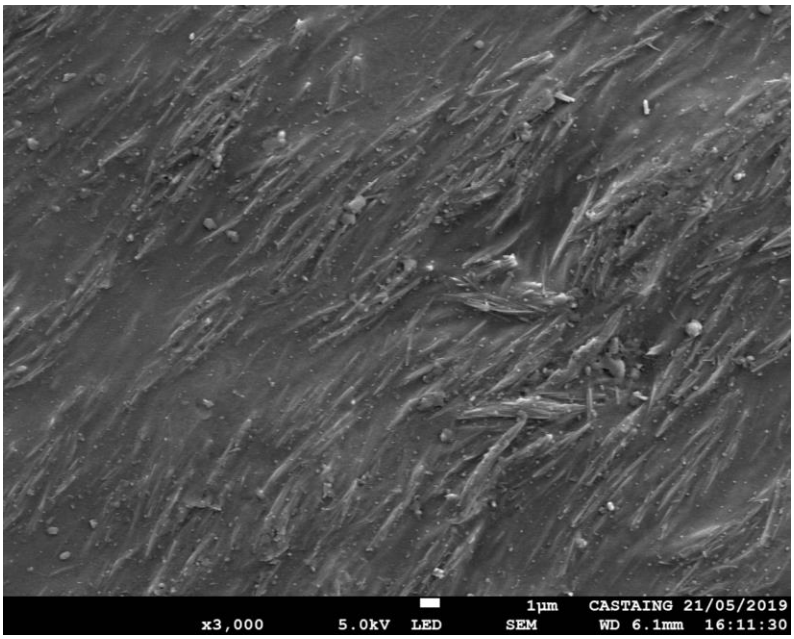

A.3.9 SEM image of the surface of bilayer actuator **7.** SCO(**7**)@P(VDF-TrFE) layer.

Annex 2: List of Publications

(1) Rat, S.; Piedrahita-Bello, M.; Salmon, L.; Molnár, G.; Demont, P.; Bousseksou, A. **Coupling Mechanical and Electrical Properties in Spin Crossover Polymer Composites**. Adv. Mater. 2018, 30 (8), 1705275. https://doi.org/10.1002/adma.201705275

(2) Piedrahita-Bello, M.; Ridier, K.; Mikolasek, M.; Molnár, G.; Nicolazzi, W.; Salmon, L.; Bousseksou, A. **Drastic Lattice Softening in Mixed Triazole Ligand Iron(ii) Spin Crossover Nanoparticles**. Chem. Commun. 2019, 55 (33), 4769–4772. https://doi.org/10.1039/C9CC01619H

(3) Piedrahita-Bello, M.; Salmon, L.; Molnar, G.; Demont, P.; Martin, B.; Bousseksou, A. **Mechano-Electric Coupling in P(VDF-TrFE)/Spin Crossover Composites**. J. Mater. Chem. C 2020. https://doi.org/10.1039/D0TC00780C

(4) Mikolasek, M.; Ridier, K.; Bessas, D.; Cerantola, V.; Félix, G.; Chaboussant, G.; Piedrahita-Bello, M.; Angulo-Cervera, E.; Godard, L.; Nicolazzi, W.; Salmon, L.; Molnár, G.; Bousseksou, A. **Phase Stability of Spin-Crossover Nanoparticles Investigated by Synchrotron Mössbauer Spectroscopy and Small-Angle Neutron Scattering**. J. Phys. Chem. Lett. 2019, 10 (7), 1511–1515. https://doi.org/10.1021/acs.jpclett.9b00335

(5) Enriquez-Cabrera, A.; Rapakousiou, A.; Piedrahita Bello, M.; Molnár, G.; Salmon, L.; Bousseksou, A. **Spin Crossover Polymer Composites, Polymers and Related Soft Materials**. Coord. Chem. Rev. 2020, 419, 213396. https://doi.org/10.1016/j.ccr.2020.213396

(6) Piedrahita-Bello, M.; Angulo-Cervera, J. E.; Courson, R.; Molnár, G.; Malaquin, L.; Thibault, C.; Tondu, B.; Salmon, L.; Bousseksou, A. **4D Printing with Spin-Crossover Polymer Composites**. J. Mater. Chem. C 2020, 8 (18), 6001–6005. https://doi.org/10.1039/D0TC01532F

(7) Shalabaeva, V.; Bas, A.; Piedrahita-Bello, M.; Ridier, K.; Salmon, L.; Thibault, C.; Nicolazzi, W.; Molnár, G.; Bousseksou, A. **Direct Visualization of Local Spin Transition Behaviors in Thin Molecular Films by Bimodal AFM**. Small 2019, 15 (47), 1903892. https://doi.org/10.1002/smll.201903892

(8) Zhang, Y.; Séguy, I.; Ridier, K.; Shalabaeva, V.; Piedrahita-Bello, M.; Rotaru, A.; Salmon, L.; Molnár, G.; Bousseksou, A. **Resistance Switching in Large-Area Vertical Junctions of the Molecular Spin Crossover Complex [Fe(HB(Tz)$_3$)$_2$]: ON/OFF Ratios and Device Stability**. J. Phys. Condens. Matter 2020, 32 (21), 214010. https://doi.org/10.1088/1361-648X/ab741e

(9) Soroceanu, I.; Lupu, S.-L.; Rusu, I.; Piedrahita-Bello, M.; Salmon, L.; Molnár, G.; Demont, P.; Bousseksou, A.; Rotaru, A**. Ligand Substitution Effects on the Charge Transport Properties of the Spin Crossover Complex [Fe(Htrz)$_{1+y-x}$(Trz)$_{2-y}$(NH$_2$Trz)$_x$](BF$_4$)$_y$·nH$_2$O**. J. Phys. Condens. Matter 2020, 32 (26), 264002. https://doi.org/10.1088/1361-648X/ab7ba2

(10) Ridier, K.; Zhang, Y.; Piedrahita-Bello, M.; Quintero, C. M.; Salmon, L.; Molnár, G.; Bergaud, C.; Bousseksou, A. **Heat Capacity and Thermal Damping Properties of Spin-Crossover Molecules: A New Look at an Old Topic**. Adv. Mater. 2020, 32 (21), 2000987. https://doi.org/10.1002/adma.202000987